APPLIED COMPUTATIONAL ELECTROMAGNETICS SOCIETY JOURNAL

October 2021
Vol. 36 No. 10
ISSN 1054-4887

The ACES Journal is abstracted in INSPEC, in Engineering Index, DTIC, Science Citation Index Expanded, the Research Alert, and to Current Contents/Engineering, Computing & Technology.

The illustrations on the front cover have been obtained from the research groups at the Department of Electrical Engineering, The University of Mississippi

OCTOBER 2021 REVIEWERS

Marco Arjona
Muhammad Bilal
Klaus Debes
Vivek Dhoot
Timothy Garner
Rowdra Ghatak
Andrey Grigoriev
Xiaoming Han
Fatih Kaburcuk
William Kefauver
Nikolai Kolev
George Kyriacou
Jin Li
Tao Liang
Umasankar Loganathan
Shengyuan Luo
Anurima Majumdar
Antonio Orlandi
Xiao-Min Pan
Camelia Petrescu
Jalil Rashed-Mohassel
Jagdishkumar Rathod
Lingyun Ren
Suganthi Santhanam
Jan Sikora
Vitawat Sittakul
Prabhu Sundaramoorthy
Xuezhe Tian
Le Huy Trinh
Yunus Uzun
Cong Wang
Joshua Wilson
Run Xiong

THE APPLIED COMPUTATIONAL ELECTROMAGNETICS SOCIETY JOURNAL

Vol. 36 No. 10 October 2021

TABLE OF CONTENTS

Analysis of Bi-Isotropic Media using Hybrid Boundary Element Method

Mirjana T. Perić, Saša S. Ilić, Ana N. Vučković, and Nebojša B. Raičević

Department of Theoretical Electrical Engineering
University of Niš, Faculty of Electronic Engineering, 18000 Niš, Serbia
{mirjana.peric, sasa.ilic, ana.vuckovic, nebojsa.raicevic}@elfak.ni.ac.rs

Abstract **–** This paper proposes the application of the hybrid boundary element method (HBEM) for analysis of bi-isotropic media of Tellegen type. In previous applications of this method it was possible to analyze only the electromagnetic problems in isotropic media. The main contribution of this paper is the modification of the method itself, in order to solve a large scale of quasi-static TEM problems in bi-isotropic media. Detailed theoretical analysis and HBEM procedure are described and applied. Characteristic parameters of a microstrip line with bi-isotropic substrate are analyzed. Obtained results have been compared with available numerical and software simulation results. A close results match can be noticed.

Index Terms **–** bi-isotropic media, characteristic impedance, effective relative permittivity, finite element methods, hybrid boundary element method, microstrip line.

I. INTRODUCTION

Analysis of the microwave transmission lines is the main subject of researches in the World for more than seven decades. Since the first publication about a stripline, back in the 1950s, [1], and its modifications that followed in the forthcoming years, scientists analyzed, simplified, and designed new structures. Nowadays, these structures have found wide applications in telecommunication systems, in microwave integrated circuits, for microwave filters and antennas design, delay lines, directional couplers, etc., [2]. Various numerical and analytical methods can be used, with more or less accuracy, for the microwave transmission lines analysis [3]. Some of those methods are: the variational method [4], the boundary element method (BEM) [5], the finite element method (FEM) [6], the method of lines [7], etc.

The hybrid boundary element method (HBEM), [8] is a simple, powerful, and accurate procedure used to analyze isotropic electric and magnetic multilayered structures. The method is developed as a combination of the equivalent electrodes method (EEM) [9] and BEM [10]. During the previous 10 years, the HBEM is applied to solve different planar and axisymmetric electromagnetic problems. In [11], the method is used for electromagnetic field determination in the vicinity of cable joints and terminations. The magnetic force of permanent magnet systems is calculated using the HBEM in [12] and [13]. Different configurations of microwave transmission lines have been successfully analyzed by HBEM in [2,14-17]. The method efficiency for electrostatic problems solving is improved in [17].

The real challenge was to extend the method for the analysis of bi-isotropic (BI) (nonreciprocal chiral) media and apply it for analysis of microstrip lines with BI substrate. In [14-17], only the transmission lines with isotropic substrates have been considered. The HBEM, described and applied in those papers, took into account only the free charges placed at perfect electric conductors (PECs) as well as the polarized electric charges placed at separating surfaces [14,17].

In order to make a base for this method application in bi-isotropic media, it was necessary to introduce a concept of fictitious magnetic polarized charges, [12,13,18]. Also, it is necessary to determine the relations between the normal component of the electric as well as the magnetic field and polarized electric and magnetic charges.

The HBEM application is now based on the electric and magnetic scalar potential determination, so only static as well as quasi-static analysis can be performed using this method.

Unlike a wide range of literature and methods that deals with the analysis of systems in isotropic materials, the BI media, due to their complexity, are not so common subject of researches. But, in the last few years, attention was paid to the bi-isotropic and anisotropic materials and their application in electromagnetics [19-28]. The method of moments and the point-matching method (PMM) have been used to solve an integral equation in [22] in order to determine characteristic parameters of multiconductor lines with bi-isotropic layers. Analysis of shielded microstrip lines with bi-isotropic substrate have been also done in [23]

Submitted On: April 12, 2021
Accepted On: September 26, 2021

https://doi.org/10.47037/2021.ACES.J.361001

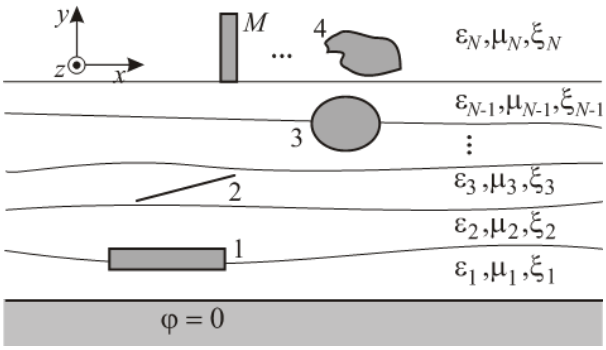

Fig. 1. Geometry of a multiconductor line in a layered bi-isotropic medium with zero potential plane.

and [24], applying strong FEM formulation and exponential matrix technique, respectively.

The geometry of a system which consists of N PECs embedded in an arbitrary number of dielectric layers is depicted in Figure 1.

The HBEM application for solving and analyzing bi-isotropic medium is described in detail in Section III. The electric and magnetic polarized surface charge distributions of a line charge placed above boundary surface of two bi-isotropic layers of Tellegen type is considered. These results will be compared with the analytical solution and used to verify the HBEM procedure. The next step is to analyze a microstrip with a ground plane of infinite width and a bi-isotropic substrate of finite width. Obtained HBEM results have been compared with results given by other researchers.

II. CONSTITUTIVE RELATIONS FOR BI-ISOTROPIC MEDIUM

A bi-isotropic medium consists of elements with electric and magnetic dipoles. The constitutive relations for bi-isotropic materials are, [29],

$$\boldsymbol{D} = \varepsilon \boldsymbol{E} + \xi \boldsymbol{H} \text{ and} \tag{1}$$

$$\boldsymbol{B} = \zeta \boldsymbol{E} + \mu \boldsymbol{H}, \tag{2}$$

where ξ and ζ are the magnetoelectric coupling coefficients, ε is the permittivity and μ is the permeability of medium. The parameters ξ and ζ are usually given in the form

$$\zeta = (\chi + j\kappa)\sqrt{\varepsilon_0 \mu_0} \text{ and} \tag{3}$$

$$\xi = (\chi - j\kappa)\sqrt{\varepsilon_0 \mu_0}. \tag{4}$$

Replacing these parameters into eqns (1) and (2),

$$\boldsymbol{D} = \varepsilon \boldsymbol{E} + (\chi - j\kappa)\sqrt{\varepsilon_0 \mu_0}\boldsymbol{H} \text{ and} \tag{5}$$

$$\boldsymbol{B} = (\chi + j\kappa)\sqrt{\varepsilon_0 \mu_0}\boldsymbol{E} + \mu \boldsymbol{H}. \tag{6}$$

Parameter κ describes the degree of chirality, ε_0 and μ_0 are the permittivity and permeability of the air. Parameter χ is a dimensionless quantity for the degree of inherent nonreciprocity. Nonreciprocal nonchiral medium ($\chi \neq 0$, $\kappa = 0$) is so-called Tellegen material, [29]. Such kind of media will be analyzed in this paper.

For Tellegen medium, it is satisfied $\zeta = \xi$, so the constitutive relations have the following form,

$$\boldsymbol{D} = \varepsilon \boldsymbol{E} + \xi \boldsymbol{H} \text{ and} \tag{7}$$

$$\boldsymbol{B} = \xi \boldsymbol{E} + \mu \boldsymbol{H}. \tag{8}$$

The parameter $p = \xi^2/(\varepsilon\mu)$, $0 < p < 1$, describes the level of bi-isotropic effect, [18]. For example, if $p = 0.1$, the media is with less expressed bi-isotropic effect. For $p = 0.9$, the media has high level of bi-isotropy.

III. HBEM APPLICATION

In order to apply the HBEM, the system given in Figure 2 is considered. A line charge q' is placed at height h above the separating surface of two BI layers with parameters ε_1, μ_1, ξ_1 for the layer 1, and ε_2, μ_2, ξ_2 for the layer 2.

The boundary surface between two BI layers of finite width $2L$ can be discretized as it is presented in Figure 3.

The surface is divided into N strips (segments) of width $\Delta l = 2L/N$. According to the HBEM application for the isotropic layers, [14], each of those segments should be replaced with equivalent electrodes (EEs) of radius $a_e = \Delta l/\pi$, placed along the segment's axis. Those EEs are polarized line charges q'_{vi} ($i = 1, 2, ..., N$), placed in the air.

In order to apply HBEM for the BI layers, the necessary modification of the method includes an introduction of fictitious magnetic line charges q'_{mi} ($i = 1, 2, ..., N$). The positions and radii of these charges are the same as for the electric charges. Those charges are also placed in the air.

Based on the described procedure, a HBEM model, shown in Figure 3, is formed.

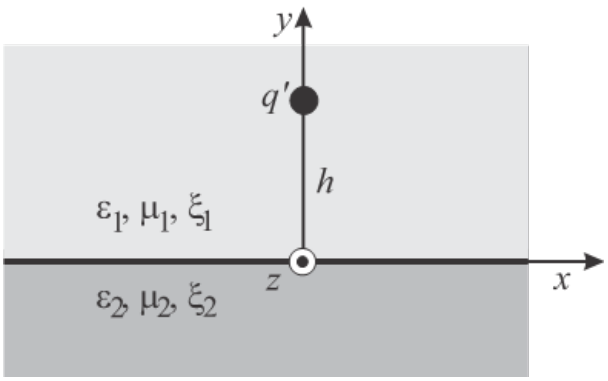

Fig. 2. Line charge placed above the boundary surface of two bi-isotropic layers.

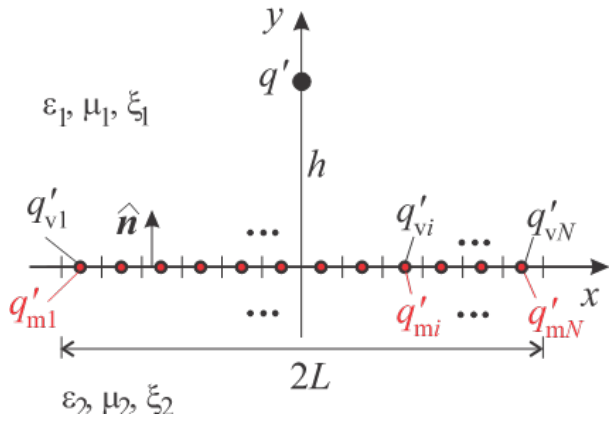

Fig. 3. HBEM application model.

The electric and magnetic scalar potentials at any point $M(x, y)$ for the considered system given in Figure 3, are

$$\varphi = -\frac{q'}{2\pi\varepsilon_1(1-p_1)}\ln\sqrt{x^2+(y-h)^2} - \\ -\sum_{i=1}^{N}\frac{q'_{vi}}{2\pi\varepsilon_0}\ln\sqrt{(x-x_i)^2+(y-y_i)^2}, \tag{9}$$

$$\varphi_m = \frac{\xi_1 q'}{2\pi\varepsilon_1\mu_1(1-p_1)}\ln\sqrt{x^2+(y-h)^2} - \\ -\sum_{i=1}^{N}\frac{q'_{mi}}{2\pi}\ln\sqrt{(x-x_i)^2+(y-y_i)^2}, \tag{10}$$

where $x_i = -L+(2i-1)\Delta l/2$ and $y_i = 0$ $(i = 1, 2, ..., N)$ are the line charges positions. The parameter p_1 is $p_1 = \xi_1^2/(\varepsilon_1\mu_1)$.

In order to determine the unknown values of the line charges, according to the HBEM procedure, [14], it is necessary to form a system of linear equations using the boundary condition, i.e. a relation between the normal component of the electric field and total surface charges. The HBEM application for BI materials needs a modification. It is necessary to use the relations between normal component of electric as well as magnetic field and total surface charges, i.e. electric and fictitious magnetic charges.

A. Relations between normal components of electric as well as magnetic field at boundary surface of two BI media and total surface charges

Using eqns (7) and (8), the relations between the electromagnetic field components in the layer 1 and 2, for the system visible in the Figure 2 are, respectively,

$$\boldsymbol{D}_1 = \varepsilon_1\boldsymbol{E}_1 + \xi_1\boldsymbol{H}_1, \tag{11}$$

$$\boldsymbol{D}_2 = \varepsilon_2\boldsymbol{E}_2 + \xi_2\boldsymbol{H}_2, \tag{12}$$

$$\boldsymbol{B}_1 = \mu_1\boldsymbol{H}_1 + \xi_1\boldsymbol{E}_1, \tag{13}$$

$$\boldsymbol{B}_2 = \mu_2\boldsymbol{H}_2 + \xi_2\boldsymbol{E}_2. \tag{14}$$

Replacing those expressions into boundary conditions for the normal components of electric and magnetic fields, the following relations are obtained:

$$\varepsilon_1 E_{1n} + \xi_1 H_{1n} = \varepsilon_2 E_{2n} + \xi_2 H_{2n} \text{ and} \tag{15}$$

$$\mu_1 H_{1n} + \xi_1 E_{1n} = \mu_2 H_{2n} + \xi_2 E_{2n}. \tag{16}$$

From those equations, it can be written

$$E_{2n} = \frac{\varepsilon_1\mu_2 - \xi_1\xi_2}{\varepsilon_2\mu_2 - \xi_2^2}E_{1n} + \frac{\xi_1\mu_2 - \xi_2\mu_1}{\varepsilon_2\mu_2 - \xi_2^2}H_{1n}, \tag{17}$$

$$H_{2n} = \frac{\xi_1\varepsilon_2 - \xi_2\varepsilon_1}{\varepsilon_2\mu_2 - \xi_2^2}E_{1n} + \frac{\varepsilon_2\mu_1 - \xi_1\xi_2}{\varepsilon_2\mu_2 - \xi_2^2}H_{1n}. \tag{18}$$

The electric polarized surface charge density, η_v, at the boundary surface between any two layers is, [18]

$$\eta_v = P_{2n} - P_{1n}, \tag{19}$$

where P_{1n} and P_{2n} are normal components of polarization vector in layers 1 and 2, respectively, defined as

$$P_{1n} = (\varepsilon_1 - \varepsilon_0)E_{1n} + \xi_1 H_{1n} \text{ and} \tag{20}$$

$$P_{2n} = (\varepsilon_2 - \varepsilon_0)E_{2n} + \xi_2 H_{2n}. \tag{21}$$

Replacing eqns. (17) and (18) into (21), the expression (19) is

$$\eta_v = \frac{\varepsilon_0[\mu_2(\varepsilon_2-\varepsilon_1) - \xi_2^2 + \xi_1\xi_2]}{\varepsilon_2\mu_2 - \xi_2^2}E_{1n}^{(0+)} + \\ + \frac{\varepsilon_0[\xi_2\mu_1 - \xi_1\mu_2]}{\varepsilon_2\mu_2 - \xi_2^2}H_{1n}^{(0+)}. \tag{22}$$

The label (0+) indicates the electric and magnetic field components in layer 1 for $y = 0$.

The magnetic polarized surface charge can be calculated as

$$\eta_m = M_{2n} - M_{1n}, \tag{23}$$

where the normal components of magnetization vector in layers 1 and 2, M_{1n} and M_{2n}, are defined as

$$M_{1n} = \left(\frac{\mu_1}{\mu_0} - 1\right)H_{1n} + \frac{\xi_1}{\mu_0}E_{1n}, \tag{24}$$

$$M_{2n} = \left(\frac{\mu_2}{\mu_0} - 1\right)H_{2n} + \frac{\xi_2}{\mu_0}E_{2n}. \tag{25}$$

Replacing eqns. (17) and (18) into (25), the expression (23) is

$$\eta_m = \frac{\xi_2\varepsilon_1 - \xi_1\varepsilon_2}{\varepsilon_2\mu_2 - \xi_2^2}E_{1n}^{(0+)} + \\ + \frac{\varepsilon_2(\mu_2-\mu_1) - \xi_2^2 + \xi_1\xi_2}{\varepsilon_2\mu_2 - \xi_2^2}H_{1n}^{(0+)}. \tag{26}$$

Using eqns (22) and (26), it is possible to express the relations between the normal components of electric

as well as magnetic field and electric and magnetic polarized surface charges,

$$\hat{n}\boldsymbol{E}_{i0}^{(0+)} = \frac{\varepsilon_2(\mu_1-\mu_2)-\xi_1\xi_2+\xi_2^2}{\varepsilon_0[(\varepsilon_1-\varepsilon_2)(\mu_2-\mu_1)+(\xi_1-\xi_2)^2]}\eta_{\mathrm{v}i}+ \\ + \frac{\mu_1\xi_2-\mu_2\xi_1}{(\varepsilon_1-\varepsilon_2)(\mu_2-\mu_1)+(\xi_1-\xi_2)^2}\eta_{\mathrm{m}i}, \quad (27)$$

$$\hat{n}\boldsymbol{H}_{i0}^{(0+)} = \frac{\varepsilon_1\xi_2-\varepsilon_2\xi_1}{\varepsilon_0[(\varepsilon_1-\varepsilon_2)(\mu_2-\mu_1)+(\xi_1-\xi_2)^2]}\eta_{\mathrm{v}i}+ \\ + \frac{\mu_2(\varepsilon_1-\varepsilon_2)-\xi_1\xi_2+\xi_2^2}{(\varepsilon_1-\varepsilon_2)(\mu_2-\mu_1)+(\xi_1-\xi_2)^2}\eta_{\mathrm{m}i}, \quad (28)$$

where $\eta_{\mathrm{v}i} = q'_{\mathrm{v}i}/\Delta l$ and $\eta_{\mathrm{m}i} = q'_{\mathrm{m}i}/\Delta l$ $(i = 1, 2, ..., N)$ are electric and magnetic polarized surface charges for $i-$th segment. $\hat{n} = \hat{y}$ is a unit normal vector. $q'_{\mathrm{v}i}$ and $q'_{\mathrm{m}i}$ expressed over the normal components of electric and magnetic fields are

$$q'_{\mathrm{v}i} = \frac{\varepsilon_0[\mu_2(\varepsilon_2-\varepsilon_1)-\xi_2^2+\xi_1\xi_2]}{\varepsilon_2\mu_2-\xi_2^2}\Delta l E_y^{(0+)}+ \\ + \frac{\varepsilon_0[\xi_2\mu_1-\xi_1\mu_2]}{\varepsilon_2\mu_2-\xi_2^2}\Delta l H_y^{(0+)}, \quad (29)$$

$$q'_{\mathrm{m}i} = \frac{\xi_2\varepsilon_1-\xi_1\varepsilon_2}{\varepsilon_2\mu_2-\xi_2^2}\Delta l E_y^{(0+)}+ \\ + \frac{\varepsilon_2(\mu_2-\mu_1)-\xi_2^2+\xi_1\xi_2}{\varepsilon_2\mu_2-\xi_2^2}\Delta l H_y^{(0+)}. \quad (30)$$

B. System of linear equations formulation

Unlike the HBEM, applied for modeling configurations presented in [14-17], where the PMM is applied only on the surfaces of electric charges (only those charges exist at separating surfaces), here it is necessary to apply the PMM on the surface of i-th magnetic line charge as well as on i-th electric line charge. So, the total number of unknowns is $2N$ and the formed system of equations has a dimension $2N \times 2N$. During this method application, it should be taken into account:

- An influence of the charge itself (electric or magnetic), with matching points: $x_{\mathrm{p}} = x_i$, $y_{\mathrm{p}} = a_{\mathrm{e}}$;
- An influence of other charge which is placed at the same position (magnetic or electric), with the matching points: $x_{\mathrm{p}} = x_i$, $y_{\mathrm{p}} = a_{\mathrm{e}}$;
- Influences of all the other electric and magnetic line charges, with the matching points: $x_{\mathrm{p}} = x_i$, $y_{\mathrm{p}} = 0$,
- An influence of primary line charge, with the matching points: $x_{\mathrm{p}} = x_i$, $y_{\mathrm{p}} = 0$.

Application of this procedure using eqns (29) and (30), gives the system of linear equations:

$$q'_{\mathrm{v}i} = \mathrm{A}\Delta l\left[\frac{q'}{2\pi\varepsilon_1(1-p_1)}\frac{-h}{x_i^2+h^2}+\frac{q'_{\mathrm{v}1}}{2\pi\varepsilon_0}\cdot 0+\right. \\ + \frac{q'_{\mathrm{v}2}}{2\pi\varepsilon_0}\cdot 0+...+\frac{q'_{\mathrm{v}i}}{2\pi\varepsilon_0}\frac{1}{a_{\mathrm{e}}}+...+\left.\frac{q'_{\mathrm{v}N}}{2\pi\varepsilon_0}\cdot 0\right]+ \\ + \mathrm{B}\Delta l\left[\frac{\xi_1 q'}{2\pi\varepsilon_1\mu_1(1-p_1)}\frac{h}{x_i^2+h^2}+\frac{q'_{\mathrm{m}1}}{2\pi}\cdot 0+\right. \\ \left. + \frac{q'_{\mathrm{m}2}}{2\pi}\cdot 0+...+\frac{q'_{\mathrm{m}i}}{2\pi}\frac{1}{a_{\mathrm{e}}}+...+\frac{q'_{\mathrm{m}N}}{2\pi}\cdot 0\right], \quad (31)$$

$$q'_{\mathrm{m}i} = \mathrm{C}\Delta l\left[\frac{q'}{2\pi\varepsilon_1(1-p_1)}\frac{-h}{x_i^2+h^2}+\frac{q'_{\mathrm{v}1}}{2\pi\varepsilon_0}\cdot 0+\right. \\ \left. + \frac{q'_{\mathrm{v}2}}{2\pi\varepsilon_0}\cdot 0+...+\frac{q'_{\mathrm{v}i}}{2\pi\varepsilon_0}\frac{1}{a_{\mathrm{e}}}+...+\frac{q'_{\mathrm{v}N}}{2\pi\varepsilon_0}\cdot 0\right]+ \\ + \mathrm{D}\Delta l\left[\frac{\xi_1 q'}{2\pi\varepsilon_1\mu_1(1-p_1)}\frac{h}{x_i^2+h^2}+\frac{q'_{\mathrm{m}1}}{2\pi}\cdot 0+\right. \\ \left. + \frac{q'_{\mathrm{m}2}}{2\pi}\cdot 0+...+\frac{q'_{\mathrm{m}i}}{2\pi}\frac{1}{a_{\mathrm{e}}}+...+\frac{q'_{\mathrm{m}N}}{2\pi}\cdot 0\right], \quad (32)$$

for $i = 1, 2, ..., N$.

The constants A, B, C, and D are

$$\mathrm{A} = \frac{\varepsilon_0[\mu_2(\varepsilon_2-\varepsilon_1)-\xi_2^2+\xi_1\xi_2]}{\varepsilon_2\mu_2-\xi_2^2}, \quad (33)$$

$$\mathrm{B} = \frac{\varepsilon_0[\xi_2\mu_1-\xi_1\mu_2]}{\varepsilon_2\mu_2-\xi_2^2}, \quad (34)$$

$$\mathrm{C} = \frac{\xi_2\varepsilon_1-\xi_1\varepsilon_2}{\varepsilon_2\mu_2-\xi_2^2} \text{ and} \quad (35)$$

$$\mathrm{D} = \frac{\varepsilon_2(\mu_2-\mu_1)-\xi_2^2+\xi_1\xi_2}{\varepsilon_2\mu_2-\xi_2^2}. \quad (36)$$

The expressions (31) and (32), after normalizations $q'_{\mathrm{v}i}{}'/q'$, $q'_{\mathrm{m}i}\sqrt{\varepsilon_0\mu_0}/q'$ and x_i/h, as well as using that $a_{\mathrm{e}} = \Delta l/\pi = 2L/\pi N$, have a form

$$\frac{q'_{\mathrm{v}i}}{q'}\left(1-\frac{\mathrm{A}}{\varepsilon_0 2}\right)-\frac{q'_{\mathrm{m}i}\sqrt{\varepsilon_0\mu_0}}{q'}\frac{\mathrm{B}}{2\sqrt{\varepsilon_0\mu_0}} = \\ = \left(-\mathrm{A}+\mathrm{B}\frac{\xi_1}{\mu_1}\right)\frac{\frac{L}{h}}{\pi\varepsilon_1(1-p_1)N\left(1+\left(\frac{x_i}{h}\right)^2\right)} \quad (37)$$

$$-\frac{q'_{\mathrm{v}i}}{q'}\frac{\mathrm{C}}{\varepsilon_0 2}+\frac{q'_{\mathrm{m}i}\sqrt{\varepsilon_0\mu_0}}{q'}\frac{1}{\sqrt{\varepsilon_0\mu_0}}\left(1-\frac{\mathrm{D}}{2}\right) = \\ = \left(-\mathrm{C}+\mathrm{D}\frac{\xi_1}{\mu_1}\right)\frac{\frac{L}{h}}{\pi\varepsilon_1(1-p_1)N\left(1+\left(\frac{x_i}{h}\right)^2\right)}, \quad (38)$$

$$i = 1, 2, ..., N.$$

After solving this system using Mathematica, the electric and magnetic polarized line charges are calculated. Also, it is possible to determine the electric and magnetic polarized surface charges.

IV. RESULTS AND DISCUSSION

The normalized electric and magnetic polarized surface charges distributions along the boundary surface between two bi-isotropic layers for the system presented in Figure 2 are shown in Figures 4–7. Different types of bi-isotropic materials are analyzed.

The values for ε_{r1}, μ_{r1}, p_1 as well as ε_{r2}, μ_{r2}, p_2 are denoted in the figures. The other parameters, necessary for the HBEM application, are:

$$L/h = 20,\ \xi_1 = \sqrt{p_1\varepsilon_0\mu_0\varepsilon_{r1}\mu_{r1}},$$
$$\xi_2 = \sqrt{p_2\varepsilon_0\mu_0\varepsilon_{r2}\mu_{r2}},\ \varepsilon_0 = 8.85\cdot 10^{-12}\,\mathrm{F/m},$$
$$\mu_0 = 4\pi\cdot 10^{-7}\,\mathrm{H/m} \text{ and } N = 100.$$

In those figures, analytical solution results are also shown. These results have been calculated using eqns (22) and (26) as well as the expressions for the electric and magnetic fields in the bi-isotropic media, obtained using image theorem, [19].

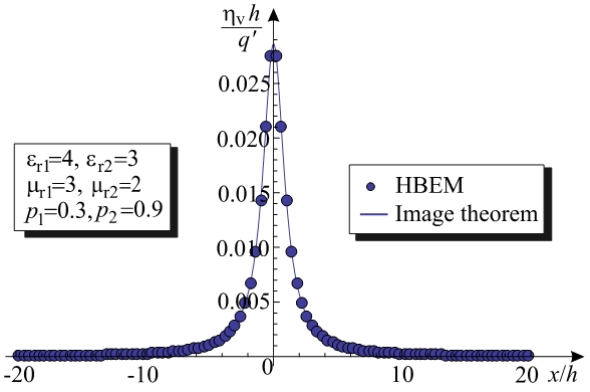

Fig. 4. Normalized electric polarized surface charges distribution on boundary surface of two layers with low and high bi-isotropic effects.

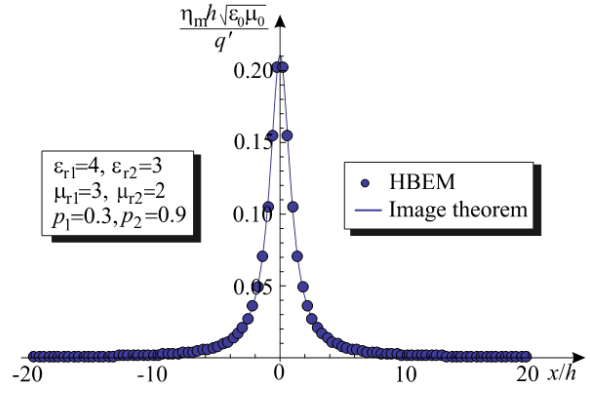

Fig. 5. Normalized magnetic polarized surface charges distribution on boundary surface of two layers with low and high bi-isotropic effects.

The total number of unknown EEs for the HBEM calculation is $N_{tot} = 2N = 200$. The computation time is less than a second. Increasing the number of unknowns, the computation time increases too.

Analyzing the figures, where different types of BI effects are given, it can be concluded that the verification of HBEM procedure is successful. An excellent results match is obtained. So, there is no need for modification of used number of unknowns.

When both layers are isotropic, which is achieved for $p_1 = p_2 = 0$, only electric polarized surface charges exists as it shown in Figures 6 and 7.

A. Microstrip line with bi-isotropic substrate

According to the procedures described in Section III for bi-isotropic layers and in [15] for the isotropic media, a quasi-static analysis of microstrip line with a BI substrate of Tellegen type (Figure 8), is performed.

In order to form an equivalent HBEM model, it was necessary to apply the image theorem, considering that the substrate is placed on the zero potential plane of infinite width. That system is shown in Figure 9. With q'_{vi}, q'_{mi} $(i = 1,...,N)$ and q'_{fj} $(j = 1,...,M)$ are denoted polarized electric (v), fictitious magnetic (m) and free (f) line charges, respectively. All those charges are placed in the air, according to the HBEM.

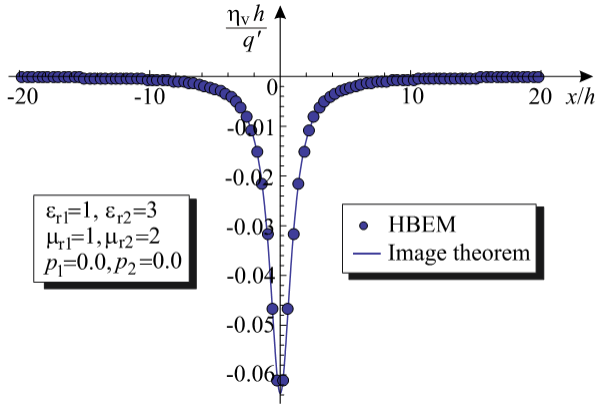

Fig. 6. Normalized electric polarized surface charges distribution on boundary surface of two isotropic layers.

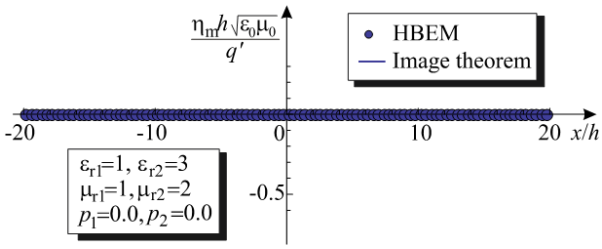

Fig. 7. Normalized magnetic polarized surface charges distribution on boundary surface of two isotropic layers.

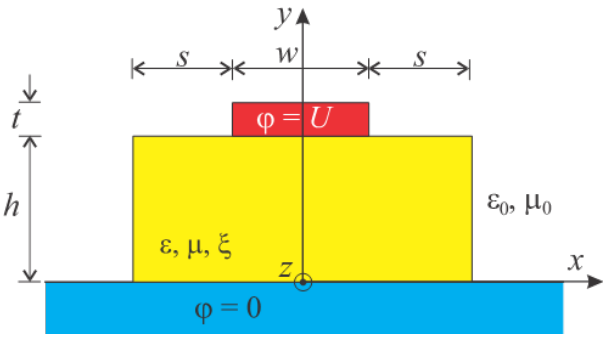

Fig. 8. Microstrip line with bi-isotropic substrate.

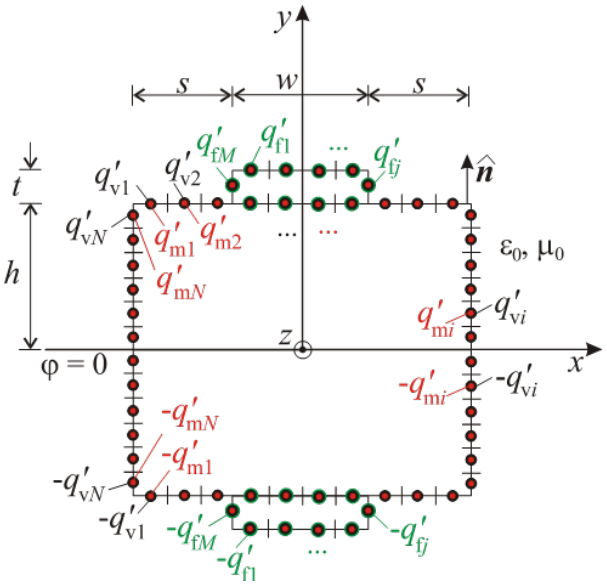

Fig. 9. HBEM application model.

The electric scalar as well as magnetic scalar potentials at any point of the system are:

$$\varphi = \sum_{j=1}^{M} \frac{q'_{\mathrm{f}j}}{2\pi\varepsilon_0} \ln \sqrt{\frac{(x-x_{\mathrm{f}j})^2+(y+y_{\mathrm{f}j})^2}{(x-x_{\mathrm{f}j})^2+(y-y_{\mathrm{f}j})^2}} + \sum_{i=1}^{N} \frac{q'_{\mathrm{v}i}}{2\pi\varepsilon_0} \ln \sqrt{\frac{(x-x_{\mathrm{v}i})^2+(y+y_{\mathrm{v}i})^2}{(x-x_{\mathrm{v}i})^2+(y-y_{\mathrm{v}i})^2}}, \tag{39}$$

$$\varphi_{\mathrm{m}} = \sum_{i=1}^{N} \frac{q'_{\mathrm{m}i}}{2\pi} \ln \sqrt{\frac{(x-x_{\mathrm{m}i})^2+(y+y_{\mathrm{m}i})^2}{(x-x_{\mathrm{m}i})^2+(y-y_{\mathrm{m}i})^2}}. \tag{40}$$

The total number of unknowns is $N_{\mathrm{tot}} = M + 2N$.

Applying the procedure described in Section III, the unknown line charges are calculated, so the capacitance per unit length can be obtained using,

$$C' = \sum_{j=1}^{M} \frac{q'_{\mathrm{f}j}}{U}. \tag{41}$$

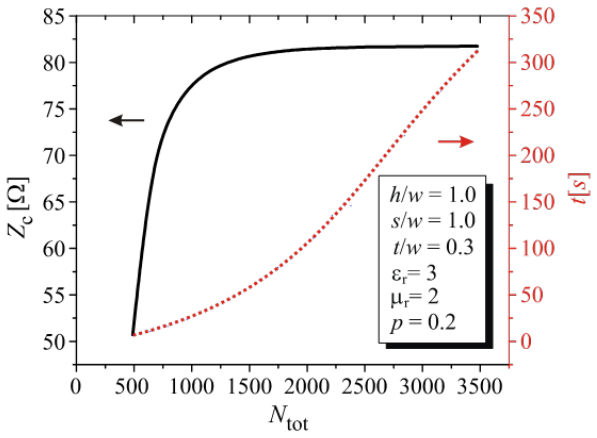

Fig. 10. Results convergence and computation time.

Table 1: Characteristic impedance and effective relative permittivity values of microstrip line

	Z_c [Ω]		$\varepsilon_r^{\mathrm{eff}}$	
p	**HBEM**	**FlexPDE**	**HBEM**	**FlexPDE**
0	76.359	76.578	2.0890	2.0921
0.2	81.346	81.137	1.8410	1.8470
0.6	95.550	95.389	1.3341	1.3360
0.9	114.080	113.694	0.9360	0.9359

The characteristic impedance is determined as $Z_c = Z_{c0} \Big/ \sqrt{\varepsilon_{\mathrm{r}}^{\mathrm{eff}}}$, with $\varepsilon_{\mathrm{r}}^{\mathrm{eff}} = C'/C'_0$ the effective dielectric permittivity is denoted. Z_{c0} is the characteristic impedance of the stripline without dielectrics (free space). An optimal number of unknowns is determined according to the characteristic impedance results convergence, shown in Figure 10. In the same figure, with a dotted red line, the computation time for parameters: $h/w = s/w = 1, t/w = 0.3$, $\varepsilon_{\mathrm{r}} = 3$, $\mu_{\mathrm{r}} = 2$ and $p = 0.2$, is also given.

For all following calculations, the total number of unknowns will be $N_{tot} = 1800$.

The results for characteristic impedance and effective relative permittivity have been compared with the results obtained using FlexPDE software, [30], in Table 1, for different values of parameter p.

The microstrip dimensions and parameters are:

$$h/w = 1.0,\ s/w = 1,\ t/w = 0.3,\ \varepsilon_r = 3 \text{ and } \mu_r = 2.$$

In this table, the values obtained for an isotropic substrate, for $p = 0$, are also included. The characteristic parameters of a microstrip line with an isotropic substrate was analyzed separately in [15] and compared with available results. From Table 1, it can be concluded that

Table 2: CPU time

	Number of unknowns	Computation (CPU) time [s]
HBEM	1800 EEs	93
FlexPDE	151,162 finite elements	345

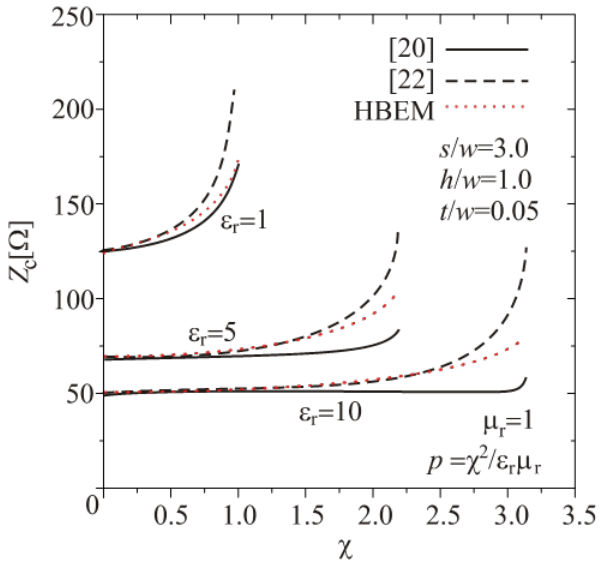

Fig. 11. Characteristic impedance as a function of parameter χ for different values of ε_r.

a close results match is obtained. The error rate is less than 0.5%. The computation (CPU) time for both methods is given in Table 2. All calculations are performed on a quad-core CPU (Intel i5) running at 3.1 GHz and 4 GB RAM in double precision.

The CPU time in the HBEM application includes the time necessary to determine the positions of EEs, to fill the matrix, solve a formed system of linear equations as well as to calculate the characteristic parameters. On the other side, the FlexPDE CPU time consists of the time to run the problem, observe the output results, and calculate characteristic parameters.

The analysis of microstrip lines with a BI substrate is not so common in practice, as it is mentioned in the introduction of this paper. In [22], the characteristic impedance distribution of microstrip line with infinitely ground plane and BI substrate of Tellegen type is given. Those results as well as the results presented in [20] have been compared in Figure 11 with the HBEM results, for different values of relative permittivity and parameter χ, where $\chi = \xi/\sqrt{\varepsilon_0\mu_0}$.

The dimensions and parameters of analyzed microstrip line are: $h/w = 1.0$, $s/w = 3$, $t/w = 0.05$, $\mu_r = 1$, and $N = 1800$.

In [22], it is mentioned that in [20] the authors made an assumption that electric charges do not create the magnetic flux, as well as the magnetic dipoles do not have any influence on the electric potential distribution. That is the main reason of large results disagreement in those two results, especially for larger values of parameter χ. Significantly smaller disagreement can be noticed between HBEM results and those from [22]. It should be emphasized that HBEM analysis has been done for a configuration where the substrate has finite width and finite thickness, since in [20] and [22] the substrate has an infinite width as well as thickness.

V. CONCLUSION

A development and implementation of HBEM, that started 10 years ago, have continued in this paper through the method extension for the analysis of BI media. It is now possible to analyze not only transmission lines, but also the other electromagnetic systems where BI materials are used. The HBEM's application has been illustrated through the examples showing its generality and accuracy.

ACKNOWLEDGMENT

This work has been supported by the Ministry of Education, Science and Technological Development of the Republic of Serbia.

REFERENCES

[1] D. M. Pozar, *Microwave Engineering*, John Wiley & Sons, New York, Chapter 1, pp. 2-6, 2012.

[2] M. Perić, *Quasi-static approach for microwave transmission lines analysis*, PhD thesis, Faculty of Electronic Engineering of Niš, Serbia, 2015. (in Serbian).

[3] T. Itoh and R. Mittra, "Analysis of microstrip transmission lines," *Advances in Microwaves*, no. 8, pp. 67-141, 1974.

[4] E. Yamashita and R. Mittra, "Variational method for the analysis of microstrip lines," *IEEE Trans. Microwave Theory Tech.*, vol. 16, no. 4, pp. 251-256, Apr. 1968.

[5] T. Chang and C. Tan, "Analysis of a shielded microstrip line with finite metallization thickness by the boundary element method," *IEEE Trans. Microwave Theory Tech.*, no. 8, pp. 1130–1132, Aug. 1990.

[6] Z. Pantic and R. Mittra, "Quasi-TEM analysis of microwave transmission lines by the finite-element method," *IEEE Trans. Microwave Theory Tech.*, vol. 34, no. 11, pp. 1096–1103, Nov. 1986.

[7] Y. M. Tao, D. G. Fang, and X. G. Li, "Full-wave hybrid-mode analysis of general structure of coplanar waveguides by using the method of lines,"

Microwave Opt. Technol. Lett., vol. 7, no. 1, pp. 17–19, Jan. 1994.

[8] N. Raičević, S. Aleksić, and S. Ilić, "A hybrid boundary element method for multi-layer electrostatic and magnetostatic problems," *Journal of Electromagnetics*, vol. 30, no. 6, pp. 507-524, 2010.

[9] D. M. Veličković, "Equivalent electrodes method," *Scientific Review*, no. 21-22, pp. 207-248, 1996.

[10] C. A. Brebbi, J. C. F. Telles, and L. C. Wrobel., *Boundary Element Techniques*: *Theory and Applications in Engineering*, Springer, Berlin, 1984.

[11] N. Raičević, S. Ilić, and S. Aleksić, "Application of new hybrid boundary element method on the cable terminations," *14th International IGTE Symposium*, Graz, Austria, pp. 56-61, Sept. 2010.

[12] A. Vučković, N. Raičević, and M. Perić, "Radially magnetized ring permanent magnet modelling in the vicinity of soft magnetic cylinder," *Safety Engineering*, vol. 8, no. 1, pp. 33-37, 2018.

[13] A. Vučković, D. Vučković, M. Perić, and N. Raičević, "Influence of the magnetization vector misalignment on the magnetic force of permanent ring magnet and soft magnetic cylinder," *Int. Journal of Applied Electromagnetics and Mechanics*, IOS Press, vol. 65, no. 3, pp. 417-430, 2021.

[14] S. Ilić, M. Perić, S. Aleksić, and N. Raičević, "Hybrid boundary element method and quasi TEM analysis of 2D transmission lines – generalization," *Electromagnetics*, vol. 33, no. 4, pp. 292-310, Apr. 2013.

[15] M. Perić, S. Ilić, S. Aleksić, and N. Raičević, "Application of hybrid boundary element method to 2D microstrip lines analysis," *Int. Journal of Applied Electromagnetics and Mechanics*, vol. 42, no. 2, pp. 179-190, 2013.

[16] M. Perić, S. Ilić, S. Aleksić, and N. Raičević, "Characteristic parameters determination of different striplines configurations using HBEM," *Applied Computational Electromagnetics Society (ACES) Journal*, vol. 28, no. 9, pp. 858-865, Sept. 2013.

[17] M. Perić, S. Ilić, A. Vučković, and N. Raičević, "Improving the efficiency of hybrid boundary element method for electrostatic problems solving," *Applied Computational Electromagnetics Society (ACES) Journal*, vol. 35, no. 8, pp. 872-877, Aug. 2020.

[18] E. Rothwell and M. Cloud, *Electromagnetics*, Chapter 2, CRC Press, 2001.

[19] D. M. Veličković and Ž. J. Mančić, "Low frequency electromagnetic field analysis in bianisotropic media," *3rd IEEE INTERMAG 93*, Stockholm, Sweden, pp. 11-14, Apr. 1993.

[20] P. Koivisto and J. Sten, "Quasi-static image method applied to bi-isotropic microstrip geometry," *IEEE Trans. Microwave Theory Tech.*, vol. 43, no. 1, pp. 169–175, Jan. 1995.

[21] F. Olyslager, E. Laermans, and D. De Zutter, "Rigorous quasi-TEM analysis of multiconductor transmission lines in bi-isotropic media – part I: theoretical analysis for general inhomogeneous media and generalization to bianisotropic media," *IEEE Trans. Microwave Theory Tech.*, vol. 43, no. 7, pp. 1409-1415, July 1995.

[22] F. Olyslager, E. Laermans, and D. De Zutter, "Rigorous quasi-TEM analysis of multiconductor transmission lines in bi-isotropic media – part II: numerical solution for layered media," *IEEE Trans. Microwave Theory Tech.*, vol. 43, no. 7, pp. 1416-1423, July 1995.

[23] Ž. J. Mančić and V. V. Petrović, "Quasi-static analysis of the shielded microstrip line with bi-isotropic substrate by the strong FEM formulation," *11th Int. Conference on Telecommunications in Modern Satellite, Cable and Broadcasting Services – TELSIKS 2013*, Serbia, Niš, pp. 513-516, Oct. 2013.

[24] C. Zebiri, D. Sayad, S. Daudi, and F. Benabdelaziz, "Microstrip line printed on a bianisotropic medium," *Icosipe 2015*, Algeria, Tlemcen, pp. 111-120, 2015.

[25] S. Daoudi, F. Benabdelaziz, C. Zebiri, and D. Sayad, "Generalized exponential matrix technique application for the evaluation of the dispersion characteristics of a chiro-ferrite shielded multilayered microstrip line," *Progress in Electromagnetic Research - PIER*, vol. 61, pp. 1-14, 2017.

[26] A. Semichaevsky, A. Akyurtlu, D. Kern, and D. Werner, "Analysis of the interaction of electromagnetic waves with a chyral cylinder using a novel FDTD approach," *20th Annual Review of Progress in Applied Computational Electromagnetics Society (ACES)*, USA, April 19-23, 2004.

[27] S. T. Imeci, F. Altunkilic, J. R. Mautz, and E. Arvas, "Transmission through an arbitrarily shaped aperture in a conducting plane separating air and a chiral medium," *Applied Computational Electromagnetics Society (ACES) Journal*, vol. 25, no. 7, pp. 587-599, July 2010.

[28] A. B. Olcen, S. T. Imeci, M. Gokten, J. Mautz, and E. Arvas, "Method of moments analysis of electromagnetic transmission though an arbitrarily shaped 3D cavity in a thick conducting plane," *Applied Computational Electromagnetics Society (ACES) Journal*, vol. 30, no. 11, pp. 1137-1145, Nov. 2015.

[29] A. H. Sihvola, "Electromagnetic modeling of bi-isotropic media," *Progress in Electromagnetic Research - PIER*, no. 9, pp. 45-86, 1994.
[30] FlexPDE, ver. 5, PDE Solutions Inc., 2009.

Mirjana Perić received the Dipl.–Ing., M.Sc. and Ph.D. degrees from the Faculty of Electronic Engineering (FEE) of Niš, Serbia. In 2001, she joined the Department of Theoretical Electrical Engineering at the FEE. She is currently an assistant professor at the same faculty.

Her researching interests are: electromagnetic field theory, analytical and numerical methods for electromagnetic field calculations, electromagnetic compatibility, and transmission line analysis.

She is a member of the ACES, IEEE MTT and IEEE EMC societies.

Saša S. Ilić received Dipl.-Ing. degree in electronics and telecommunications in 1995 from the Faculty of Electronic Engineering (FEE) of Niš, Serbia. At the same faculty he received M.Sc. and Ph.D. degrees in theoretical electrical engineering in 2001 and 2014, respectively.

From January 1998 up to now, he has engaged to the Department of Theoretical Electrical Engineering, at the FEE.

His researching areas are: lightning protection systems, low-frequency electromagnetic fields penetrated into human body and microstrip transmission lines analysis with isotropic, anisotropic, and bianisotropic media.

Ana Vučković received the Dipl.-Ing., M.Sc., and Ph.D. degrees from the Faculty of Electronic Engineering of Niš, Serbia. In 2003, she joined the Department of Theoretical Electrical Engineering at the FEE. She works as an assistant professor at the same faculty.

Her main research area is computational electromagnetics (electromagnetic field theory, analytical and numerical methods for electromagnetic field calculations, electromagnetic compatibility and permanent magnet analysis). Also, she took part in numerous international projects and projects supported by the Serbian Ministry of Education and Science. She is a member of the ACES society.

Nebojša Raičević received his Dipl.-Ing., M. Sc., and Ph.D. degrees at the Faculty of Electronic Engineering (FEE) of Niš, Serbia, in 1989, 1998, and 2010, respectively. He received the Dr.-Ing. degree with a PhD-thesis dealing with the numerical electromagnetic field calculations.

He is currently an associate professor at the FEE. His research interests include: cable terminations and joints, numerical methods for EM problems solving, microstrip transmission lines with isotropic, anisotropic, and bianisotropic media, metamaterial structures, EMC, nonlinear electrostatic problems, magnetic field calculation of coils and permanent magnets. He is a member of the IEEE AP Society, IEEE EMC Society, IEEE Dielectrics and Electrical Insulation Society, and IEEE Magnetics Society.

Efficient Method Based on SMW Formula for Analyzing PEC Targets with Partial and Thin Coatings

Zhiwen Dong[1], Xinlei Chen[1,2,3], Guiyue Yu[1], Ziwei Li[1], Lichang Lu[1], and Changqing Gu[1]

[1]Key Laboratory of Radar Imaging and Microwave Photonics, College of Electronic and Information Engineering, Nanjing University of Aeronautics and Astronautics, Nanjing, China
dongzw@nuaa.edu.cn, chenxl@nuaa.edu.cn, yuguiyue@nuaa.edu.cn, liziwei@nuaa.edu.cn, llchang@nuaa.edu.cn, gucq@nuaa.edu.cn

[2]Key Laboratory of Meteorological Disaster (KLME) Ministry of Education & Collaborative Innovation Center on Forecast and Evaluation of Meteorological Disasters (CIC-FEMD), Nanjing University of Information Science & Technology, Nanjing, China

[3]State Key Laboratory of Millimeter Waves, Southeast University, China

Abstract – The analysis of the electromagnetic scattering from the perfect electric conductor (PEC) partially coated with thin material is a significant task in stealth design. Previous research has shown the scattering can be calculated by only discretizing the current on PEC in the case of thin coating layers. However, it has a downside that it will recalculate a complete solution when the geometry or electromagnetic properties of the coating changes. In this paper, a Sherman–Morrison–Woodbury (SMW) formula-based method is proposed to address this problem. According to the SMW formulation, it can reuse the inverse impedance matrix of the PEC part to efficiently obtain the solutions when local coating changes, so it can avoid the subsequent complete inverse of the new impedance matrix. Furthermore, it employs the fast direct solution method based on the SMW formulation to accelerate the calculation of inverse matrix of the PEC part. Numerical results demonstrate the performance of the proposed method.

Index Terms – electromagnetic scattering, method of moments, Sherman–Morrison–Woodbury formula, thin coating.

I. INTRODUCTION

It is a significant task to calculate the radar cross section (RCS) of a target accurately and efficiently, especially for the perfect electric conductor (PEC) coated by material layers, cause of its wide application in stealth design. In the context of MoM [1], the surface integral equation (SIE) [2] and the volume surface integral equation (VSIE) [3] are usual ways to solve the type of problem. According to the equivalence principle, the SIE will induce the electric current and the magnetic current on the interface between different materials. The VSIE will discrete the material part into tetrahedral meshes.

For analyzing the scattering of PEC coated by thin material layer, the thin dielectric sheet (TDS) [4], [5] method can be employed. It requires less basis functions and is more efficient than the conventional SIE and VSIE [4], [5], however, it still employs extra basis functions to expand the electric current within material layers, compared with calculating the PEC without coating. Recently, another way to solve the thin coating problem is regarding the polarization sources as constant and using the surface current on the PEC to express them [6], [7]. As a result, no additional basis functions are needed compared to analyze the scattering of PEC without coating.

Nevertheless, a problem in the approach [6], [7] is the repetitive computation of impedance matrix and the LU decomposition when analyzing the scattering of the PEC with different local coating situations, which results in intensely expensive CPU time just for the same PEC model. In this paper, a scheme based on the Sherman–Morrison–Woodbury (SMW) formula [8]-[11] is proposed to address this problem. It divides the total impedance matrix into two parts. One is the PEC matrix which is the invariable part. The other one is the polarization part that is varying in each coating situation. In accordance with SMW formula [8]-[11], the inverse of impedance matrix is transformed to another form containing the inverse of the unchanged PEC matrix. The inverse of the PEC matrix only needs to be calculated once and can be reused

Submitted On: May 9, 2021
Accepted On: September 9, 2021

https://doi.org/10.47037/2021.ACES.J.361002

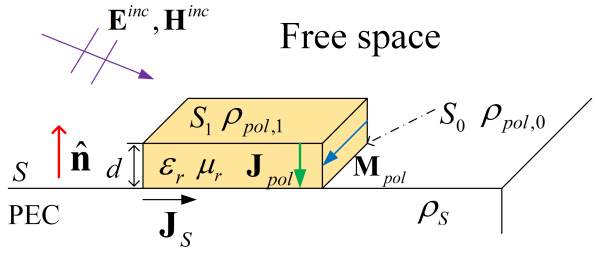

Fig. 1. A PEC partially coated with thin material. S_0 is the interface between the conductor and thin material. S_1 is the interface between the free space and thin material.

for different coatings. No recalculation of the complete impedance matrix and another LU decomposition are needed in different local coating schemes. Furthermore, in order to further enhance the computational efficiency, the fast direct solver [12]-[14] based on the SMW formula, termed the SMW algorithm (SMWA) in [12], is applied to accelerate the inverse of the PEC matrix.

II. FORMULATION

A. Conventional method for PEC with thin coating

A PEC partially coated by thin material is illuminated by an incident plane wave (E^{inc}, H^{inc}), as shown in Figure 1. The relative permittivity, relative permeability, and thickness of the material layer are ε_r, μ_r and d, respectively. The scattering electric field can be expressed through the source induced by the plane wave. There are five forms of the source: surface electric current J_s and surface charges ρ_s on the conductor, polarization surface charges $\rho_{pol,0}$ on the interface S_0 between the conductor and the material, polarization surface charges $\rho_{pol,1}$ on the interface S_1 between the material and the free space, and polarization volume electric current J_{pol} and polarization volume magnetic current M_{pol} within the material layer. According to the relation between the field and the source, the electric field integral equation (EFIE) on the surface of the PEC can be expressed as [6], [7]

$$\begin{aligned}&\mathbf{E}^{inc}\big|_t = -\mathbf{E}^{sca}\big|_t \\ &= \Big[j\omega\mu_0 \int_S \mathbf{J}_s(\mathbf{r}')\, G\mathrm{d}s' + \tfrac{1}{\varepsilon_0}\int_S \rho_s(\mathbf{r}')\nabla G\mathrm{d}s' \\ &+ j\omega\mu_0 \int_V \mathbf{J}_{pol}(\mathbf{r}')\, G\mathrm{d}v' + \tfrac{1}{\varepsilon_0}\int_{S_0} \rho_{pol,0}(\mathbf{r}')\nabla G\mathrm{d}s' \\ &+ \tfrac{1}{\varepsilon_0}\int_{S_1} \rho_{pol,1}(\mathbf{r}')\nabla G\mathrm{d}s' + \int_V \nabla G \times \mathbf{M}_{pol}(\mathbf{r}')\,\mathrm{d}v' \Big]_t\end{aligned} \quad (1)$$

where $G(\mathbf{r},\mathbf{r}')$ is the scalar Green's function in free space. The integral domain V means the volume of thin material.

When the thickness of material layer is very thin relative to wavelength in material, only normal component of the polarization volume electric current and tangential component of the polarization volume magnetic current in the layer can be remained and regarded as constants [6], [7]. Then, the volume integrals can be transformed into surface integrals written as follows

$$\begin{aligned}&\mathbf{E}^{inc}\big|_t = \Big[j\omega\mu_0 \int_S \mathbf{J}_s(\mathbf{r}')\, G\mathrm{d}s' + \frac{1}{\varepsilon_0}\int_S \rho_s(\mathbf{r}')\nabla G\mathrm{d}s' \\ &+ j\omega\mu_0 d \int_{S_m} \mathbf{J}_{pol}(\mathbf{r}')\, G\mathrm{d}s' + \frac{1}{\varepsilon_0}\int_{S_0} \rho_{pol,0}(\mathbf{r}')\nabla G\mathrm{d}s' \\ &+ \frac{1}{\varepsilon_0}\int_{S_1} \rho_{pol,1}(\mathbf{r}')\nabla G\mathrm{d}s' + d\int_{S_m} \nabla G \times \mathbf{M}_{pol}(\mathbf{r}')\,\mathrm{d}s' \Big]_t\end{aligned} \quad (2)$$

by using the relation $\mathrm{d}v' = d \times \mathrm{d}s'$. S_m represents the middle surface of layer V.

The charges ρ_s on the conductor can be obtained by the electric current continuity equation

$$-j\omega\rho_s = \nabla_s \cdot \mathbf{J}_s. \quad (3)$$

The polarization volume electric current and the polarization volume magnetic current in material can be expressed by the electric field and the magnetic field [6], [7]

$$\mathbf{J}_{pol} = j\omega\varepsilon_0(\varepsilon_r - 1)\mathbf{E}, \quad (4)$$

$$\mathbf{M}_{pol} = j\omega\mu_0(\mu_r - 1)\mathbf{H}. \quad (5)$$

According to the boundary condition on PEC surface

$$\hat{\mathbf{n}} \cdot \mathbf{D} = \rho_s, \quad (6)$$

$$\hat{\mathbf{n}} \times \mathbf{H} = \mathbf{J}_s, \quad (7)$$

where $\hat{\mathbf{n}}$ is the unit normal vector from the inside to the outside of the PEC part, as shown in Figure 1. And with the help of the relation

$$\mathbf{D} = \varepsilon\mathbf{E}, \quad (8)$$

$$-\mathbf{H} = \hat{\mathbf{n}} \times (\hat{\mathbf{n}} \times \mathbf{H}), \quad (9)$$

we can get the relations

$$\hat{\mathbf{n}} \cdot \varepsilon\mathbf{E} = \rho_s, \quad (10)$$

$$\mathbf{H} = -\hat{\mathbf{n}} \times \mathbf{J}_s. \quad (11)$$

Substituting (10) and (11) into (4) and (5), and according to (3), the polarization volume electric current and the polarization volume magnetic current within the material layer can be represented by the surface current J_s on PEC [6], [7].

$$\mathbf{J}_{pol} = -\frac{\varepsilon_r - 1}{\varepsilon_r}(\nabla \cdot \mathbf{J}_s)\hat{\mathbf{n}}, \quad (12)$$

$$\mathbf{M}_{pol} = -j\omega\mu_0(\mu_r - 1)\hat{\mathbf{n}} \times \mathbf{J}_s. \quad (13)$$

As to the polarization surface charges $\rho_{pol,i}$, the expression can derive from the boundary situation that the polarization charges can only remain in the material,

here expressed as [6]

$$-j\omega\rho_{pol,0} = \hat{\mathbf{n}} \cdot \left(\mathbf{J}_{pol} - \mathbf{0}\right), \tag{14}$$

$$-j\omega\rho_{pol,1} = \hat{\mathbf{n}} \cdot \left(\mathbf{0} - \mathbf{J}_{pol}\right), \tag{15}$$

because of no polarization volume current existing in conductor or free space. The polarization surface charge $\rho_{pol,i}$ can be eventually expressed as [6]

$$\rho_{pol,0} = -\rho_{pol,1} = \frac{1}{j\omega} \cdot \frac{\varepsilon_r - 1}{\varepsilon_r} \nabla \cdot \mathbf{J}_s. \tag{16}$$

Substituting (3), (12), (13), (16) into (2), we can find that the only unknown is $\mathbf{J}_s$ and the number of unknowns for this model is equal to that of unknowns required only for PEC surface of this model. No additional basis functions are needed, and no additional memory storage is required.

By applying the MoM [1], (2) can be converted into the matrix equation

$$\mathbf{Z}^t \mathbf{I} = \mathbf{V}^i, \tag{17}$$

where the elements of Z^t and V^i are

$$\begin{aligned} Z^t_{mn} = {} & j\omega\mu_0 \int_{T_m}\int_{T_n} \left(\mathbf{f}_m \cdot \mathbf{f}_n - \frac{1}{k_0^2} \nabla \cdot \mathbf{f}_m \nabla' \cdot \mathbf{f}_n\right) G \mathrm{d}s' \mathrm{d}s \\ & - j\omega\mu_0 \frac{\varepsilon_r - 1}{\varepsilon_r} d \int_{T_m}\int_{T_n^{S_m}} \mathbf{f}_m \cdot \left[\nabla' \cdot \mathbf{f}_n\right] \hat{\mathbf{n}}\left(\mathbf{r}'\right) G \mathrm{d}s' \mathrm{d}s \\ & + \frac{1}{j\omega\varepsilon_0} \frac{\varepsilon_r - 1}{\varepsilon_r} \int_{T_m}\int_{T_n} \mathbf{f}_m \cdot \left[\nabla' \cdot \mathbf{f}_n\right] \nabla G \mathrm{d}s' \mathrm{d}s \\ & - \frac{1}{j\omega\varepsilon_0} \frac{\varepsilon_r - 1}{\varepsilon_r} \int_{T_m}\int_{T_n^{S_1}} \mathbf{f}_m \cdot \left[\nabla' \cdot \mathbf{f}_n\right] \nabla G \mathrm{d}s' \mathrm{d}s \\ & + j\omega\mu_0 \left(\mu_r - 1\right) d \int_{T_m}\int_{T_n^{S_m}} \mathbf{f}_m \cdot \left[\hat{\mathbf{n}}\left(\mathbf{r}'\right) \times \mathbf{f}_n \times \nabla G\right] \mathrm{d}s' \mathrm{d}s \end{aligned} \tag{18}$$

$$V^i_m = \int_{T_m} \mathbf{f}_m \cdot \mathbf{E}^{inc} \mathrm{d}s, \tag{19}$$

$\mathbf{f}_m$ and $\mathbf{f}_n$ stand for the mth test Rao–Wilton–Glisson (RWG) function [17] and the nth RWG basis function, respectively. The integral domain $T_n^{S_1}$ and $T_n^{S_m}$ in (18) represent T_n shifted along the normal vector $\hat{\mathbf{n}}$ to surface S_1 and S_m, respectively.

B. Efficient method for PEC with partial and thin coating

Only the same conductor partially covered by different thin material is considered in this paper. For the conventional method, if either the electromagnetic properties of local coating or its geometry such as area, position, or thickness changes several times, $\mathbf{Z}^t$ and its LU decomposition need to be calculated repeatedly when the metal part of the model remains in its original form. The conventional method is expensive for this situation. In this section, an efficient method based on the SMW formula [8]-[11] is proposed to address this problem.

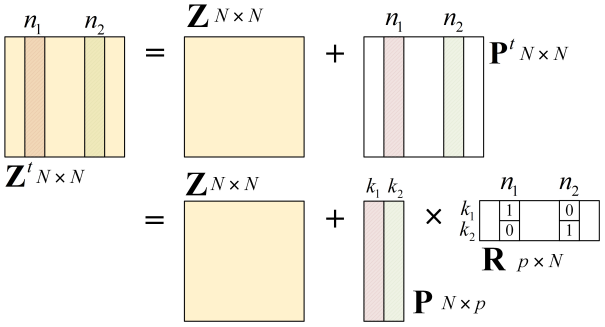

Fig. 2. The total impedance matrix Z^t is divided into two parts.

It can be seen from (18) that the element Z^t_{mn} consists of two parts, PEC part Z_{mn} and polarization part P^t_{mn}

$$Z^t_{mn} = Z_{mn} + P^t_{mn}, \tag{20}$$

where the element Z_{mn} of the PEC impedance matrix $\mathbf{Z}$ and P^t_{mn} of the polarization impedance matrix $\mathbf{P}^t$ are

$$Z_{mn} = j\omega\mu_0 \int_{T_m}\int_{T_n} \left(\mathbf{f}_m \cdot \mathbf{f}_n - \frac{1}{k_0^2} \nabla \cdot \mathbf{f}_m \nabla' \cdot \mathbf{f}_n\right) G \mathrm{d}s' \mathrm{d}s, \tag{21}$$

$$\begin{aligned} P^t_{mn} = {} & -j\omega\mu_0 \frac{\varepsilon_r - 1}{\varepsilon_r} d \int_{T_m}\int_{T_n^{S_m}} \mathbf{f}_m \cdot \left[\nabla' \cdot \mathbf{f}_n\right] \hat{\mathbf{n}}\left(\mathbf{r}'\right) G \mathrm{d}s' \mathrm{d}s \\ & + \frac{1}{j\omega\varepsilon_0} \frac{\varepsilon_r - 1}{\varepsilon_r} \int_{T_m}\int_{T_n} \mathbf{f}_m \cdot \left[\nabla' \cdot \mathbf{f}_n\right] \nabla G \mathrm{d}s' \mathrm{d}s \\ & - \frac{1}{j\omega\varepsilon_0} \frac{\varepsilon_r - 1}{\varepsilon_r} \int_{T_m}\int_{T_n^{S_1}} \mathbf{f}_m \cdot \left[\nabla' \cdot \mathbf{f}_n\right] \nabla G \mathrm{d}s' \mathrm{d}s \\ & + j\omega\mu_0 \left(\mu_r - 1\right) d \int_{T_m}\int_{T_n^{S_m}} \mathbf{f}_m \cdot \left[\hat{\mathbf{n}}\left(\mathbf{r}'\right) \times \mathbf{f}_n \times \nabla G\right] \mathrm{d}s' \mathrm{d}s \end{aligned} \tag{22}$$

It suggests that for the same conductor the PEC matrix $\mathbf{Z}$ is unchanged and can be reused for different coatings. If somewhere on a metal surface is not covered by coatings, the corresponding polarization element P^t_{mn} is zero and the corresponding column of the polarization matrix $\mathbf{P}^t$ is zero, as shown in Figure 2.

The polarization matrix $\mathbf{P}^t$ can be further expressed as a product of two matrices, so (17) can be rewritten as

$$\mathbf{Z}^t \mathbf{I} = \left(\mathbf{Z} + \mathbf{P}^t\right) \mathbf{I} = \left(\mathbf{Z} + \mathbf{PR}\right) \mathbf{I} = \mathbf{V}^i, \tag{23}$$

where $\mathbf{P}$ is the impedance matrix of the polarization part, and $\mathbf{R}$ is the matrix consisting of 0 and 1. The matrix element P_{mk} is the same as the element P^t_{mn}, which means if the n_lth column of $\mathbf{P}^t$ is at the k_lth column of matrix $\mathbf{P}$, then the expression of matrix $\mathbf{R}$ is

$$R_{ij} = \begin{cases} 1 & i = k_l, j = n_l \\ 0 & else \end{cases}. \tag{24}$$

Assuming that the number of columns in $\mathbf{P}$ is p, the number of rows in $\mathbf{R}$ is also p, where p is the number of

the basis function covered by material. The number of rows in $\mathbf{P}$ and the number of columns in $\mathbf{R}$ still are N. N is the total number of basis functions. In situation of local coating, p is very small compared to N. A simple example is shown in Figure 2 with $p = 2$.

With the change of coating geometry or coating properties, $\mathbf{Z}$ remains unchanged while $\mathbf{P}$ and $\mathbf{R}$ change. Utilizing the SMW formula [8]-[11], the current coefficient matrix $\mathbf{I}$ can be deduced

$$\begin{aligned}\mathbf{I} &= (\mathbf{Z}+\mathbf{PR})^{-1}\mathbf{V}^i \\ &= \left(\mathbf{Z}^{-1}\mathbf{V}^i\right) - \left(\mathbf{Z}^{-1}\mathbf{P}\right)\left[\mathbf{1}+\mathbf{R}\left(\mathbf{Z}^{-1}\mathbf{P}\right)\right]^{-1}\mathbf{R}\left(\mathbf{Z}^{-1}\mathbf{V}^i\right),\end{aligned} \tag{25}$$

where $\mathbf{1}$ represents the identity matrix. The LU decomposition of $\mathbf{Z}$ only needs to be computed once. The size of $\mathbf{1}+\mathbf{RZ}^{-1}\mathbf{P}$ is p, which is much smaller than the size of $\mathbf{Z}$ of N, so it takes less time to compute the LU decomposition of $\mathbf{1}+\mathbf{RZ}^{-1}\mathbf{P}$ than the LU decomposition of $\mathbf{Z}^t$. For the analysis of a variety of different coating material, the inverse of PEC matrix can be reused rather than recalculating the inverse of a new matrix. As the number of changes increases, this method is more efficient than the conventional method.

In (25), the matrix equation needs to be solved

$$\mathbf{Z}^{-1}\mathbf{B}, \tag{26}$$

where $\mathbf{B}$ denotes $\mathbf{V}^i$ or $\mathbf{P}$. Although the inverse of $\mathbf{Z}$ only needs to be computed once, it is still expensive to calculate the inverse of $\mathbf{Z}$ when the unknowns increase. To address this problem, the SMWA [12]-[14], which is also based on the SMW formula, is used to efficiently solve (26). In the SMWA, a binary tree is used to divide the impedance matrix $\mathbf{Z}$ into different blocks in order to avoid calculating the inverse of the complete matrix $\mathbf{Z}$ and instead calculate the inverse of small blocks. The matrix after the partitioning of the one-level binary tree is shown as

$$\mathbf{Z} = \begin{bmatrix} {}^1\mathbf{Z}_{11} & {}^1\mathbf{Z}_{12} \\ {}^1\mathbf{Z}_{21} & {}^1\mathbf{Z}_{22} \end{bmatrix}, \tag{27}$$

where ${}^1\mathbf{Z}_{11}$ and ${}^1\mathbf{Z}_{22}$ are the self-impedance matrices of block 1 and 2 in matrix $\mathbf{Z}$, respectively, while ${}^1\mathbf{Z}_{12}$ and ${}^1\mathbf{Z}_{21}$ are the mutual-impedance matrices between block 1 and 2 in matrix $\mathbf{Z}$. The initial matrix $\mathbf{Z}$ can be represented as the product of a block diagonal matrix only containing self-impedance blocks ${}^q\mathbf{Z}_d$ and a special form matrix $\mathbf{Z}_q$containing identity matrix block and mutual-impedance blocks updated by self-impedance block expressed as

$$\mathbf{Z} = {}^1\mathbf{Z}_d\mathbf{Z}_1 = \begin{bmatrix} {}^1\mathbf{Z}_{11} & \mathbf{0} \\ \mathbf{0} & {}^1\mathbf{Z}_{22} \end{bmatrix}\begin{bmatrix} \mathbf{1} & {}^1\mathbf{Z}_{11}^{-1}{}^1\mathbf{Z}_{12} \\ {}^1\mathbf{Z}_{22}^{-1}{}^1\mathbf{Z}_{21} & \mathbf{1} \end{bmatrix}. \tag{28}$$

The special form matrix $\mathbf{Z}_q$ consists of 2^{q-1}diagonal blocks if a q-level binary tree is taken while the block diagonal matrix ${}^q\mathbf{Z}_d$ contains 2^q self-impedance blocks. The partition can be further written as follows if a two-level tree is taken

$$\begin{aligned}\mathbf{Z} = {}^2\mathbf{Z}_d\mathbf{Z}_2\mathbf{Z}_1 = &\begin{bmatrix} \begin{bmatrix} {}^2\mathbf{Z}_{11} & \mathbf{0} \\ \mathbf{0} & {}^2\mathbf{Z}_{22} \end{bmatrix} & \mathbf{0} \\ \mathbf{0} & \begin{bmatrix} {}^2\mathbf{Z}_{33} & \mathbf{0} \\ \mathbf{0} & {}^2\mathbf{Z}_{44} \end{bmatrix} \end{bmatrix} \\ &\times \begin{bmatrix} \begin{bmatrix} \mathbf{1} & {}^2\mathbf{Z}_{11}^{-1}{}^2\mathbf{Z}_{12} \\ {}^2\mathbf{Z}_{22}^{-1}{}^2\mathbf{Z}_{21} & \mathbf{1} \end{bmatrix} & \mathbf{0} \\ \mathbf{0} & \begin{bmatrix} \mathbf{1} & {}^2\mathbf{Z}_{33}^{-1}{}^2\mathbf{Z}_{34} \\ {}^2\mathbf{Z}_{44}^{-1}{}^2\mathbf{Z}_{43} & \mathbf{1} \end{bmatrix} \end{bmatrix}, \\ &\times \begin{bmatrix} \mathbf{1} & {}^1\mathbf{Z}_{11}^{-1}{}^1\mathbf{Z}_{12} \\ {}^1\mathbf{Z}_{22}^{-1}{}^1\mathbf{Z}_{21} & \mathbf{1} \end{bmatrix}\end{aligned} \tag{29}$$

where

$$\begin{aligned}{}^1\mathbf{Z}_{11} &= \begin{bmatrix} {}^2\mathbf{Z}_{11} & {}^2\mathbf{Z}_{12} \\ {}^2\mathbf{Z}_{21} & {}^2\mathbf{Z}_{22} \end{bmatrix} \\ &= \begin{bmatrix} {}^2\mathbf{Z}_{11} & \mathbf{0} \\ \mathbf{0} & {}^2\mathbf{Z}_{22} \end{bmatrix}\begin{bmatrix} \mathbf{1} & {}^2\mathbf{Z}_{11}^{-1}{}^2\mathbf{Z}_{12} \\ {}^2\mathbf{Z}_{22}^{-1}{}^2\mathbf{Z}_{21} & \mathbf{1} \end{bmatrix},\end{aligned} \tag{30}$$

$$\begin{aligned}{}^1\mathbf{Z}_{22} &= \begin{bmatrix} {}^2\mathbf{Z}_{33} & {}^2\mathbf{Z}_{34} \\ {}^2\mathbf{Z}_{43} & {}^2\mathbf{Z}_{44} \end{bmatrix} \\ &= \begin{bmatrix} {}^2\mathbf{Z}_{33} & \mathbf{0} \\ \mathbf{0} & {}^2\mathbf{Z}_{44} \end{bmatrix}\begin{bmatrix} \mathbf{1} & {}^2\mathbf{Z}_{33}^{-1}{}^2\mathbf{Z}_{34} \\ {}^2\mathbf{Z}_{44}^{-1}{}^2\mathbf{Z}_{43} & \mathbf{1} \end{bmatrix}.\end{aligned} \tag{31}$$

The block matrix ${}^q\mathbf{Z}_{ii}$ is the self-impedance matrix of block i and the block matrix ${}^q\mathbf{Z}_{ij}$ is the mutual-impedance matrix of block i and j in level q of the tree.

The mutual-impedance matrix is the low rank matrix which can be compressed by ACA [15],[16]

$${}^q\mathbf{Z}_{ij} = {}^q\mathbf{U}_{ij}{}^q\mathbf{V}_{ij}, \tag{32}$$

where the size of ${}^q\mathbf{U}_{ij}$ is $(N_q/2)\times r$, and the size of ${}^q\mathbf{V}_{ij}$ is $r\times(N_q/2)$. N_q is the size of ${}^q\mathbf{Z}_{ij}$. r is the effective rank of the mutual-impedance matrices ${}^q\mathbf{Z}_{ij}$, which is typically much smaller than $N_q/2$.

The special form matrix $\mathbf{Z}_1$ on the rightmost side of (28) can be rewritten as

$$\begin{aligned}\mathbf{Z}_1 &= \begin{bmatrix} \mathbf{1} & {}^1\mathbf{Z}_{11}^{-1}{}^1\mathbf{Z}_{12} \\ {}^1\mathbf{Z}_{22}^{-1}{}^1\mathbf{Z}_{21} & \mathbf{1} \end{bmatrix} \\ &= \begin{bmatrix} \mathbf{1} & {}^1\mathbf{Z}_{11}^{-1}{}^1\mathbf{U}_{12}{}^1\mathbf{V}_{12} \\ {}^1\mathbf{Z}_{22}^{-1}{}^1\mathbf{U}_{21}{}^1\mathbf{V}_{21} & \mathbf{1} \end{bmatrix} \\ &= \begin{bmatrix} \mathbf{1} & \mathbf{0} \\ \mathbf{0} & \mathbf{1} \end{bmatrix} + \begin{bmatrix} \mathbf{0} & {}^1\mathbf{Z}_{11}^{-1}{}^1\mathbf{U}_{12} \\ {}^1\mathbf{Z}_{22}^{-1}{}^1\mathbf{U}_{21} & \mathbf{0} \end{bmatrix}\begin{bmatrix} {}^1\mathbf{V}_{21} & \mathbf{0} \\ \mathbf{0} & {}^1\mathbf{V}_{12} \end{bmatrix}\end{aligned}, \tag{33}$$

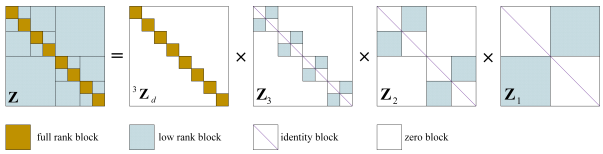

Fig. 3. A division of the initial matrix $\mathbf{Z}$ with a three-level binary tree.

On the basis of SMW formula [8][12], the inverse of matrix (33) is equivalent to the following

$$\begin{aligned}\mathbf{Z}_1^{-1} &= \begin{bmatrix} \mathbf{1} & {}^1\mathbf{Z}_{11}^{-1}{}^1\mathbf{U}_{12}{}^1\mathbf{V}_{12} \\ {}^1\mathbf{Z}_{22}^{-1}{}^1\mathbf{U}_{21}{}^1\mathbf{V}_{21} & \mathbf{1} \end{bmatrix}^{-1} \\ &= \begin{bmatrix} \mathbf{1} & \mathbf{0} \\ \mathbf{0} & \mathbf{1} \end{bmatrix} - \begin{bmatrix} \mathbf{0} & {}^1\mathbf{Z}_{11}^{-1}{}^1\mathbf{U}_{12} \\ {}^1\mathbf{Z}_{22}^{-1}{}^1\mathbf{U}_{21} & \mathbf{0} \end{bmatrix} \\ &\times \begin{bmatrix} \mathbf{1} & {}^1\mathbf{V}_{21}{}^1\mathbf{Z}_{11}^{-1}{}^1\mathbf{U}_{12} \\ {}^1\mathbf{V}_{12}{}^1\mathbf{Z}_{22}^{-1}{}^1\mathbf{U}_{21} & \mathbf{1} \end{bmatrix}^{-1} \begin{bmatrix} {}^1\mathbf{V}_{21} & \mathbf{0} \\ \mathbf{0} & {}^1\mathbf{V}_{12} \end{bmatrix}\end{aligned} \tag{34}$$

After the conversion of using the SMW formula, the size of the inverse matrix needing to be calculated is $2r \times 2r$, instead of the original size of $N \times N$. The inverse of any other matrix with the same structure as $\mathbf{Z}_1$ can be solved in the same way.

Size of both ${}^1\mathbf{Z}_{11}$ and ${}^1\mathbf{Z}_{22}$ are $N/2$, which means the direct calculation of the inverse is also expensive for large N. So just like what is done for the initial matrix $\mathbf{Z}$, using the one-level SMWA to calculate the inverse of ${}^1\mathbf{Z}_{11}$ and ${}^1\mathbf{Z}_{22}$ until the size of the self-impedance matrix block is considered small enough. That is the multilevel version of the SMWA [12]-[14]. If a q-level binary tree is taken, the initial matrix Z can be represented as the multiplication of a series of matrices

$$\mathbf{Z} = {}^q\mathbf{Z}_d\mathbf{Z}_q \cdots \mathbf{Z}_3\mathbf{Z}_2\mathbf{Z}_1. \tag{35}$$

The pictorial representations of the matrices in the SMWA with a three-level binary tree are shown in Figure 3. Eventually, the linear system (26) can be efficiently calculated as

$$\mathbf{Z}^{-1}\mathbf{B} = \mathbf{Z}_1^{-1}\mathbf{Z}_2^{-1}\mathbf{Z}_3^{-1} \cdots \mathbf{Z}_q^{-1}{}^q\mathbf{Z}_d^{-1}\mathbf{B}. \tag{36}$$

III. NUMERICAL RESULTS

This section is divided into two parts. The first part is to verify the correctness of our code. And then the second part is to illustrate the effectiveness of our work. The example to validate our code is to calculate the bistatic RCS of a PEC sphere of radius 1.0 m, but entirely coated by the material with $d = 0.0125$m, $\varepsilon_r = 4$ and $\mu_r = 4$. The coated sphere is illuminated by an **x**-polarized incident plane wave from the direction at $\theta_i = 0°$, $\varphi_i = 0°$ with a frequency at 300 MHz, and only the PEC surface of the sphere is discretized into flat triangles with the mean size of $0.1\lambda_0$. λ_0 is the wavelength in free space. The results are shown in Figure 4. It can be seen that the RCS calculated by our code matches the solution of the business software FEKO well.

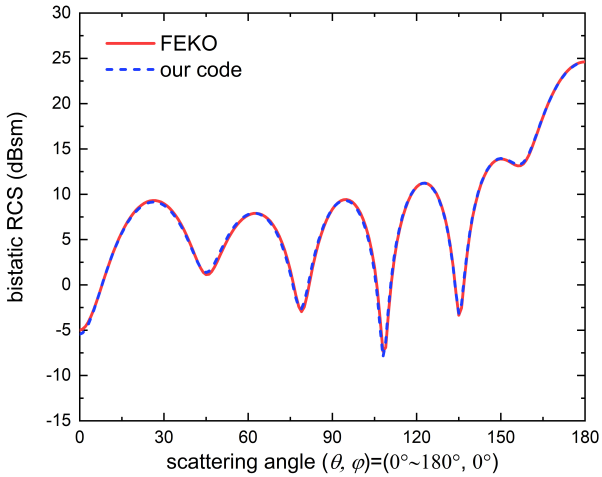

Fig. 4. The bistatic RCS of a sphere with radius 1.0 m entirely coated by the thin material with $d = 0.0125$m, $\varepsilon_r = 4$ and $\mu_r = 4$.

In the next step, different coating conditions will be discussed. One example is analyzing the bistatic RCS of a simplified missile model with different coating location to demonstrate the efficiency of the proposed method. The tolerance of the ACA algorithm is 10^{-4}. A level-6 binary tree is employed. The model consists of a cylinder, a hemisphere and several cuboids, as shown in Figure 5. The cylinder is 5.0 m high with a radius of 0.25 m, and the radius of the hemisphere is 0.25 m. The cuboid at the middle of a cylinder is 2.6 m long, 0.05 m wide, and 0.3 m high and its long side is parallel to the **x**-axis. The cuboid at the tail is 1.5 m long, 0.05 m wide, and 0.2 m high. The head of the missile is facing positive **z**-axis. The missile model is illuminated by an **x**-polarized incident plane wave from the direction at $\theta_i = 0°$, $\varphi_i = 0°$, with a frequency of 1.0 GHz. The discrete size is $0.1\lambda_0$. This model contains 33,648 RWGs. Five positions are selected for the coating and each time only one position is coated. The first position is the head of the missile. The rest of the position is one position every 0.5 m from the head down on the cylinder surface. The relative permittivity, relative permeability, and thickness of coated material are $\varepsilon_r = 2 - j1$, $\mu_r = 2 - j1$, and $d = 0.0075$m, respectively.

Figure 5 shows the result in position 1 that a good agreement can be found by comparing the proposed method and the conventional method [6], [7]. Table 1 gives the CPU time consumption. The conventional method directly applies the LU decomposition to

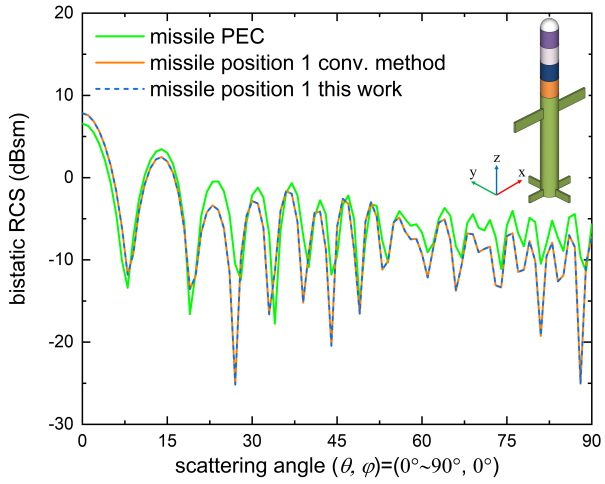

Fig. 5. The bistatic RCS of a simplified missile model with different coating positions.

Table 1: CPU time for different coating positions

Coating position	Conventional method		Proposed method	
	Voltage and impedance generation	LU	Voltage and impedance generation	Solve
PEC	1296 s		836 s	
1	164 s	746 s	164 s	54 s
2	283 s	747 s	283 s	100 s
3	280 s	747 s	280 s	100 s
4	280 s	746 s	280 s	101 s
5	281 s	752 s	281 s	100 s
Total	6325 s		2579 s	

calculate the solution. The proposed method takes the same amount of time as the conventional method for computing the voltage and impedance matrix, however, the time saved is in the solution. When the analysis of five changes are completed, the total computational time is saved by more than half by the proposed method. Why the time of LU in conventional method looks the same is because the total unknown is the same each time. The conventional method has a maximum memory footprint of 8650 MB for one coating situation while the proposed method has 4970 MB.

IV. CONCLUSION

In this paper, an efficient method for analyzing the scattering of a PEC object with partial different thin coatings is presented. The proposed method only needs to calculate the inverse of PEC matrix once, which can be reused to efficiently acquire the outcome of local thin coating at different locations or with different electromagnetic parameters. In the proposed method, the employment of the SMWA speeds up the calculation of the inverse of the PEC matrix, which further accelerates the solution. For analyzing a PEC object with partial and thin coatings, the proposed method has a remarkable enhancement in computing time and memory requirement compared with the conventional method [6], [7].

ACKNOWLEDGMENT

This work was supported by the Fundamental Research Funds for the Central Universities (NS2020028), the National Nature Science Foundation of China (61771238), the Joint Open Project of KLME & CIC-FEMD, NUIST (KLME201910), the Foundation of State Key Laboratory of Millimeter Waves, Southeast University, China, (K202035), and the Project of Key Laboratory of Radar Imaging and Microwave Photonics (Nanjing University of Aeronautics and Astronautics), Ministry of Education (RIMP2020006), the Open Fund of Graduate Innovation Base for Nanjing University of Aeronautics and Astronautics (KFJJ20200418). Thanks to Altair for providing software and technical support.

REFERENCES

[1] W. C. Gibson, *The Method of Moments in Electromagnetics*. Boca Raton, FL, USA: CRC Press, Nov. 2007.

[2] O. Ergul and L. Gurel, *The Multilevel Fast Multipole Algorithm (MLFMA) for Solving Large-Scale Computational Electromagnetics Problems*. John Wiley & Sons, Apr. 2014.

[3] C. C. Lu and W. C. Chew, "A coupled surface-volume integral equation approach for the calculation of electromagnetic scattering from composite metallic and material targets," *IEEE Trans. Antennas Propag.*, vol. 48, no. 12, pp. 1866-1868, Dec. 2000.

[4] I. Chiang and W. C. Chew, "Thin dielectric sheet simulation by surface integral equation using modified RWG and pulse bases," *IEEE Trans. Antennas Propag.*, vol. 54, no. 7, pp. 1927-1934, Jul. 2006.

[5] I. Chiang and W. C. Chew, "A coupled PEC-TDS surface integral equation approach for electromagnetic scattering and radiation from composite metallic and thin dielectric objects," *IEEE Trans. Antennas Propag.*, vol. 54, no. 11, pp. 3511-3516, Nov. 2006.

[6] S. Tao, Z. Fan, W. Liu, and R. Chen, "Electromagnetic scattering analysis of a conductor coated by multilayer thin materials," *IEEE Antennas Wirel. Propag. Lett.*, vol. 12, pp. 1033-1036, Aug. 2013.

[7] S. Tao, D. Ding, and R. Chen, "Electromagnetic scattering analysis of a conductor coated by thin bi-isotropy media," *Microw. Opt. Technol. Lett.*, vol. 55, no. 10, pp. 2354-2358, Oct. 2013.

[8] W. Hager, "Updating the inverse of a matrix," *SIAM Rev.*, vol. 31, no. 2, pp. 221-239, Jun. 1989.

[9] E. Yip and B. Tomas, "Obtaining scattering solution for perturbed geometries and materials from moment method solutions," *Applied Computational Electromagnetics Society (ACES) Journal,* vol. 3, no. 2, pp. 95-118, Jul. 1988.

[10] A. Boag, A. Boag, E. Michielssen, and R. Mittra. "Design of electrically loaded wire antennas using genetic algorithms," *IEEE Trans. Antennas Propag.*, vol. 44, no. 5, pp. 687-695, May 1996.

[11] X. Chen, X. Liu, Z. Li, and C. Gu, "Efficient calculation of interior scattering from cavities with partial IBC wall," *Electronics Letters*, vol. 56, no. 17, pp. 871-873, Aug. 2020.

[12] X. Chen, C. Gu, Z. Li, and Z. Niu, "Accelerated direct solution of electromagnetic scattering via characteristic basis function method with Sherman-Morrison-Woodbury formula-based algorithm," *IEEE Trans. Antennas Propag.*, vol. 64, no. 10, pp. 4482-4486, Oct. 2016.

[13] W. Y. Kong, J. Bremer, and V. Rokhlin, "An adaptive fast direct solver for boundary integral equations in two dimensions," *Appl. Comput. Harmon. Anal.*, vol. 31, no. 3, pp. 346-369, Jan. 2011.

[14] S. Ambikasaran and E. Darve, "An O(NlogN) fast direct solver for partial hierarchically semi-separable matrices," *J. Sci. Comput.*, vol. 57, no. 3, pp. 477-501, Apr. 2013.

[15] M. Bebendorf, "Approximation of boundary element matrices," *Numer. Math.*, vol. 86, no. 4, pp. 565-589, Jun. 2000.

[16] K. Zhao, M. Vouvakis, and J.-F. Lee, "The adaptive cross approximation algorithm for accelerated method of moments computations of EMC problems," *IEEE Trans. Electromagn. Compat.*, vol. 47, no. 4, pp. 763-773, Nov. 2005.

[17] S. Rao, D. Wilton, and A. Glisson, "Electromagnetic scattering by surfaces of arbitrary shape," *IEEE Trans. Antennas Propag.*, vol. AP-30, no. 3, pp. 409-418, May 1982.

Research on EBE-FEM Parallel Algorithm Combined with Fast Color Marking Method Based on CUDA Platform

Xvdong Ren, Xiuke Yan, Jinpeng Lan, Ziyan Ren, and Yanli Zhang

School of Electrical Engineering
Shenyang University of Technology, Shenyang, 110870, China
yanxke@126.com

Abstract **–** The element-by-element finite element method (EBE-FEM) parallel algorithm has been realized on Compute Unified Device Architecture (CUDA) platform in this paper. An improved fast color marking method (FCM) combined with tabu search algorithm is proposed to solve the problem that the elements sharing a node wait for accessing the same memory space in parallel computation. The elements in the same color can be processed at the same time without waiting. This method can get more even color grouping faster than the classical coloring method (CCM). Combining it with the EBE parallel algorithm can achieve faster element-level operations. The validity and accuracy of the method has been verified by comparing the computed results with the analytical solution of the magnetic field produced by the solenoid. The parallel program is applied to analyze the main magnetic field of a single-phase transformer, which shows higher speedup performance.

Index Terms **–** EBE-FEM, parallel computation, fast color marking, element grouping.

I. INTRODUCTION

Large-scale numerical calculation is usually involved in electromagnetic field analysis of large power equipment. It is difficult to obtain accurate and reasonable results by traditional serial finite element method (FEM) [1]. In recent years, parallel finite element methods and advanced computing platforms are developed and applied to numerical computation [2]. The traditional FEM realizes parallel computing by using Internet resources and cloud computing, splitting the program into multiple subprograms, which are computed simultaneously by multiple processors and returned to the terminal. In order to realize the complete parallel calculation of FEM, it is necessary to change the solution process of traditional FEM and add parallel algorithm into it. The element-by-element finite element method (EBE-FEM) is different from the traditional FEM [3, 4]. It does not form the global system matrix, solves the equation for each element, which can save the memory storage space and perform the solving process in parallel. The operations of each element are independent of each other, so it is easy to achieve parallelism between elements [5, 6]. The EBE-FEM is a method which transforms a highly memory dependent problem to a massively computational dependent one, the latter can be parallelized efficiently.

Compute Unified Device Architecture (CUDA) is a CPU + GPU heterogeneous computing platform, in which GPU is one of the newest types of parallel processors [7], its multi-core nature can fully exploit the parallelism of EBE-FEM. When implementing parallel computation of EBE-FEM on CUDA, to avoid race conditions, different threads cannot access the same memory space simultaneously. Generally, two methods have been used to solve this problem. One is "atomic operation," on the early Nvidia GPU architectures such as Fermi, the storage space is protected and only one thread is allowed to access, which will affect the parallel efficiency of the algorithm [8]. On new architectures such as Kepler, these operating instructions have the "fire-and-forget" semantics and can be returned immediately. The conflict resolution is the responsibility of the cache system [9]. Another method is coloring [10, 11]. The elements with the common node have been given different colors to achieve the purpose of grouping. Elements in different colors are not calculated at the same time. The coloring result is repeatable, because each run will produce the same sequence of operations with the same round-off error accumulation, which is impossible for atomic addition. Different color grouping methods have different processor resource utilization, and the grouping results are also different [12].

In the classical coloring method (CCM), color A is marked first by traversing all elements, then mark color B [13, 14], only one color is marked in one traversal process. It introduces a lot of nested loops, which makes it run slowly and unevenly grouped. While the coloring efficiency and the grouping rationality will directly affect the calculation efficiency of EBE-FEM parallel

Submitted On: April 20, 2021
Accepted On: August 22, 2021

https://doi.org/10.47037/2021.ACES.J.361003

algorithm. The fast color marking method (FCM) colors the elements sequentially, and all the elements need to be traversed only once. The FCM can obtain even grouping of elements quickly, and it has been used for element coloring in traditional FEM. However, all nodes still need to be traversed once when coloring an element, which leads to insufficient efficiency, especially for dealing with large-scale meshes.

In this paper, the parallel computation of EBE-FEM for engineering electromagnetic field analysis is implemented on CUDA platform. An optimized fast color marking method (OFCM) which combines FCM with tabu search algorithm is proposed to improve computational efficiency. The magnetic field produced by solenoid and single-phase transformer have been analyzed by EBE-FEM combined with FCM and OFCM respectively. The results have been compared and discussed. The corresponding FEM programs are developed in C++ language.

II. METHOD DESCRIPTION

A. EBE-FEM parallel algorithm based on CUDA

Using FEM, the Maxwell electromagnetic field equations can be discretized as linear equations

$$\boldsymbol{A}\boldsymbol{x} = \boldsymbol{b}, \tag{1}$$

where $\boldsymbol{A}$ is the global coefficient matrix, $\boldsymbol{x}$ is the vector of unknowns, $\boldsymbol{b}$ is the right-hand vector.

The EBE establishes the relationship between the local quantity and the global quantity through the transition matrix

$$\boldsymbol{Q} = (\boldsymbol{Q}^{(1)T}, \boldsymbol{Q}^{(2)T}, \cdots, \boldsymbol{Q}^{(e)T})^T \ (\boldsymbol{e} \in \boldsymbol{E}), \tag{2}$$

where $\boldsymbol{Q}^{(e)}$ is the connection matrix between the coefficient matrix of the element e and the global coefficient matrix, $\boldsymbol{E}$ is the set of elements. (1) can be transformed as

$$\begin{aligned} \boldsymbol{A}\boldsymbol{x} &= \sum_{e\in\boldsymbol{E}} (\boldsymbol{Q}^{(e)})^T \boldsymbol{A}^{(e)} \boldsymbol{Q}^{(e)} \boldsymbol{x} \\ &= \sum_{e\in\boldsymbol{E}} (\boldsymbol{Q}^{(e)})^T \boldsymbol{A}^{(e)} \boldsymbol{x}^{(e)} \end{aligned} \tag{3}$$

$$\boldsymbol{b} = \sum_{e\in\boldsymbol{E}} (\boldsymbol{Q}^{(e)})^T \boldsymbol{b}^{(e)}, \tag{4}$$

where $\boldsymbol{A}^{(e)}$ is the matrix of element coefficients, which is directly obtained by finite element analysis. $\boldsymbol{b}^{(e)}$ is the element right-hand.

The main operation of CG method is the inner product of vectors, which are appropriate to realize parallel computation. Therefore, CG method has been used to solve the equations of EBE-FEM.

$$\boldsymbol{r} = \boldsymbol{A}\boldsymbol{x} - \boldsymbol{b}, \tag{5}$$

where $\boldsymbol{r}$ is global residual vector. In EBE-FEM, it can be expressed by,

$$\boldsymbol{r} = \sum_{e\in\boldsymbol{E}} (Q^{(e)})^T \boldsymbol{r}^{(e)}, \tag{6}$$

where $\boldsymbol{r}^{(e)}$ is the element residual.

In CG, ($\boldsymbol{r}$, $\boldsymbol{r}$) and ($\boldsymbol{p}$, $\boldsymbol{Ap}$) are the most important calculations, occupying the most computer resources. In EBE-FEM, the inner product can be calculated on each element as

$$\begin{aligned} (\boldsymbol{r},\boldsymbol{r}) = \boldsymbol{r}^T\boldsymbol{r} &= (\boldsymbol{Q}^T\boldsymbol{R}^e)^T\boldsymbol{Q}^T\boldsymbol{R}^e = (\boldsymbol{R}^e)^T\boldsymbol{Q}\boldsymbol{Q}^T\boldsymbol{R}^e \\ &= (\boldsymbol{R}^e)^T\boldsymbol{R}^{(e)} = \sum_{e\in\boldsymbol{E}} (\boldsymbol{r}^e)^T\boldsymbol{r}^{(e)} \end{aligned}, \tag{7}$$

$$\boldsymbol{r}^{(e)} = \boldsymbol{r}^e \oplus \sum_{j\in adj(e)} \boldsymbol{r}^j, \tag{8}$$

$$\boldsymbol{R}^e = (\boldsymbol{r}^1, \boldsymbol{r}^2, \cdots, \boldsymbol{r}^e)^T, \tag{9}$$

where *adj*(*e*) represents the adjacent element which share the common node with element *e*.

$$\begin{aligned} (\boldsymbol{p},\boldsymbol{Ap}) = \boldsymbol{p}^T\boldsymbol{Ap} &= \boldsymbol{p}^T\boldsymbol{Q}^T\boldsymbol{A}^e\boldsymbol{Q}\boldsymbol{p} = (\boldsymbol{Q}\boldsymbol{p})^T\boldsymbol{A}^e\boldsymbol{Q}\boldsymbol{p} \\ &= (\boldsymbol{P}^{(e)})^T\boldsymbol{A}^e\boldsymbol{P}^{(e)} = \sum_{e\in\boldsymbol{E}} (\boldsymbol{p}^{(e)})^T\boldsymbol{A}^e\boldsymbol{p}^{(e)} \end{aligned}, \tag{10}$$

$$\boldsymbol{P}^{(e)} = (\boldsymbol{p}^{(1)}, \boldsymbol{p}^{(2)}, \cdots \boldsymbol{p}^{(e)})^T, \tag{11}$$

where $\boldsymbol{p}$ is global direction vector, $\boldsymbol{p}^{(e)}$ is the local element direction vector.

The equations obtained by discretization are ill-conditioned, which causes the convergence speed of the CG method to slow down or even not converge. In order to improve the convergence, the Jacobi preconditioned (JP) technology is applied to EBE-CG. The Jacobi preconditioner is a simple preconditioned method with good parallelism [15]. The Jacobi preconditioned factor consists of the diagonal elements of the coefficient matrix and does not increase memory and communication time. The Jacobi preconditioned factor can be calculated on each element as

$$\boldsymbol{m}^{(e)} = \boldsymbol{m}^e \oplus \sum_{j\in adj(e)} \boldsymbol{m}^j, \tag{12}$$

where $\boldsymbol{m}$ is the Jacobi preconditioned factor.

The computation for all the elements will be executed in parallel through thousands of threads on CUDA platform.

B. Classical coloring method

Coloring problem is a branch of graph theory problems in mathematics. The coloring method needs to group the elements as even as possible with as few colors as possible [16]. The number of colors is not the smaller the better, it should meet the needs of the current calculation. CCM is shown in Algorithm 1.

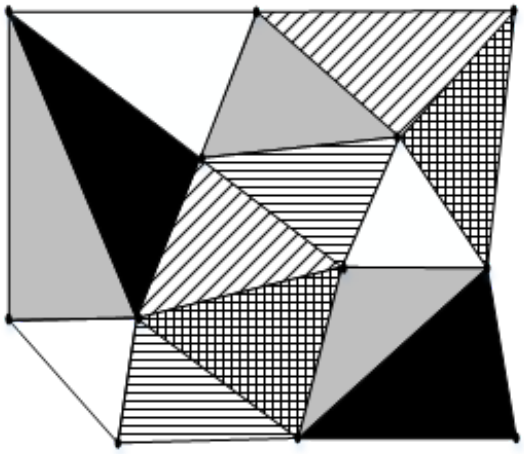

Fig. 1. A 2D coloring group diagram.

Algorithm 1: Classical coloring method
1: Use a new color.
2: Get the nodes of the adjacent element.
3: Get all the element numbers associated with the nodes.
4: Get the color numbers of adjacent elements.
5: If the current color is not used for adjacent elements, provide it for the current element. Otherwise, return to 2.
6: If all elements are colored, stop. Otherwise, return to 1.

The CCM can obtain crude element grouping, but the grouping is uneven; there are "rich" groups containing too many elements and "poor" groups with too few elements. The grouping diagram is shown in Figure 1.

These groups require additional operation to make them more even. In addition, the CCM has the problem of excessive nesting of loops. These problems make the coloring time long and efficiency low.

C. Fast color marking method

To solve the problems of the CCM, the FCM is proposed to get more even groups faster. The FCM is as follows:

Algorithm 2: Fast color marking method
1: Get the nodes of the current element.
2: Get all the element numbers associated with the nodes.
3: Get the color numbers of adjacent elements.
4: Provide the current element with the smallest number among the unused color numbers of adjacent elements.
5: If all elements are colored, stop. Otherwise, return to 1.

The FCM colored the elements sequentially, it reduces the loop nesting existed in CCM and makes the grouping more uniform.

D. Optimized fast color marking method

When using FCM, all nodes need to be traversed once and the color numbers of adjacent elements also need to be retrieved once, which greatly increases the number of instructions to be executed.

In this paper, tabu search algorithm is introduced into FCM to improve grouping efficiency. A new array is set as a tabu table, in which the information of the elements that share the same nodes have been recorded as tabu object, and then marks the color of the current element, which can avoid repeated searches for nodes and the color serial. After optimization, the number of instructions has been reduced greatly, while the memory occupied by the new array is very small, therefore, the execution speed of the program can be improved obviously.

OFCM simplifies the looping process and logic judgment in FCM by introducing new arrays to record key information, the coloring process has been speeded up significantly. The optimized coloring algorithm can also be applied to face shading, edge shading, or vertex shading. Algorithm 3 shows the OFCM. The mathematical model of OFCM can be expressed as,

$$\min f(x) = \sum_{k\in \boldsymbol{C}} \left(\sum_{i\in \boldsymbol{E}} x_{ik}\right)$$
$$s.t. \begin{cases} \sum\limits_{k\in \boldsymbol{C}} x_{ik} = 1, for\ each\ element\ i \\ \sum\limits_{i\in adj(j)} x_{ik}\cdot x_{jk} = 0 \end{cases}, \tag{13}$$

$$x_{ij} = \begin{cases} 1, & for\ element\ i\ with\ color\ j \\ 0, & otherwise \end{cases}, \tag{14}$$

where $\boldsymbol{C}$ is the set of colors.

Algorithm 3: Optimized fast color marking method
1: Get the nodes of the current element.
2: Get all the element numbers associated with the nodes.
3: Create an array A to record the color of the current element, and retrieve the color numbers of adjacent elements from array A.
4: Provide the current element with the smallest number among the unused color numbers of adjacent elements.
5: Record the color of the current element in array A.
6: If all elements are colored, stop. Otherwise, return to 1.

Three coloring methods have been researched and programmed in this paper, a set of meshes has been

Table 1: Comparison of three coloring methods

Method	Elements	Nodes	Coloring times (ms)	Colors used
OFCM	24106	12260	7634	7
FCM	24106	12260	19028	7
CCM	24106	12260	41358	8

colored by them respectively. The results are shown in Table 1.

From Table 1, it can be seen that the OFCM saves the execution time greatly, OFCM and FCM use less colors than CCM. Moreover, the grouping uniformity of OFCM and FCM is much higher than that of CCM. The number of elements in each group is about 3500 for FCM and OFCM, while the number of elements in each group varies greatly for CCM, ranging from 100 to 12,000. Based on the above results, in the following calculation examples, only FCM and OFCM are compared and discussed, and CCM is no longer used.

E. Parallel EBE-FEM combined with OFCM

For EBE-FEM algorithm, the iterative solving process is performed for each element, and all elements can be solved at the same time by GPU. The local vector is pre-calculated and stored in memory. However, when the local element residual vector $\boldsymbol{r}^{(e)}$ and the vector $\boldsymbol{m}^{(e)}$ are accumulated in Jacobi preconditioner, if there are common nodes between adjacent elements, the access conflict will occur. Access conflict will reduce the calculation efficiency and even make calculation errors. After the coloring method divides the elements with common nodes into different groups, the element vectors of all elements in a group can be calculated simultaneously by EBE-FEM. In this way, access conflicts and calculation errors can be avoided, and complete parallelism within the group can be achieved. The loops between groups are still serial. The coloring process is executed by the CPU, and the EBE-FEM computing process is executed by the GPU, in which one element is processed by one thread.

The combination part of EBE and OFCM is shown in Algorithm 4.

Algorithm 4: The combination part of EBE and OFCM

```
for all colors c do                          // compute m^(e)
   for e ∈ ε^(c) do
      M^(e) ←diag(e)
      α ← e
   end for
end for
for e ∈ α do
   m^(e) ← m^(e) + M^(e)
end for
solve m^(e) z^(e) ← r^(e)
for all colors c do                          // compute r^(e)
   for e ∈ ε^(c) do
      Z^(e) ← r^(e)
      β ← e
   end for
end for
for e ∈ β do
      z^(e) ← z^(e) + Z^(e)
end for
```

III. APPLICATION AND ANALYSIS

The proposed method has been applied to analyze the magnetic field produced by a solenoid and a single-phase power transformer. All the programs have been developed in C++. The computations have been carried out on a heterogeneous CUDA platform with a quad-core Intel i7-6700 CPU and an NVIDIA GTX 965m GPU.

A. Calculation and comparison of solenoid magnetic field

In order to verify the validity and accuracy of the algorithm and program, the magnetic field of a solenoid has been analyzed by the parallel EBE-FEM combining the OFCM and the FCM respectively. According to Biot–Savart Law, the analytical solution of the magnetic field at the points on the central axis can be calculated by

$$dB = \frac{\mu_0 n I R^2}{2(R^2 + x^2)^{3/2}} dx, \tag{15}$$

where $\boldsymbol{\mu}_0$ is the permeability in vacuum, n is the number of turns, I is the current, R is the radius of the solenoid.

A rectangle region is set as the solution domain, and the magnetic field distribution is shown in Figure 2.

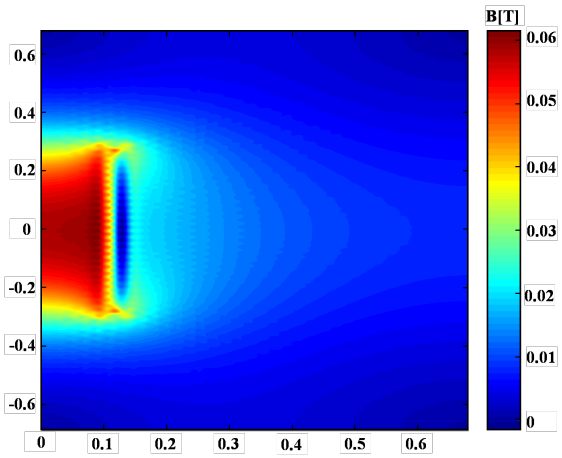

Fig. 2. The magnetic field distribution of the solenoid.

Table 2: Calculated results of EBE method with different coloring method

Method	Elements	Nodes	Coloring times (ms)	Execution time (ms)	Max relative error (%)
OFCM+EBE	4260	2224	227	2562	4.51
FCM+EBE	4260	2224	534	3008	4.43
Serial EBE	4260	2224	0	6441	4.50

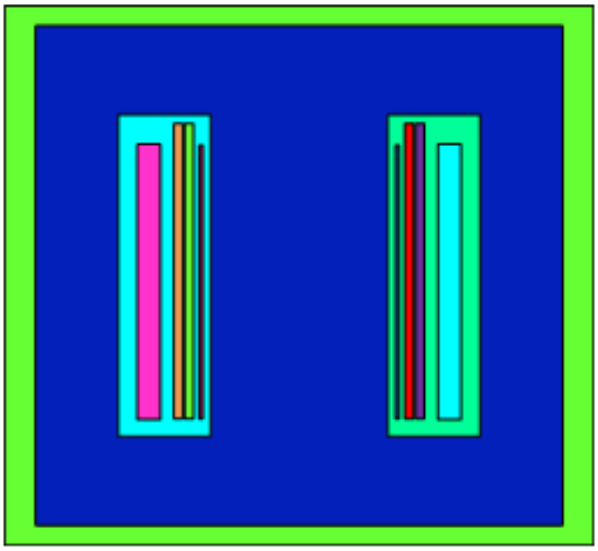

Fig. 3. The model of the single-phase transformer.

Comparing the calculation results on the central axis of the solenoid with the analytical solution, the relative errors can be determined. The maximum relative errors are showed in Table 2.

It can be seen from Table 2 that the proposed method is valid and accurate, the OFCM is more efficient than FCM. The serial EBE-FEM only runs on the CPU without parallel computing and element coloring. The results show that the algorithm proposed in this paper has more advantages in calculation efficiency. The coloring algorithm does not change the calculation process and input variables of the EBE-FEM, the difference of relative errors is produced by the round-off error of the computer.

B. Magnetic field in single-phase transformers

EBE-FEM parallel algorithm combined with different coloring methods have been investigated and applied to calculate the magnetic field produced by single-phase DSP-241000kVA/500kV transformer. The secondary side of the transformer is opened and the primary side is excited by rated current. The model of the transformer is shown in Figure 3. The model is subdivided into a triangular mesh, as shown in Figure 4.

The distribution of the magnetic flux density and the magnetic lines are shown in Figures 5 and 6.

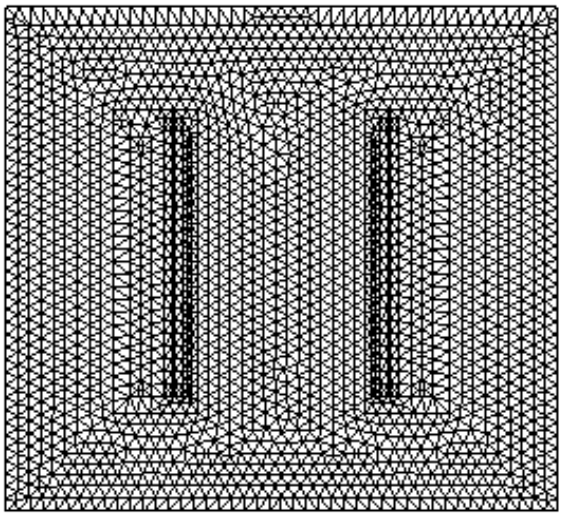

Fig. 4. The mesh of the single-phase transformer.

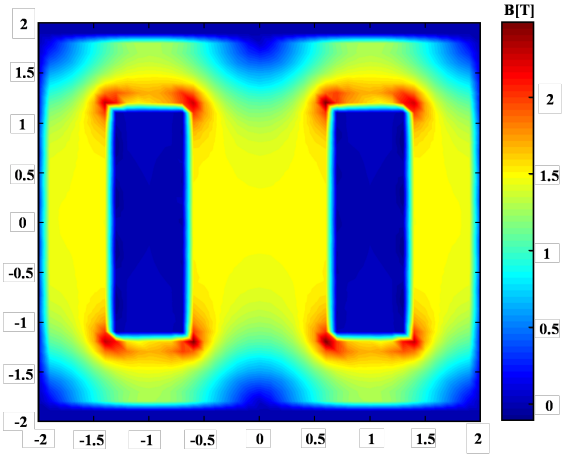

Fig. 5. The magnetic field distribution of the transformer.

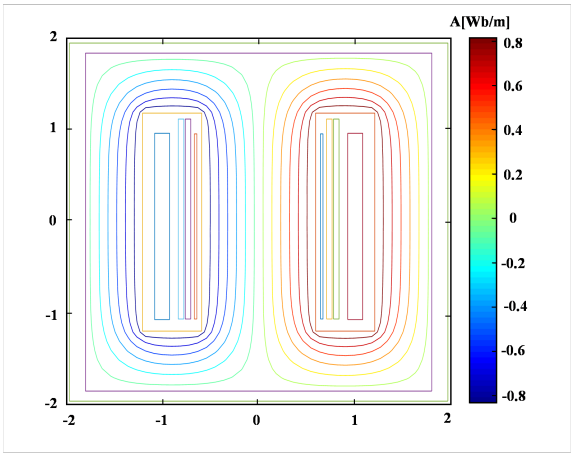

Fig. 6. The magnetic lines of transformer.

Table 3: Calculated results of EBE method with different coloring method

Test case	Elements	Nodes	Coloring time (ms)		Computation time of EBE-FEM	
			OFCM	FCM	OFCM	FCM
1	11,443	5860	1862	4269	5704	5755
2	19,328	9848	5971	12,267	11,776	11,670
3	40,816	20,685	24,642	55,691	27,173	28,015
4	61,390	31,028	56,019	122,850	45,783	45,616
5	171,338	86,223	275,698	702,756	82,900	83,387

The calculation results of EBE-FEM combined with different coloring methods are shown and compared in Table 3. From Table 3, it can be seen that the coloring time of OFCM is twice faster than that of FCM. The larger scale mesh is involved, the higher efficiency can be obtained. The number and uniformity of the groups obtained by two coloring methods are similar, which can be seen from the similar calculation time of EBE-FEM.

IV. CONCLUSION

In this paper, the EBE-J-PCG method has been implemented in parallel on CUDA platform, an optimized fast color marking method is proposed to solve the access conflict in parallel computation. The OFCM can use less colors to get even grouping in the least coloring time, and even and reasonable color grouping is important for large-scale EBE parallel computing. The OFCM can be applied to face shading or vertex shading.

ACKNOWLEDGMENT

This work is supported in part by the National Natural Science Foundation under Grant 51777128.

REFERENCES

[1] M. Macedonia, "The GPU enters computing's mainstream," *IEEE Computer*, vol. 36, no. 10, pp. 106-108, Oct. 2003.

[2] N. Godel, N. Nunn, T. Warburton, and M. Clemens, "Accelerating multi GPU based discontinuous Galerkin FEM computations for electromagnetic radio frequency problems," *Applied Computational Electromagnetics Society (ACES) Journal,* vol. 25, no. 4, pp. 331-338, Apr. 2010.

[3] T. Hughus, I. Levit, and J. Winget, "An element-by-element solution algorithm for problems of structural and solid mechanics," *Computer Methods in Applied Mechanics and Engineering,* vol. 36, no. 2, pp. 241-254, Feb. 1983.

[4] W. Dongyang, Y. Xiuke, T. Renyuan, X. Dexin, and R. Ziyan, "Parallel realization of element by element analysis of eddy current field based on graphic processing unit," *Applied Computational Electromagnetics Society (ACES) Journal*, vol. 33, no. 2, pp. 168-171, Feb. 2018.

[5] C. Cecka, A. J. Lew, and E. Darve, "Assembly of finite element methods on graphics processors," *International Journal for Numerical Methods in Engineering,* vol. 85, no. 5, pp. 40-669, Aug. 2011.

[6] Z. Yan, Y. Xiuke, R. Xvdong, W. Sheng, and W. Dongyang, "Parallel implementation and branch optimization of EBE-FEM based on CUDA platform," *Applied Computational Electromagnetics Society (ACES) Journal,* vol. 35, no. 6, pp. 595-600, Jun. 2020.

[7] Y. Jararweh, M. Jarrah, A. Bousselham, and S. Hariri, "GPU-based Personal Supercomputing," *Proceedings of the 2013 IEEE Conference on Applied Electrical Engineering and Computing Technologies (AEECT)*, Amman, Jordan, Dec. 2013.

[8] I. Kiss, S. Gyimothy, Z. Badics, and J. Pavo, "Parallel Realization of the Element-by-Element FEM Technique by CUDA," *IEEE Transactions on Magnetics,* vol. 48, no. 2, pp. 507-510, Feb. 2012.

[9] M. Kronbichler and K. Ljungkvist, "Multigrid for matrix-free high-order finite element computations on graphics processors," *ACM Transactions on Parallel Computing,* vol. 6, no. 1, pp. 3-34, May 2019.

[10] G. F. Carey, E. Barragy, R. Mclay, and M. Sharma, "Element-by-element vector and parallel computa-tions," *Communications in Numerical Methods in Engineering,* vol. 4, no. 3, pp. 299-307, 1988.

[11] K. Kormann and M. Kronbichler, "Parallel finite element operator application: graph partitioning and coloring," *IEEE Seventh International Conference on E-Science,* Dec. 2011.

[12] A. Czumaj, K. Jansen, M. Friedhelm, and I. Schiermeyer, *Algorithmic Graph Theory*, Cambridge University Press, 1985.

[13] D. Komatitsch, D. Michea, and G. Erlebacher, "Porting a high-order finite-element earthquake modeling application to NVIDIA graphics cards using CUDA," *Journal of Parallel and Distributed Computing,* vol. 69, no. 5, pp. 451-460, Jan. 2009.

[14] U. Kiran, D. Sharma, and S. Singh Gautam, "GPU-warp based finite element matrices generation and assembly using coloring method," *Journal of Computational Design and Engineering,* vol. 4, no. 4, pp. 705-718, Nov. 2018.

[15] Y. Xiuke, H. Xiaoyu, W. Dongyaong, X. Dexin, B. Baodong, and R. Ziyan, "Research on preconditioned conjugate gradient method based on EBE-FEM and the application in electromagnetic

field analysis," *IEEE trasactions on Magnetics,* Jan. 2017.

[16] G. Chunlei and T. Hubing, "Development and application of a fast multipole method in a hybrid FEM/MoM field solver," *Applied Computational Electromagnetics Society (ACES) Journal,* vol. 19, no. 3, pp. 126-134, Nov. 2004.

Xvdong Ren Mr. Ren received a B.S degree in electrical engineering from Shandong Jianzhu University, China, in 2018. Currently studying at Shenyang University of Technology, studying for a Ph.D. in electrical engineering, and his research direction is numerical analysis and optimization of engineering electromagnetic fields.

Xiuke Yan (correspondence author) Ms. Yan received her B.S degree, M.S degree, and Ph.D. degree in electrical engineering from Shenyang University of Technology, China, in 1996, 1999, and 2005, respectively. She is currently a professor in Shenyang University of Technology. Her research interests include numerical analysis of coupled field and optimization design of electrical equipment, parallel algorithm research of finite element method.

Uncertainty Quantification and Global Sensitivity Analysis of Radiated Susceptibility in Multiconductor Transmission Lines using Adaptive Sparse Polynomial Chaos Expansions

Yu Zhu[1], Yinhao Wang[1], Quanyi Yu[1], Dayong Wu[1,2], Yang Zhang[1*], and Tong Zhang[3]

[1]College of Instrumentation and Electrical Engineering
Jilin University, Changchun, 220000, 130061 China
zhuyu202114@126.com, wangyinhao202020@126.com, qyyu20@mails.jlu.edu.cn, wudy20@mails.jlu.edu.cn,
*zhangyang19@jlu.edu.cn

[2]EMC Center
FAW-Volkswagen Automotive Company Ltd., Changchun, 220000, 130061 China
wudy20@mails.jlu.edu.cn

[3]Network Department, Changchun Branch,
China Mobile Communications Corporation Jilin Company Ltd, Changchun, 220000, 130061 China
zhangtong201919@126.com

Abstract – This study analyzes the uncertainties of the radiated susceptibility in multiconductor transmission lines (MTLs), and introduces an adaptive sparse polynomial chaos expansion combining hyperbolic truncation scheme with orthogonal matching pursuit method (AS-PCE (OMP)). This method is used as the basis to realize the uncertainty quantification (UQ) of radiated susceptibility and global sensitivity analysis (GSA) of input variables to output variables. GSA considers the influencing factors of the incident field and transmission-line geometric parameters. The global sensitivity indices of each input variable are calculated for varying impedance loads. The accuracy and efficiency of the proposed method are verified compared with the results of the polynomial chaos expansion based least angle regression method and Monte Carlo methods.

Index Terms – adaptive sparse polynomial chaos expansion, multiconductor transmission lines (MTLs), radiated susceptibility, uncertainty quantization.

I. INTRODUCTION

Recently, considerable literature has grown up around the theme of multiconductor transmission lines (MTLs) radiated susceptibility uncertainty analysis. Given the change of the electromagnetic environment where electronic equipment is located, the electromagnetic interference that equipment receives through the field-line coupling will be uncertain. Owing to the production process, actual layout, and environmental factors (e.g., temperature) of the transmission lines in the equipment, the transmission-line geometric parameters also have uncertainties, which likewise affects electromagnetic interference. The aforementioned reasons have prompted engineers to consider these uncertainties when designing the electromagnetic compatibility of products. Moreover, researchers are considerably interested in the uncertainty quantification (UQ) of the model and global sensitivity analysis (GSA) of input variables. Numerous methods, such as Monte Carlo (MC) [1], stochastic reduced order models [2], probabilistic immunity [3], support vector machine [4], first- and second-order reliability [5], gradient boosting algorithms [6], Bayesian optimization [7], stochastic collocation [8], and polynomial chaos expansions (PCE) [9]-[12] have been successfully applied to UQ and GSA of EMC in MTLs. MC method is a classical uncertainty numerical analysis method. Although the calculation results are accurate, convergence speed is slow and calculation cost is high, and MC is often used as a comparison method of new methods.

The PCE has developed rapidly in recent years, and uses orthogonal polynomials of random input variables to establish surrogate model for uncertainty analysis. Under the premise of ensuring the accuracy of calculation, PCE can effectively improve the efficiency of calculation. Some experts combined the generalized polynomial chaos expansions with least angle regression method as bases to analyze uncertainties and global sensitivity of PCB-radiated susceptibility [13]. The current research used the PCE as basis to combine the hyperbolic truncation scheme and orthogonal matching pursuit

Submitted On: January 18, 2021
Accepted On: July 7, 2021

https://doi.org/10.47037/2021.ACES.J.361004

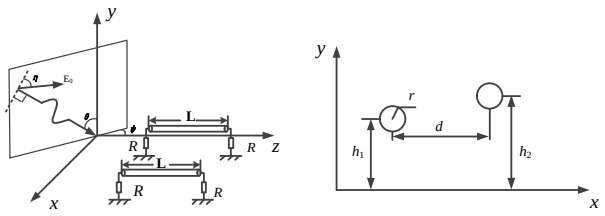

Fig. 1. Incident field and MTLs model.

method. Accordingly, adaptive sparse polynomial chaos expansions (AS-PCE (OMP)) is established to realize UQ and GSA of the transmission line radiated susceptibility.

The remainder of this paper is organized as follows. Section II introduces the physical model of the research. Section III presents AS-PCE (OMP) theory. Section IV analyzes the simulation results of AS-PCE (OMP) theory on UQ and GSA, and compares them with those of MC and adaptive sparse polynomial chaos expansion based on Least Angle Regression (AS-PCE(LARS)).

II. PHYSICAL MODEL

In order to analyze which of the geometric variables and incident field variables of the transmission lines has a greater impact on the radiation sensitivity under the low and high impedance conditions in low-frequency band, the uncertainties of radiation sensitivity of MTLs are studied in this paper, particularly for a (2+1) transmission-line system with ground as reference conductor. As shown in Figure 1, the uncertain factors include the variables involved in the incident field and geometric parameters of the transmission lines. In particular, E_0, θ, η, and ψ are the field amplitude, elevation angle, polarization angle, and azimuth angle of the incident plane wave, respectively. The geometric parameters of the transmission line include the length L, radius r, heights h_1 and h_2 above ground, and transverse distance d between the two transmission lines. The impedance loads of transmission lines are R. This study uses MTLs theory [14] to calculate the radiated susceptibility in transmission lines.

III. PCE METHODOLOGY

Polynomial chaos originated from the homogeneous function in Wiener theory, then the Askey scheme extended PCE to more variable distribution types [15].

The original model is set as $Y = y(\xi)$ and $\boldsymbol{\xi}$ is $[\xi_1, \xi_2, \xi_3, \ldots, \xi_d]$, which is the set of d-dimensional input variables. The model can be expressed in the form of polynomial chaos expansion as follows:

$$Y = \sum_{\alpha \in \mathcal{A}} c_\alpha \Phi_\alpha(\xi). \tag{1}$$

where $\Phi_\alpha(\boldsymbol{\xi})$ are multivariate polynomials orthonormal, $\mathcal{A}$ is a multidimensional index set that can identify multidimensional polynomial $\Phi_\alpha(\xi)$, $\Phi_\alpha(\xi)$ is composed of the tensor product of the orthogonal polynomials corresponding to the d-dimensional single variables (i.e., $\Phi_\alpha(\xi) = \prod_{i=1}^{d} \phi_{\alpha_i}(\xi_i)$),$c_\alpha$are unknown coefficients of expansion, and $\frac{(p+d)!}{p!d!}$ is the total number of components after the truncation of order p. The highest order of each polynomial in the standard truncation scheme is the sum of the corresponding polynomial orders of each single variable: $\sum_{k=1}^{d}(l_k) = l_1 + l_2 + \cdots l_d$.

A. Sparse polynomial chaos expansion based on hyperbolic truncation and orthogonal matching pursuit

The effects of the sparsity and hierarchy principles of the model [16] indicate that the low-order effect in the model is more important than the high-order effect. The hyperbolic truncation scheme can use norm q to deal with the model sparsely: $\left(\sum_{k=1}^{d}(l_k)^q\right)^{1/q}$, where $0 < q \leq 1$. When q = 1, the effect of the hyperbolic truncation corresponds exactly to the standard truncation.

When calculating c_α, this study uses the OMP to further sparse the model. This method uses the idea of greedy iteration to calculate the polynomial elements basis that are most related to the current residual. Moreover, using such a technique can minimize the residual and effectively sparse the model. The main steps of the OMP algorithm are as follows:

Input: iterations k, initial residual $r^{(0)}=Y$, expected error ε

Output: activity set Γ, coefficients c_α

1. k=0, $\Gamma=\varnothing$, $r^{(0)}=Y$.
2. **while** $\left\|r^{(k)}\right\| > \varepsilon$
3. $k=k+1$.
4. Find the polynomial most related to the current residual: $\Phi_{\alpha_k} = \arg\max \left|\left\langle \Phi_{\alpha_k}, r^{(k)} \right\rangle\right|$.
5. Merge Φ_{α_k} into activity set: $\Gamma = \Gamma \cup \Phi_{\alpha_k}$.
6. Use the least square method to calculate the $c^{(k)}$ in Γ.
7. Update residual $r^{(k)}=Y - \Phi_\Gamma c^{(k)}$.
8. **end while**

B. Truncated order p-adaptive method based on the leave-one-out error

When the OMP is used to calculate the coefficients of expansion, an adaptive algorithm based on the leave-one-out error ε_{LOO} is used to select the truncation order p and verify the accuracy of the model.ε_{LOO} can be expressed as follows:

$$\varepsilon_{LOO} = \frac{\sum_{i=1}^{N} \left(\mathcal{M}\left(x^{(i)}\right) - \mathcal{M}^{PC\setminus i}\left(x^{(i)}\right) \right)^2}{\sum_{i=1}^{N} \left(\mathcal{M}\left(x^{(i)}\right) - \hat{\mu}_Y \right)^2}, \quad (2)$$

where $\mathcal{M}(x^{(i)})$ is the response value of the model at point $x^{(i)}$ of the ith metamodel, $\mathcal{M}^{PC\setminus i}(x^{(i)})$ is the response value of the PCE at the ith metamodel $x^{(i)}$, and $\hat{\mu}$ is the mean. After the p is selected using the adaptive algorithm, a sparse polynomial chaos surrogate model can be established, which can be used for efficient uncertainty analysis. The main steps of the adaptive selection algorithm are as follows:

Input: max truncation order p_{max}, expected error ε_{LOO}
Output: truncation order p
1.**while** $\varepsilon > \varepsilon_{LOO}$ and $p < p_{max}$
2. p=p+1; calculate ε.
3.**end while**

C. Statistical moment calculation and Sobol global sensitivity analysis based on PCE

Given the orthogonality of the basis function in the PCE, the mean and variance of the output Y can be obtained as follows:

$$E[Y] = c_0. \quad (3)$$

$$Var[Y] = \sum_{\alpha \in \mathcal{A}\setminus\{0\}} c_\alpha^2. \quad (4)$$

When the PCE is combined with the Sobol global sensitivity analysis method [17], which is based on the idea of variance decomposition, the first-order sensitivity indices S_i and total sensitivity indices $S_{T,i}$ of the random input variables ξ_i can be expressed as follows:

$$S_i = \frac{\sum_{\alpha \in \mathcal{A}_i} c_\alpha^2}{Var[Y]}. \quad (5)$$

$$S_{T,i} = \frac{\sum_{\alpha \in \mathcal{A}_{T,i}} c_\alpha^2}{Var[Y]}. \quad (6)$$

where $\mathcal{A}_i = \{\alpha \in \mathcal{A} : \alpha_i > 0, \alpha_j = 0 \ \forall i \neq j\}$, $\mathcal{A}_{T,i} = \{\alpha \in \mathcal{A} : \alpha_i \neq 0\}$

IV. NUMERICAL EXAMPLE RESULT

We will combine the numerical example of the MTLs to verify and analyze the previously described method. Combined with the physical model discussed in section II, the random input variables are made to follow different random distribution. Take the common uniform distribution and normal distribution as examples, the ranges of input parameters are $\theta \in U(0, 0.5\pi)$, $\psi \in U(-\pi, \pi)$, $\eta \in U(0, 2\pi)$, $E_0 \in N(1, 0.1^2)V$, $r \in U(0.4, 0.6)mm$, $h_1 \in U(20, 25)mm$, $h_2 \in U(20, 25)mm$, $d \in U(5, 7)mm$and $L \in N(1, 0.1^2)m$. The transmission-line loads can be divided into two cases: low impedance (50 Ω) and high impedance (10 kΩ).

Table 1: Calculation time comparison

Sampling size	Time/s
600	526.74
700	732.22
800	1015.31

A. Uncertainty analysis

In the following, we combine AS-PCE (OMP) to analyze the uncertainties of the transmission lines with low and high impedance loads at frequency 50 MHz. To this end, we choose Latin hypercube sampling (LHS) as the sampling method. In order to select the appropriate sample size, different sampling sizes: 50, 100, 200, 300, 400, 500, 600, 700, and 800 are calculated for 50 times to estimate confidence intervals for ε_{LOO}. Considering the cost and accuracy of calculation, we let the q-norm be 0.8 [18].

It can be shown in Figure 2, the median ε_{LOO} of 600 samples size is acceptable and nearly the same as 700. Given the calculation time is basically the same for different impedance, we compare the time taken for 50 times of calculation at 600, 700, and 800 with low impedance:

All simulations in this paper were carried out on a standard laptop computer with an Intel Core i5 CPU operating at 2.3 GHz and equipped with 8 GB memory. It can be shown in Table 1 that the calculation time of 600 samples is shorter on the premise of sufficient calculation accuracy. In this case, the maximum truncation degree p is 12. Therefore, 600 LHS samples is considered as a good tradeoff between accuracy and numerical cost to constructed the surrogate model.

The probability distribution of the induced current of the low and high impedance loads calculated using the different methods at frequency 50 MHz is shown in Figure 3.

In the same selection range of the adaptive truncation order p, the minimum ε_{LOO} of AS-PCE (OMP) is 3.01×10^{-18}, while the minimum ε_{LOO} of AS-PCE (LARS) is 0.088. Note that the calculation accuracy of AS-PCE (OMP) is considerably higher than that of AS-PCE (LARS). This is because AS-PCE (OMP) is a

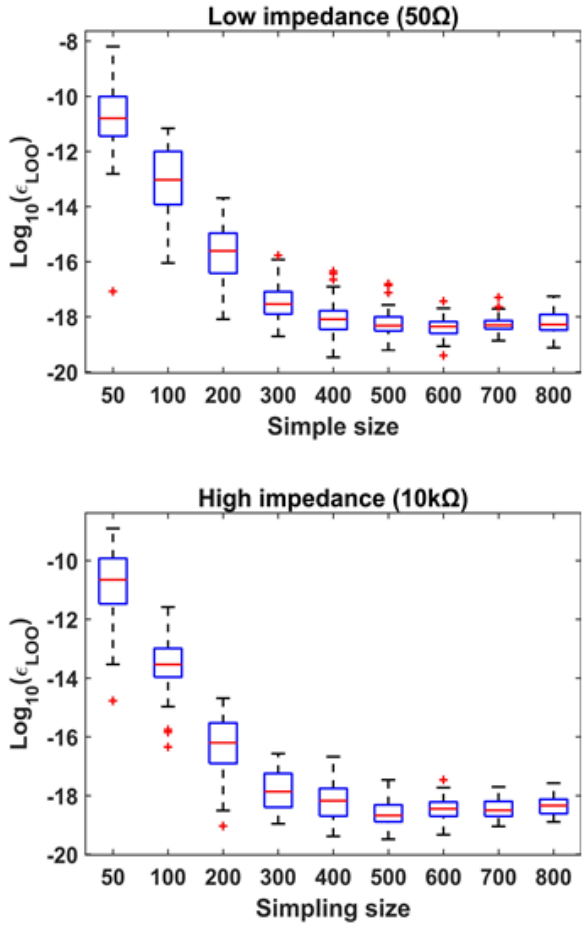

Fig. 2. ε_{LOO} of different sampling sizes.

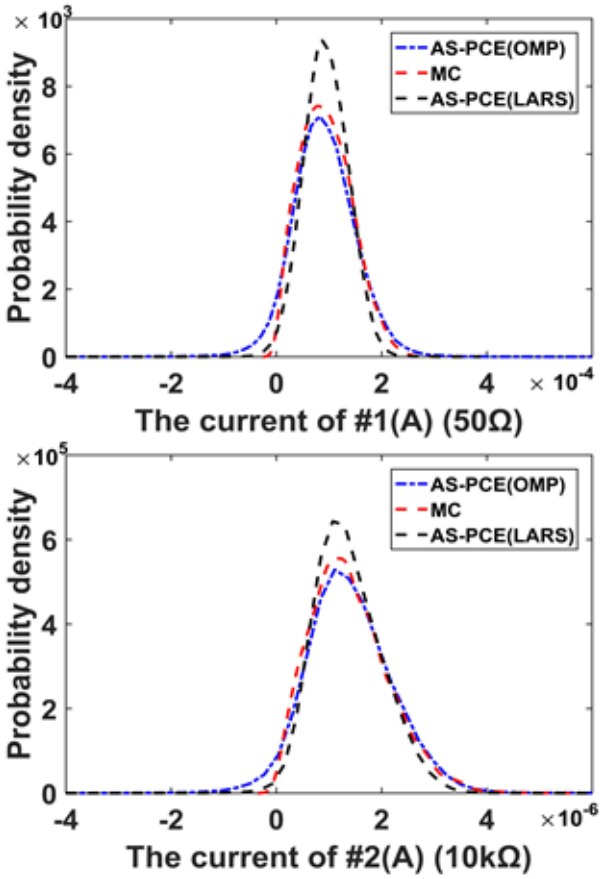

Fig. 3. Comparison of the probability distribution of the induced current with low and high impedances.

greedy algorithm, and it will find the most relevant vector in each iteration, so the accuracy of AS-PCE (OMP) is higher than AS-PCE (LARS). We compare the calculation efficiency of the two methods at the same ε_{LOO}:

Note that when ε_{LOO} of AS-PCE (OMP) approximates ε_{LOO} of AS-PCE (LARS), the calculation time of the former is substantially less than that of the latter. Therefore, AS-PCE (OMP) is considerably efficient and has more advantages in calculation.

We likewise calculate the mean and standard deviation of the induced current of low impedance loads (50 Ω) and high impedance loads (10 kΩ) in the [10 MHz, 200 MHz]. The results are compared with the AS-PCE (LARS) and 10k MC simulations.

Table 2: Calculation efficiency comparison

	ε_{LOO}	Time/s
AS-PCE (OMP)	0.095	3.73
AS-PCE (LARS)	0.092	26.86
MC (10k)	——	1037.77

As shown in Figure 4, AS-PCE (OMP) can effectively calculate the statistical information of transmission-line radiated susceptibility compared with AS-PCE (LARS) and 10k MC simulations. Given that OMP adopts the greedy iteration method, there will be a slight overfitting phenomenon when calculating the expansion coefficients with the least square method, thereby resulting in a slightly large mean square deviation.

B. Sensitivity analysis

On the basis of the method described in section III, the global sensitivity of each uncertain variable in the transmission-line radiated susceptibility is calculated and analyzed. The results are compared with the 10k MC simulations. First, we use 50 MHz as an example to calculate the total sensitivity indices of each variable.

As shown in Figure 5, the method described in section III can effectively calculate the global sensitivity indices of each variable of the transmission-line radiated susceptibility. Moreover, the global sensitivity indices of the variables of the incident field at 50 MHz is sig-

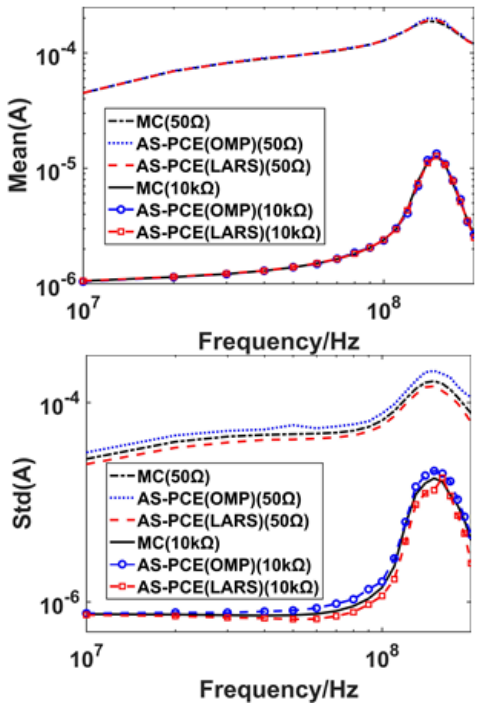

Fig. 4. Comparison of the mean and standard deviation of the induced current between low and high impedance loads.

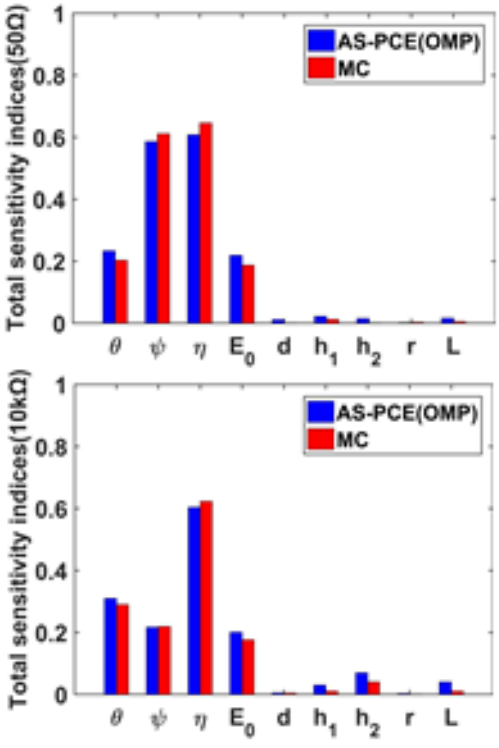

Fig. 5. Comparison of the total sensitivity indices between low and high impedances.

nificantly higher than that of the transmission-line geometric parameters, whether it is a low or high impedance loads. For further comparative analysis, the total sensitivity indices of each input variable in [10 MHz, 200 MHz] are calculated based on AS-PCE (OMP) and their influence degrees are compared.

Figure 6 shows that in the low impedance loads condition, the transmission-line geometric parameters in [10 MHz, 200 MHz] have minimal impact on the radiated susceptibility and nearly no impact in [10 MHz, 100 MHz]. Among the relevant parameters of the input field, the influence of ψ and η is greater, but the total sensitivity indices of η in [150 MHz, 200 MHz] is relatively small. In the case of high impedance loads, the influence degree of the relevant parameters of the incident field is not as substantial as that of the low impedance loads. In [10 MHz, 100 MHz], η has a high influence on the radiated susceptibility. In [100 MHz, 200 MHz], the variable that has the highest impact is length L, whereas the other geometric parameters of transmission lines have a low impact on the radiated susceptibility. Therefore, if the incident field is known in the early stage of product design, the influence of ψ and η of the incident field should be avoided. When the impedance loads of transmission lines are high, their length should be properly controlled to avoid EMC problems.

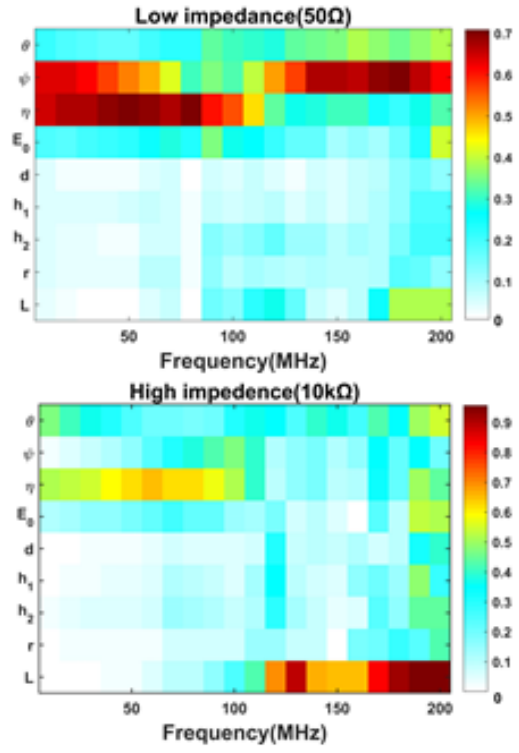

Fig. 6. Global sensitivity indices of each variable with frequency variation.

V. CONCLUSION

To analyze the uncertainties of the radiated susceptibility in MTLs, this study introduces a non-intrusive AS-PCE based on the OMP. The adaptive algorithm based on the leave-one-out error is used to determine the truncation order of the PCE. Combined with the hyperbolic truncation scheme, AS-PCE (OMP) is established. The proposed method is a greedy sparse algorithm, which is more efficient than MC method and has higher accuracy than the AS-PCE (LARS). It can ensure the accuracy of calculation and improve the efficiency of calculation, and can effectively calculate the statistical information of the radiated susceptibility of transmission lines with different impedance loads. Moreover, Sobol global sensitivity analysis is used to quantify the influence of each input variable on the radiated susceptibility. Compared with 10k simulation results of the MC method, AS-PCE (OMP) can be used to calculate at a lower cost and with evident advantages. Hence, the proposed method can be formulated in an efficient way for the EMC design of products.

ACKNOWLEDGMENT

This work was supported in part by the National Natural Science Foundation of China under Grant 51707080 and Grant No. 61903151, and in part by the Jilin Scientific and Technological Development Program under Grant 20180101032JC, Grant 20190103055JH, and Grant 20190303097SF.

REFERENCES

[1] S. Arianos, M. A. Francavilla, M. Righero, F. Vipiana, P. Savi, S. Bertuol, M. Ridel, and J. Parmantier, "Evaluation of the modeling of an EM illumination on an aircraft cable harness," *IEEE Trans. Electromagn. Compat.,* vol. 56, no. 2, pp. 844-853, Apr. 2014.

[2] Z. Fei, Y. Huang, J. Zhou, and C. Song, "Numerical analysis of a transmission line illuminated by a random plane-wave field using stochastic reduced order models," *IEEE Access,* vol. 5, pp. 8741-8751, May 2017.

[3] D. Bellan and S. Pignari, "A probabilistic model for the response of an electrically short two-conductor transmission line driven by a random plane wave field," *IEEE Trans. on Electromagn. Compat.,* vol. 43, no. 2, pp. 130-139, May 2001.

[4] R. Trinchero, I. S. Stievano, and F. G. Canavero, "Black-box modeling of the maximum currents induced in harnesses during automotive radiated immunity tests," *IEEE Trans. Electromagn. Compat.,* vol. 62, no. 2, pp. 627-630, Apr. 2019.

[5] A. Kouassi, J. Bourinet, S. Lalléchère, P. Bonnet, and M. Fogli, "Reliability and sensitivity analysis of transmission lines in a probabilistic EMC context," *IEEE Trans. Electromagn. Compat.,* vol. 58, no. 2, pp. 561-572, Apr. 2016.

[6] H. Karami, A. Mostajabi, M. Azadifar, M. Rubinstein, C. Zhuang, and F. Rachidi, "Machine learning-based lightning localization algorithm using lightning-induced voltages on transmission lines," *IEEE Trans. Electromagn. Compat.,* vol. 62, no. 6, pp. 2512-2519, Dec. 2020.

[7] S. De Ridder, D. Spina, N. Toscani, F. Grassi, D. V. Ginste, and T. Dhaene, "Machine-learning-based hybrid random-fuzzy uncertainty quantification for EMC and SI assessment," *IEEE Trans. Electromagn. Compat.,* vol. 62, no. 6, pp. 2538-2546, Dec. 2020.

[8] T. Wang, W. Yan, L. Wang, and G. Zhang, "Uncertainty analysis of random field coupling to Stochastic cables," Shenzhen, China, *APEMC. IEEE,* pp. 17-21, May 2016

[9] P. Manfredi and F. G. Canavero, "Polynomial chaos for random field coupling to transmission lines," *IEEE Trans. Electromagn Compat.,* vol. 54, no. 3, pp. 677-680, Jun. 2012.

[10] M. Larbi, I. S. Stievano, F. G. Canavero, and P. Besnier, "Variability impact of many design parameters: the case of a realistic electronic link," *IEEE Trans. Electromagn. Compat.,* vol. 60, no. 1, pp. 34-41, Jul. 2017.

[11] Q. Yu, W. Liu, K. Yang, X. Ma, and T. Wang, "Uncertainty quantification of the crosstalk in multiconductor transmission lines via degree adaptive stochastic response surface method," *Applied Computational Electromagnetics Society (ACES) Journal,* vol. 36, no. 2, pp. 174-183, Feb. 2021.

[12] T. Wang, Q. Yu, X. Li, G. Le, and H. Zhao, "Radiated susceptibility analysis of multiconductor transmission lines based on polynomial chaos," *Applied Computational Electromagnetics Society (ACES) Journal,* vol. 35, no. 12, pp. 1556-1566, Dec. 2020.

[13] T. Bdour and A. Reineix, "Global sensitivity analysis and uncertainty quantification of radiated susceptibility in PCB using nonintrusive polynomial chaos expansions," *IEEE Trans. Electromagn. Compat.,* vol. 58. no. 3, pp. 939-942, Jun. 2016.

[14] C. R. Paul, *Analysis of Multiconductor Transmission Lines*, 2nd ed. New York, NY, USA: Wiley, 2008.

[15] D. Xiu and G. E. Karniadakis, "Modeling uncertainty in flow simulations via generalized polynomial chaos," *J. Comput. Phys.,* vol. 187, no. 1, pp. 137-167, Oct. 2003.

[16] R. Mukerjee and C. F. J. Wu, *A Modern Theory of Factorial Designs*, New York: Springer, 2006.

[17] I. M. Sobol, "Sensitivity estimates for nonlinear mathematical models," *Math. Model. Comput. Exp.*, vol. 1, no. 1, pp. 112-118, Jan. 1993.
[18] M. Larbi, I. S. Stievano, F. G. Canavero, and P. Besnier, "Identification of main factors of uncertainty in a microstrip line network," *Prog. Electromagn. Res.*, vol. 162, pp. 61-72. Jan. 2018.

Yu Zhu received the B.S. degree in electrical engineering and the M.S. degree in measuring and testing technologies and instruments from Jilin University, Changchun, Jilin, China, in 2010 and 2013, respectively, where he is currently pursuing the Ph.D degree with the College of Instrumentation and Electrical Engineering.

His research interests include the analysis method in electromagnetic compatibility simulation and the uncertainty analysis methods in electromagnetic compatibility simulation.

Yinhao Wang received the B.S. degree in electrical engineering from Jilin University, Changchun, Jilin, in 2020, where he is currently pursuing the M.S degree with the College of Instrumentation and Electrical Engineering.

His research interests include the analysis method in electromagnetic compatibility simulation and credibility evaluation of electromagnetic compatibility uncertainty simulation model.

Quanyi Yu received the B.S. degree in automation and the M.S. degree in instrument and meter engineering from Jilin University, Changchun, Jilin, China, in 2016 and 2020, respectively, where he is currently pursuing the Ph.D degree with the College of Instrumentation and Electrical Engineering.

His research interests include the analysis method in electromagnetic compatibility simulation and the uncertainty analysis methods in electromagnetic compatibility simulation.

Dayong Wu received the B.S. degree in electrical engineering and the M.S. degree in measuring and testing technologies and instruments from Jilin University, Changchun, Jilin, China, in 2010 and 2013, respectively, where he is currently pursuing the Ph.D degree with the College of Instrumentation and Electrical Engineering.

His research interests include the analysis method in automotive electromagnetic compatibility and the uncertainty analysis methods in electromagnetic compatibility simulation.

Yang Zhang received the B.S. degree and the M.S. degree in electrical engineering in physics college from northeast normal university, Changchun, Jilin, China, in 2012 and 2015, respectively, and the Ph.D degree in the College of Instrumentation and Electrical Engineering, Jilin University, Changchun, Jilin, China, in 2018.

His research interests include the analysis method in electromagnetic compatibility simulation and the uncertainty analysis methods in electromagnetic compatibility simulation.

Tong Zhang received the master's degree from the Changchun University of Science and Technology, Changchun, Jilin, China, in 2013.
He is currently an Engineer with the Changchun Branch, China Mobile, China. His research interests include the areas of network communication and optical communication.

Convolution Operations on Coding Metasurface for RCS Reduction

Tingting Shang, Jianping Zhao, and Juan Xu

School of Cyber Science and Engineering
Qufu Normal University, Qufu 273165, People's Republic of China
tingzi2046@163.com, zjp-wlx@163.com, xujuan125@163.com

***Abstract* –** In this paper, a polarization conversion unit is designed as the coding unit. The units are arranged in a regular cross-arrangement. Convolution operation is composed of the Dirac-delta function and the principle of scattering-pattern shift. The Dirac-delta is optimized by generalized Snell's law and addition theorem. According to the convolution operations, the cross-arrangement pattern is shifted to multiple directions to reduce the backscattering field. Compared with regularly arranged metasurface, this method can reduce the radar cross section (RCS) of single station by at least 10 dB. Compared with the traditional intelligent optimization algorithm, this method provides a new route to reduce RCS by random distribution of elements.

***Index Terms* –** Convolution operations, cross-arrangement pattern, polarization conversion, metasurface, principle of scattering-pattern shift, radar cross section, the Dirac-delta function.

I. INTRODUCTION

The reduction of radar cross section (RCS) is obtained by redirecting the backscattering waves to multiple directions. The research focus is using the optimization algorithm to realize random cell placement and ultra-wideband RCS reduction. In 2011, the generalized Snell's law was proposed by Yu. The abnormal reflection and refraction in the optical band were realized by introducing gradient phase into the metasurface. A "V" shaped element was designed and the gradient phase was adjusted by controlling its opening angle and rotation angle in [1]. In 2014, the concept of coding metasurface was first proposed by Professor Cui Tie Jun. He designed 1-bit and 2-bit coding metasurfaces in microwave band with rectangular patch structure, which can reduce RCS by more than 10 dB in 7.8–12 GHz and 7.5–15 GHz bands respectively in [2]. In 2017, Liu realized πphase difference of broadband by AMC unit in [3]. However, Su achieved πphase difference by adjusting size of square ring structure in ultra-wide frequency band. Particle swarm optimization (PSO) is used to optimize the arrangement sequence of cells, and finally multi-beam distribution with broadband RCS reduction is obtained in [4]. In 2020, the programmable metasurface for multi-beam control using deep learning technology was proposed by Shan to reduce RCS in [5]. The random distribution of metasurface elements is realized by the optimization algorithm, which is time-consuming in programming and slow in running. The metasurface can be transformed from a regular metasurface to a random metasurface by shifting the regular metasurface scattering pattern to multiple directions. This convolution operation can not only avoid programming and iteration problems, but also achieve RCS reduction.

In this paper, the cross-arrangement matrix is added by the Dirac-delta function to realize the shift of scattering pattern. The function is optimized by using generalized Snell's law and addition theorem. The RCS is further reduced by shifting the cross-arrangement scattering pattern to multiple directions. Because the effect of RCS reduction by metal plate is poor, we choose to compare the metasurface which cross-arrangement scattering pattern is shifted to multiple directions with cross-arrangement metasurface with the same size. Finally, this metasurface achieves single station RCS reduction of more than 10 dB.

II. MATERIALS AND METHODS

A. Principle of scattering-pattern shift

The convolution theorem in Fourier transform describes the common multiplication of signals in time domain and the convolution of corresponding frequency spectrum in frequency domain.

$$f(t) \cdot g(t) \Leftrightarrow F(\omega) * G(\omega). \tag{1}$$

Equation (1) can be simplified as frequency-shift function when$G(\omega)$ becomes a Dirac-delta function, the equation (1) is rewritten as:

$$f(t)\cdot\exp(j\omega_0 t) \Leftrightarrow F(\omega)*\delta(\omega-\omega_0) = F(\omega-\omega_0). \tag{2}$$

Referring to the theory in [6], the electric field distribution on the coding metasurface and the scattering pattern in the far-field region are Fourier transform pairs. Which can connect the coding-pattern domain (in analogy to the time domain) with the scattering-pattern domain (in analogy to the frequency domain). As is mathematically expressed as:

$$e(x_\lambda) \cdot g(x_\lambda) \Leftrightarrow E(\sin\theta) * G(\sin\theta), \tag{3}$$

Submitted On: April 12, 2021
Accepted On: July 25, 2021

https://doi.org/10.47037/2021.ACES.J.361005

where $x_\lambda$is the electrical length, $\theta$is the angle with respect to the normal direction. Equation (3) is rewritten into the form of the equation (2):

$$e(x_\lambda) \cdot \exp(jx_\lambda \sin\theta_0) \Leftrightarrow E(\sin\theta_0) * \delta(\sin\theta - \sin\theta_0) = E(\sin\theta - \sin\theta_0). \quad (4)$$

The multiplication of $e(x_\lambda)$by a gradient sequence $\exp(jx_\lambda \sin\theta_0)$ is the multiplication of $\exp(j\varphi_1)$by $\exp(j\varphi_2)$.

$$\exp(j\varphi_1) \cdot \exp(j\varphi_2) = \exp(j(\varphi_1 + \varphi_2)). \quad (5)$$

Taking $\varphi_1 = 0$and $\varphi_2 = \pi$ in equation (5), it can be rewritten as equation (6). Selectingφ of $\exp(j\varphi)$ in equation (6), it can be abbreviated as equation (7).

$$\exp(j0) \cdot \exp(j\pi) = \exp(j(0+\pi)) = \exp(j\pi). \quad (6)$$

$$0 + \pi = \pi. \quad (7)$$

Because 0 in the coding matrix represents $\varphi = 0$ and 1 represents $\varphi = \pi$, the coding matrix is associated with the phase of the unit.

$$0 + \pi = \pi \Leftrightarrow 0 + 1 = 1. \quad (8)$$

In fact the operation on the coding matrix is to operate on the phase distribution, so as to shift the scattering pattern. The above equations relate the coding matrix to the far-field pattern. As shown in Figure 1, the addition of coding matrix means the far-field pattern is shifted.

B. Optimization of dirac-delta function

To reduce RCS as much as possible, it is necessary to shift the cross-arrangement scattering pattern to more directions. In other words, the Dirac-delta function needs to be optimized. Beam steering is realized by generalized Snell's law. Then, coding matrices are superimposed by addition theorem [7]. Therefore, a Dirac-delta function is generated that can be shifted to four directions, six directions, and more.

Taking Figure 2 as an example to introduce the generation of Dirac-delta function that shift the scatter pattern to four directions. When the coding sequence of the coding metasurface is 0101... / 0000... or 0000... / 0101..., it can be obtained that the metasurface has two scattering beams according to the generalized Snell's law. Using the addition coding theorem, the coding sequence 0101... / 0101... can be obtained. It can integrate the far-field scattering characteristics of coding sequence 0101... / 0000... and coding sequence 0000... / 0101... to generate four scattering beams. To better visualize the direction of scattering beam, Figure 2 gives the corresponding 2D scattering pattern in a polar coordinate system. From the 2D scattering pattern, four lighter spots represent not only the four main lobes but also the four directional points of the Dirac-delta function that shift the scattering pattern to four directions.

Based on the above theory, the Dirac-delta function is selected in Figure 2. The cross-arrangement scattering pattern is shifted to four directions by the

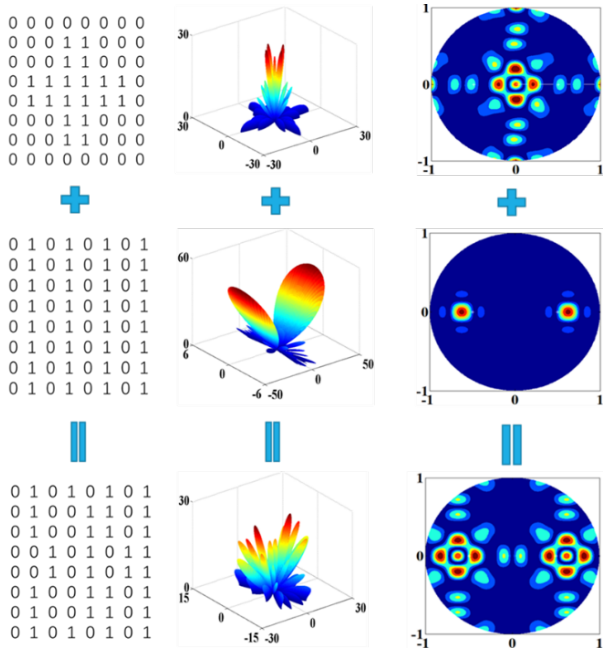

Fig. 1. Schematic diagram of scattering-pattern shift.

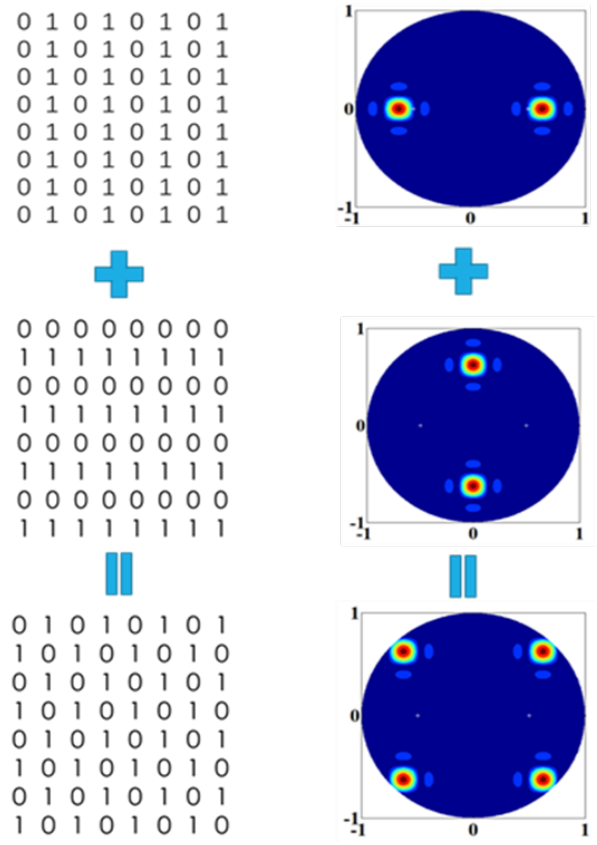

Fig. 2. Schematic diagram of addition theorem.

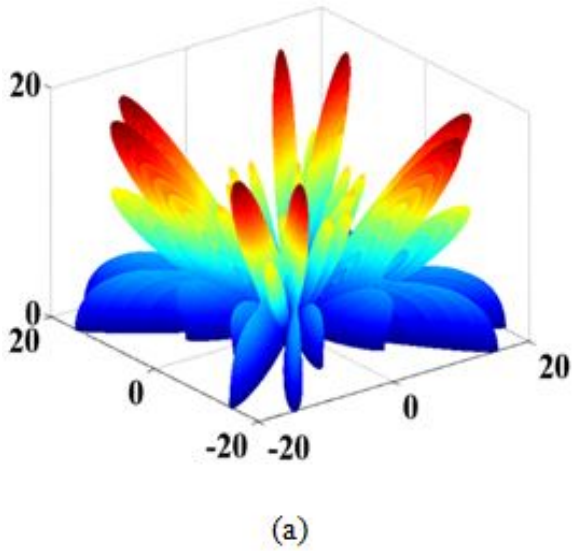

(a)

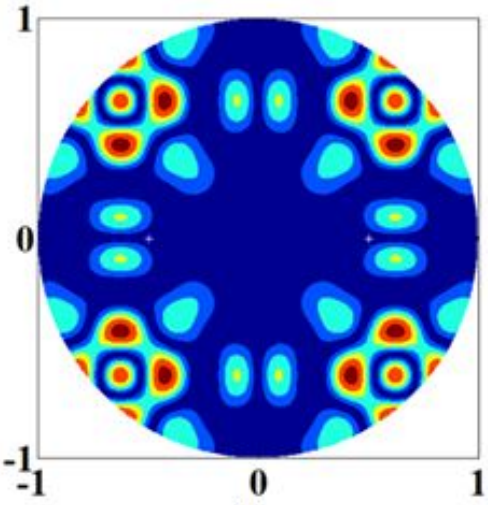

(b)

Fig. 3. Pattern of metasurface which cross-arrangement scattering pattern is shifted to four directions. (a) 3D view. (b) 2D polar view.

principle of scattering-pattern shift. In an ideal situation, the cross-arrangement scattering pattern is shifted to four directions in 3D pattern in Figure 3 (a) and the energy distribution in 2D polar coordinates in Figure 3 (b).

III. PERFORMANCE CHARACTERIZATION

A. Design of the metasurface unit

In order to better verify the above theory, a polarization conversion [8] metasurface element is proposed as shown in Figure 4 (a). The unit structure includes three layers, which are metal floor, dielectric substrate, and structural layer from bottom to top. Rogers 5880 substrate is used as the dielectric plate. The relative dielectric constant is 2.2 and the loss tangent angle is 0.0009. The size parameters are shown in Table 1.

Table 1: Size parameter of the unit

Variables	l	k	d	c	w	h
Size(mm)	4	0.52	4.3	0.9	0.3	1.75

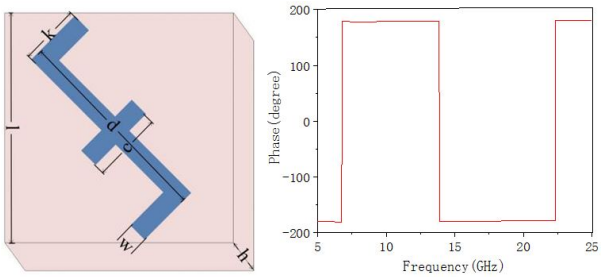

(a) (b)

Fig. 4. (a) Structure diagram of polarization conversion unit. (b) Cross-polarization phase difference.

The corresponding mirror unit can be obtained by mirroring the unit. The unit realizes wave cancellation by converting incident electromagnetic wave (EM) into cross-polarization component. As shown in Figure 4(b), because the cross polarization [9] phase difference between polarization conversion unit and its mirror unit is π, it is regarded as coding unit ("0" unit, "1" unit).

B. Optimization of unit arrangement

According to the coding matrix, the coding units are arranged in a cross-arrangement and metasurface which the cross-arrangement scattering pattern is shifted to two, four, or six directions. The metasurface is composed of 8×8 super-units with dimensions of 64 mm $\times$ 64 mm, where the super-unit is composed of 2×2 anisotropic unit cells. The metasurface is simulated and analyzed by commercial simulation software HFSS. Figures 5 and 6

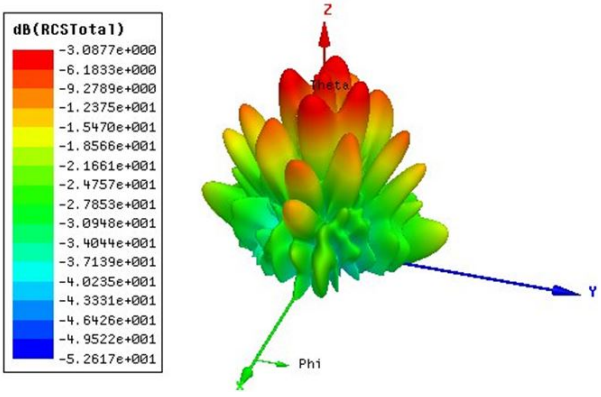

Fig. 5. The cross-arrangement scattering pattern at f = 32GHz.

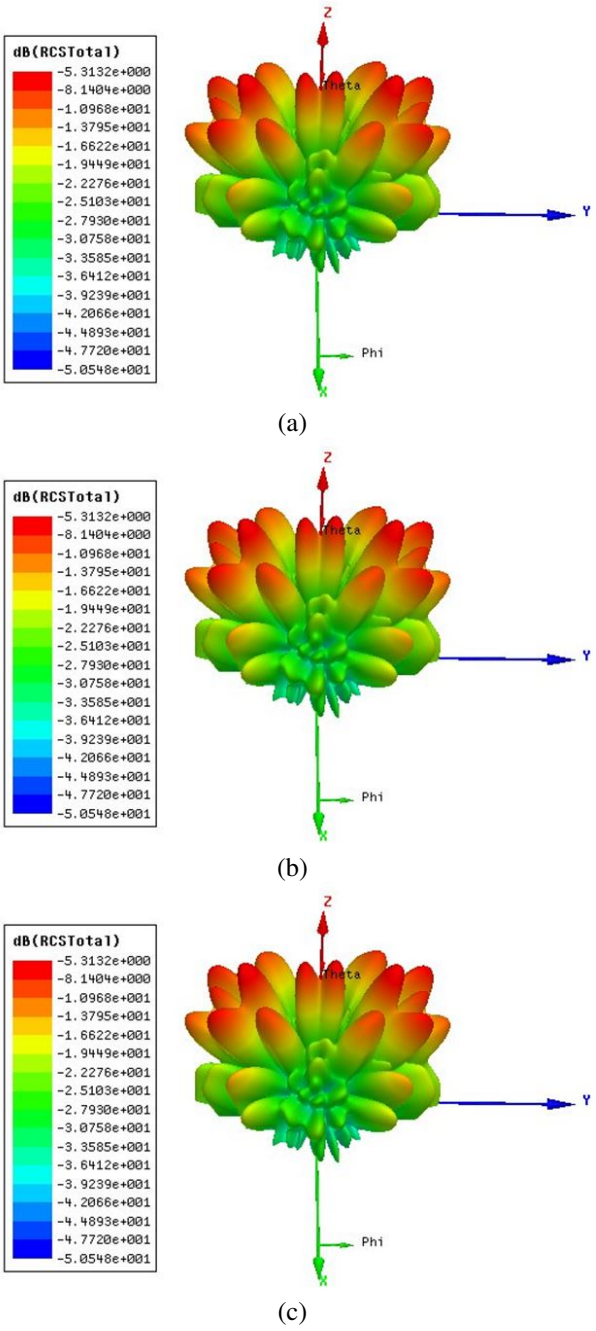

Fig. 6. The cross-arrangement scattering patterns are shifted to multiple directions at f = 32GHz.

show the scattering pattern at f = 32GHz when plane waves are incident vertically. The cross-arrangement scattering patterns is shown in Figure 5. The cross-arrangement scattering patterns are shifted to two directions in Figure 6 (a), four directions in Figure 6 (b), and six directions in Figure 6 (c). With the increase of shift direction, the energy distribution is more uniform. The incident electromagnetic energy is scattered

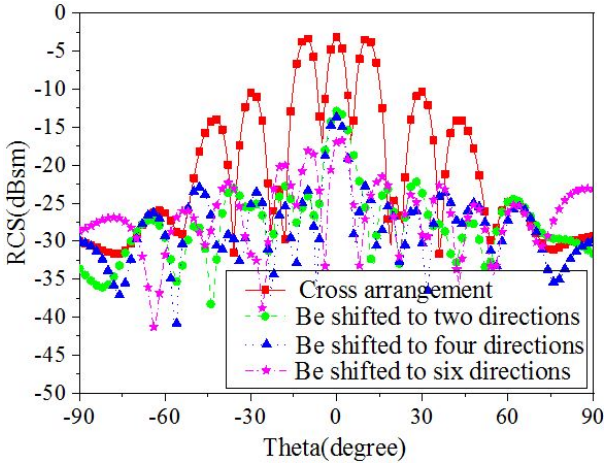

Fig. 7. 2D far-field scattering pattern plotted in y-z plane.

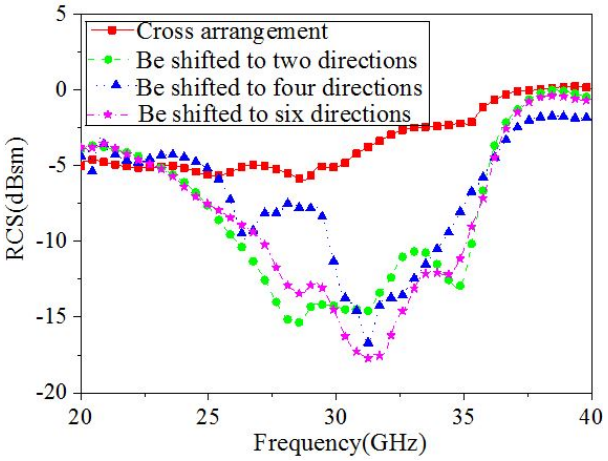

Fig. 8. The simulation results of RCS over a wide frequency range from 20 to 40 GHz.

in all directions after being reflected by the metasurface. According to the energy conservation theorem, the energy of each beam is very low, so the RCS in the vertical direction is obviously reduced. Figure 7 also proved that with the increase of the shift direction, the RCS in vertical direction decreases gradually.

In order to compare the RCS reduction of four electromagnetic metasurface more intuitively, Figure 8 shows the graph of single-station RCS change in 20–40 GHz band. The RCS of the metasurface which cross-arrangement scattering pattern is shifted to multiple directions is lower than the cross-arrangement metasurface. As the shift direction increases, so does the RCS reduction.

Compared with the cross-arrangement, the RCS reduction of the designed metasurfaces are illustrated in Figure 9. The metasurface is an array formed by the

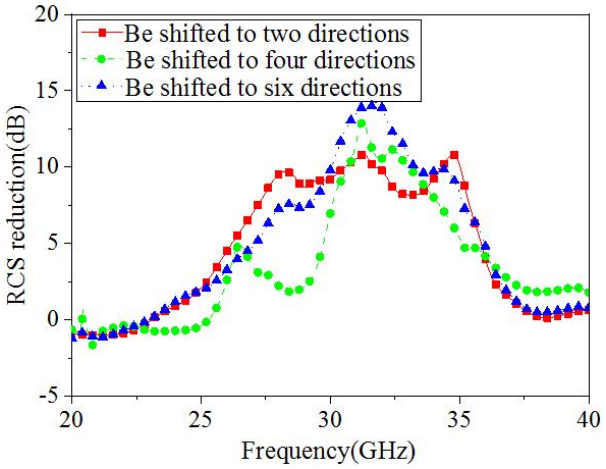

Fig. 9. Simulation results of RCS reduction.

cross-arrangement scattering pattern shifting to multiple directions. It shows that RCS reduction increases with the increase of the shifted direction of scattering pattern. Therefore, RCS reduction can be realized by designing the metasurface which regular arrangement scattering pattern is shifted to multiple directions. The more the shift direction, the greater the degree of RCS reduction.

IV. EXPERIMENTAL VERIFICATION

A prototype measuring 64 mm × 64 mm was fabricated using printed circuit board technology to verify the RCS reduction characteristics of the metasurface which regular arrangement scattering pattern is shifted to six directions, as shown in Figure 10.

Fig. 10. Photographic view of fabricated sample.

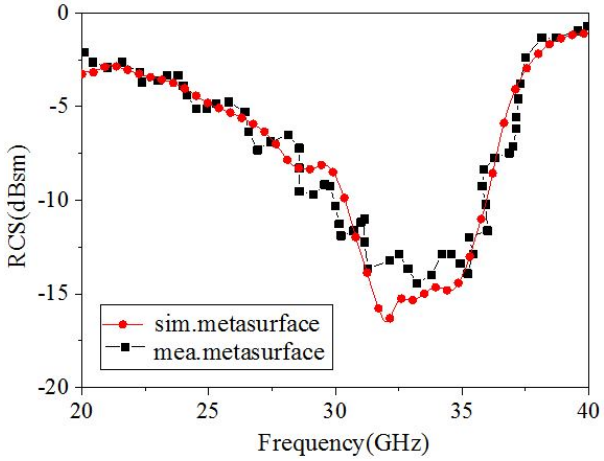

Fig. 11. Comparison of single-station RCS results of metasurface under normal incident of electromagnetic wave.

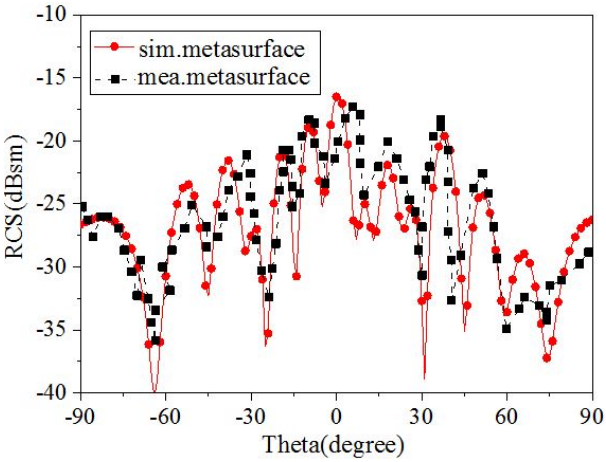

Fig. 12. Comparison of 2D far-field scattering pattern of metasurface under normal incident of electromagnetic wave.

The measurement was carried out in a microwave darkroom using the free space method. When the electromagnetic wave is normal incident, the characteristics of the single-station RCS of the metasurface changing with frequency are shown in Figure 11. As expected, the measured single-station RCS results matched well with the simulation results. And the measured RCS results in the vertical direction is also matched well with the simulation results in Figure 12. Of course, there are some errors within the acceptance range, which can be attributed to the following two reasons: (1) the incident wave in the simulation process is an ideal plane wave, while the plane incident wave in the actual measurement is approximately equivalent to the far-field radiation of

the horn antenna; (2) manufacturing tolerances in physical processing and inevitable deviations of naked eyes in measurement.

V. CONCLUSION

In this paper, a polarization conversion unit is designed, which is used as the coding unit because the phase difference between the polarization conversion unit and its mirror unit is π. Dirac-delta function is selected by using generalized Snell's law and addition theorem. Then the pattern is shifted to different directions by convolution theorem of Fourier transform. Finally, the radar cross section is reduced. The simulation results show that the metasurface which regular cross-arrangement scattering pattern is shifted to multiple directions can reduce RCS more effectively.

ACKNOWLEDGMENT

This work was supported in part by the National Natural Science Foundation of China (61701278).

REFERENCES

[1] Nanfang Yu, P. Genevet, M. A. Kats, F. Aieta, J. -P. Tetienne, F. Capasso, and Z. Gaburro, "Light propagation with phase discontinuities: generalized laws of reflection and refraction," *Science*, vol. 33, pp. 333-337, 21 Oct. 2011.

[2] Tie-Jun Cui, Mei-Qing Qi, Xiang Wan, Jie Zhao, and Qiang Cheng, "Coding metamaterials, digital metamaterials and programmable metamaterials," *Light: Sci. Appl.*, vol. 3, pp. 1–9, Sep. 2014.

[3] Xiao Liu, Jun Gao, Li-Ming Xu, Xiang-Yu Cao, Yi Zhao, and Si-Jia Li, "A coding diffuse metasurface for RCS reduction," *IEEE Antennas and Wireless Propagation Letters*, vol. 16, pp. 724-727, Apr. 2017.

[4] Jian-Xuan Su, Yao Lu, and Zeng-Rui Li, "Ultra-wideband Metasurface for Radar Cross Section Reduction," *ACES Conference*, pp. 1-2, 2017.

[5] Tao Shan, Xiao-Tian Pan, and Mao-Kun Li, Shen-Heng Xu, and Fan Yang, "Coding programmable metasurfaces based on deep learning techniques," *IEEE Journal on Emerging and Selected Topics in Circuits and Systems*, vol. 10, no. 1, pp. 114-125, Mar. 2020.

[6] Liu Shuo, Tie-Jun Cui, and Zhang Lei, "Metasurfaces: convolution operations on coding metasurface to reach flexible and continuous controls of terahertz beams," *Advanced Science*, pp. 1-12, Mar. 2016.

[7] Rui-Yuan Wu, Chuan-Bo Shi, Shuo Liu, Wei Wu, and Tie-Jun Cui, "Addition theorem for digital coding metamaterials," *Advanced Optical Materials*, pp. 1-10, Jun. 2018.

[8] Brian A. Lail and Kyu Y. Han, "Low-profile, broadband polarization converting surface ground planes for antenna polarization diversity," *Applied Computational Electromagnetics Society (ACES) Journal*, vol. 25, no. 1, pp. 54-60, Jan. 2010.

[9] J. Su, C. Kong, Z. Li, X. Yuan, and Y. L. Yang, "Ultra-wideband and polarization conversion metasurface," *Applied Computational Electromagnetics Society (ACES) Journal*, vol. 32, no. 6, pp. 524-530, Jun. 2017.

Tingting Shang was born in Liaocheng, Shandong Province, China in 1996. She obtained her B.S. degree in engineering from Jining University, China, in 2019. In the same year, she was admitted to QuFu Normal University and became a graduate student.

Her research interest includes the design and optimization of electromagnetic metasurface.

Jianping Zhao was born in Heze, Shandong Province, China in 1964. He received his B.S. degree in physics from QuFu Normal University Qufu, China, in 1985. In 1988, he studied in Wuhan University for master's degree in radio and information engineering.

Since 1985, he has been working at QuFu Normal University. He was promoted to associate professor in 1997 and professor in 2002. Since 1992, he has been the director of the Radio Teaching and Research Section. He has been engaged in application of electronic technology and scientific research in communication and information system of electronic information engineering and communication engineering.

Juan Xu was born in Jining, Shandong Province, China, in 1982. She received her Ph.D. degree in electronic science and technology from Nanjing University of Science and Technology, Nanjing, China, in 2016. Since 2016, she has been working at QuFu Normal University. She has been an associate professor since 2019.

Her research interests include simulation, design and experimental measurement of new high performance RF, microwave and millimeter wave passive devices, antennas, and antenna arrays.

Fast Power Series Solution of Large 3-D Electrodynamic Integral Equation for PEC Scatterers

Yoginder Kumar Negi[1], N. Balakrishnan[1], and Sadasiva M. Rao[2]

[1]Supercomputer Education Research Centre,
Indian Institute of Science, Bangalore, India
yknegi@gmail.com, balki@iisc.ac.in

[2]Naval Research Laboratory
Washington DC 20375, USA
sadasiva.rao@nrl.navy.mil

***Abstract* –** This paper presents a new fast power series solution method to solve the Hierarchal Method of Moment (MoM) matrix for a large complex, perfectly electric conducting (PEC) 3D structures. The proposed power series solution converges in just two (2) iterations which is faster than the conventional fast solver–based iterative solution. The method is purely algebraic in nature and, as such applicable to existing conventional methods. The method uses regular fast solver Hierarchal Matrix (H-Matrix) and can also be applied to Multilevel Fast Multipole Method Algorithm (MLFMA). In the proposed method, we use the scaling of the symmetric near-field matrix to develop a diagonally dominant overall matrix to enable a power series solution. Left and right block scaling coefficients are required for scaling near-field blocks to diagonal blocks using Schur's complement method. However, only the right-hand scaling coefficients are computed for symmetric near-field matrix leading to saving of computation time and memory. Due to symmetric property, the left side-block scaling coefficients are just the transpose of the right-scaling blocks. Next, the near-field blocks are replaced by scaled near-field diagonal blocks. Now the scaled near-field blocks in combination with far-field and scaling coefficients are subjected to power series solution terminating after only two terms. As all the operations are performed on the near-field blocks, the complexity of scaling coefficient computation is retained as $O(N)$. The power series solution only involves the matrix-vector product of the far-field, scaling coefficients blocks, and inverse of scaled near-field blocks. Hence, the solution cost remains $O(NlogN)$. Several numerical results are presented to validate the efficiency and robustness of the proposed numerical method.

***Index Terms* –** Integral Equations, Method of Moment (MoM), H-Matrix, Adaptive Cross Approximation (ACA), Power Series.

I. INTRODUCTION

The integral equation-based Method of Moments (MoM) [1] is one of the popular methods for solving complex 3D electromagnetics problems. A few of the problems include scattering, radiation, EMI-EMC, etc. Compared to differential equation-based methods like Finite Difference Time Domain (FDTD) [2] and Finite Element Method (FEM) [3], the integral equation-based method results in fewer unknowns and is more stable and well-conditioned. With the recent advancement of computer speed and memory, the need for solving large size and complex problems in electromagnetics has increased rapidly. Conventional MoM is limited by quadratic memory storage, quadratic matrix fill time, and cubic solution time, which limits the application of MoM to resonance-size problems. To mitigate this issue and exploit the robustness of MoM, in the last few decades, more researchers have proposed fast solvers with $O(N\log N)$ matrix fill time and solution time, where N represents the matrix size. A few of the popular fast solver methods for solving complex electrodynamic problems are Fast Fourier Transform (FFT), Multilevel Fast Multipole Algorithm (MLFMA) [4], IE-QR [5, 6], Adaptive Cross Approximation (ACA) [7], etc. Most of these methods rely on the analytical or numerical matrix compression and fast matrix-vector product for solution leading to $O(NlogN)$ matrix fill and matrix-vector product cost. For multiple Right-Hand Side (RHS) problems like Mono-static Radar Cross Section (RCS) and Multi-port network with N_{rhs} ports, and with N_{itr} iterations for each solution, the total cost of the solution will be $O(N_{rhs}N_{itr}NlogN)$. Each solution of RHS is iteration dependent, and the iterations for desired tolerance depends on the condition number of the matrix. It is well known that an ill-conditioned matrix will lead to a high number of iterations, thus increasing the overall solution time. To improve the

Submitted On: July 8, 2020
Accepted On: July 28, 2021

https://doi.org/10.47037/2021.ACES.J.361006

condition number of the matrix, researchers have suggested various types of matrix preconditioning methods like incomplete LU factorized ILUT [8], diagonal block-based Null-Field [9, 10] and Schur complement [11, 12]. But the effectiveness of these preconditioners is limited by precondition computation time and condition number improvement of the entire matrix. In contrast, the direct solver has an edge over the iterative solver, giving a solution in fixed single forward and backward solution operation for each RHS. However, the high-cost factorization, forward and back substitution limit the application of a direct solver for a large-size matrix. Recently, there is more inclination toward the development of fast direct solvers and various methods based on H [13–16].

In this work, we propose a method on par with a fast direct solver using the power series method, which converges in fixed 2 iterations. Recently, S. M. Rao and Michael S. Kluskens in [17] has proposed a method to solve the electromagnetic MoM matrix for electrically large conducting bodies by applying the power series method. The procedure involves the computation of the MoM matrix and dividing the matrix into relatively large subsections. The mutual coupling between a given subsection and related nearby subsections is transformed into self-coupling. The resulting current distribution is obtained by developing a power series solution. The power series method is suitable for solving bi-static and mono-static problems. The present work adopts the central idea of [17] and improves upon it to obtain a much faster solution.

In the present work, the procedure presented in [17] is modified using several essential steps. These steps include scaling near-field block matrices to diagonal block matrix and converting the scaled near-field in conjunction with far-field blocks to a power series format. Further, the diagonalization cost of computation and storage is reduced by using symmetric near-field blocks and adopting Adaptive Cross Approximation (ACA) for the far-field blocks [7]. As the diagonalization operation includes only near-field, the power series computation cost remains $O(N)$. The overall solution includes the matrix-vector product of the compressed far-field blocks and near-field blocks, retaining the overall solution cost as $O(NlogN)$. Further, extensive numerical experimentation shows that the proposed power series method converges in just two iterations. The present procedure is faster and efficiently applicable to large complex practical problems.

The paper is organized as follows: in section II, a brief description of multi-level CFIE H-Matrix 3D full-wave MoM is presented. Improved re-compressed ACA is used for matrix compression of the far-field blocks. In section III, the proposed power series format conversion from H-Matrix is presented along with the convergence criteria for the series. In section IV, complexity analysis of power series computation and memory cost is presented, and in section V, the efficiency and accuracy of the proposed power series solution are presented. Section VI concludes the paper.

II. FAST H-MATRIX METHOD OF MOMENT

The 3D-electrodynamic problem for a PEC body can be solved using the Electric Field Integral Equation (EFIE), Magnetic Field Integral Equation (MFIE), or a Combined Field Integral equation (CFIE). The governing equation for EFIE states that the total electric field E_{total} for a conducting 3D object is a combination of the incident field E_{inc} and the scattered field, $\boldsymbol{E}_{scatt}$

$$\boldsymbol{E}_{total} = \boldsymbol{E}_{inc} + \boldsymbol{E}_{scatt}. \tag{1}$$

Applying the boundary condition for PEC surfaces, we have

$$\begin{aligned}\boldsymbol{E}_{inc} =& j\omega\mu \int\int \mathbf{J}\left(\boldsymbol{r}'\right)\, G(\boldsymbol{r},\boldsymbol{r}')\, ds'ds \\ &+ \frac{j}{\omega\epsilon}\int\int \boldsymbol{\rho}(\boldsymbol{r}')G(\boldsymbol{r},\boldsymbol{r}')\, ds'ds,\end{aligned} \tag{2}$$

where $\mathbf{J}(\boldsymbol{r}')$ and $\boldsymbol{\rho}(\boldsymbol{r}')$ represent the current density and charge density on the surface respectively, μ and ϵ represent the permeability and permittivity of the background material, ω is the angular frequency. In equation (2) G is free-space Green's function and is given as

$$G(\boldsymbol{r},\boldsymbol{r}') = \frac{e^{jk\boldsymbol{R}}}{4\pi\boldsymbol{R}}, \tag{3}$$

where k is the wave-number, $\boldsymbol{r}$ and $\boldsymbol{r}'$ represent observer and source points and distance $\boldsymbol{R} = |\boldsymbol{r} - \boldsymbol{r}'|$. Integration is performed over observation surface s' and source surface s.

Similarly, for MFIE [18], the boundary condition states that tangential total magnetic field $(\widehat{\boldsymbol{n}} \times \boldsymbol{H}_{total})$ over a surface is equivalent to the electric current $(\boldsymbol{J}(\boldsymbol{r}))$ over the surface, as

$$\widehat{\boldsymbol{n}} \times \boldsymbol{H}_{total} = \mathbf{J}(\boldsymbol{r}), \tag{4}$$

where, $\widehat{\boldsymbol{n}}$ is a unit outward normal to the closed scattering surface. Now, the total magnetic field is a sum of incidence $(\boldsymbol{H}_i)$ and scattered magnetic field $(\boldsymbol{H}_{total})$

$$\widehat{\boldsymbol{n}} \times (\boldsymbol{H}_{inc} + \boldsymbol{H}_{scatt}) = \mathbf{J}(\boldsymbol{r}). \tag{5}$$

Equation (5) can be extended further as

$$\widehat{\boldsymbol{n}} \times \boldsymbol{H}_{inc} = \frac{\mathbf{J}\left(\boldsymbol{r}\right)}{2} - \widehat{\boldsymbol{n}} \times \int_{s'} \mathbf{J}\left(\mathbf{r}'\right) \times \nabla' G(\boldsymbol{r},\boldsymbol{r}')\, ds'. \tag{6}$$

In the above equation $\nabla' G$ can be further simplified as

$$\nabla' G(\boldsymbol{r},\boldsymbol{r}') = \left(jk + \frac{1}{\boldsymbol{R}}\right)\boldsymbol{G}(\boldsymbol{r},\boldsymbol{r}')\widehat{\boldsymbol{R}}. \tag{7}$$

Note that the EFIE is applicable for both open and closed surfaces, whereas MFIE is only applicable for a closed surface geometry. Combining EFIE and MFIE gives Combined Field Integral Equation (CFIE), given by

$$CFIE = \alpha EFIE + Z_o(1-\alpha)MFIE, \tag{8}$$

where α is a control parameter to control the contribution of EFIE and MFIE, ranging from 0 to 1 and Z_o is the free space impedance. The primary advantage of CFIE is that it is robust and generates a stable solution at internal resonances of the closed body and a well-conditioned MoM matrix. For an open surface, α is taken as 1, and for closed surfaces, α is taken as 0.5.

Current and charge density in surface integral equations EFIE and MFIE is modeled by RWG basis function [19], and Galerkin testing strategy is employed for MoM matrix computation. The final combined CFIE matrix is given as:

$$[\boldsymbol{Z}]x = b, \tag{9}$$

where $[\boldsymbol{Z}]$ is a dense matrix of size $N \times N$ and x and b are unknown and known vectors of size $N \times 1$.

The CFIE dense matrix in equation (9) presents a time and memory bottleneck, with $O(N^2)$ memory, $O(N^2)$ matrix fill time, $O(N^3)$ for a direct solution and, $O(N_{itr}N^2)$ for iterative solver with N_{itr} iterations. The iterative solution of the MoM matrix can be accelerated by exploiting the compressibility of the far-field sub-matrices. Compression also expedites the cost of matrix fill time and matrix-vector multiplication time in an iterative solver. Compression can be done analytically, like in the case of MLFMA or algebraically using IE-QR or ACA. Due to the kernel-independent property of the algebraic compression method, recently, ACA has gained popularity among researchers for the development of fast solvers. These compression methods can be applied in conjunction with binary-tree–based multilevel Hierarchal Matrix (H-Matrix). In the binary-tree decomposed 3D geometry, the matrix compression is applied for block interaction at each level, satisfying the admissibility condition given below

$$\eta\, dis\,(\Omega_t, \Omega_s) \geq \min\left(dia(\Omega_t), dia(\Omega_s)\right). \tag{10}$$

The admissibility condition states that the minimum of the block diameter of the test block (Ω_t) and source block (Ω_s) should be less than or equal to the admissibility constant (η) times the distance between the test and source blocks. The binary-tree partition of the geometry is carried out until the block size is greater than or equal to 0.5λ. The criteria for binary-tree truncation are discussed in section V. At the leaf level, the block interaction not satisfying the admissibility condition is considered as a near-field interaction.

In this work, the re-compressed ACA method [20, 21] is employed for the computation of multi-level H-Matrix. For the $m \times n$ rectangular sub-matrix $\boldsymbol{Z}_{sub}^{m\times n}$ representing the coupling between two well-separated groups of m observer bases and n source bases, the ACA algorithm aims to approximate $\boldsymbol{Z}_{sub}^{m\times n}$ by $\boldsymbol{A}^{m\times r}$ and $\boldsymbol{B}^{r\times n}$ such that:

$$\boldsymbol{Z}_{sub}^{m\times n} \approx \boldsymbol{A}^{m\times r} \times \boldsymbol{B}^{r\times n}, \tag{11}$$

where r is the effective rank of the matrix $Z_{sub}^{m\times n}$ such that $r \ll \min(m,n)$, $\boldsymbol{A}^{m\times r}$ and $\boldsymbol{B}^{r\times n}$ are two low rank dense rectangular matrices, satisfying the accuracy condition

$$\left\|\boldsymbol{Z}_{sub}^{m\times n} - \boldsymbol{A}^{m\times r} \times \boldsymbol{B}^{r\times n}\right\| \leq \varepsilon \left\|\boldsymbol{Z}_{sub}^{m\times n}\right\|. \tag{12}$$

For a given tolerance $\boldsymbol{\varepsilon}$ $||.||$ refers to the matrix Frobenius norm. Traditional ACA-based methods suffer from higher rank and error for the desired tolerance. To mitigate this, a re-compression scheme is suggested in [20, 21]. The compression cost for each sub-matrix is given by $r^2(m+n)$ and the storage and matrix-vector product cost by $r(m+n)$. The multi-level binary-tree matrix decomposed H-Matrix method leads to $O(NlogN)$ matrix fill and matrix-vector product time for each iteration. However, the final solution cost is highly iteration dependent as for N_{itr} iterations, the solution cost scales to $O(N_{itr}NlogN)$. Further, for the case of multiple RHS with N_{rhs} vectors, the solution cost scales to $O\left(N_{rhs}N_{itr}NlogN\right)$. To mitigate this iteration-dependent solution, we have proposed a power series–based iterative solver which converges in fixed 2 iterations maintaining the optimum cost of a fast solver.

III. POWER SERIES SOLUTION

In this section, we present a new fast power series solution method for solving large H-Matrix. The method follows Schur's complement procedure used for matrix diagonalization and precondition computation [11, 12]. Power series is an infinite series and a well-known method for solving an ordinary and partial differential equation. The advantage of the power series is that it converges in a very small region. Since a conventional MoM matrix cannot be applied for the power series solution, we propose a method to convert to the H-matrix format. We note that the H-matrix is suitable for the power series solution, as discussed further in the section. H-Matrix is a combination of the far-field and near-field matrices. In the following subsections, the details of the conversion process are presented.

A. Preparing for power series computation

As a first step, the geometry is divided into blocks based on the same binary tree as used in the compression algorithm. In a multi-level H-Matrix compression scheme, as described in section II, the MoM matrix $[\boldsymbol{Z}]$ in equation (9) can be represented as a combination of the near-field $[\boldsymbol{Z}_N]$ matrix at the leaf level and the compressed far-field $[\boldsymbol{Z}_F]$ matrix obtained at multiple levels of far-interaction.

$$[\boldsymbol{Z}]\,\boldsymbol{x} = [\boldsymbol{Z}_N + \boldsymbol{Z}_F]\,\boldsymbol{x} = \boldsymbol{b}, \tag{13}$$

where $\boldsymbol{x}$ represents the unknown coefficient vector, $\boldsymbol{b}$ is the excitation vector. To maintain the optimum cost, symmetric near-field matrix is used. To explain the

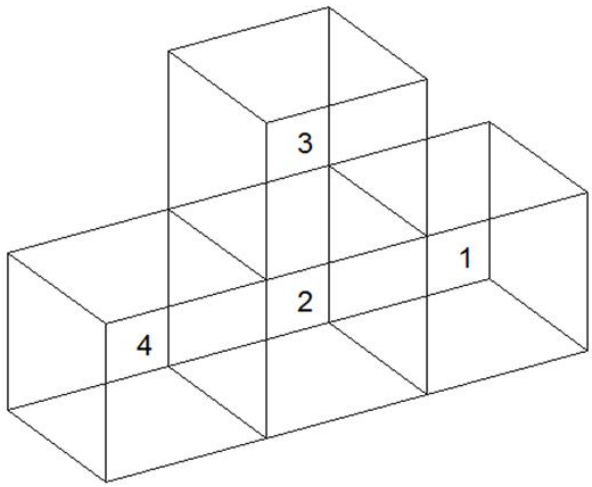

Fig. 1. Representative leaf-level cubes for illustration of Schur's process.

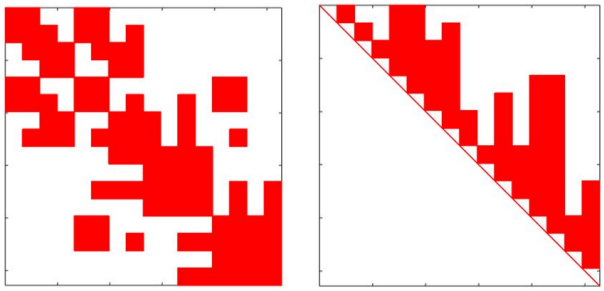

(a) (b)

Fig. 2. Sparsity pattern of the (a) near-field matrix, (b) right-hand scaling coefficient.

procedure, a leaf-level cube structure comprised of four cubes, as shown in Figure 2, is considered.

For Figure 1, block interaction between 1 and 4 forms the far-field interaction and rest form the near-field interaction. So near-field block matrix $[\boldsymbol{Z}_N]$ in the case of Figure 1 is given as:

$$[\boldsymbol{Z}_N] = \begin{bmatrix} Z_{11} & Z_{12} & Z_{13} & 0 \\ Z_{21} & Z_{22} & Z_{23} & Z_{24} \\ Z_{31} & Z_{32} & Z_{33} & Z_{34} \\ 0 & Z_{42} & Z_{43} & Z_{44} \end{bmatrix}. \tag{14}$$

Now, the near-field can be scaled completely to a diagonal block by using the left- and right-hand scaling coefficients. Right scaling coefficient $[\boldsymbol{\alpha}_1]$ for scaling the first-row blocks Z_{11} and Z_{13}can be represented as:

$$[\boldsymbol{\alpha}_1] = \begin{bmatrix} I_{11} & \alpha_{12} & \alpha_{13} & 0 \\ 0 & I_{22} & 0 & 0 \\ 0 & 0 & I_{33} & 0 \\ 0 & 0 & 0 & I_{44} \end{bmatrix}, \tag{15}$$

where, I_{11}, I_{22}, I_{33}, and I_{44} are the identity block matrices. In the null-field method [9, 10], either left- or right-hand scaling is performed for the near-field scaling to diagonal blocks ignoring the fill-in blocks. In contrast, in the proposed Schur's complement method, both left- and right-hand scaling are performed simultaneously, considering fill-in blocks for complete far-field scaling to diagonal blocks. The fill-ins in the scaling matrix are described in the following subsection for row scaling, the values in $[\boldsymbol{\alpha}_1]$ can be given as:

$$[\boldsymbol{\alpha}_1] = \begin{bmatrix} I_{11} & -Z_{11}^{-1}Z_{12} & -Z_{11}^{-1}Z_{13} & 0 \\ 0 & I_{22} & 0 & 0 \\ 0 & 0 & I_{33} & 0 \\ 0 & 0 & 0 & I_{44} \end{bmatrix}. \tag{16}$$

Similarly, for the complete scaling of column blocks Z_{21} and Z_{31} the left scaling coefficient $[\boldsymbol{\alpha'}_1]$ is used and $[\boldsymbol{\alpha}'_1]$ can be given as:

$$[\boldsymbol{\alpha}'_1] = \begin{bmatrix} I_{11} & 0 & 0 & 0 \\ \alpha'_{12} & I_{22} & 0 & 0 \\ \alpha'_{13} & 0 & I_{33} & 0 \\ 0 & 0 & 0 & I_{44} \end{bmatrix}, \tag{17}$$

$$[\boldsymbol{\alpha}'_1] = \begin{bmatrix} I_{11} & 0 & 0 & 0 \\ -Z_{21}Z_{11}^{-1} & I_{22} & 0 & 0 \\ -Z_{31}Z_{11}^{-1} & 0 & I_{33} & 0 \\ 0 & 0 & 0 & I_{44} \end{bmatrix}. \tag{18}$$

Now, equations (14), (16), and (18) can be combined to scale the first row and column block of $[\boldsymbol{Z}_N]$ to diagonal block and the system of the equation can be given as:

$$\left[\widetilde{\boldsymbol{Z}}_N^1\right] = \begin{bmatrix} I_{11} & 0 & 0 & 0 \\ \alpha'_{12} & I_{22} & 0 & 0 \\ \alpha'_{13} & 0 & I_{33} & 0 \\ 0 & 0 & 0 & I_{44} \end{bmatrix} \begin{bmatrix} Z_{11} & Z_{12} & Z_{13} & 0 \\ Z_{21} & Z_{22} & Z_{23} & Z_{24} \\ Z_{31} & Z_{32} & Z_{33} & Z_{34} \\ 0 & Z_{42} & Z_{43} & Z_{44} \end{bmatrix} \times \begin{bmatrix} I_{11} & \alpha_{12} & \alpha_{13} & 0 \\ 0 & I_{22} & 0 & 0 \\ 0 & 0 & I_{33} & 0 \\ 0 & 0 & 0 & I_{44} \end{bmatrix}. \tag{19}$$

Equation (19) can be represented as:

$$[\widetilde{\boldsymbol{Z}}_N^1] = [\boldsymbol{\alpha}'_1]\,[\boldsymbol{Z}_N]\,[\boldsymbol{\alpha}_1]. \tag{20}$$

Performing the block multiplication in equation (19), $[\widetilde{\boldsymbol{Z}}_N^1]$ can be represented as a block matrix form as:

$$\left[\widetilde{\boldsymbol{Z}}_N^1\right] = \begin{bmatrix} Z_{11} & 0 & 0 & 0 \\ 0 & Z_{22} - Z_{21}Z_{11}^{-1}Z_{12} & Z_{23} - Z_{21}Z_{11}^{-1}Z_{13} & Z_{24} \\ 0 & Z_{32} - Z_{31}Z_{11}^{-1}Z_{12} & Z_{33} - Z_{31}Z_{11}^{-1}Z_{13} & Z_{34} \\ 0 & Z_{42} & Z_{43} & Z_{44} \end{bmatrix}. \tag{21}$$

Equation (21) gives Schur's complement of the first block near-field matrix. Likewise, each row and column block can be scaled to form a diagonal block matrix and is of the form:

$$[\widetilde{\boldsymbol{Z}}_N] = [\,\boldsymbol{\alpha}'_3\,][\,\boldsymbol{\alpha}'_2\,][\,\boldsymbol{\alpha}'_1][\boldsymbol{Z}_N][\boldsymbol{\alpha}_1][\boldsymbol{\alpha}_2]][\boldsymbol{\alpha}_3], \tag{22}$$

$$[\widetilde{\boldsymbol{Z}}_N] = \begin{bmatrix} Z_{11} & 0 & 0 & 0 \\ 0 & \tilde{Z}_{22} & 0 & 0 \\ 0 & 0 & \tilde{Z}_{33} & 0 \\ 0 & 0 & 0 & \tilde{Z}_{44} \end{bmatrix}. \quad (23)$$

Equation (23) gives the complete diagonal form of the near-field matrix. For solving the complete system of equations with left- and right-hand scaling coefficients, the final system of equation (9) can be represented as:

$$[\,\boldsymbol{\alpha}'_3\,][\,\boldsymbol{\alpha}'_2\,][\,\boldsymbol{\alpha}'_1\,]\,[\boldsymbol{Z}][\boldsymbol{\alpha}_1][\boldsymbol{\alpha}_2]][\boldsymbol{\alpha}_3]\,[\widetilde{\boldsymbol{x}}] = \left[\widetilde{\boldsymbol{b}}\right]. \quad (24)$$

Now, $[\boldsymbol{b}]$ and $[\boldsymbol{x}]$ in equation (9) can be extracted by

$$\left[\widetilde{\boldsymbol{b}}\right] = [\,\boldsymbol{\alpha}_3^{\mathrm{T}}\,][\,\boldsymbol{\alpha}_2^{\mathrm{T}}\,][\,\boldsymbol{\alpha}_1^{\mathrm{T}}\,][\boldsymbol{b}], \quad (25)$$

$$[\boldsymbol{x}] = [\boldsymbol{\alpha}_1]\,[\boldsymbol{\alpha}_2]][\boldsymbol{\alpha}_3][\,\widetilde{\boldsymbol{x}}]. \quad (26)$$

Equation (24) can be defined as the sum of the near and far-field as in equation (13) and is given as:

$$[\,\boldsymbol{\alpha}'_3\,][\,\boldsymbol{\alpha}'_2\,][\,\boldsymbol{\alpha}'_1\,]\,[\boldsymbol{Z}_N + \boldsymbol{Z}_F][\boldsymbol{\alpha}_1][\boldsymbol{\alpha}_2][\boldsymbol{\alpha}_3]\,[\widetilde{\boldsymbol{x}}] = \left[\widetilde{\boldsymbol{b}}\right], \quad (27)$$

where, $[\boldsymbol{Z}_F]$ is the far-field compressed ACA matrix blocks and $[\boldsymbol{Z}_N]$ is the dense near-field block matrices. Equation (27) can be further simplified by as:

$$[\boldsymbol{\alpha}'_3][\,\boldsymbol{\alpha}'_2\,][\boldsymbol{\alpha}'_1][\boldsymbol{Z}_N][\boldsymbol{\alpha}_1][\boldsymbol{\alpha}_2][\boldsymbol{\alpha}_3]\,[\widetilde{\boldsymbol{x}}] + [\boldsymbol{\alpha}'_3][\boldsymbol{\alpha}'_2][\boldsymbol{\alpha}'_1][\boldsymbol{Z}_F][\boldsymbol{\alpha}_1][\boldsymbol{\alpha}_2][\boldsymbol{\alpha}_3]\,[\widetilde{\boldsymbol{x}}] = \left[\widetilde{\boldsymbol{b}}\right]. \quad (28)$$

The first part of the above equation represents the block diagonal near-field as in equation (28), and then the equation can be further simplified as:

$$[\widetilde{\boldsymbol{Z}}_N]\,[\widetilde{\boldsymbol{x}}] + [\boldsymbol{\alpha}'_3][\boldsymbol{\alpha}'_2][\boldsymbol{\alpha}'_1][\boldsymbol{Z}_F][\boldsymbol{\alpha}_1][\boldsymbol{\alpha}_2][\boldsymbol{\alpha}_3]\,[\widetilde{\boldsymbol{x}}] = \left[\widetilde{\boldsymbol{b}}\right], \quad (29)$$

where, $\left[\widetilde{\boldsymbol{Z}}_N\right]$ is a scaled near-field block diagonal matrix. Due to the symmetric property of the near-field matrix, we only need to compute and store right-hand scaling coefficients $[\boldsymbol{\alpha}_1]$, $[\boldsymbol{\alpha}_2]$, and $[\boldsymbol{\alpha}_3]$ since left-hand scaling coefficients $[\boldsymbol{\alpha'}_1]$, $[\boldsymbol{\alpha'}_2]$, and $[\boldsymbol{\alpha'}_3]$ are mere transpose of right-hand coefficients. Figure 2 below shows the sparsity pattern of the near-field and right-hand scaling coefficient matrix for $5\lambda \times 5\lambda$ plate. Sloan's graph ordering is used to reduce the fill-in and computation cost for the scaling coefficient, as suggested in [11].

Now equation (29) can be converted to power series solution format by moving the scaled diagonal near-field to the right-hand side of the equation leads to

$$\left[[\boldsymbol{I}] + \left[\widetilde{\boldsymbol{Z}}_N\right]^{-1}[\boldsymbol{\alpha}'_3][\boldsymbol{\alpha}'_2][\boldsymbol{\alpha}'_1][\boldsymbol{Z}_F][\boldsymbol{\alpha}_1][\boldsymbol{\alpha}_2][\boldsymbol{\alpha}_3]\right][\widetilde{\boldsymbol{x}}] = \left[\widetilde{\boldsymbol{Z}}_N\right]^{-1}\left[\widetilde{\boldsymbol{b}}\right]. \quad (30)$$

Each term in equation (30) can be represented as

$$[\boldsymbol{U}] = \left[\widetilde{\boldsymbol{Z}}_N\right]^{-1}[\boldsymbol{\alpha}'_3][\boldsymbol{\alpha}'_2][\boldsymbol{\alpha}'_1][\boldsymbol{Z}_F][\boldsymbol{\alpha}_1][\boldsymbol{\alpha}_2][\boldsymbol{\alpha}_3], \quad (31)$$

$$[\boldsymbol{b_o}] = \left[\widetilde{\boldsymbol{Z}}_N\right]^{-1}\left[\widetilde{\boldsymbol{b}}\right]. \quad (32)$$

Substituting equation (31) and (32) in equation (30) leads to

$$[[\boldsymbol{I}] + [\boldsymbol{U}]]\,[\widetilde{\boldsymbol{x}}] = [\boldsymbol{b_o}], \quad (33)$$

$$[\widetilde{\boldsymbol{x}}] = [[\boldsymbol{I}] + [\boldsymbol{U}]]^{-1}\,[\boldsymbol{b_o}]. \quad (34)$$

Equation (34) can be solved using power series solution

$$[\widetilde{\boldsymbol{x}}] = \left[[\boldsymbol{I}] - [\boldsymbol{U}] + [\boldsymbol{U}]^2 - [\boldsymbol{U}]^3 + \ \ldots\ldots\right][\boldsymbol{b_o}], \quad (35)$$

$$[\widetilde{\boldsymbol{x}}] = [\boldsymbol{b_o}] - [\boldsymbol{U}\boldsymbol{b_o}] + [\boldsymbol{U}\,[\boldsymbol{U}\boldsymbol{b_o}]] - [\boldsymbol{U}\,[\boldsymbol{U}\,[\boldsymbol{U}\boldsymbol{b_o}]]] + \ldots. \quad (36)$$

Equation (36) shows that solving equation (34) is an iterative matrix-vector product of the inverse of the scaled diagonal block near-field, scaling coefficients and far-field blocks.

B. Convergence

Power series always converges in the radius of convergence. The necessary and sufficient condition for the power series equation (35) to converge in the radius of convergence is the Frobenius norm, $\|\boldsymbol{U}\| \leq 1$ in equation (31). Defining

$$[\widetilde{\boldsymbol{Z}}_F] = [\,\boldsymbol{\alpha}'_3\,][\,\boldsymbol{\alpha}'_2\,][\,\boldsymbol{\alpha}'_1][\boldsymbol{Z}_F][\boldsymbol{\alpha}_1][\boldsymbol{\alpha}_2]][\boldsymbol{\alpha}_3]. \quad (37)$$

Equation (30) can be re-written as

$$\left[[\boldsymbol{I}] + \left[\widetilde{\boldsymbol{Z}}_N\right]^{-1}\left[\widetilde{\boldsymbol{Z}}_F\right]\right][\widetilde{\boldsymbol{x}}] = \left[\widetilde{\boldsymbol{Z}}_N\right]^{-1}\left[\widetilde{\boldsymbol{b}}\right]. \quad (38)$$

To achieve the convergence, we can enforce the condition $\left\|\left[\widetilde{\boldsymbol{Z}}_N\right]^{-1}\right\| \cdot \left\|\left[\widetilde{\boldsymbol{Z}}_F\right]\right\| \leq 1$ for the final solution of the power series. Since the process of norm computation for a large matrix is compute-intensive, alternatively, one can adopt the following procedure.

We note that

$$\left\|\left[\widetilde{\boldsymbol{Z}}_N\right]^{-1}\right\| = \frac{\left\|\left[\widetilde{\boldsymbol{Z}}_N\right]^{-1}\right\| \cdot \left\|\left[\widetilde{\boldsymbol{Z}}_N\right][\boldsymbol{b_o}]\right\|}{\left\|\left[\widetilde{\boldsymbol{Z}}_N\right][\boldsymbol{b_o}]\right\|} \leq \frac{\left\|\left[\widetilde{\boldsymbol{Z}}_N\right]^{-1}\right\| \cdot \left\|\left[\widetilde{\boldsymbol{Z}}_N\right]\right\| \cdot \|[\boldsymbol{b_o}]\|}{\left\|\left[\widetilde{\boldsymbol{b}}\right]\right\|} = k_{nf}\frac{\|[\boldsymbol{b_o}]\|}{\left\|\left[\widetilde{\boldsymbol{b}}\right]\right\|}, \quad (39)$$

where, $k_{nf} = \left\|\left[\widetilde{\boldsymbol{Z}}_N\right]^{-1}\right\| \cdot \left\|\left[\widetilde{\boldsymbol{Z}}_N\right]\right\|$ represents the condition number of $\left[\widetilde{\boldsymbol{Z}}_N\right]$.

Next, we define $[\boldsymbol{b_e}] = \left[\widetilde{\boldsymbol{Z}}_F\right][\boldsymbol{b_o}]$ and we have

$$\left\|\left[\widetilde{\boldsymbol{Z}}_F\right]\right\| = \frac{\left\|\left[\widetilde{\boldsymbol{Z}}_F\right]\right\| \cdot \left\|\left[\left[\widetilde{\boldsymbol{Z}}_F\right]^{-1}\right][\boldsymbol{b_e}]\right\|}{\left\|\left[\widetilde{\boldsymbol{Z}}_F\right]^{-1}[\boldsymbol{b_e}]\right\|} \leq \frac{\left\|\left[\widetilde{\boldsymbol{Z}}_F\right]\right\| \cdot \left\|\left[\widetilde{\boldsymbol{Z}}_F\right]^{-1}\right\| \cdot \|[\boldsymbol{b_e}]\|}{\|\ [\boldsymbol{b_o}]\ \|}$$

$$= k_{ff} \frac{\|[\boldsymbol{b_e}]\|}{\| [\boldsymbol{b_o}] \|}, \tag{40}$$

where, $k_{ff} = \left\| \left[\widetilde{\boldsymbol{Z}}_F\right]^{-1} \right\| . \left\| \left[\widetilde{\boldsymbol{Z}}_F\right] \right\|$ represents the condition number of $\left[\widetilde{\boldsymbol{Z}}_F\right]$.

Combining equations (39) and (40), we have

$$\left\| \left[\widetilde{\boldsymbol{Z}}_N\right]^{-1} \right\| . \left\| \left[\widetilde{\boldsymbol{Z}}_F\right] \right\| \leq k_{nf}\, k_{ff} \frac{\|[\boldsymbol{b_e}]\|}{\left\| \left[\widetilde{\boldsymbol{b}}\right] \right\|}. \tag{41}$$

To satisfy the condition $\|\boldsymbol{U}\| \leq 1$ we must ensure that

$$\frac{\|[\boldsymbol{b_e}]\|}{\left\| \left[\widetilde{\boldsymbol{b}}\right] \right\|} \leq \frac{1}{k_{nf} k_{ff}}, \tag{42}$$

$$\left\| \left[\widetilde{\boldsymbol{Z}}_N\right]^{-1} \left[\widetilde{\boldsymbol{Z}}_F\right] \right\| \leq \frac{1}{k_{nf} k_{ff}}. \tag{43}$$

Now, let us consider each right-hand side term in equation (36) is represented as the sum of iteration terms $\boldsymbol{it_o},\ \boldsymbol{it_1},\ \boldsymbol{it_2} \ldots\ \boldsymbol{it_n}$ leading to

$$[\widetilde{\boldsymbol{x}}] = \boldsymbol{it_o} - \boldsymbol{it_1} + \boldsymbol{it_2} \ldots . (-1)^n\, \boldsymbol{it_n}. \tag{44}$$

For the convergence test, we can check the iteration norm ratio as:

$$\frac{\|\boldsymbol{it_n}\|}{\| \boldsymbol{it_{n-1}} \|} = \|\boldsymbol{U}\| = \left\| \left[\widetilde{\boldsymbol{Z}}_N\right]^{-1} \left[\widetilde{\boldsymbol{Z}}_F\right] \right\| \leq \frac{1}{k_{nf} k_{ff}}. \tag{45}$$

Note that it is not really necessary to compute the condition numbers k_{nf} and k_{ff} but ensure that the fraction $\frac{\|\boldsymbol{it_n}\|}{\| \boldsymbol{it_{n-1}} \|}$ is a small number. Our various numerical experiments suggested that this number must be less than $1e^{-1}$. It is because the described numerical implementation ensures that matrices $\left[\widetilde{\boldsymbol{Z}}_N\right]$ and $\left[\widetilde{\boldsymbol{Z}}_F\right]$ are well-conditioned matrices. Obviously, if the $\frac{\|\boldsymbol{it_n}\|}{\| \boldsymbol{it_{n-1}} \|}$ is not less than the empirical value, then the solution may diverge.

IV. COMPLEXITY ANALYSIS

In this section, the linear order complexity for power series set-up time is presented. For the complexity analysis, a uniform distribution of N RWG bases in 3D grouped in a cube, and following a multi-level binary-tree decomposition, each cube is recursively subdivided into two cubes starting from level 0 to level *L*. Therefore, at the lowest level, there are 2^L leaf-level cubes. Assuming a uniform distribution, the number of basis functions in each leaf-level cube is $\frac{N}{2^L}$. Also, following the theory of most fast solver algorithms, it can be shown that for optimal efficiency of matrix storage and matrix-vector product cost $L = \log_2 N$.

A. Computation cost

The power series set-up cost includes scaling the near-field matrix to diagonal format and arranged scaled near-field, far-field, and near-field scaling coefficients to a power series format. Near-field scaling cost is the high cost of power series set-up. The near-field scaling consists of a computation right scaling coefficients $[\boldsymbol{\alpha}]$ as in equation (16). Due to the symmetric property, left scaling coefficients are just the transpose of right-hand scaling coefficients. Right-hand scaling coefficient computation cost can be represented as C_1. The second cost includes the scaling of the near-field to the diagonal block form by $[\boldsymbol{\alpha}'] [\boldsymbol{Z}_N] [\boldsymbol{\alpha}]$ operation. For each row and column block in equations (18) and (20), this cost can be represented as C_2. Therefore, the total cost can be summed up as:

$$C_{TOTAL} = C_1 + C_2. \tag{46}$$

1. Scaling coefficient computation cost

For the scaling coefficient computation, the high cost includes the inversion (C_{MI}) cost for diagonal block and the solving the inverse (C_{SOL}) for the row and column block near-fields as in equations (16) and (18). Therefore C_{SCC} can be further be divided as the summation of inversion and solution cost as:

$$C_1 = C_{MI} + C_{SOL}. \tag{47}$$

Inversion cost includes the single matrix inversion of a diagonal block for scaling near-field of each row and column block. Therefore, the matrix inversion cost of one matrix of a diagonal block at leaf level is given as:

$$C^1_{MI} = k_1 \times \left[\frac{N}{2^L}\right]^3, \tag{48}$$

where, k_1 is a constant, the total cost for matrix inversion for the leaf level blocks is given by

$$C_{MI} = \sum_{i=1}^{2^L} C^i_{MI} = k_1 \times \left[\frac{N}{2^L}\right]^3 \times 2^L, \tag{49}$$

$$C_{MI} = k_1 \times N = O(N). \tag{50}$$

For the computation of the scaling coefficient, the inverted matrix has to be solved for all row and column near-field blocks. Cost of matrix solution for one block at leaf level can be given as:

$$C^1_{SOL} = k_2 \times \left[\frac{N}{2^L}\right]^2 \times \left[\frac{N}{2^L}\right], \tag{51}$$

where, k_2 is a constant. For a 3D structure, each block is surrounded by 26 near-field blocks. Therefore, the matrix solution cost for each row is given by:

$$C^{1R}_{SOL} = k_2 \times \left[\frac{N}{2^L}\right]^2 \times 26 \times \left[\frac{N}{2^L}\right]. \tag{52}$$

The total cost of the matrix solution at the leaf level blocks is the summation of the cost of each row and is given as:

$$C_{SOL} = \sum_{i=1}^{2^L} C^{iR}_{SOL} = k_2 \times \left[\frac{N}{2^L}\right]^2 \times 26 \times \left[\frac{N}{2^L}\right] \times 2^L, \tag{53}$$

$$C_{SOL} = k_2 \times 26 \times N = O(N). \tag{54}$$

2. Near-field scaling cost

For converting near-field to a diagonal block matrix format, the near-field block matrix has to be multiplied by the left and right scaling coefficients as given in equations (19) and (20). From equation (21), the multiplication involves block near-field matrix and column block matrix

$$c_S^1 = k_3 \times \left[26\frac{N}{2^L} \times 26\frac{N}{2^L}\right] \times \left[\frac{N}{2^L} \times 26\frac{N}{2^L}\right], \quad (55)$$

where k_3 is a constant. Therefore, the total cost of scaling the near-field blocks with the right-hand scaling coefficients blocks is

$$C_S = \sum_{i=1}^{2^L} C_S^i \approx O(N). \quad (56)$$

Equations (50), (54), and (56) show that the cost of the power series computation, for a uniform 3D distributed basis function, is $O(N)$. As the storage of scaling coefficient and scaled near-field block is half the near-field matrix size, the memory cost scales to $O(N)$. The $O(N)$ complexity of power series computation and memory is experimentally shown in Figure 3 for the increasing number of unknowns and the size of a sphere.

V. NUMERICAL RESULTS

In this section, we show the binary-tree truncation criteria and solution complexity for the power series solution. The accuracy and efficiency are shown by RCS comparison for different geometries. All the computations were carried out for double-precision data type on the system with 128 GB memory and Intel Xeon E5-2670 processor. The comparisons are made for an open and closed structure.

A. Binary-tree truncation

For binary-tree truncation, we tested the accuracy of the power series solution vector from 2λ sphere of 20,802 unknowns for varying binary-tree leaf-level sizes. For accuracy check, Frobenius norm error was calculated between solution vectors from direct LU factorized solution $\boldsymbol{SOL_{dir}}$ and power series solution $\boldsymbol{SOL_{ps}}$ by computing $\|\boldsymbol{SOL_{dir}} - \boldsymbol{SOL_{ps}}\| / \|\boldsymbol{SOL_{dir}}\|$. The error plot is shown in Figure 4 below

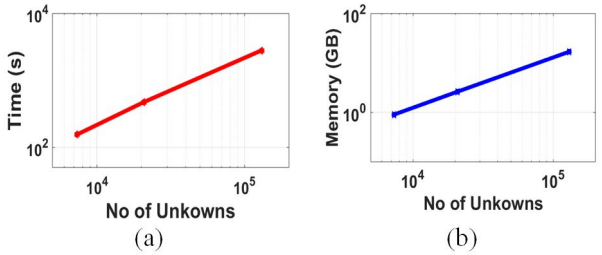

(a) (b)

Fig. 3. (a) Power series set-up time, (b) Memory in GB for scaling coefficient and scaled near-field with increasing unknowns.

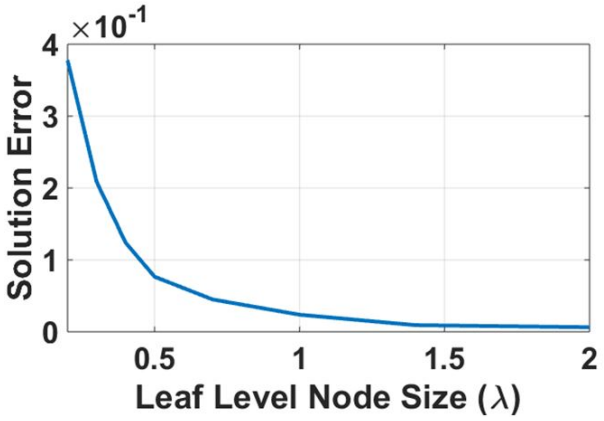

Fig. 4. Power Series Solution error with increasing leaf level node size.

It can be observed from Figure 4 above that for the leaf level truncation size greater than $0.5\ \lambda$ we get the desired accuracy. Hence, for all simulations shown in this work, the binary-tree leaf node is truncated for a size greater than 0.5.

B. Solution complexity

In Figure 5, we demonstrate that the proposed power series method retains the $O\,(NlogN)$ solution complexity of H-Matrix. The experiment is carried out for sphere meshed with increasing sphere size and unknowns.

C. Accuracy and efficiency

In this subsection, to validate the accuracy of the proposed method, we have compared the RCS results of different geometries with the analytical results. Also, to demonstrate the efficiency of the proposed method, solution time is compared with regular iterative and preconditioned [11] iterative solutions. For all comparative case

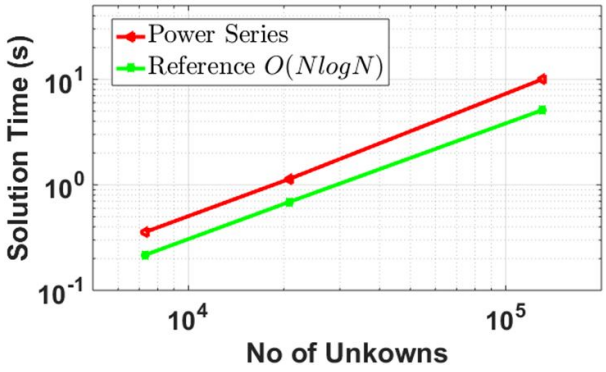

Fig. 5. Power Series solution time with increasing unknown.

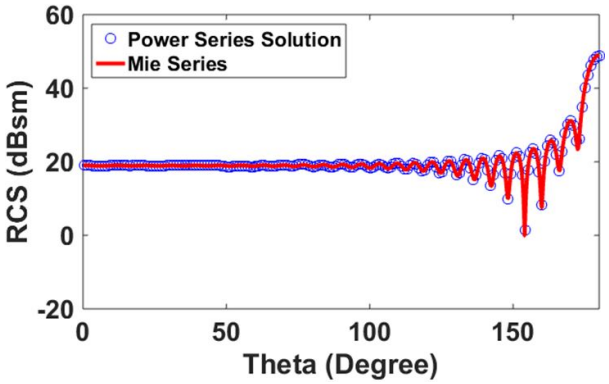

Fig. 6. Bi-static RCS of 5λ sphere for observation angles $\theta = 0^o$ to 180^o, $\phi = 0^o$ and VV polarized plane wave incident at $\theta = 0^o, \phi = 0^o$.

studies, iterative solver GMRES with an error tolerance of 1e-6 is considered.

1. Bi-static RCS of a sphere

As a first example, we consider bi-static RCS of a $5\lambda - radius$ sphere discretized with a $\lambda/10$ mesh resulting in 130,293 unknowns. The solution from the method described in this work is compared with the Mie series analytical solution. Figure 6 shows the agreement of bi-static RCS from the present method with the Mie series. RCS is computed for observation angle $\theta = 0^o$ to 180^o for $\phi = 0^o$ with VV polarized plane wave incident at $\theta = 0^o$ and $\phi = 0^o$. We note excellent agreement between the two results.

2. Mono-static RCS of a square plate

To show the accuracy and efficiency of the proposed power series method, an open structure, a square plate of 20λ size, is considered. The solution is obtained using EFIE only with $\alpha = 1$ in equation (8). Figure 7 shows mono-static RCS of the plate using the present method and compared with a conventional iterative method. The plate is discretized with $\lambda/10$ element size for 119,600 unknowns. The square plate is located in the XY plane and illuminated by a plane wave incident with θ varying from $0\ to\ 180^o$ and $\phi = 0^o$. It can be observed from the figure that there is a very favorable agreement of RCS between the two methods.

Table 1: Solution time of square plate

Method	Setup Time (H)	Solution Time (H)
Power Series Solver	1.61	0.57
Preconditioned Iterative Solver	1.61	3.760
Iterative Solver	———	89.97

In Table 1, we present the comparison of solution time for the results presented in Figure 7. We show solution times for iterative solvers with and without preconditioning. It is evident that the present work is much more efficient than the other two cases.

3. Mono-static RCS of a cube

Next, we consider a conducting cube of 1 m meshed with $\lambda/10$ element size giving 45,975 unknowns. Since the scattering body is a closed structure, we use CFIE with $\alpha = 0.5$. The operating frequency is 1.3 GHz and compared with the iterative solution [20], as shown in Figure 8. Further, in Table 2, we present a comparison of solution time for this example.

It can be observed that the RCS result from the power series completely matches with the regular H-matrix iterative solver [22].

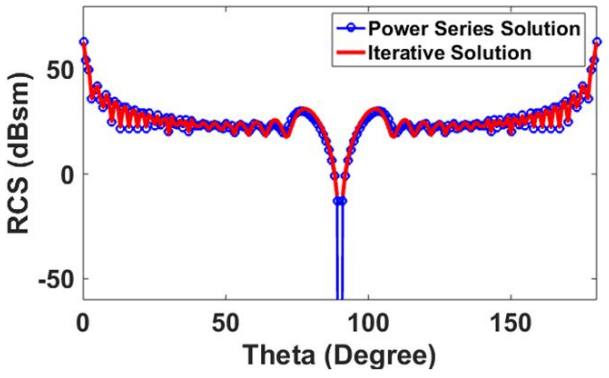

Fig. 7. Mono-static RCS of 20λ square plate with VV polarized incident plane wave and observation angles at $\theta = 0^o$ to 180^o, $\phi = 0^o$.

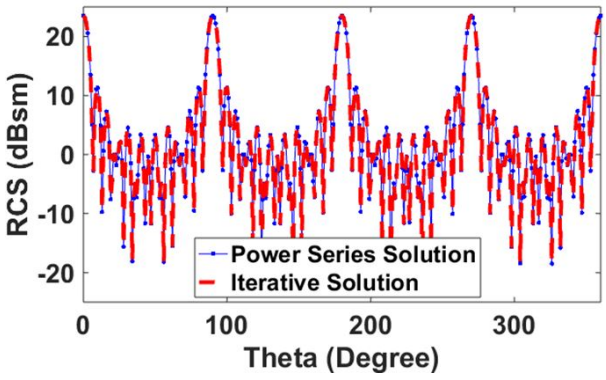

Fig. 8. Mono-static RCS of $1\ m$ cube at 1.3 GHz for HH polarized plane wave incident and observation angles at $\theta = 0^o$ to 360^o, $\phi = 0^o$.

Table 2: Solution time of a cube

Method	Setup Time (H)	Solution Time (H)
Power Series Solver	1.32	0.551
Preconditioned Iterative solver	1.32	1.377
Iterative solver	———	7.640

Table 3: Solution time of a model fighter aircraft

Method	Setup Time (H)	Solution Time (H)
Power Series Solver	1.66	0.46
Preconditioned Iterative solver	1.66	1.95
Iterative solver	———	191.73

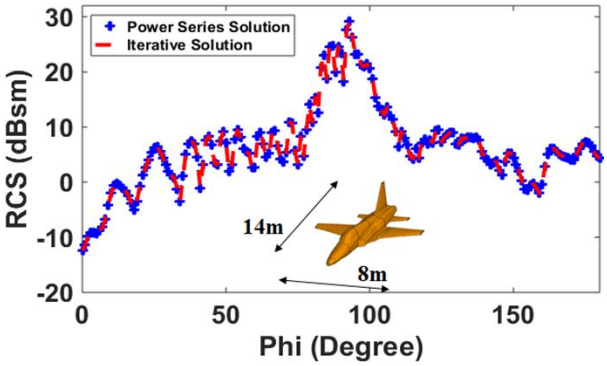

Fig. 9. Mono-static RCS of model fighter aircraft at 300 MHz for VV polarized plane wave incident and observation angles at $\theta = 90^o$, $\phi = 0^o$ to 180^o.

4. Mono-static RCS of a model fighter aircraft

As the last example, we consider the geometry of model fighter aircraft with length 14 m and wingspan 8 m. With λ/10 discretization of the geometry, the meshing scheme generates 93,819 unknowns. Figure 9 shows the computed mono-static RCS with $\alpha = 0.5$ in CFIE equation (8) at 300 MHz in the X-Y plane with VV polarized plane wave incident and observation angle at the nose to tail $\phi = 0^o$ to 180^o and $\theta = 90^o$.

Mono-static RCS (180 RHS) solution time comparisons of power series and iterative solver with and without preconditioned are shown in Table 3.

It can be observed from Figure 9 that for this complex geometry, RCS from the power series solution entirely agrees with the H-Matrix iterative solution and results in a much higher efficient solution.

VI. CONCLUSION

In this work, we propose a new power series solution method for solving 3D MoM-based integral equations. It can be observed from the numerical experimentation that the proposed method is as accurate as of the conventional iterative H-Matrix solution. Also, the proposed power series method results in significantly lower solution time compared to regular iterative and preconditioned iterative solutions. The method is based on the near-field matrix operation, thus maintaining $O(N)$ complexity for computation and $O(NlogN)$ solution time. The solution converges in fixed 2 iterations. The proposed method is a kernel-independent algebraic method and can be applied to other acceleration algorithms like MLFMA.

REFERENCES

[1] R. F. Harrington, *Field Computation by Moment Methods*, Wiley-IEEE Press, 1993.

[2] A. Taflove and S. C. Hagness, *Computational Electrodynamics The Finite-Difference Time-Domain Method*, Third edition, Artech House, 2005.

[3] Jin, Jian-Ming, *The Finite Element Method in Electromagnetics*, John Wiley & Sons, 2015.

[4] W. C. Chew, J. M. Jin, E. Michielssen, and J. Song, *Fast Efficient Algorithms in Computational Electromagnetics*, Artech House, Boston, London, 2001.

[5] S. Kapur and D. E. Long, "IES3: efficient electrostatic and electromagnetic solution," *IEEE Computer Science and Engineering*, vol. 5, no. 4, pp. 60-67, Oct.-Dec. 1998.

[6] D. Gope and V. Jandhyala, "Efficient solution of EFIE via low-rank compression of multilevel predetermined interactions," *IEEE Transactions on Antennas and Propagation*, vol. 53, no. 10, pp. 3324-3333, Oct. 2005.

[7] K. Zhao, M. N. Vouvakis, and J. F. Lee, "The adaptive cross approximation algorithm for accelerated method of moments computations of EMC problems," *IEEE Transactions on Electromagnetic Compatibility,* vol. 47, no. 4, pp. 763-773, Nov. 2005.

[8] Y. Saad, "ILUT: a dual threshold incomplete LU factorization," *Numerical Linear Algebra with Applications*, vol. 1, no. 4, pp. 387-402, 1994.

[9] Y. K. Negi, N. Balakrishnan, S. M. Rao, and D. Gope, "Null-field preconditioner for fast 3D full-wave MoM package-board extraction," *Proceedings IEEE conference on Electrical Design of Advanced Packaging and Systems*, pp. 57-60, Dec. 2014.

[10] Y. K. Negi, N. Balakrishnan, S. M. Rao, and D. Gope, "Null-field preconditioner with selected far-field contribution for 3-D full-wave EFIE," *IEEE Transactions on Antennas and Propagation*, vol. 64, no. 11, pp. 4923-4928, 2016.

[11] Y. K. Negi, N. Balakrishnan, S. M. Rao, and D. Gope, "Schur complement preconditioner for

fast 3D full-wave MoM package-board extraction," *Proceedings IEEE conference on Electrical Design of Advanced Packaging and Systems (EDAPS)*, pp. 163-165, 2016.

[12] Y. K. Negi, N. Balakrishnan, and S. M. Rao, "Symmetric near-field Schur's complement preconditioner for hierarchal electric field integral equation solver," *IET Microwaves, Antennas & Propagation,* vol. 14, no. 14, pp. 1846-1856, 2020.

[13] O. Bruno and L. Kunyansky, "A sparse matrix arithmetic based on H-matrices. Part I: introduction to h-matrices, computing," *Computing*, vol. 62, no. 2, pp. 89-108, 1999.

[14] W. Hackbusch and B. N. Khoromskij, "A sparse H -matrix arithmetic. Part II: application to multi-dimensional problems," *Computing,* vol. 64, no. 1, pp. 21–47, Jan. 2000.

[15] W. Chai and J. Dan, "A complexity-reduced H-matrix based direct integral equation solver with prescribed accuracy for large-scale electrodynamic analysis," *IEEE Antennas and Propagation Society International Symposium*, pp. 1-4. 2010.

[16] Y. K. Negi, "Memory reduced half hierarchal matrix (H-matrix) for electrodynamic electric field integral equation," *Progress In Electromagnetics Research Letters*, vol. 96, pp. 91-96, 2021.

[17] S. M. Rao and M. S. Kluskens, "A new power series solution approach to solving electrically large complex electromagnetic scattering problems," *Applied Computational Electromagnetics Society (ACES) Journal*, vol. 31, no. 9, 2016.

[18] R. E. Hodges and Y. Rahmat-Samii, "The evaluation of MFIE integrals with the use of vector triangle basis functions," *Microwave and Optical Technology Letters,* vol. 14, no. 1, pp. 9-14, 1997.

[19] S. M. Rao, D. R. Wilton, and A. W. Glisson, "Electromagnetic scattering by surfaces of arbitrary shape," *IEEE Transactions on Antennas and Propagation*, vol. 30, no. 3, pp. 409-418, May 1982.

[20] M. Bebendorf and S. Kunis, "Recompression techniques for adaptive cross approximation," *Journal of Integral Equations and Applications*, vol. 21, no. 3, pp. 331–357, 2009.

[21] Y. K. Negi, V. P. Padhy, and N. Balakrishnan. "Recompressed H-matrices for fast electric field integral equation," *IEEE-International Conference on Computational Electromagnetics (ICCEM 2020)*, Singapore, 24-26, August 2020.

[22] A. Greenwood, "Electromagnetic code consortium benchmarks". No. AFRL-DE-TR-2001-1086. Air Force Research Lab Kirtland AFB NM Directed Energy Directorate, 2001.

Yoginder Kumar Negi obtained the B.Tech degree in Electronics and Communication Engineering from Guru Gobind Singh Indraprastha University, New Delhi, India, in 2005, M.Tech degree in Microwave Electronics from Delhi University, New Delhi, India, in 2007 and the PhD degree in engineering from Indian Institute of Science (IISc), Bangalore, India, in 2018.

Dr Negi joined Supercomputer Education Research Center (SERC), IISc Bangalore in 2008 as a Scientific Officer. He is currently working as a Senior Scientific Officer in SERC IISc Bangalore. His current research interests include numerical electromagnetics, fast techniques for electromagnetic application, bio-electromagnetics, high-performance computing, and antenna design and analysis.

B. Narayanaswamy received the B.E. degree (Hons.) in Electronics and Communication from the University of Madras, Chennai, India, in 1972, and the Ph.D. degree from the Indian Institute of Science, Bengaluru, India, in 1979.

He joined the Department of Aerospace Engineering, Indian Institute of Science, as an Assistant Professor, in 1981, where he became a Full Professor in 1991, served as the Associate Director, from 2005 to 2014, and is currently an INSA Senior Scientist at the Supercomputer Education and Research Centre. He has authored over 200 publications in the international journals and international conferences. His current research interests include numerical electromagnetics, high-performance computing and networks, polarimetric radars and aerospace electronic systems, information security, and digital library.

Dr. Narayanaswamy is a fellow of the World Academy of Sciences (TWAS), the National Academy of Science, the Indian Academy of Sciences, the Indian National Academy of Engineering, the National Academy of Sciences, and the Institution of Electronics and Telecommunication Engineers.

Sadasiva M. Rao obtained his Bachelors, Masters, and Doctoral degrees in electrical engineering from Osmania University, Hyderabad, India, Indian Institute of Science, Bangalore, India, and University of Mississippi, USA, in 1974, 1976, and 1980, respectively. He is well known in the electromagnetic engineering community and included in the Thomson Scientifics' *Highly Cited Researchers List*.

Dr. Rao has been teaching electromagnetic theory, communication systems, electrical circuits, and other related courses at the undergraduate and graduate level for the past 30 years at various institutions. At present, he is working at Naval Research Laboratories, USA. He published/presented over 200 papers in various journals/conferences. He is an elected Fellow of IEEE.

Novel Broadband Circularly Polarized Monopole Antenna for Multi-communication Systems

Hua Chen, Quanyuan Feng, Yan Wen, and Qiang Fu

School of Information Science and Technology
Southwest Jiaotong University, Chengdu, China
15175279665@163.com, fengquanyuan@163.com

***Abstract* –** This paper proposes a novel coplanar waveguide (CPW) fed broadband circularly polarized (CP) monopole antenna, which applies to C-band and various wireless communication systems. The antenna consists of the double circular-shaped patch (DCSP) with square and L-shaped slots, and an improved asymmetric ground plane. The prototype of the designed antenna has been fabricated. The results of the measurement show that the 10-dB impedance bandwidth (ZBW) is 117.8% (2.2–8.5 GHz), the 3-dB axial ratio bandwidth (ARBW) is 62% (4.45–8.45 GHz).

***Index Terms* –** Broadband, Circularly Polarized (CP), Coplanar Waveguide (CPW) Fed, Monopole Antenna.

I. INTRODUCTION

In recent years, the research on the broadband and circular polarization (CP) performance of the antenna has become critical increasingly. Broadband CP antennas are gradually being utilized in various wireless communication systems due to their advantages, such as increasing the flexibility of antenna radiation directions, suppressing multipath interference, and working in multiple frequency bands at the same time [1].

A variety of low-profile, low-cost, and easy-to-manufacture CP monopole antenna structures have been proposed through researches [2–6]. These proposed structures include cutting the width of the left ground plane and introducing an L-shaped strip on the right ground [2], using the semi-circular monopole with lateral strips and its complementary structure to generate the CP mode [3], introducing a complementary L-shaped strip above the ground plane with an L-shaped slot [4], using the inclined D-shaped radiator composed of inclined I-shaped and inverted C-shaped patches [5], adding two unequal arms perpendicular to each other in the Y-shaped monopole [6]. However, the CP antennas mentioned above have narrow ARBW, which can no longer meet the multi-band requirements of current communication systems.

In order to improve the ARBW, several broadband CP monopole antennas [7–15] have been proposed. An L-shaped slot is introduced at the corresponding position of the ground with the slotted rectangular stub [7]. In [8], the inverted C-shaped monopole couples with the parasitic rectangular open-loop patch to produce CP. The inverted C-shaped monopole is coupled with the G-shaped parasitic strip, and the ground plane inserts two symmetrical square slots [9]. Adding a vertical rectangular branch above the ground with a horizontal slot to broaden the ARBW and the ZBW [10]. Two antisymmetric parasitic spiral bands are introduced to achieve CP [11]. The coupling between the moon-shaped monopole and the ground with a semi-circular slot extends the ARBW [12]. In [13], irregular trapezoidal radiation patch is used, inverted L-shaped strips and rectangular slots are introduced into the diagonal corners of the square slot grounding plane to realize a wide ZBW. In the process of in-depth research on the monopole antenna, we find that several antennas have problems with complex structures. The challenge we need to overcome is to design the CP monopole antenna with a simple structure and broadband performance.

A novel double circular-shaped monopole antenna with a simple structure is proposed in this letter. An inverted L-shaped slot is opened inside the double circular-shaped patch (DCSP) to excite a CP mode at lower frequency. Subsequently, an improved ground is introduced to widen the ZBW effectively and obtain a new CP mode at middle frequency. Finally, a square slot is etched in the upper left corner of the DCSP to change the current path of x and y directions, resulting in two orthogonal modes with equal amplitude and 90° phase difference in the upper frequency band. The broadband ZBW and ARBW of the designed antenna reach 117.8% and 62.0%, respectively. The data analysis process and design results are discussed in detail in this article.

II. ANTENNA DESIGN AND ANALYSIS

A. Antenna design

The geometry diagram and prototype of the proposed broadband CP monopole antenna are shown in Figure 1. The antenna is fabricated on an FR4 ($\varepsilon_r = 4.4$,

Submitted On: May 20, 2021
Accepted On: June 21, 2021

https://doi.org/10.47037/2021.ACES.J.361007

tan δ = 0.02) substrate with an overall size of $40 \times 40 \times 0.8$ mm^3. The antenna is the CPW-fed structure, which is consisted of a 50 Ω feedline, the DCSP, and an improved ground plane. The optimal sizes obtained by the software HFSS 15.0 are shown in Table 1.

Figure 2 shows five statuses of proposed antenna to better understand the design process (Ant.1–Ant.5). The simulated S11 and AR results for each model are compared in Figure 3. Ant. 1 is composed of a symmetrical ground plane and the DCSP. Compared with the traditional circular radiator, the DCSP can provide a longer current path to achieve the broadband CP bandwidth more easily while obtaining the ideal impedance matching.

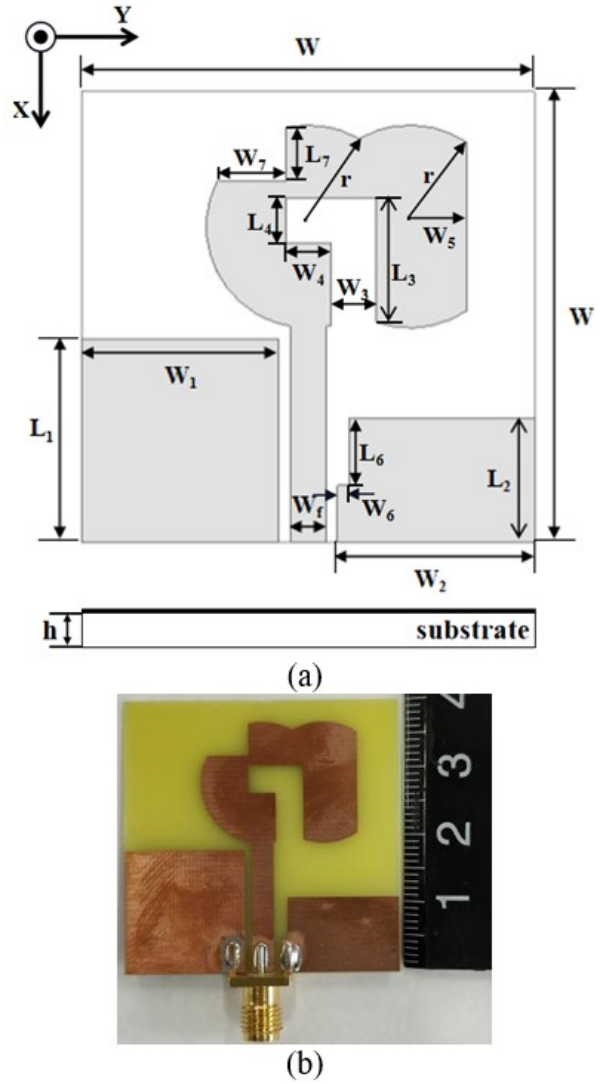

Fig. 1. (a) The geometry diagram, (b) prototype of the proposed antenna.

Table 1: Dimensions of the proposed antenna (unit: mm)

Parameter	Value	Parameter	Value
W	40	W8	2
r	9	L9	4
h	0.8	W9	2
L_f	28	L_3	11.5
W_f	3.2	W_3	4
L_1	18	L_4	4
W_1	17.4	W_4	4
L_2	11	L_5	15
W_2	17.4	W_5	5
L_7	4.8	L_6	6
W_7	6	W_6	1
L8	2.5		

In Ant. 2, an inverted L-shaped slot is etched inside the DCSP. L-shaped slot is a common structure for CP design, which can extend the current path to obtain a new resonance frequency and excite the CP mode by orthogonal current components around the L-shaped slot. It can be seen from Figure 3 that the simulated S11 produces a new resonance frequency at 2.1 GHz, the simulated AR curve moves down and generates a basic CP mode at 6 GHz. The circumference (L) of the inverted L-shaped slot should be a quarter of the free space wavelength corresponding to the resonance frequency (f) of the S11. L is 35 mm, f is calculated to be about 2.14 GHz according to formula (1), (2). Thus, the simulated and calculated results are consistent.

$$L = \lambda/4, \tag{1}$$

$$\lambda = c/f, \tag{2}$$

where λ is the wavelength, c is the speed of light in free space, and f is the resonance frequency.

Ant. 3 improves the basic ground into an asymmetric structure. The antenna impedance matching enhances effectively in the entire frequency band, and different impedance bandwidths combine into a broadband ZBW.

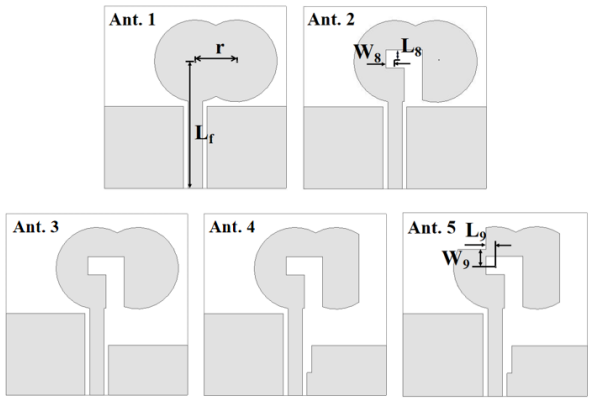

Fig. 2. Design procedures of the proposed antenna.

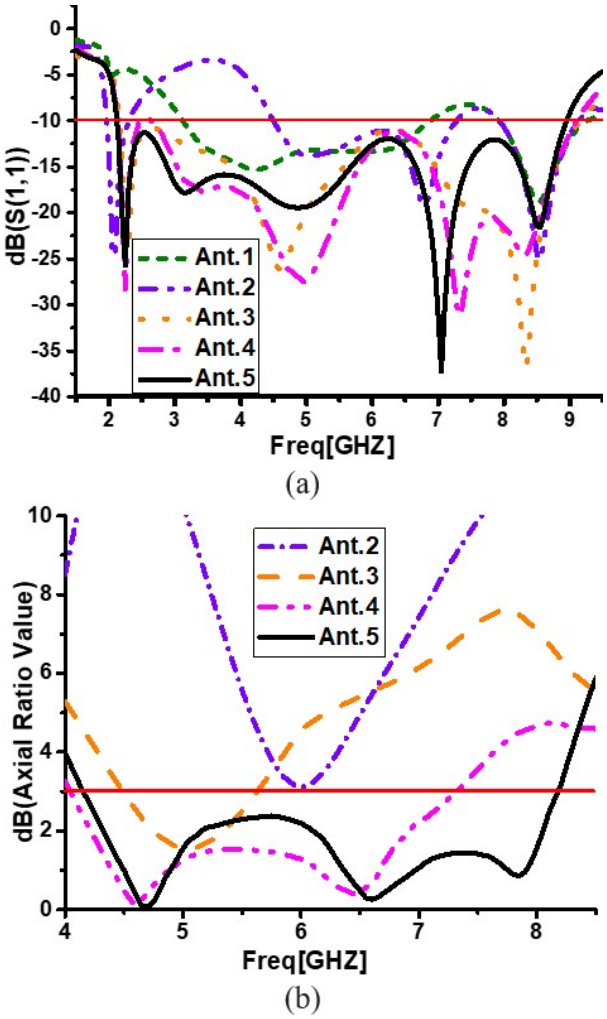

Fig. 3. Simulated results of the antenna improvement steps. (a) *S*11, (b) AR.

Simultaneously, the CP mode at 6 GHz shifts to the lower band (5 GHz) and obtains the CP bandwidth.

In Ant. 4, a rectangular slot is inserted in the upper left corner of the right ground to reduce the coupling between the feedline and ground. Thereby weakening the current intensity at the edge of the ground to balance orthogonal electric field components, and exciting a new CP mode at 6.5 GHz. By adjusting the length and width of this rectangular slot, two narrow CP modes combine into a wide ARBW. A vertical slot is cut off on the right side of the DCSP to enhance the current in the +x direction, which expands the ARBW. Finally, Ant. 5 creates a new CP mode at 7.85 GHz by etching a square slot in the upper left corner of the DCSP. Adjust W_7 and L_7 to change the amplitude of orthogonal currents in x and y directions around the slot. Finally, three CP modes are combined to realize the broadband CP feature, and the simulated ARBW reaches 4.15 to 8.14 GHz.

B. CP mechanism analysis

To understand the CP mechanism of antenna design process, the surface current distributions of the antenna modules at 5 GHz (Ant. 3), 6.5 GHz (Ant. 4), and 7.85 GHz (Ant. 5) at 0° and 90° phases are shown in Figure 4.

The main currents are marked with dashed lines, the vector sum of the current is marked with the solid line. The currents at 180° and 360° are equal-amplitude and opposite to the currents at 0° and 90° phases, respectively. In Figure 4, the surface currents are concentrated

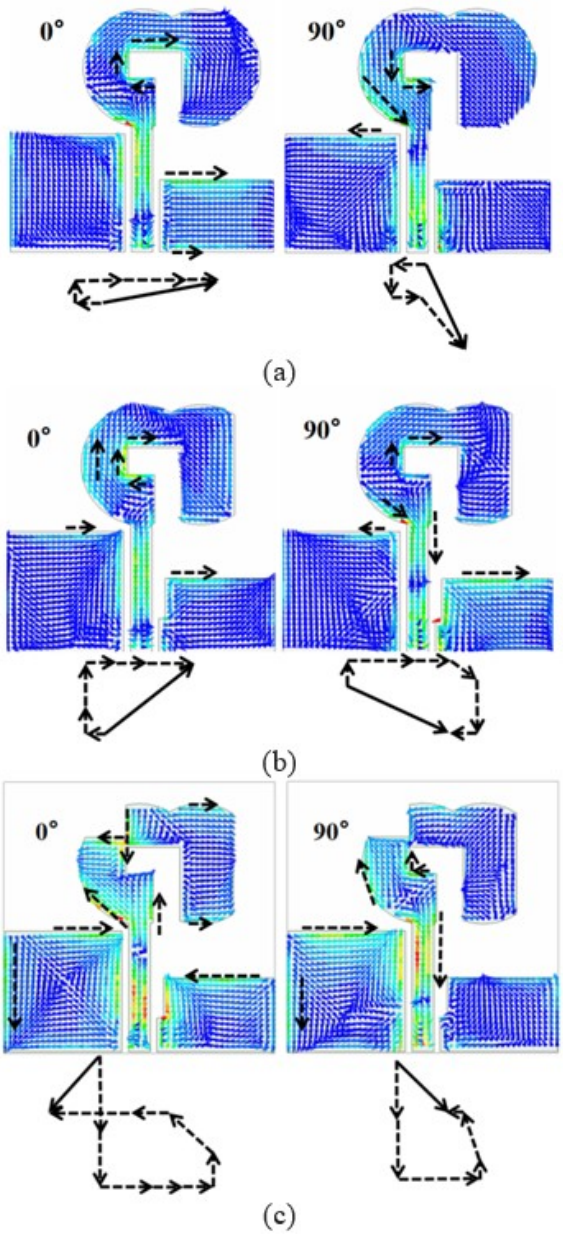

Fig. 4. Surface current distributions over antennas (a) Ant. 3 at 5 GHz, (b) Ant. 4 at 6.5 GHz, (c) Ant. 5 at 7.85 GHz with phases of 0°, 90°.

near the edge of the ground plane, feedline, and slots of the DCSP. The parameters at these positions can be adjusted to obtain perfect CP performance.

Figure 4 (a) shows that the current vector sum of Ant. 3 at 5 GHz points to -20° and +70° relative to the +y axis at 0° and 90° phases, respectively. Two equal-amplitude orthogonal electric field components are obtained under far-field conditions, which proves that the CP mode can be achieved in this frequency band. The antenna radiates left-handed circular polarization (LHCP) in the +z direction. The same conclusions can be drawn for the current surface distributions at 6.5 GHz and 7.85 GHz in Figure 4 (b), (c). Finally, three CP modes can be obtained on the overall frequency band and combined into a broadband ARBW.

III. PARAMETRIC ANALYSIS

The antenna parameters need to be continuously analyzed and adjusted to obtain the best broadband CP performance. Figures 5, 6, and 7 illustrate the effects

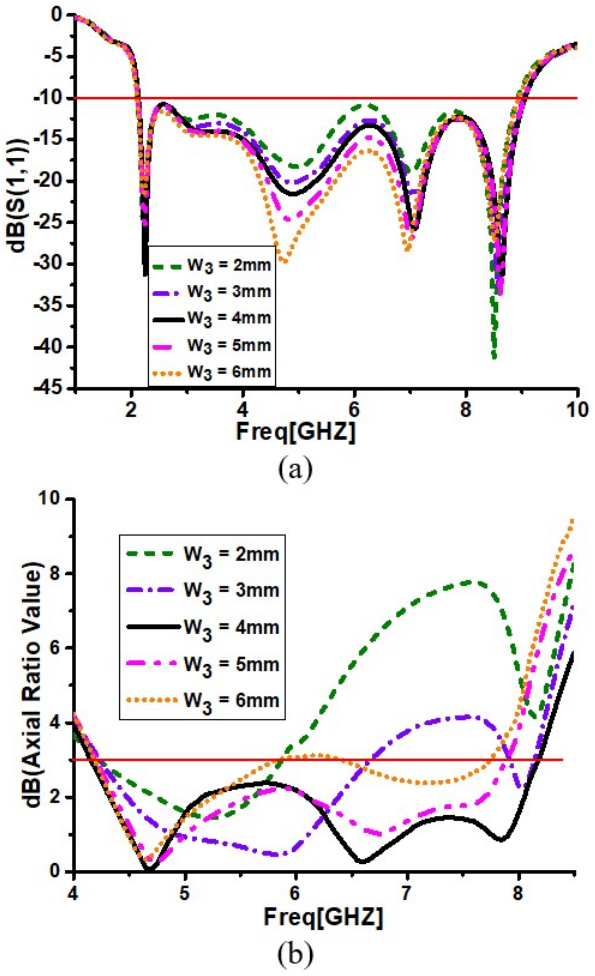

Fig. 5. Effects of W_3 on the antenna performance. (a) *S*11, (b) AR.

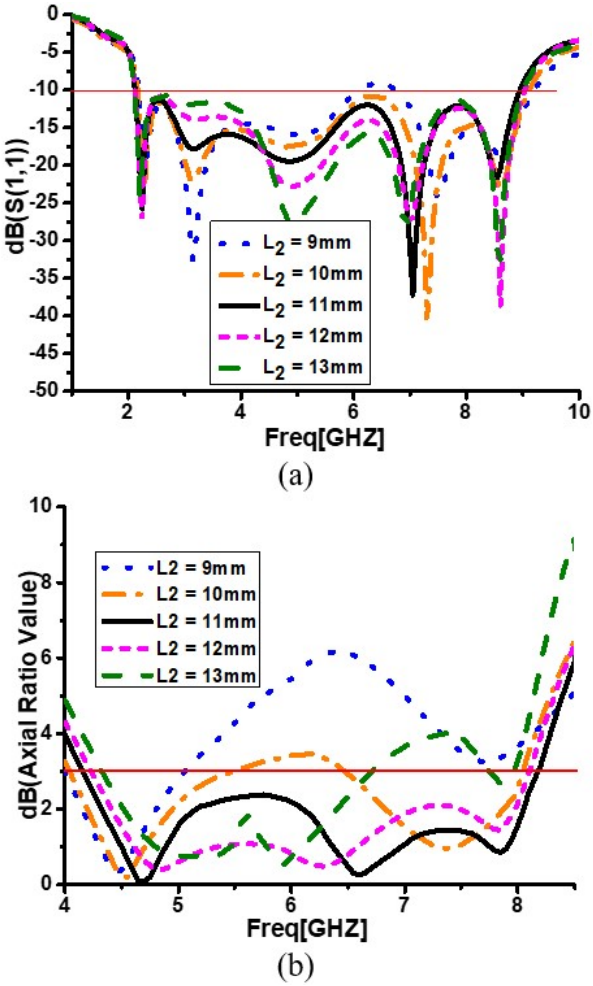

Fig. 6. Effects of L_2 on the antenna performance. (a) *S*11, (b) AR.

of varying the key parameters (L_2, W_3, and W_7) on the S11 and AR. In the process of parametric analysis, other parameters keep the final optimized value unchanged.

A. Effects of the width of the L-shaped slot (W_3)

Figure 5 displays that W_3 has a great impact on the mid-band S11 due to the coupling effect between both sides of the L-shaped slot. As W_3 increases, the mid-band impedance matching of the antenna enhances. In addition, W_3 also has great effects on AR bandwidth. With W_3 increasing from 2 mm to 4 mm, the CP mode in the upper band shifts down and extends ARBW. However, CP performance deteriorates with the continued increase of W_3. Finally, to realize the widest ARBW, the value of W_3 is selected as 4 mm.

B. Effects of the height of the right ground plane (L_2)

It can be seen from Figure 3 that asymmetric ground plays an important role in optimizing impedance

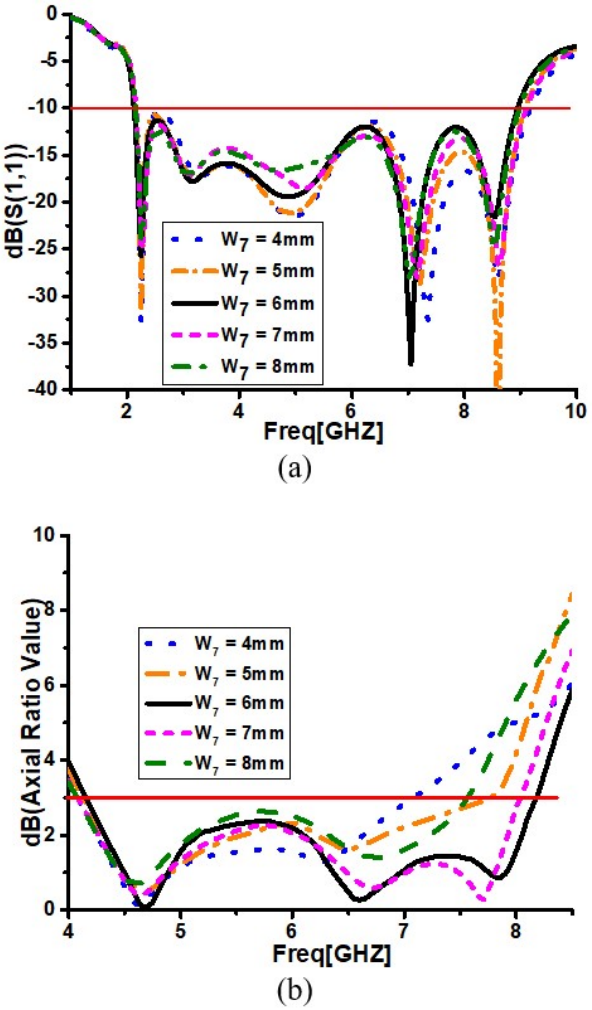

Fig. 7. Effects of W_7 on the antenna performance. (a) *S*11, (b) AR.

characteristics and achieving basic CP mode. Changing the height of the right ground (L_2) can influence current intensity at top edge of the right ground and the coupling effect between the right ground and radiator to alter the CP behavior. Figure 6 (b) exhibits that the CP modes in the middle- and high-frequency bands are sensitive to the variety of L_2. Through comprehensive comparison, it is determined that when the value of L_2 is 11 mm, the antenna gets vintage performance.

C. Effects of the width of the square slot (W_7)

The introduction of the square slot in the upper left corner of DCSP generates a CP mode at high frequency. W_7 influences the y-direction current component around the slot, which strongly affects CP performance at high frequency. This effect can also be observed in Figure 7, high-frequency CP mode keeps changing with the variation of W_7. However, the S11 is affected slightly by W_7. Finally, the value of W_7 is chosen as 6 mm.

IV. EXPERIMENTAL VERIFICATION

In Figure 1 (b), the prototype has been fabricated according to optimal sizes shown in Table 1. The simulated and measured S11, AR, and gain are compared in Figures 8 (a), (b), respectively. The measured ZBW is 117.8% (2.2–8.5 GHz), and measured ARBW of the antenna is 62% (4.45–8.45 GHz), which are consistent with the simulation results, except for slight offsets in the upper and lower bands, respectively. The overall variation trend of the measured peak gain is consistent with the simulated result, but it is slightly larger than the simulation result by 1 dBic in most frequency bands and slightly lower than the simulation result above 7.4 GHz, as shown in Figure 8 (b). These differences between the measured and simulated results can be attributed to the manufacturing tolerance, the process error of welding

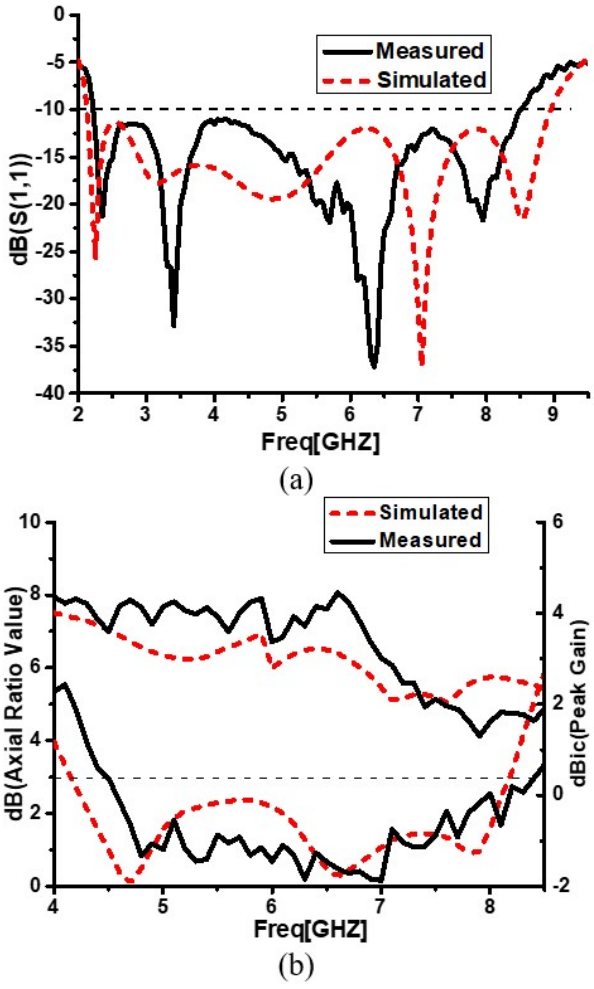

Fig. 8. Simulated and measured performance for the designed antenna. (a) *S*11 and (b) AR and gain.

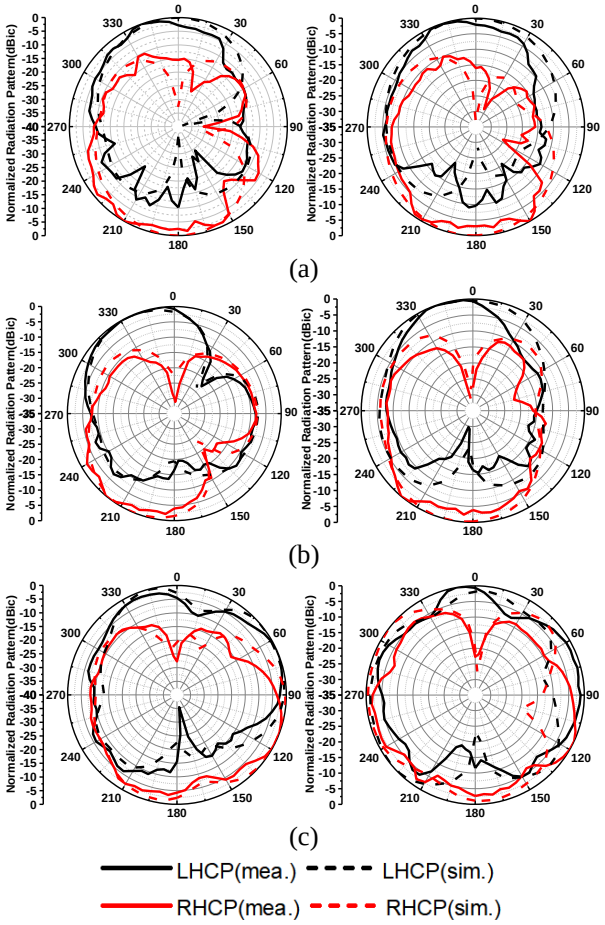

Fig. 9. Simulated and measured normalized radiation patterns at (a) 4.7, (b) 6.0, and (c) 7.5 GHz.

SMA interface, and the impact of the measurement environment, but the overall measurement results are satisfactory.

The normalized radiation patterns of the proposed antenna at 4.7, 6.0, and 7.5 GHz in xz ($\varphi = 0\ ^\circ$) and yz ($\phi = 90^\circ$) planes are shown in Figures 9 (a), (b), and (c), respectively. The proposed antenna radiates LHCP wave in the positive direction (+z) and RHCP wave in the opposite direction (-z) of the ground plane. The measured results agree well with simulated radiation patterns.

V. CONCLUSION

A novel wideband CP monopole antenna with a simple and easily fabricated structure has been proposed in this paper. Utilizing the DCSP with an L-shaped slot and the modified asymmetric ground, broadband ARBW and ZBW is achieved. The square slot etched on the left upper of DCSP further expands ARBW. The measured ZBW of the designed antenna is 117.8%, which fully covers the ARBW of 62%. And the measured maximum peak gain is 4.6 dBic. The proposed antenna is suitable for WLAN/WiMAX/ISM (5 GHz) and C-band wireless communication systems.

ACKNOWLEDGMENT

This work was supported by 19-163-21-TS-001-062-01, and Key Project of the National Natural Science Foundation of China under Grant 62090012, 62031016, 61831017, and the Sichuan Provincial Science and Technology Important Projects under Grant 2019YFG0498, 2020YFG0282, 2020YFG0452, and 2020YFG0028.

REFERENCES

[1] U. Ullah and S. Koziel, "A broadband circularly polarized wide-slot antenna with a miniaturized footprint," *IEEE Antennas and Wireless Propagation Letters*, vol. 17, no. 12, pp. 2454-2458, Dec. 2018.

[2] C. Wang and K. Hsiao, "CPW-fed monopole antenna for multiple system integration," *IEEE Transactions on Antennas and Propagation*, vol. 62, no. 2, pp. 1007-1011, Feb. 2014.

[3] W. Liang, Y. Jiao, Y. Luan, and C. Tian, "A dual-band circularly polarized complementary antenna," *IEEE Antennas and Wireless Propagation Letters*, vol. 14, pp. 1153-1156, 2015.

[4] S. Ahdi Rezaeieh, A. Abbosh, and M. A. Antoniades, "Compact CPW-fed planar monopole antenna with wide circular polarization bandwidth," *IEEE Antennas and Wireless Propagation Letters*, vol. 12, pp. 1295-1298, 2013.

[5] A. Altaf and M. Seo, "A tilted-D-shaped monopole antenna with wide dual-band dual-sense circular polarization," *IEEE Antennas and Wireless Propagation Letters*, vol. 17, no. 12, pp. 2464-2468, Dec. 2018.

[6] A. Ghobadi and M. Dehmollaian, "A printed circularly polarized Y-shaped monopole antenna," *IEEE Antennas and Wireless Propagation Letters*, vol. 11, pp. 22-25, 2012.

[7] K. O. Gyasi, G. Wen, D. Inserra, Y. Huang, J. Li, A. E. Ampoma, and H. Zhang, "A compact broadband cross-shaped circularly polarized planar monopole antenna with a ground plane extension," *IEEE Antennas and Wireless Propagation Letters*, vol. 17, no. 2, pp. 335-338, Feb. 2018.

[8] K. Ding, C. Gao, T. Yu, and D. Qu, "Broadband C-shaped circularly polarized monopole antenna," *IEEE Transactions on Antennas and Propagation*, vol. 63, no. 2, pp. 785-790, Feb. 2015.

[9] M. Midya, S. Bhattacharjee, and M. Mitra, "Broadband circularly polarized planar monopole antenna with G-shaped parasitic strip," *IEEE Antennas and Wireless Propagation Letters*, vol. 18, no. 4, pp. 581-585, Apr. 2019.

[10] L. Zhang, Y. Jiao, Y. Ding, B. Chen, and Z. Weng, "CPW-fed broadband circularly polarized planar monopole antenna with improved ground-plane structure," *IEEE Transactions on Antennas and Propagation*, vol. 61, no. 9, pp. 4824-4828, Sep. 2013.

[11] K. Ding, C. Gao, Y. Wu, D. Qu, and B. Zhang, "A broadband circularly polarized printed monopole antenna with parasitic strips," *IEEE Antennas and Wireless Propagation Letters*, vol. 16, pp. 2509-2512, Jul. 2017.

[12] B. Hu, Nasimuddin, and Z. Shen, "Broadband circularly polarized moon-shaped monopole antenna," *Microwave and Optical Technology Letters*, vol. 57, no. 5, pp. 1135–1139, May 2015.

[13] M. Shokri, S. Asiaban, and Z. Amiri, "Study, design and fabrication of a CPW fed compact monopole antenna with circular polarization for ultra wide band systems application," *Applied Computational Electromagnetics Society (ACES) Journal*, vol. 32, no. 9, pp. 749-753, Sep. 2017.

[14] F. Azamian, Fateme, M. N. Azarmanesh, and C. Ghobadi, "A novel compact CPW-fed antenna with circular polarization characteristics for UWB applications," *Applied Computational Electromagnetics Society (ACES) Journal*, vol. 30, no. 1, pp. 93-98, Jan. 2015.

[15] B. Xiao, L. Zhong, J. S. Hong, and S. L. Li, "A novel compact planar spiral-shaped antenna," *Applied Computational Electromagnetics Society (ACES) Journal*, vol. 28, no. 1, pp. 57-63, Jan. 2013.

Hua Chen was born in Baoding, Hebei, China, in 1997. She is currently working toward her Master's degree in Electronic and Communication Engineering at Southwest Jiaotong University, Chengdu, China. Ms, Chen's main research content is antenna design and theory, mainly in circularly polarization antennas.

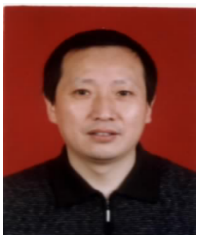

Quanyuan Feng (M'06–SM'08) received his M.S. degree in microelectronics and solid electronics from the University of Electronic Science and Technology of China, Chengdu, China, in 1991, and Ph.D. degree in EM field and microwave technology from Southwest Jiaotong University, Chengdu, China, in 2000. He is the Head of Institute of Microelectronics, Southwest Jiaotong University, Chengdu, China. Mr. Feng has been honored as the "Excellent Expert" and the "Leader of Science and Technology" of Sichuan Province owing to his outstanding contributions. In the recent 5 years, more than 500 of his papers have been published on IEEE Transactions on Antennas and Propagation, IEEE Transactions on Microwave Theory and Techniques, IEEE Antennas and Wireless Propagation Letters, etc., among which more than 300 were registered by SCI and EI. His research interests include integrated circuits design, RFID technology, embedded system, wireless communications, antennas and propagation, microwave & millimeter wave technology, smart information processing, electromagnetic compatibility, RF/microwave devices and materials, etc.

Yan Wen received the B.S. degree in Transportation from Southwest Jiaotong University, Chengdu, China, and is currently working in Southwest Jiaotong University. Herresearch interests include circuit design and antennas.

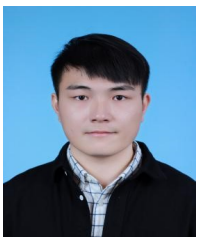

Qiang Fu (1997) received his B.E. degree from Nanchang Hangkong University, Nanchang, China, in 2019. He is currently pursuing M.Eng degree with the School of Information and Communication Engineering, Southwest Jiaotong University, Chengdu, China. Mr. Fu's current research interests include circularly polarized antennas, and wideband antennas.

A Dual-Array Antenna System for 5G Millimeter-Wave Applications

Hafiz Usman Tahseen[1], Lixia Yang[2], and Wang Hongjin[1]

[1]School of Computer Science and Communication Engineering
Jiangsu University, Zhenjiang, 212013, China
drengrtahseen@gmail.com, 2405302396@qq.com

[2]Department of Communication Engineering
Anhui University, Hefei, 230601, China
Lixiayang@yeah.net

Abstract – Millimeter-wave (mm-Wave) technology has opened a new era of wireless communication systems in various fields like automotive, mobile devices, Internet of Things (IoT), military, medical, and others. The benefit of adopting the unconventional frequency spectrum of large bandwidth under an mm-Wave spectrum is the availability of large bandwidth and lesser chances of interferences from various technologies. In the recent 5G communication systems either cellular or other wireless applications, many researchers have focused on mm-Wave antennas and arrays. In this paper, a dual-array antenna system is designed for various 5G mm-Wave wireless applications. It has two arrays on the same substrate edges with a series feed line compact technique. The profile antenna system has two 1×16 arrays on the same substrate edges. Each array gives 17.3 dB and 16.4 dB simulated and measured gains and impedance bandwidth 31.30 GHz to 39 GHz at 38 GHz center frequency. The feature to use both arrays at the same time for two different applications within the operational band for same or different center frequencies makes this proposed dual-array antenna system a good candidate for 5G mm-Wave wireless IoT and broadcast applications.

Index Terms – Internet of Things (IoT), antenna array, millimeter-wave (mm-Wave).

I. INTRODUCTION

The technological development in cellular devices, androids, and broadcast applications with the passage of time has inspired a high-speed data rate demand that leads to a 5G communication system. The high frequency bands in millimeter-wave (mm-Wave) range, i.e., n258, n257, n261, n260, n260, and n257 have already been allocated by the FCC for 5G communication systems.

The three main factors, i.e., arbitrary mobile device orientation, indoor outdoor propagation environment, and user mobility are really important for designing antennas in cellular communication systems [1]. The high path losses in communication systems are due to the high operating frequencies that are compensated with high gain directional antennas [2]. The high frequency mm-Wave antennas provide high data rate in communication systems [3]. In high frequency communication systems, directional antenna is a good choice to reduce delay spread, Doppler shift spread, and path loss exponent [4]-[6]. The high frequency 5G antennas have become a hot topic these days for wireless networks that cover multiple bands with wide bandwidths [7]. In [8], a proximity-coupled planar antenna array is presented that gives 21 dBi high gain with impedance bandwidth 27.5–28.5 GHz for cellular 5G applications. In [1], a multi-mode phased antenna array is proposed to cover the frequency band 25–33 GHz. In [9], the 8-element antenna array is designed for 5G wireless cellular applications that give 12 dBi gain with 26.5–38 GHz impedance bandwidth with low side lobes. In [10]-[21], a substrate integrated waveguide (SIW) feed network is used to get large impedance bandwidth and high gain. In [22], A SIW-fed 8×8 antenna array is presented that gives 26.7 dBi gain with impedance bandwidth 35.4–41.7 GHz. A series-parallel feeding technique is preferred instead of traditional parallel power divider networks for tight planar array configurations and compact sizes [23]. A novel method is used in [24] to reduce mutual reduction in 8-element antenna array that gives 11.32 dBi gain with the impedance bandwidth 24.75–28.5 GHz.

This article presents a dual-array antenna system with a compact feeding network for various 5G mm-wave multiple wireless applications as shown in Figure 1. The compact feeding structure is based on a series-parallel technique as in [23].

All patch elements are in parallel connection with a single series feed line. So, they all are excited with a single port. The profile antenna element has a half-moon slot at the center and is excited at 38 GHz

Submitted On: March 3, 2021
Accepted On: July 7, 2021

https://doi.org/10.47037/2021.ACES.J.361008

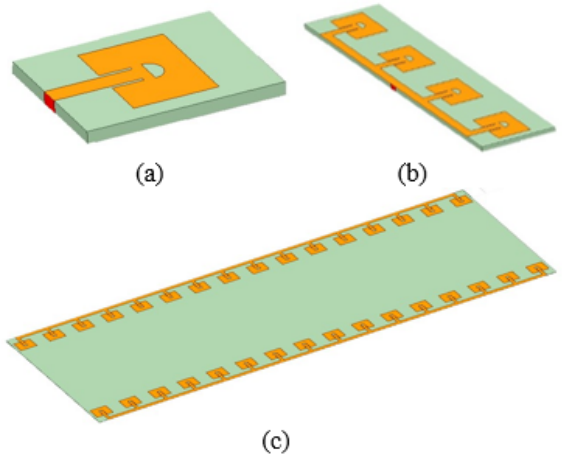

Fig. 1. 5G antennas; (a) single antenna element, (b) 1×4 antenna array, (c) 1×16 antenna array.

center frequency antenna to operate for n260 5G band for high-speed data rate applications. Each array exhibits equal broad bandwidth with high gain and negligible side lobes. There is a little drop or discrimination of gain at edge frequencies for the entire bandwidth.

The operation of dual-array antenna structure with compact feed network for two different applications at the same or different frequencies within the operational band makes this proposed array a good candidate for multi-wireless mm-Wave applications. The profile 1×16 dual-array antenna can be used for Internet of Things (IoT) and cellular applications in smartphones with two 1×4 antenna arrays for end-fire coverage. Furthermore, the proposed 1×16 dual-array antenna is also a good candidate for indoor and outdoor mm-Wave broadcast and IoT applications. The simulation results from ANSYS 18.2 HFSS are compared with the measured results for validity check.

The paper is organized as follows: section II discusses the antenna design and principle of operation. Results and discussions lie in section III. Final summary is in section IV.

II. ANTENNA DESIGN AND PRINCIPLE

A. Antenna design

It is really important to design a broadband mm-Wave antenna element with high gain for array configuration as shown in Figure 1. In the first step, an antenna element is simulated without any slot on the patch at 38 GHz center frequency on a Rogers-5880 dielectric substrate with basic micro strip antenna design formulae as follows in [25, 26]. The antenna element gives 7.15 dBi gain with impedance bandwidth 36.16–39.27 GHz with 32.78 dB return loss as shown in Figure 2 (a) and (b). In the 2nd step, a half-moon slot is added on the patch

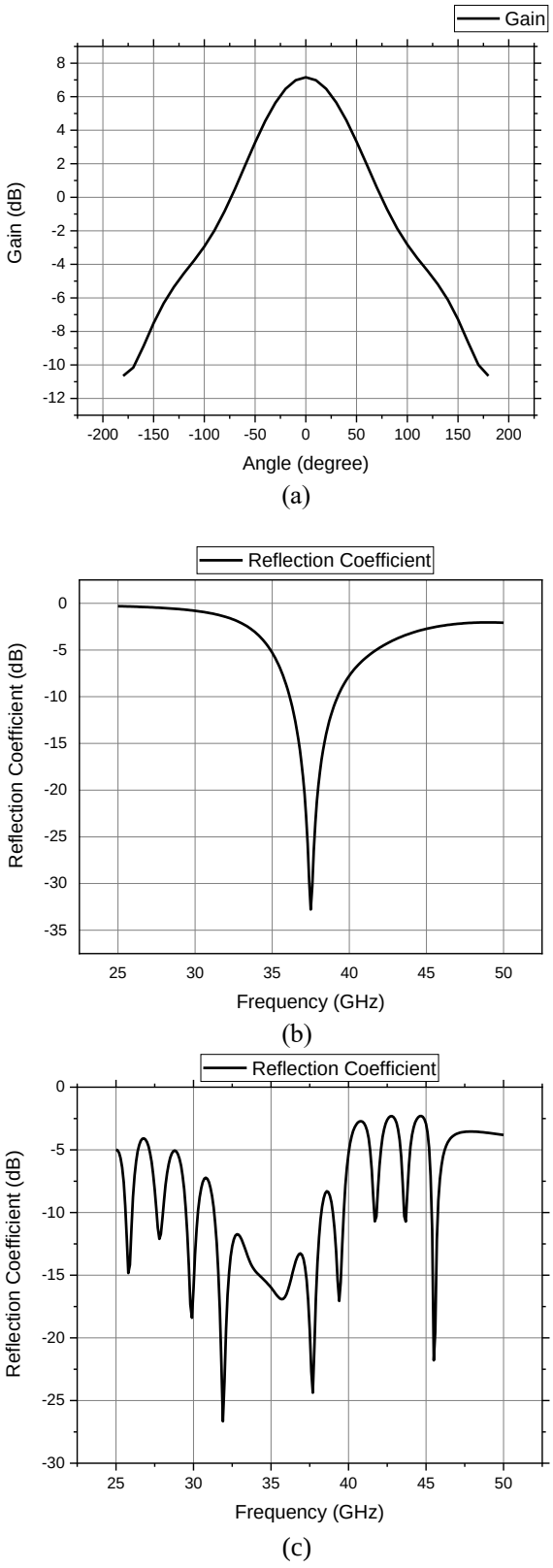

Fig. 2. Single element antenna results; (a) realized gain, (b) simulated reflection coefficient without slot, (c) simulated reflection coefficient with half-moon slot.

Table 1: Specifications of antenna element

No.	Description	Units/quantity
1	Patch length	2.34 mm
2	Patch width	3.12 mm
3	Substrate length	5.43 mm
4	Substrate width	4.21 mm
5	Substrate height	0.5 mm
6	Feed line length	2.413 mm
7	Feed line width	0.543 mm
8	Inset gap	0.1003 mm
9	Moon slot radius	0.4 mm
10	Series line width	0.543 mm
11	Frequency	38 GHz

to improve the bandwidth. The antenna parameters are mentioned in Table 1. The antenna element with half-moon slot gives an improved bandwidth 31.30–39 GHz at 38 GHz center frequency as shown in Figure 2 (c).

Firstly, a 1×4 array is simulated at 38 GHz center frequency as shown in Figure 1 (b) for demonstration and then two 1×16 antenna arrays on the same substrate edges are designed. Each array has a separate feed port. The antenna elements are connected in a compact series feed line mechanism. Each series feed line has an mm-Wave port connector at the center.

B. Dual-array antenna

With the optimized configuration of antenna element, a dual-array mm-Wave 5G antenna is designed with high gain and large bandwidth. The antenna array with 4-element configuration is simulated for array demonstration. The main dual-array antenna consists of two 1×16 antenna arrays on a single substrate edge in the broadside direction with two separate ports. The proposed dual-array antenna can be used for mm-Wave 5G multi-wireless applications. It is also applicable to mm-Wave 5G base stations, broadcast, and IoT applications. So, the proposed dual-array antenna structure looks a good candidate for strong signal coverage for 5G applications. The antenna uses Rogers-5880 dielectric substrate with 0.5 mm height, 0.002 loss tangents, and 2.2 relative permittivity. Each antenna element has dimensions as mentioned in Table 1. The substrate size of 1×4 antenna array is 3.43 mm × 29.80 mm × 0.5 mm and each 1×16 antenna array has 29.80 mm × 90.49 mm × 0.5 mm dimensions. The antenna array elements are spaced and are connected with a series feed line mechanism.

III. RESULTS AND DISCUSSIONS

The proposed dual-array antenna system is a prototype as shown in Figures 3 (a) and (b). In dual-array antenna system, each array is connected to a 2.92k mm-Wave connector separately. Each 1×16 antenna array exhibits high gain with a large impedance bandwidth in

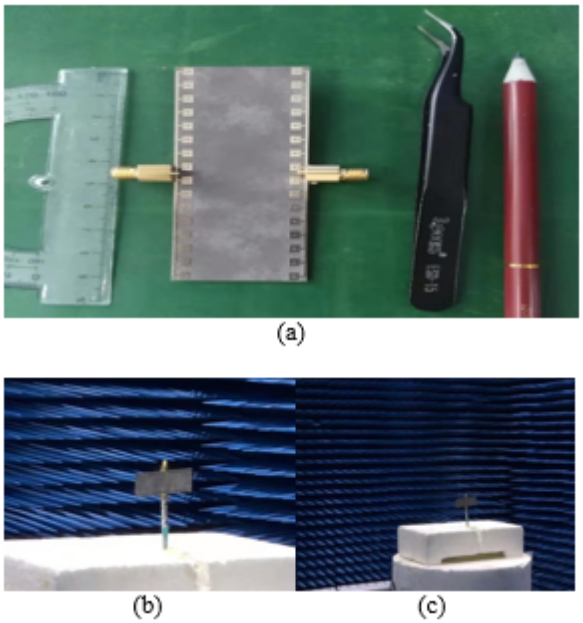

Fig. 3. Fabricated dual antenna array; (a), (b), and (c).

mm-Wave frequency range. Firstly, a single patch element is simulated without any slot. It gives a wide radiation pattern with narrow bandwidth. In the next step, a half-moon slot is added on the patch to improve the band width as shown in Figures 2 (a), (b), and (c).

Secondly, a 1×4 antenna array is simulated for array description, design confirmation, and end-fire coverage demonstration for smartphone application. The 1×4 antenna array exhibits 12.91 dB simulated gain as shown in Figure (4). With these parameters, a dual-array antenna with two 1×16 antenna arrays is simulated

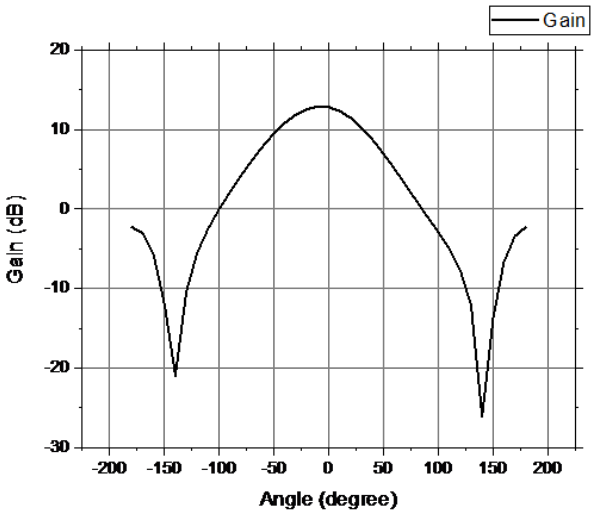

Fig. 4. Simulated realized gain of 1×4 antenna array.

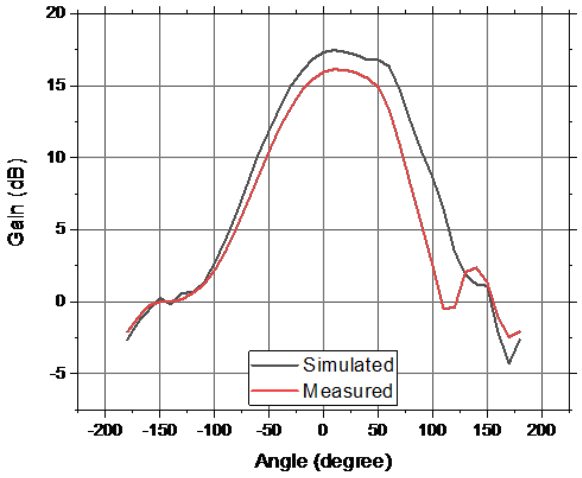

Fig. 5. Simulated and measured realized gain of 1×16 antenna array.

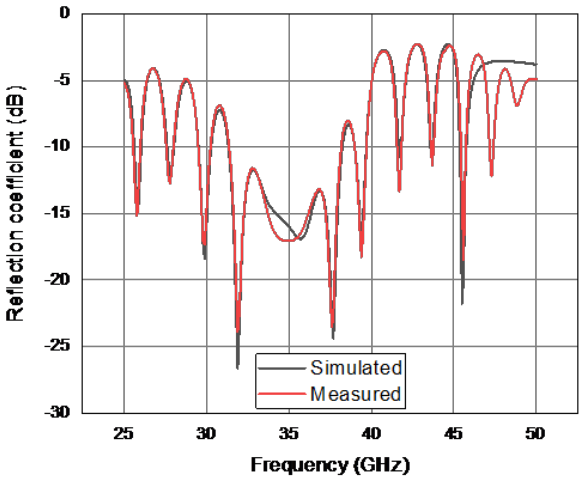

Fig. 6. Reflection coefficient of 1×16 antenna array.

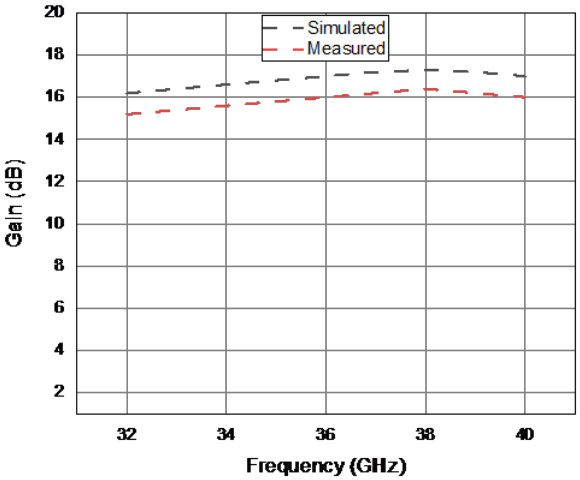

Fig. 7. Gain curve of 1×16 antenna array.

and then fabricated for mm-Wave 5G multi-wireless applications. It exhibits high gain with large impedance bandwidth. In dual-array antenna system, both arrays give almost the same radiation pattern and impedance bandwidth. Figure 5 shows the simulated and measured radiation patterns for one of the 1×16 antenna arrays at 38 GHz center frequency. The plot in Figure 6 gives the measured and simulated reflection coefficient of 1×16 antenna array with the impedance bandwidth 31.30–39 GHz. It shows that the profile dual-array antenna system with a compact feed mechanism is a good candidate to achieve broad bandwidth. There is no evident influence looks on antenna performance from simulated and measured results.

Figure 7 shows the measured and simulated antenna gains of the proposed dual-array antenna system for the entire bandwidth. It is clear that the gain slightly drops for the entire bandwidth. A little discrimination is observed between simulated and measured results due to the high-frequency mm-Wave connector and soldering effect.

IV. CONCLUSION

This paper presents a design of dual-array antenna system with compact feed network. The profile antenna array structure is based on a series feed mechanism for a tight planar configuration, easy fabrication, and broad bandwidth. It is applicable to where compact size is required. Both arrays can be operated for two different applications within the operational band for same or different center frequencies for cellular, IoT, and different broadcast mm-Wave applications. This makes the proposed dual-array antenna system a good candidate for 5G mm-Wave multi-wireless applications. It may further be enhanced for phased antenna array cellular applications. A good agreement between measured and simulated results makes this profile dual-array antenna structure suitable for mm-Wave 5G multi-wireless applications.

ACKNOWLEDGMENT

This paper is supported by National Science Foundation of China under Grant 62071003, Grant 41874174, Grant 61901004, and Grant 61801194, the Opening Foundation of National Key Laboratory of Electromagnetic Environment under Grant 201802003, the fund for key Laboratory of Electromagnetic scattering under Grant 61424090107, and the Natural Science Foundation of Anhui Province under Grant 2008085MF186.

REFERENCES

[1] I. Syrytsin, S. Zhang, G. F. Pedersen, and A. Morris, “Compact quad-mode planar phased array with

wideband for 5G mobile terminals," *IEEE Transactions on Antennas and Propagation*, vol. 66, no. 9, pp. 4648-4657, Sep. 2018.

[2] W. Roh, J. Y. Seol, J. Park, B. Lee, J. Lee, Y. Kim, J. Cho, K. Cheun, and F. Aryanfar, "Millimeter-wave beam forming as an enabling technology for 5G cellular communications: theoretical feasibility and prototype results," *IEEE Commun. Mag*., vol. 52, pp. 106-113, Feb. 2014.

[3] M. S. Sharawi, M. Ikram, and A. Shamim, "A two concentric slot loop based connected array MIMO antenna system for 4G/5G terminals," in *IEEE Transactions on Antennas and Propagation*, vol. 65, no. 12, pp. 6679-6686, Dec. 2017, doi: 10.1109/TAP.2017.2671028.

[4] S. J. Nawaz, N. M. Khan, M. N. Patwary, and M. Moniri, "Effect of directional antenna on the doppler spectrum in 3-D mobile radio propagation environment," *IEEE Trans. Veh. Technol*., vol. 60, no. 7, pp. 2895-2903, 2011.

[5] T. Manabe, Y. Miura, and T. Ihara, "Effects of antenna directivity and polarization on indoor multipath propagation characteristics at 60 GHz," *IEEE Journal on Selected Areas in Communications*, vol. 14, pp. 441-448, Apr. 1996.

[6] Y. Azar, G. N. Wong, K. Wang, R. Mayzus, J. K. Schulz, H. Zhao, F. Gutierrez, D. Hwang, and T. S. Rappaport, "28 GHz propagation measurements for outdoor cellular communications using steerable beam antennas in New York city," *IEEE International Conference on Communications (ICC)*, pp. 5143-5147, 2013.

[7] J. G. Andrews, S. Buzzi, W. Choi, S. V. Hanly, A. Lozano, A. C. K. Soong, and J. C. Zhang, "What will 5G be?," *IEEE Journal on Selected Areas in Communications*, vol. 32, no. 6, pp. 1065-1082, Jun. 2014.

[8] H. A. Diawuo and Y. Jung, "Broadband proximity-coupled microstrip planar antenna array for 5G cellular applications," in *IEEE Antennas and Wireless Propagation Letters*, vol. 17, no. 7, pp. 1286-1290, July 2018, doi: 10.1109/LAWP.2018.2842242.

[9] S. X. Ta, H. Choo, and I. Park, "Broadband printed-dipole antenna and its arrays for 5G applications," in *IEEE Antennas and Wireless Propagation Letters*, vol. 16, pp. 2183-2186, 2017, doi: 10.1109/LAWP.2017.2703850.

[10] Y. Li and K.-M. Luk, "Wide band perforated dense dielectric patch antenna array for millimeter-wave applications," *IEEE Trans. Antennas Propag*., vol. 63, no. 8, pp. 3780-3786, Aug. 2015.

[11] Y. Li and K.-M. Luk, "Low-cost high-gain and broadband substrate integrated-waveguide-fed patch antenna array for 60-GHz band," *IEEE Trans. Antennas Propag*., vol. 62, no. 11, pp. 5531-5538, Nov. 2014.

[12] Q. Zhu, K.-B. Ng, and C. H. Chan, "Printed circularly polarized spiral antenna array for millimeter-wave applications," *IEEE Trans. Antennas Propag*., vol. 65, no. 2, pp. 636-643, Feb. 2017.

[13] Y. Li and K.-M. Luk, "60-GHz substrate integrated waveguide fed cavity backed aperture-coupled micro strip patch antenna arrays," *IEEE Trans. Antennas Propag*., vol. 63, no. 3, pp. 1075-1085, Mar. 2015.

[14] H. Jin, W. Che, K. S. Chin, W. Yang, and Q. Xue, "Millimeter-wave TE20 mode SIW dual-slot-fed patch antenna array with a compact differential feeding network," *IEEE Trans. Antennas Propag*., vol. 66, no. 1, pp. 456-461, Jan. 2018.

[15] Y. Li and K.-M. Luk, "60-GHz dual-polarized two-dimensional switch beam wideband antenna array of aperture-coupled magneto-electric dipoles," *IEEE Trans. Antennas Propag*., vol. 64, no. 2, pp. 554-563, 2016.

[16] J. Xu, Z. N. Chen, X. Qing, and W. Hong, "Bandwidth enhancement for a 60 GHz substrate integrated waveguide fed cavity array antenna on LTCC," *IEEE Trans. Antennas Propag*., vol. 59, no. 3, pp. 826-832, Mar. 2011.

[17] W. Yang, H. Wang, W. Che, Y. Huang, and J. Wang, "High-gain and low-loss millimeter-wave LTCC antenna array using artificial magnetic conductor structure," *IEEE Trans. Antennas Propag*., vol. 63, no. 1, pp. 390-395, Jan. 2015.

[18] J. Xu, Z. N. Chen, X. Qing, and W. Hong, "140-GHz TE20-mode dielectric-loaded SIW slot antenna array in LTCC," *IEEE Trans. Antennas Propag*., vol. 61, no. 4, pp. 1784-1793, Apr. 2013.

[19] H. Jin, W. Che, K. S. Chin, G. Shen, W. Yang, and Q. Xue, "60-GHz LTCC differential-fed patch antenna array with high gain by using soft-surface structures," *IEEE Trans. Antennas Propag*., vol. 65, no. 1, pp. 206-216, 2017.

[20] B. Cao, H. Wang, Y. Huang, and J. Zheng, "High-gain L-probe excited substrate integrated cavity antenna array with LTCC-based gap waveguide feeding network for W-band application," *IEEE Trans. Antennas Propag*., vol. 63, no. 12, pp. 5465-5474, Dec. 2015.

[21] J. Xu, Z. N. Chen, X. Qing, and W. Hong, "140-GHz planar broadband LTCC SIW slot antenna

array," *IEEE Trans. Antennas Propag*., vol. 60, no. 6, pp. 3025-3028, Jun. 2012.

[22] X. Li, J. Xiao, Z. Qi, and H. Zhu, "Broadband and high-gain SIW-fed antenna array for 5G applications," in *IEEE Access*, vol. 6, pp. 56282-56289, 2018, doi: 10.1109/ACCESS.2018.2873392.

[23] H. A. Diawuo and Y. Jung, "Broadband proximity-coupled microstrip planar antenna array for 5G cellular applications," in *IEEE Antennas and Wireless Propagation Letters*, vol. 17, no. 7, pp. 1286-1290, July 2018, doi: 10.1109/LAWP.2018.2842242.

[24] S. Zhu, H. Liu, Z. Chen, and P. Wen, "A compact gain-enhanced vivaldi antenna array with suppressed mutual coupling for 5G mmWave application," in *IEEE Antennas and Wireless Propagation Letters*, vol. 17, no. 5, pp. 776-779, May 2018, doi: 10.1109/LAWP.2018.2816038.

[25] R. Garg, *Microstrip Antenna Design Handbook,* Reading, MA: Artech House, Boston, 2011.

[26] C. A. Balanis, *Antenna Theory: Analysis and Design*, Third Edition, John Wiley & Sons, Inc., Publication, New Jersey, 2005.

Hafiz Usman Tahseen was born in 1983 in Pakistan. He completed his graduation and then Masters in Electronic Engineering in 2017 from University of Engineering and Technology Lahore, Pakistan. He further completed his Ph.D. in Communication Engineering in 2021 from Jiangsu University, China. He is now with the School of Computer Science and Communication Engineering, Jiangsu University, China.

Lixia Yang born in Ezhou, Hubei, China, in 1975. He received his B.S. degree in Physics from Hubei University, Wuhan, China, in 1997, and Ph.D. degree in Radiophysics from Xidian University, Xi'an, China, in 2007. Since 2010, he has been an Associate Professor with the Communication Engineering Department, Jiangsu University. During 2010–2011, he was a Postdoctoral Research Fellow with the Electro Science Laboratory (ESL), The Ohio State University. During 2015–2016, he was a Visiting Scholar with the Institute of Space Science, The University of Texas, Dallas, TX, USA. Since 2016, he has been a Professor, a Ph.D. Supervisor, and the Chairman of the Communication Engineering Department, Jiangsu University. He is the author of a book and more than 100 articles, and has more than 10 inventions in his name. He holds four patents. His research interests include wireless communication technique, radio sciences, computational electromagnetics, and the antenna theory and design in wireless communication systems. He is a member of the Editor Board of Radio Science Journal in China.

Dual-band (28/38 GHz) Yagi–Uda Antenna with Corrugated Radiator and Triangular Reflectors for 5G Mobile Phones

Asmaa E. Farahat and Khalid F. A. Hussein

Microwave Engineering Department
Electronics Research Institute, Cairo, 11843, Egypt
e_asma_e@yahoo.com, Khalid_elgabaly@yahoo.com

Abstract – A novel printed design of a Yagi–Uda antenna is introduced for dual-band operation at 28/38 GHz. A corrugated strip dipole with a capacitively end-coupled extension strip is employed as the driven element. The proposed antenna has two triangular-shaped reflectors and one director. The driven dipole is fed through a coaxial feed line constructed as three unequal length transition strips. A four-port MIMO antenna system constructed using the proposed Yagi–Uda is suggested for mobile phones. CST® simulator is used to study the effect of the different design parameters on the antenna gain and the operating bands. Numerical and experimental investigations are achieved to assess the performance of both the single-element antenna and the four-port MIMO antenna system. It is shown that the simulation results agree with the experimental measurements and both show good performance of the single antenna as well as the MIMO antenna system. The bandwidths achieved around 28 GHz and 38 GHz are about 4 GHz and 1.4 GHz, respectively. The gain of the antenna is about 9 and 10 dB at 28 and 38 GHz, respectively. The four-antenna configuration shows radiation pattern diversity required for MIMO system. The envelope correlation coefficient (ECC) and the diversity gain (DG) are calculated and the results show that the proposed MIMO antenna system is suitable for the forthcoming 5G mobile communications.

Index Terms – MIMO, Yagi–Uda, spatial diversity.

I. INTRODUCTION

It has been recently reported that mm-wave in the 28 GHz and 38 GHz frequency bands can be used in wireless cellular communication systems [1]. The future fifth generation (5G) applications require higher bandwidths for higher data rates provided by the millimeter wave bands [2]. However, as the operating frequency increases, the wavelength of the signal becomes shorter and consequently the free-space path loss is higher, according to Friis transmission equation [3], [4]. Thus, high-gain antennas may be needed to compensate for the large free-space path losses and various forms of fading that can be observed in the communication channel [5], [6]. MIMO antenna system can offer advantages when considering multipath effects. The combination of both high gain and MIMO configurations can provide some novel antenna and circuit solutions for mobile communication applications at mm-wave frequencies. This can minimize the operating costs of any supporting power amplifiers and other control circuitry [7].

The frequency spectrum around 28 GHz, 38 GHz, 60 GHz, and 73 GHz are estimated bands under consideration for 5G technology. These millimeter wave bands would bring new challenges in the implementation of MIMO antennas for handheld devices [8]. With the fast development of the industry of wireless communication, there is an increase in the demand of multiband and highly isolated MIMO antennas for terminal users of cellular networks. Various dual-band MIMO antennas have been reported in literature. In [8], a 4×4 28/38 dual-band MIMO antenna system employing a round patch EBG Cell is introduced with low mutual coupling at both bands even at a close distance of 0.7 mm. In [9], a linear array of dual band 28/38 GHz Yagi–Uda antennas for 5G mobile MIMO systems is introduced. In [10], a dual-band MIMO antenna system composed of two orthogonal elements operating in the frequency bands 1.62–3.2 GHz and 4.4–5.9 GHz. In [11], a 28/38 dual-band slotted rectangular patch antenna with proximity coupled feed was built on a multilayer substrate of low-temperature co-fiber ceramics. The antenna achieves wide bandwidth of more than 4 GHz at both operating frequencies. In [12], a dual-band 28/45 circular microstrip patch antenna with an elliptical slot is presented with bandwidths of 1.3 GHz and 1 GHz at 28 GHz and 45 GHz, respectively. A circular radiating patch placed non-concentrically inside a circular slot etched off the ground plane is presented in [13], operating at 28 and 38 GHz bands.

Yagi–Uda antennas are good candidates for millimeter wave and microwave applications due to their high

Submitted On: February 27, 2020
Accepted On: July 6, 2021

https://doi.org/10.47037/2021.ACES.J.361009

gain, high efficiency, low-cost, and ease of fabrication. They are one of the most known endfire radiation pattern antennas that can achieve medium gain. In [14], a Yagi–Uda antenna operating at 24 GHz has been implemented in an 11-beam system using a planar array and a two-inch Teflon spherical lens. The use of Yagi–Uda for mm-wave applications has also been demonstrated in [15], where a corrugated ground plane is employed as a reflector to improve the gain for a linear antenna array operating at 60 GHz. A substrate-integrated waveguide Yagi–Uda antenna having the advantages of low profile and light weight was reported in [16]. A dual-band printed Yagi–Uda with enhanced reflectors to increase the gain is introduced in [17]. In [18], a modified Rotman lens feeding an antipodal Yagi–Uda antenna array is designed and fabricated for 5G wireless communications at the 28 GHz band. Other types of high-gain antennas are investigated in literature for mm-wave MIMO application. For example, the antenna proposed in [19] consisting of a substrate integrated waveguide (SIW) slot and two SIW grooves operating in the Ka-band with a gain of 9.5–11 dBi and good isolation in the frequency range 26.8–28.4 GHz, but this antenna occupies large space (39.8 mm × 33.4 mm) on the board.

This paper presents a compact printed dual-band Yagi–Uda MIMO antenna system for 5G mobile communication. The modified Yagi–Uda proposed design in this work can be very attractive for next generation wireless terminals due to its high gain, good wideband performance, and small form factor. Practically, the proposed MIMO antenna system can be integrated on the far top or bottom side corners of a mobile phone backplane, or positioned at the edges of the mobile chassis. The detailed literature review described above shows that the simple MIMO antenna design, as proposed in this paper, has not been investigated previously offering good integration, compact size, high gain, and simple fabrication for 5G mm-wave mobile handset applications.

II. THE PROPOSED DUAL-BAND YAGI–UDA ANTENNA

A. Design of the driven dipole, reflectors, and director

The present section describes the design of the proposed Yagi–Uda antenna. The antenna is fed through a microstrip line. A microstrip line to CPS line transition is employed. The length of a resonant free-standing dipole can be approximated,

$$L_o \approx 0.46 \times \lambda_o, \tag{1}$$

where, L_o is the free-standing dipole length, and λ_o is the free space wavelength. A dipole printed on a substrate's Rogers RO3003® with epsilon $\varepsilon = 3$ requires the dipole length to be modified as,

$$L = \frac{0.46 \times \lambda_o}{\sqrt{\frac{\in+1}{2}}}. \tag{2}$$

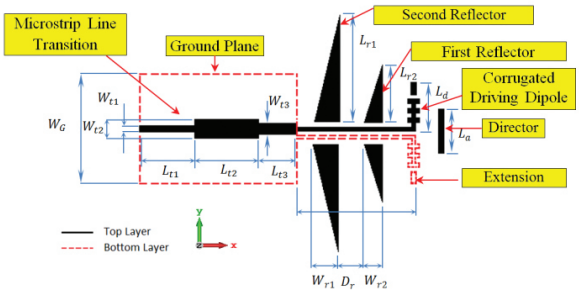

Fig. 1. Schematic of the proposed design for the Yagi–Uda antenna.

To get the printed dipole with dual resonant frequencies at 28 and 3 GHz, the value of λ_o in (1) is set to the free space wavelength corresponding to 38 GHz and then an extension strip is capacitively end-coupled to each of the dipole arms through an infinitesimal gap. The length of the strip and the gap are set so that the extended dipole structure has two resonances at 28 and 38 GHz. Each dipole arm has three equally spaced corrugations with dimensions set for good impedance matching. Two reflectors and one director are employed to enhance the antenna gain. The preliminary dimension of the director is 5% shorter than the driven dipole, while each reflector is 5% longer than the driven dipole. The accurate length of the director and the reflectors are set with the aid of electromagnetic simulation using the CST® simulator.

B. Design of the feeding balun

The feeding balun is composed of four stages. The first three stages are cascaded microstrip line regions with different lengths and widths designed for 50 Ω impedance matching. The fourth stage is parallel strip (twins) transmission line. One of the dipole arms and its extension strip are printed on the bottom layer of the substrate and connected to the ground plane. The geometry with indicated symbolic dimensional parameters of the proposed antenna is shown in Figure 1. The dotted red line denotes the borders of the printed regions on the back side of the substrate.

III. MIMO ANTENNA SYSTEM FOR MOBILE 5G PHONES

A MIMO antenna system is constructed using four elements of the proposed dual-band Yagi–Uda antennas operating in the 28/38 GHz bands for the forthcoming 5G mobile phones. The four antennas are suggested to be placed on the edges of a mobile phone as shown in Figure 2. The separations between the four antennas lead

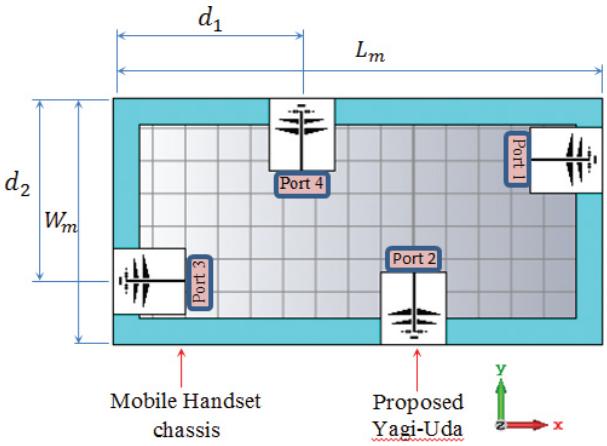

Fig. 2. The four-port MIMO antenna system proposed for 5G mobile phones.

to the spatial diversity required for the target 5G applications allowing high performance at high bit rates. The performance of the MIMO antenna system including the return loss at each antenna port and the coupling coefficients between the different ports is investigated. The radiation patterns produced when each port is excited alone are shown to be suitable for the pattern diversity scheme.

IV. RESULTS AND DISCUSSIONS

In this section, both the numerical results obtained by electromagnetic simulations and the experimental results obtained by microwave measurements for the fabricated prototypes of the single antenna and the MIMO antenna system are presented, discussed and compared. The presented results are concerned with investigating the return loss and radiation patterns of the single CPS- and MS-fed Yagi–Uda antenna. Also, the results are concerned with the coupling coefficients, the radiation patterns, and the diversity gain (and the corresponding envelope correlation coefficient) of the four-port MIMO antenna configuration.

A. Performance assessment of the proposed dual-band antenna

A.1 Return loss and bandwidth

The proposed Yagi–Uda antenna is designed on Rogers RO3003C® with dielectric constant $\varepsilon_r = 3$, dielectric loss tangent $\tan\delta = 0.0021$ and height $h = 0.25$ mm . The metal strips and ground are made of copper with conductivity $\sigma = 5.6 \times 10^7 \mathrm{S/m}$ and thickness t = 0.032 mm. The design parameters are listed in Table 1. The antenna is placed in the xy-plane with the feed line aligned with the x-axis. The dependency of the reflection coefficient, $|S_{11}|$, on the frequency over a wide band for the proposed dual-band Yagi–Uda antenna is presented in Figure 3. It is clear

Table 1: Dimensional parameters for the proposed Yagi–Uda antenna

Name	Value (mm)	Name	Value (mm)
L_a	2.4	W_{t1}	0.5
L_{t1}	3.62	L_{t2}	4.02
W_{r2}	1.0	D_r	1.95
L_{r2}	3.4	L_d	2.79
W_{t2}	0.62	W_{t3}	0.35
L_{t3}	2.5	W_{r1}	1.0
W_G	6.72	L_{r1}	7.6
L_{ext}	0.8	W_{ext}	0.2

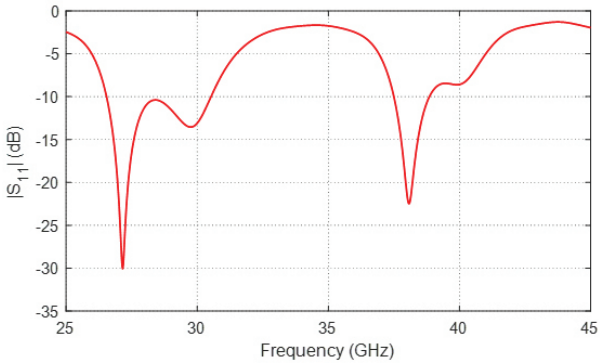

Fig. 3. The frequency responses of the reflection coefficients $|S_{11}|$ of the proposed CPS-fed and MS-fed Yagi–Uda antennas with the dimensional parameters listed in Table 1.

that the impedance is perfectly matched at the two frequencies 28 and 38 GHz. At 28 GHz, the band width is about 4 GHz $(26.5 - -30.5\ \mathrm{GHz})$, whereas at 38 GHz, the band width is about 1.5 GHz and can operate with matched impedance over the frequency range $(37.4 - -38.9\ \mathrm{GHz})$. The radiation efficiencies are 96% at 28 GHz and 84% at 38 GHz.

A.2. Radiation patterns

The normalized radiation patterns for the proposed dual-band Yagi–Uda antenna at 28 GHz and 38 GHz in the planes $\phi = 0^\circ\ (xz - plane)$ and $\theta = 90^\circ\ (xy - plane)$ are presented in Figures 4 (a) and 4 (b), respectively. The maximum gain is 8.84 dBi at 28 GHz and 9.97 dBi at 38 GHz. Such radiation patterns are proper for MIMO antenna system composed of multiple units of such dual-band radiating elements for pattern diversity schemes.

B. Parametric study for optimum design of the proposed antenna

The CST® simulator is used to study the effects of the geometric parameters of the proposed antenna presented in Figure 1 on the antenna performance. The purpose of the parametric study is to arrive at the optimum

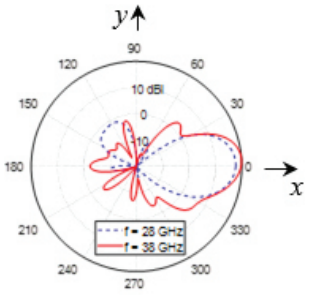

(a) $\theta = 90^{\circ}$ $(xy-plane)$

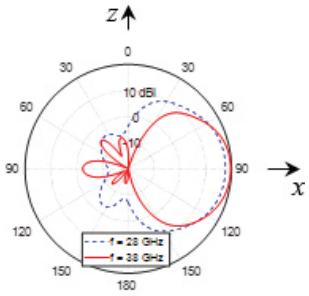

(b) $\phi = 0^{\circ}(xz-plane)$

Fig. 4. Gain patterns of the proposed dual-band antenna at 28 and 38 GHz in the $xy-$plane $(\phi = 0^{\circ})$ and $xz-$plane $(\theta = 90^{\circ})$.

design that gives good values of the reflection coefficient ($|S_{11}|$) such that $|S_{11}| \leq -10$ dB and to maximize the gain at the required operating frequencies 28/38 GHz.

B.1. Parametric study for optimum return loss

The most effective parameter that controls the input impedance of the proposed Yagi–Uda and, hence, the operating resonance frequencies is the dipole length L_d. The effect of L_d on the operating frequencies and bandwidth is illustrated in Figure 5. As shown in Figure 5, this parameter has significant effects on the resonant frequency as well as the value of $|S_{11}|$ at these resonances. It should be noted that the other dimensional parameters have the values given in Table 1. The value of $L_d = 2.8$ mm gives the best matching bandwidth at the required 28/38 GHz operating frequencies. The bandwidth at 28 and 38 GHz is about 4 and 1.5 GHz, respectively.

Another parameter that affects the value of the reflection coefficient at the resonance frequencies is the length of the extension strip L_{ext}. This extension strip is capacitively coupled to the dipole and acts as a capacitive impedance which improves the impedance matching at the operating frequencies. The dependence of the reflection coefficient on frequency for different lengths of the extension strip is presented in Figure 6.

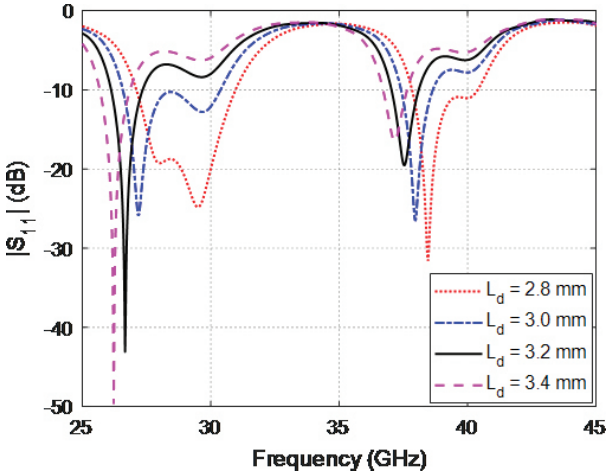

Fig. 5. Dependence of $|S_{11}|$ on the frequency for different values of the geometrical parameter L_d.

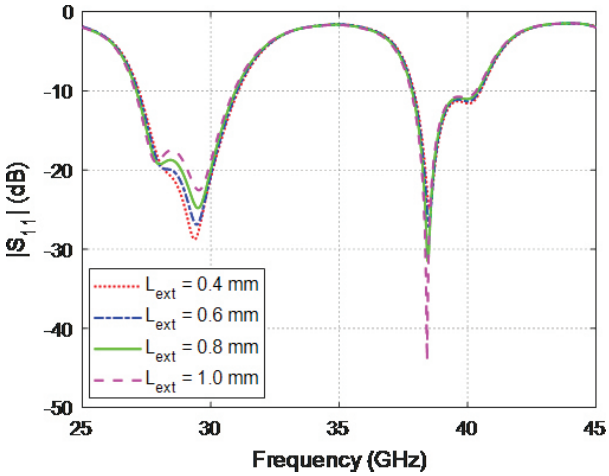

Fig. 6. Dependence of $|S_{11}|$ on the frequency for different values of the geometrical parameter L_{ext}.

B.2. Parametric study for optimum gain

The most important parameters which affect the gain of the antenna at the operating bands are the length L_{r1}, L_{r2} of the first and second reflectors, respectively, and their locations. Another parameter which controls the value of the gain is the length of the director L_a and its location. The dependence of the value of the gain in the forward direction (θ=90° *and* $\phi = 0^{\circ}$) on the location of the first reflector for different values of the reflector length is presented in Figure 5. The other design parameters are set according to the values in Table 1. The effect of the second reflector length and location on the gain is shown in Figure 6. The rest of the design parameters are as shown in Table 1.

The director length and where it is placed behind the antenna effect on the gain is studied for different director

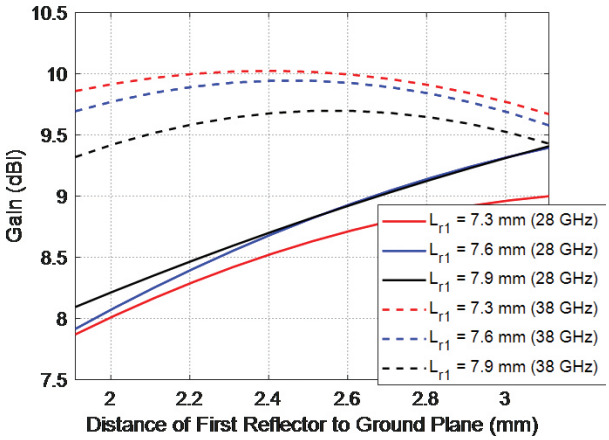

Fig. 7. Effect of the first reflector length and location on the gain at the two operating frequencies 28/38 GHz.

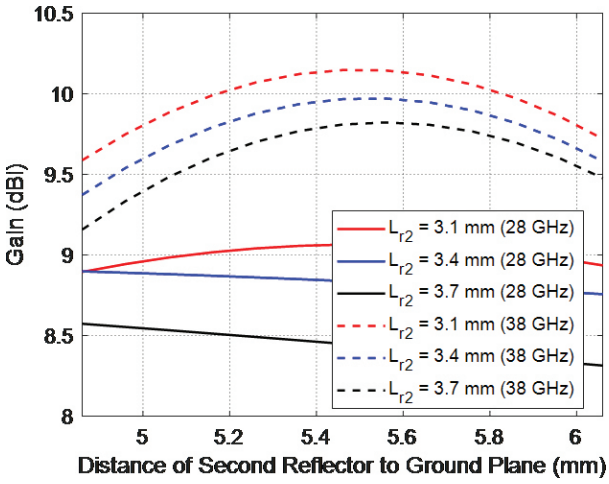

Fig. 8. Effect of the second reflector length and location on the value of the gain at both operating bands.

lengths and locations and presented in Figure 7. It is clear from Figures 5, 6, and 7, that there is an optimum location for placing each of the reflectors and the director to obtain the highest gain.

It is clear from the Figures 5 and 6 that the gain is almost linearly varying with the reflector length for the 38 GHz and has a peak at specific location for the 28 GHz. In Figure 7, the value of the gain by varying the director location is almost constant at 28 GHz, and has a peak value at certain location at 38 GHz.

C. Performance assessment of the proposed four-port MIMO antenna system

C.1. Impedance matching and coupling coefficients

A four-port MIMO antenna configuration mounted on a mobile phone chassis with dimensions $L_m = 150mm$ and $W_m = 75mm$, and separation distances between the

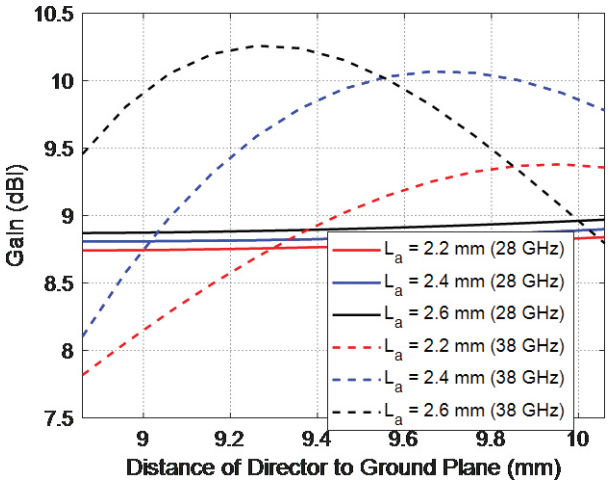

Fig. 9. Effect of the director length and location on the gain at the two operating frequencies 28/38 GHz.

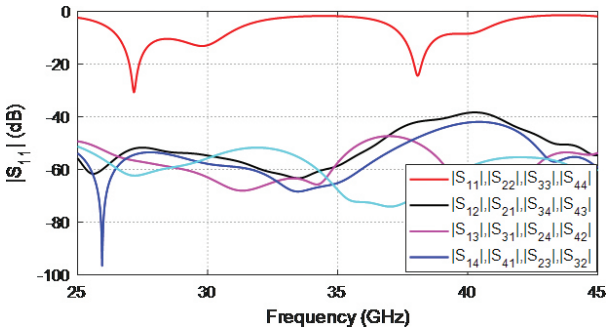

Fig. 10. Simulated frequency response of the reflection and transmission coefficient of the four-port Yagi–Uda MIMO antenna system.

antennas $d_1 = 58mm$ and $d_2 = 56mm$ as that shown in Figure 3 is studied. Each antenna is printed on a 0.25 mm Rogers RO3003® substrate with the dimensional parameters listed in Table 1. Figure 10 shows the dependence of the self and mutual scattering parameters on the frequency over a very wide band. It is shown that the reflection coefficients at the different antenna ports are almost identical and satisfy the impedance matching condition (low return loss $< -25dB$) over the lower and upper operational frequency bands which are centered at 28 and $38GHz$, respectively. On the other hand, the mutual scattering parameters show very weak coupling between the antenna ports, where all these coefficients are maintained below $-35dB$ over the entire frequency range.

C.2. Radiation patterns of the MIMO antenna system

The radiation patterns produced by the proposed MIMO antenna system when exciting each port alone are

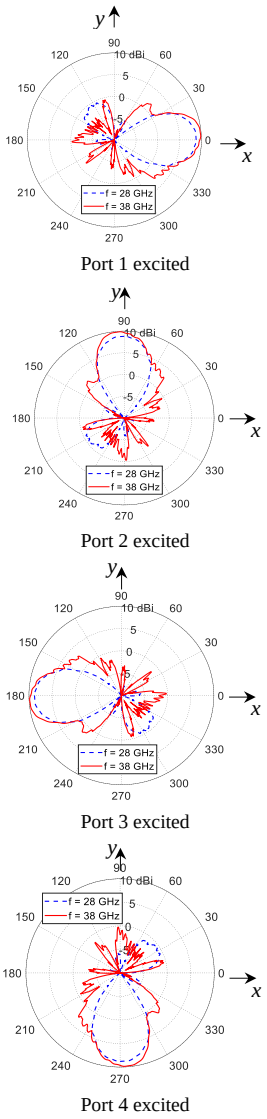

Fig. 11. Radiation patterns in the antenna plane for the four-port MIMO antenna using the proposed dual-band antenna at 28 and 38 GHz.

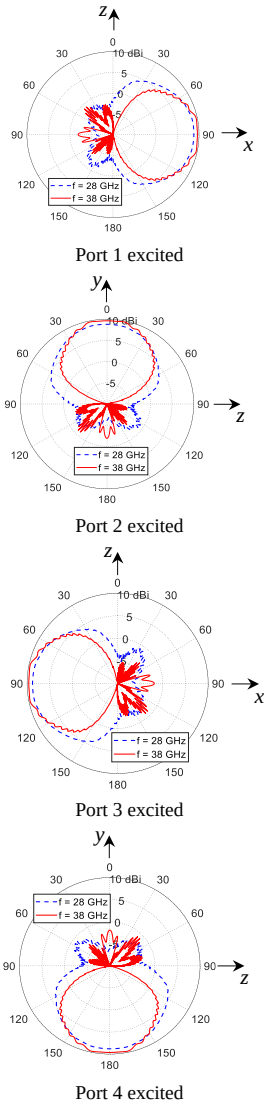

Fig. 12. Radiation patterns in the plane normal to the antenna plane for the four-port MIMO antenna using the proposed dual-band antenna at 28 and 38 GHz.

presented in Figures 11 and 12 at 28 and 38 GHz, where the radiation patterns are shown to satisfy the diversity required for the mobile phone MIMO systems. The maximum achieved gain at 28 GHz is about 8.9 dBi for both antenna 1 and antenna 3, and 9.05 dBi for antenna 2 and antenna 4. Whereas, the maximum gain at 38 GHz is about 9.78 dBi for both antenna 1 and antenna 3, and 9.89 dBi for antenna 2 and antenna 4. Besides the reasonable size of the MIMO antenna system and the fairly wide separations between the antennas that produce high-diversity gain, the obtained pattern diversity provides excellent solution for the forthcoming 5G mobile communication systems.

C.3. Envelope correlation coefficient and diversity gain of the four-port MIMO antenna system

The frequency responses of the envelope correlation coefficient (ECC) and the diversity gain (DG) of the proposed four-port MIMO antenna system are presented in Figure 13. It is shown that the ECC is almost 0 and, consequently, the DG is almost 10 over the lower and upper frequency bands (centered at 28 and 38 GHz), which is the best achievable performance for a MIMO antenna system.

D. MIMO antenna fabrication and experimental assessment

This section is concerned with the presentation and discussions of the experimental measurements of the

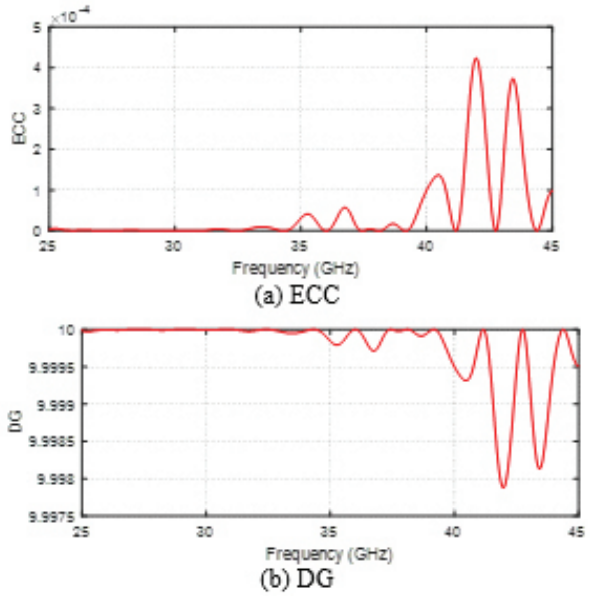

Fig. 13. Frequency dependence of the ECC and DG of the four-port MIMO antenna proposed in the present work.

dual-band Yagi–Uda antenna and the proposed MIMO antenna system whose simulation results are presented and discussed in the previous sections. Prototypes are fabricated for the single antenna as well as the four-port MIMO antenna system. To confirm the accuracy of the assessed performance for both the single antenna and the MIMO system, the measurement results are compared to those obtained by electromagnetic simulation using the commercially available CST® software package.

D.1. Fabrication and measurements of the single antenna prototype

D.1.1. Measurement of the return loss

A prototype of the proposed dual-band Yagi–Uda antenna is fabricated for experimental verification of the simulation results concerning the dependence of the reflection coefficient on the frequency and the radiation patterns. The substrate used for fabrication is Rogers RO3003®, with substrate height $h = 0.25mm$, dielectric constant $\varepsilon_r = 3$ and dielectric loss tangent $\delta = 0.0013$. The same design dimensions given in section 4.1.1 are used for the fabrication process. Top and bottom views of the fabricated prototype are presented in Figure 14. The 2.4 mm end launch connector from Southwest Microwave Inc. is used to measure the port performance of the prototype antenna shown in Figure 14 using the vector network analyzer (VNA) from Rohde and Schwartz model ZVA67. After performing the required settings and calibration procedure, antenna prototype under test is connected to the VNA as shown

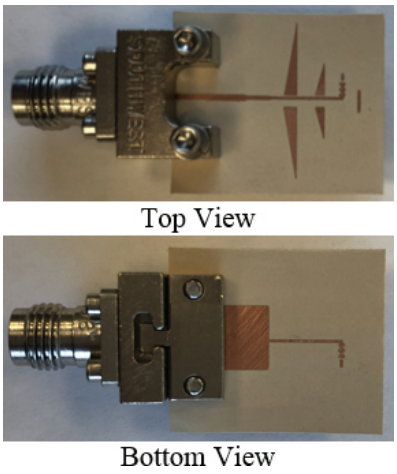

Fig. 14. Photograph of the fabricated prototype of the dual-band 28/38 GHz Yagi–Uda proposed for MIMO antenna systems of 5G mobile handsets.

in Figure 15 (a) and the return loss $|S_{11}|$ is measured. The result measurements are compared to that obtained by simulation using the CST® software package and plotted in Figure 15 (b) showing good agreement. The measurement results for $|S_{11}|$ show that the proposed antenna has an impedance matching bandwidth of about 2.7 GHz (27.5-30.2 GHz) for reflection coefficient <-10dB around the 28 GHz band, and 1.7 GHz (37.3-39 GHz) around the 38 GHz band.

D.1.2. Measurements of the radiation patterns and maximum gain

For experimental measurement of the radiation pattern of the fabricated dual-band antenna, the standard gain linear-polarized horn antenna model LB-018400 is used as a reference antenna and the experimental setup is made as shown in Figure 16. The measurements are performed in an anechoic chamber with the vector network analyzer Rohde and Schwartz model ZVA67. The distance between the reference antenna and the antenna under test is 60 cm. The radiation patterns are measured at 28 and 38 GHz in the two principal planes $x-z$ ($\phi = 0°$) and $x-y$ ($\theta = 90°$). The radiation patterns obtained through simulation and experimental measurements are presented in Figure 17 showing good agreement. The measured maximum gain is 8.7 dB at 28 GHz and 9.5 dB at 38 Ghz.

D.2. Fabrication and measurements of the MIMO antenna system

In this section, the proposed dual-band antenna is employed to construct a four-port MIMO antenna system mobile handset antenna mockup as shown in Figure 18. The mockup is constructed of a solid rectangle shape of dimensions $75 \times 150mm^2$ with four openings of the

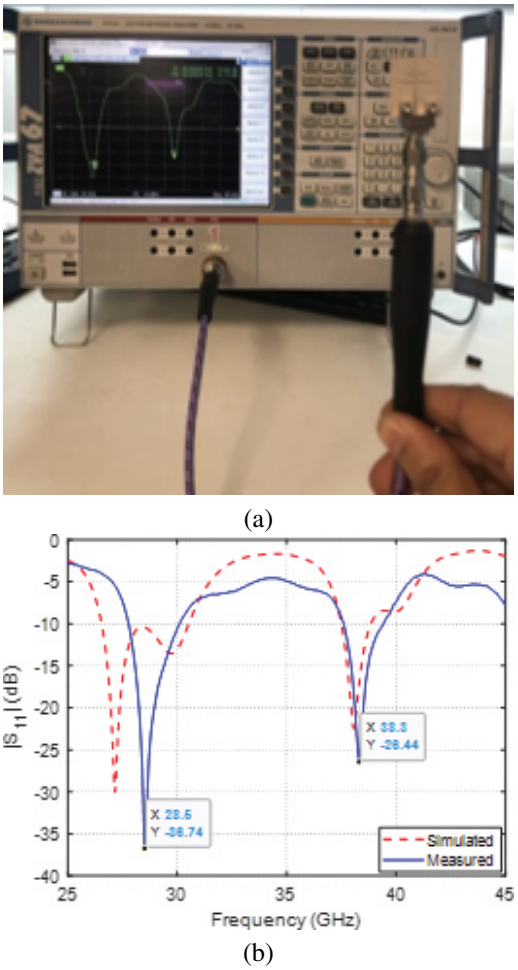

Fig. 15. (a) Experimental setup for measuring the return loss of the dual-band antenna. (b) Measured frequency response of the return loss of the dual-band antenna compared with the simulation results.

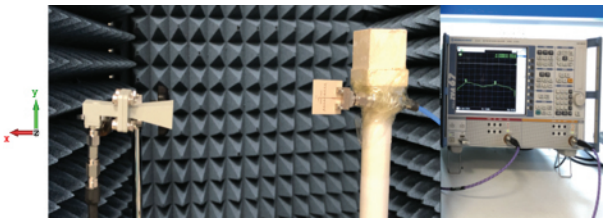

Fig. 16. Experimental setup for measuring the radiation pattern and gain of the dual-band antenna.

same size as the single antenna at the specified locations shown in Figure 3 with $d_1 = 58mm$ and $d_2 = 56mm$. The four-port MIMO antenna system mounted on the antenna mockup is shown in Figure 18. The 2.4 mm end launch connectors from Southwest Microwave Inc. are used for measuring the return loss of each antenna

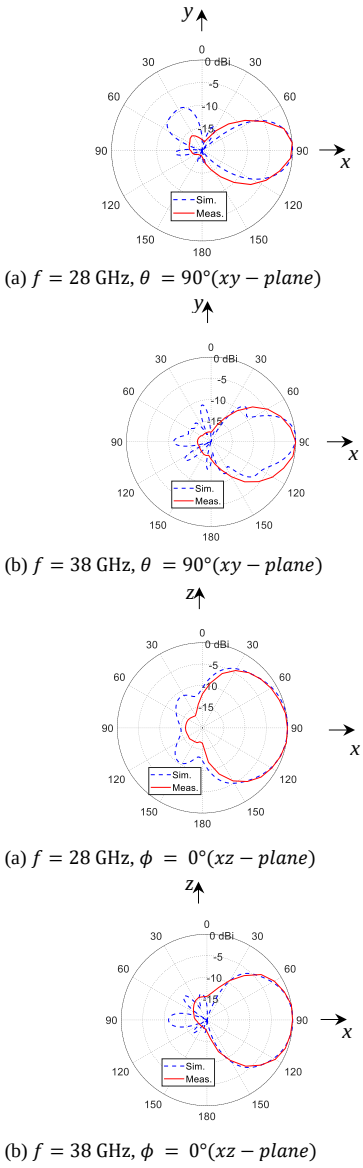

(a) $f = 28$ GHz, $\theta = 90°(xy-plane)$

(b) $f = 38$ GHz, $\theta = 90°(xy-plane)$

(a) $f = 28$ GHz, $\phi = 0°(xz-plane)$

(b) $f = 38$ GHz, $\phi = 0°(xz-plane)$

Fig. 17. Measured radiation patterns of the dual-band antenna compared with the simulation results.

and the mutual coupling between each antenna pair using the VNA Rhode & Schwartz model ZVA67. During the measurement process, 50Ω loads are connected to the elements not under test to avoid their effects. Figure 19 illustrates the measured return loss for each antenna in the frequency band 25-45 GHz. It is evident that the MIMO antenna system exhibits good impedance matching at both the operating frequencies 28 and 38 GHz. The mutual coupling coefficients are measured and plotted as shown in Figure 20. It is clear that the MIMO antenna system has very low mutual coupling <-38dB over the entire frequency range.

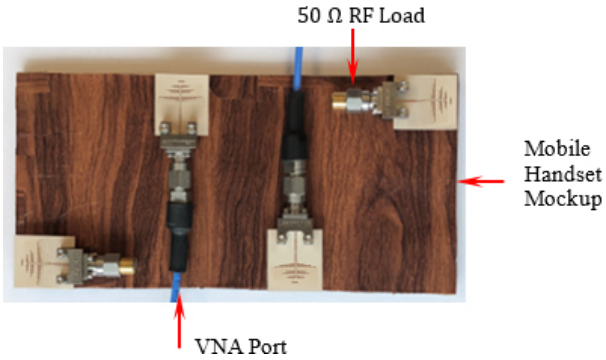

Fig. 18. Fabricated prototype for the four-port MIMO antenna system constructed on a mockup with four Yagi–Uda antennas arranged on the edges.

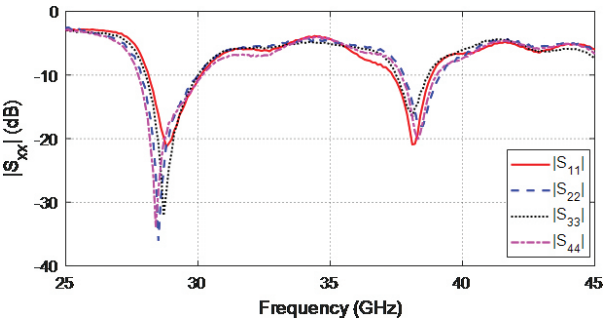

Fig. 19. Measured frequency response of the return loss of the four-port MIMO antenna system.

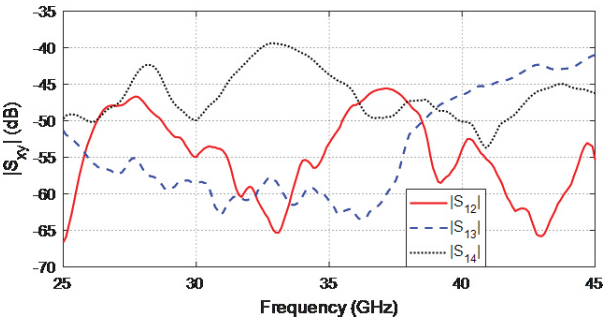

Fig. 20. Measured frequency response of the mutual coupling coefficient of the four-port MIMO antenna system.

V. CONCLUSIONS

An enhanced modified Yagi–Uda antenna design is introduced for the 28/38 GHz dual-band operation. The antenna is constructed from a driving corrugated dipole and a capacitively end-coupled extension strip with two reflectors and one director. A four-port MIMO antenna system for mobile handsets is constructed using the proposed Yagi–Uda. Numerical and experimental investigations are achieved to assess the performance of both the single antenna and the four-port MIMO antenna system. It is shown that the simulation results agree with the experimental measurements and both show good performance of the single antenna as well as the MIMO antenna system. The bandwidths achieved around 28GHz and 38GHz are about 4GHz and 1.5GHz, respectively. The four-antenna configuration shows radiation pattern diversity which is required for MIMO system operation. The calculated envelope correlation coefficient (ECC) and diversity gain (DG) show that the proposed MIMO antenna system can serve as a mobile phone antenna.

REFERENCES

[1] T. S. Rappaport, S. Sun, R. Mayzus, H. Zhao, Y. Azar, K. Wang, G. N. Wong, J. K. Schulz, M. Samimi, and F. Gutierrez, "Millimeter wave mobile communications for 5G cellular: it will work!," *IEEE Access*, vol. 1, pp. 335-349, 2013.

[2] T. S. Rappaport, F. Gutierrez, E. Ben-Dor, J. N. Murdock, Y. Qiao, and J. I. Tamir, "Broadband millimeter-wave propagation measurements and models using adaptive-beam antennas for outdoor urban cellular communications," *IEEE Trans. Antennas Propag.*, vol. 61, no. 4, pp. 1850-1859, 2013.

[3] C. Narayan, *Antennas and Propagation*. Technical Publications, 2007.

[4] A. V. Alejos, M. G. Sanchez, and I. Cuinas, "Measurement and analysis of propagation mechanisms at 40 ghz: viability of site shielding forced by obstacles," *IEEE Trans. Veh. Technol.*, vol. 57, no. 6, pp. 3369-3380, 2008.

[5] S. Rajagopal, S. Abu-Surra, Z. Pi, and F. Khan, "Antenna array design for multi-gbps mm wave mobile broadband communication," in *Global Telecommunications Conference (GLOBECOM). IEEE*, pp. 1-6, 2011.

[6] A. I. Sulyman, A. T. Nassar, M. K. Samimi, G. R. MacCartney, T. S. Rappaport, and A. Alsanie, "Radio propagation path loss models for 5G cellular networks in the 28 GHz and 38 GHz millimeterwave bands," *IEEE Communications Magazine*, vol. 52, pp. 78-86, 2014.

[7] M. S. Sharawi, S. K. Podilchak, M. T. Hussain, and Y. M. M. Antar, "Dielectric resonator based MIMO antenna system enabling millimeter-wave mobile devices," *IET Microwaves, Antennas & Propagation*, pp. 287-293, 2017.

[8] D. T. T. Tu, N. G. Thang, and N. T. Ngoc, "28/38 GHz dual-band MIMO antenna with low mutual coupling using novel round patch EBG cell

for 5G applications," *International Conference on Advanced Technologies for Communications*, 2017.

[9] A. E. Farahat and K. F. A. Hussein, "Dual-band (28/38 GHz) MIMO antenna system for 5G mobile communications with efficient DoA estimation algorithm in noisy channels," *Applied Computational Electromagnetics Society (ACES) Journal*, vol. 36, no. 3, Mar. 2021.

[10] J.-F. Li and Q.-X. Chu "A compact dual-band MIMO antenna of mobile phone," *J. of Electromagn. Waves and Appl.*, vol. 25, pp. 1577-1586, 2011.

[11] M. M. Amin, M. Mansor, N. Misran, and M. Islam, "28/38 GHz dual band slotted patch antenna with proximity-coupled feed for 5G communication," *2017 International Symposium on Antenna and Propagation (ISAP)*, pp. 1-2, 2017.

[12] M. I. Khattak, A. Sohail, U. Khan, Z. Barki, and G. Witjaksono, "Elliptical slot circular patch antenna array with dual band behavior for future 5G mobile communication networks," *Progress In Electromagnetics Research C*, vol. 89, pp. 133-147, 2019.

[13] O. M. Haraz, M. M. M. Ali, S. Alshebeili, and A.-R. Sebak, "Design of a 28/38 GHz dual-band printed slot antenna for the future 5G mobile communication networks," *The 2015 IEEE AP-S Symposium on Antennas and Propagation and URSI CNC/USNC Joint Meeting*, 2015.

[14] P. R. Grajek, B. Schoenlinner, and G. M. Rebeiz, "A 24-GHz high-gain Yagi-Uda antenna array," *IEEE Trans. Antennas Propag.*, vol. 52, pp. 1257-1261, May 2004.

[15] S. X. Ta, S.-g. Kang, J. J. Han, and I. Park, "High-efficiency, high-gain, broadband quasi-yagi antenna and its array for 60-GHz wireless communications," *Journal of Electromagnetic Engineering and Science*, vol. 13, no. 3, pp. 178-185, Sep. 2013.

[16] X. Y. Wu and P. S. Hall, "Substrate integrated waveguide Yagi-Uda antenna," *Electronics Letters*, vol. 46, no. 23, pp. 1541-1542, Nov. 2010.

[17] A. E. Farahat and K. F. A. Hussein, "28/38 GHz dual-band Yagi-Uda antenna with corrugated radiator and enhanced reflectors for 5G MIMO antenna systems," *Progress In Electromagnetics Research*, vol. 101, pp. 159-172, 2020.

[18] M. R. Naeini and M. Fakharzadeh, "A 28 GHz beam-switching Yagi-Uda array using rotman lens for 5G wireless communications," *International Symposium on Antennas and Propagation & USNC/URSI National Radio Science*, 2017.

[19] M. Lin, P. Liu, and Z. Guo, "Gain-enhanced Ka-band MIMO antennas based on the SIW corrugated technique," *IEEE Antennas Wirel. Propag. Lett.*, vol. 16, pp. 3084-3087, 2017.

Asmaa E. Farahat received her B.Sc. and M.Sc. in the Department of Biomedical Engineering, Faculty of Engineering, Cairo University, 2002 and 2006, respectively. She received the PhD in 2012, Ain Shams University. She is currently associate professor at the Department of Microwave Engineering at the Electronics Research Institute. She has work experience in scientific research for about 17 years. She has published more than 28 papers in international, regional, and local scientific journals and conferences. She has worked as secondary investigator for three research projects. Her research interests are in the areas of antennas, electromagnetic wave propagation, risk assessment of human exposure to microwave radiation, remote sensing systems, and radar systems.

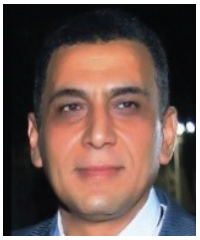

Khalid F.A. Hussein received his B.Sc., M.Sc., and Ph.D. degrees in the Department of Electronics and Electrical Communications, Faculty of Engineering, Cairo University, 1990, 1995, and 2001, respectively. He is currently a professor at the Department of Microwave Engineering at the Electronics Research Institute. He has work experience in scientific research for more than 30 years. He has more than 20 years' experience in teaching in engineering colleges under many universities. He has supervised more than 70 doctoral and master theses. He has published more than 100 papers in international, regional, and local scientific journals and conferences. He has served as the Head of Microwave Engineering Department at the Electronics Research Institute for up to four years. He has been a Member of the Egyptian Space Program (currently the Egyptian Space Agency) for more than eight years. He has worked as Principal Investigator for four research projects and Head of Research Group in four other research projects. He designed and implemented several satellite antennas between prototypes and finished products. He has provided scientific consultations and conducted field measurements related to the design and distribution of mobile communication base station antennas for good signal coverage in behalf of many Egyptian and international companies. His research interests are in the areas of antennas, electromagnetic wave propagation, risk assessment of human exposure to microwave radiation, optical communications, photonics, quantum computing, radar systems, particularly ground penetrating radar (GPR), synthetic aperture radar (SAR), and remote sensing systems.

Possible Leaky Wave Antennas for Propagation Therapy using SAR Analysis

Masoud Sarabi and Warren F. Perger

Department of Electrical & Computer Engineering
Michigan Technological University, Houghton, 49931, USA
msarabi@mtu.edu, wfp@mtu.edu

Abstract **–** This paper presents an overview of design and functionality of three novel leaky wave antennas (LWAs) that are proposed as a possible hyperthermia system using LWA logic. LWAs are best known for their interesting property of frequency scanning. This makes them appealing for beam steering applications such as biomedical hyperthermia and radar applications. Regarding the biomedical hyperthermia application, the property of beam scanning could be used for treatment of tumors found in different regions and depths of a given tissue. The proposed antennas are as follows: (1) mushroom-typed leaky wave antenna, (2) two-dimensionally (2D) periodically slotted leaky wave antenna, (3) belt-shaped leaky wave antenna. Each antenna provides distinguished advantages for hyperthermia therapy which will be discussed in the corresponding sections. For example, the belt-shaped leaky wave antenna is a conformal antenna that could follow the cylindrical shape of the patient's neck and focus the electromagnetic beam on the neck tumors. Two-dimensional LWAs such as mushroom-typed leaky wave antennas provide more beam steering flexibility compared to 1D types such as 1D slotted leaky wave antennas.

Index Terms **–** hyperthermia, leaky wave antenna (LWA), mushroom-typed leaky wave antenna, 2D periodically slotted leaky wave antenna, belt-shaped leaky wave antenna.

I. INTRODUCTION

A promising therapeutic treatment for dealing with cancerous tumors, is a nonsurgical modality known as hyperthermia. Hyperthermia can be applied to a human body tissue in which the electromagnetic radiation of the near field of an antenna or applicator is exposed to that tissue and elevates the temperature of it. Hyperthermia is applied to a target tissue such that the regions other than the cancerous ones are not affected by this radiation and thus no temperature elevation should happen in the surrounding healthy regions [1, 2]. Hyperthermia is not necessarily the final treatment for cancerous tumors but could be used in combination with other treatment methods such as chemotherapy to achieve the best results [3, 4]. Hyperthermia has two types: superficial hyperthermia (SHT) and deep hyperthermia (DHT). SHT is usually used for the tumors that are found in depths of about 4 cm or less and DHT is used for tumors that are situated in regions deeper than 4 cm. Usually the frequency ranges that are used for SHT are about 915 MHz or 2.45 GHz for US and 434 MHz for Europe and Japan [5]. The efficient temperature elevation for hyperthermia treatment is between $40^{\circ}C - 45^{\circ}C$. The metabolism and the blood flow of the malignant cells are different from the normal cells and they are more vulnerable to temperature elevation. Different antenna types and beam focusing methods have been proposed in the corresponding literature. The treatment efficiency of each antenna or applicator depends on the dimensions of a tumor, depth of the tumor, size, and the intrinsic characteristics of the tissue such as conductivity. For superficial tumors, microstrip patch antennas have been used while for deep-seated tumors slot antennas have been proposed to be inserted into a tissue since for such tumors, heat needs to be transferred to the tissue depth [4]. In [8], a microwave hyperthermia system using a coaxial-slot antenna in both single and array forms has been introduced. The single antenna was used to treat a shallow tumor in the right shoulder area of a 60-year-old patient and the array applicator was used for the treatment of a tumor in the right shoulder region of a 61-year-old patient. Another literature [9] proposes a balun-free helical antenna with two different matching systems of quarter-wave network and also a Π-network. This system was tested upon a bovine liver tissue using the input power of 42W for a time length of 5–10 minutes. Another design has been introduced in our earlier work [10] that proposes a substrate integrated waveguide LWA for hyperthermia functionality in frequency range of 13.8–15.2 GHz which is capable of addressing superficial cancerous tumors. Antenna arrays are typically used to illuminate the beam on a tissue with higher focusing capability compared to single-antenna systems. A promising application of antenna arrays has been in imaging of the leukemia, breast cancer [17]-[42], and cardiac anomalies [43, 44]. For example,

Submitted On: March 26, 2021
Accepted On: September 26, 2021

https://doi.org/10.47037/2021.ACES.J.361010

[2] introduces a hexagonal focused array that operates at 433 MHz. In this design, there is an array of patch antennas located on each side of the hexagon and the sample bio-tissue is placed at the center of this structure to be heated up. In [3], a SIGMA-Eye applicator array has been designed. The applicator system consists of three rings of dipole antennas. The best performance with this applicator array has been observed when all the antennas were in phase and fed with the same power. In [4], the authors have introduced two types of antennas that both function at the frequency of 2.45 GHz. Usually, in order to treat malignant tumors that are in-depth, antenna arrays are used. Lower working frequencies such as 915 MHz could provide a considerable heat penetration. In order to avoid having superficial skin burns, a water bolus is basically used that is placed between the antenna system and the tissue [5]. Some designs are introduced to have hyperthermia treatment for a specific part of the body. For example, in [6], a patch antenna design is used as a phased-array head and neck applicator. Based on [7] and [8] the most optimal configuration for head and neck hyperthermia is a circular array, and in [6] the same setup is used that consists of 12 antennas. This paper is organized as follows: in section II, we are going to discuss the proposed antenna structures and evaluation of their electromagnetic performances such as propagation patterns and return loss. In section III the specific absorption ratio (SAR) mechanism and heating methodology will be discussed. Section IV will contain the results and discussion, and the conclusion will be given in section V.

The state-of-the-art hyperthermia solutions use antenna arrays which have higher complexities and higher manufacture cost, while in the present work, we have proposed simple and cheap solutions for hyperthermia therapy. The design and methodology of each antenna system will be explained in the corresponding sections but in short, we have focused on planar antennas with different feeding mechanisms and structural topology which would offer diverse hyperthermia treatment depending on the geometry of the focused beams on tissue. In each study, the antenna has been designed using CST software and after calculation of the propagation patterns, return loss and power loss density, finally the SAR on a slice of tissue has been calculated. The biotissue has been selected from the library of materials in CST Software and the slice has been placed in close proximity to each antenna, while this whole antenna-tissue set has been considered as a closed thermal system for thermal simulations. Finally, all the SAR maps have been analyzed using a developed MATLAB code and comparisons regarding the geometry of the heated tissue regions and the corresponding areas have been summarized in tables.

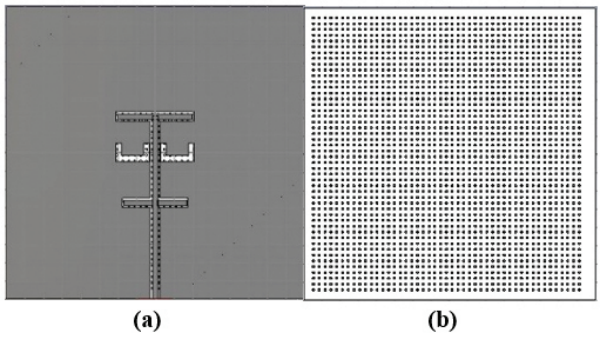

Fig. 1. The structure of 2D mushroom-type leaky wave antenna: (a) back side, (b) front side.

II. ANTENNA STRUCTURES AND PERFORMANCE

In the following sections A, B, and C, we will introduce three antennae. For each antenna, the main features such as return loss, propagation patterns, and directivity will be discussed. The functionality of each antenna as a candidate hyperthermia system will be investigated using SAR analysis results and the comparison with internationally accepted SAR values for biomedical instruments as a numerical validation tool for each antenna system. Investigation of the SAR results illuminate at which frequency points each antenna system tends to generate focal beams and at which frequencies wider areas of biotissues can be affected by heat. It is significant to have an estimate of the dimensions of the tissue areas affected by temperature elevation, which is calculated in mm^2 using MATLAB as discussed in section IV.

A. 2D mushroom-type leaky wave antenna

The mushroom-type leaky wave antenna is composed of a ground plane of a perfect electric conductor (PEC) with dimensions 159.7 mm $\times$ 159.7 mm, a substrate of TMM 10i with permittivity of $\varepsilon_r = 9.8$, the same planar dimensions as the ground plane and the thickness of H_s = 1.7 mm. There are 47 by 48 square cells that are each connected to the ground plane by via. The ground plane has two U-shaped slots and a microstrip line. This antenna is fed through the ground plane using an aperture coupling feed mechanism. The excitation signal of the antenna is a default gaussian signal used in CST Microwave Studio software within the frequency range of $f = 2$ GHz to $f = 4$ GHz. The benefit of the aperture coupling feed is that it minimizes the spurious radiation. The advantage of the rectangular PEC cells is that they form a mushroom structure which suppresses surface waves and hence improves the radiation.

As we can see on Figure 2 (a), there are several beams with directivity of about 5.44 dBi at f = 2.5 GHz. The return loss graph on Figure 2 (b), illustrates three

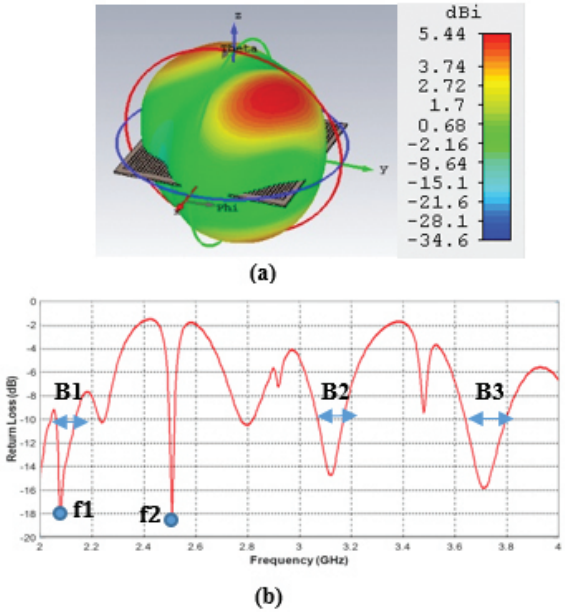

Fig. 2. (a) Propagation pattern of mushroom-type LWA at 2.5 GHz, (b) Return loss graph.

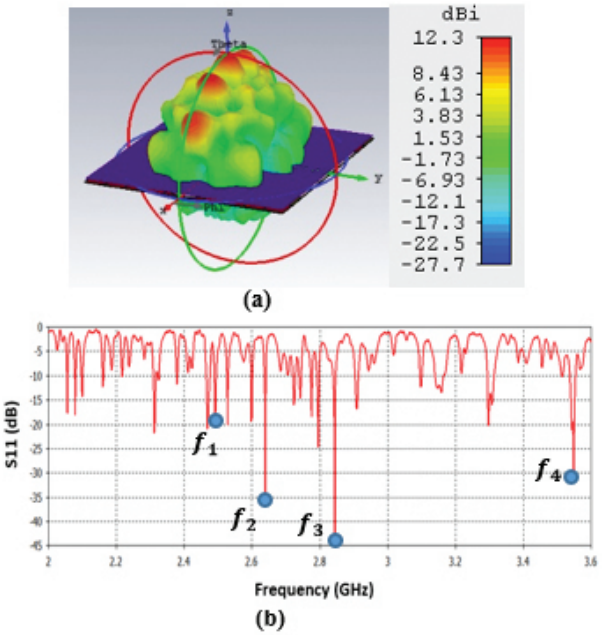

Fig. 4. (a) Propagation pattern of 2D periodically LWA at 2.45 GHz, (b) Return loss graph.

decent frequency bands of operation, B1, B2, and B3 which have return loss values of less than -10 dB. For the two frequency points of f_1=2.15 GHz and f_2 = 2.5 GHz, the mushroom-type leaky wave antenna shows return loss values of less than -18 dB. Especially, the frequency point of about 2.5 GHz is a common frequency for many medical instruments that work in ISM bands.

B. Two dimensionally periodically slotted leaky wave antenna

In this type of LWA shown on Figure 3, there is a ground plane of PEC with dimensions of 400 mm × 400 mm and two different substrates, Rogers RT6010 with permittivity ε_r= 10.2 and RO3003 with permittivity ε_r= 3. Each individual substrate cell is 40 mm × 40 mm and the whole substrate consists of 100 cells shown in red and yellow. The authors believe

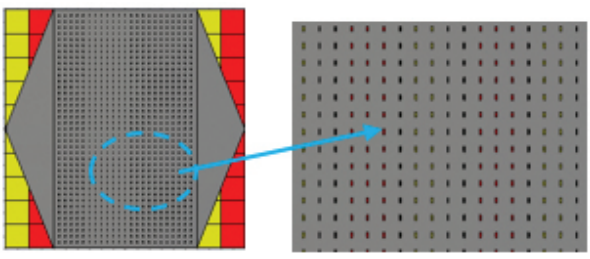

Fig. 3. The structure of 2D periodically slotted leaky wave antenna.

that by using two different columns of higher permittivity and lower permittivity, one could achieve better propagation characteristics such as having more beam directivity, that could be of high interest in biomedical applications that need considerable beam focusing. Figure 4 (a) shows that beam directivities of up to 12.3 dBi have been achieved. The superstrate is a PEC which has 39 by 23 slots. The slots cause the leakage mechanism in this antenna and give the antenna the capability to produce scanned beams over a wide range of angles from broadside to end-fire directions. There are two tapered feeding lines connected to both sides of the superstrate. The purpose of tapered feedlines is for having better impedance matching properties which lead to more decent return loss values.

Figure 4 (a) illustrates the propagation pattern of this antenna at 2.45 GHz with highly directive beams, and Figure 4 (b) shows the return loss graph for frequency range of 2-3.6 GHz. The antenna shows very decent impedance matching around 2.5 GHz, 2.65 GHz, 2.85 GHz, and 3.55 GHz as marked by points f_1, f_2, f_3, and f_4 on Figure 4 (b).

C. Belt-shaped leaky wave antenna

In this section, we would like to introduce the belt-shaped leaky wave antenna for the first time. In the belt-shaped leaky wave antenna, we actually have a 1D slotted antenna with a tapered microstrip feeding mechanism as shown in Figure 5. In this structure, the main moti-

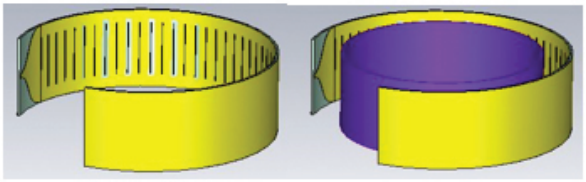

Fig. 5. The structure of ring-shaped leaky wave antenna.

vation is to have a conformal antenna that could fit the shape of the head or neck to focus on cancerous tumors of these regions. In the simulation environment, the tissue was placed at the center of the antenna, which is shown as violet cylinder on Figure 5 and the thermal distribution patterns of the given tissue were studied. The substrate is TMM10 with a permittivity value of $\varepsilon_r = 9.2$. In LWAs, we consider the mode $n = -1$ as a fast mode, i.e., $V_{phase} > c$ (c=speed of light) and plugging it into the Floquet formula (1)

$$\beta_n = \beta_0 + \frac{2\pi n}{p}. \quad (1)$$

Will give the following inequality (2):

$$\left|\beta_0 - \frac{2\pi n}{p}\right| < |\beta_0|. \quad (2)$$

And solving for p will lead to the following design condition (3):

$$p < \frac{\lambda_0}{2}. \quad (3)$$

In simpler words, the mode $n = -1$, which is considered as a fast mode, enforces some design principles on LWAs. This fast mode actually excites other slow modes and leads to wave propagation from the antenna. A portion of the EM wave leaks out of each slot as the wave travels along the structure. The frequency range for simulation is $f = 2$ GHz to $f = 6$ GHz. This antenna could be designed with a considerably thin substrate to increase the bendability of it.

Figure 6 (a) illustrates the propagation pattern of this antenna at 2.45 GHz as well as the return loss graph. The propagation pattern at 2.45 GHz looks like a fan beam rather than pencil beam which is applicable to hyperthermia treatment scenarios that need larger tissue area is to be targeted with temperature elevation. Figure 6 (b), illustrates the return loss graph for this antenna. Sample frequency points of f_1, f_2, f_3, f_4, and f_5 correspond to 2.45 GHz, 2.9 GHz, 3.7 GHz, 4 GHz, and 5.2 GHz which show very decent return loss values such as –20 dB or –25 dB.

III. SAR AND METHODOLOGY

SAR gives a measure of the rate of the absorption of energy by a human body tissue. This measure can be expressed by electric field intensity or temperature variation. SAR is expressed as equation (4),

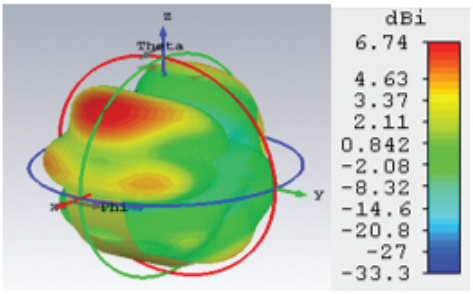

(a)

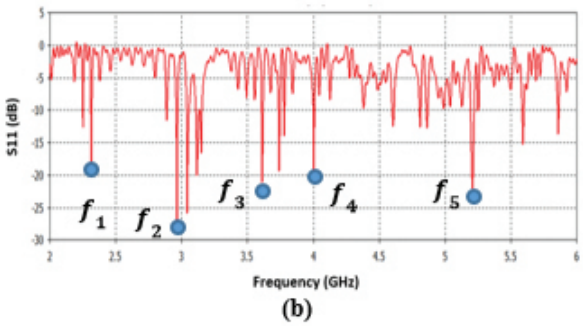

(b)

Fig. 6. (a) Propagation pattern of ring-shaped LWA at 2.45 GHz, (b) Return loss graph.

$$SAR = \frac{\sigma |E_{inc}|^2}{2\rho}. \quad (4)$$

In which, σ is the conductivity of tissue, E_{inc} is the electric field intensity of the incident wave and ρ is the density of tissue. In other words, *SAR* is defined as the average power loss density mathematically expressed as $\sigma |E_{inc}|^2$ in density volume of a given tissue in human body (ρ). It is important to note that a given tissue is composed of four layers: bone, muscle, fat, and skin. In the simulation steps of CST software, we can set field monitors for calculation of power loss density as explained in the SAR formula and finally the software is able to give us the SAR as thermal maps expressed in W/Kg (Watt per Kilogram of a tissue). There are two main methods for SAR analysis in CST software which are average SAR and point SAR. In the average SAR, basically a cube of 1 g or 10 g is considered and power loss density is calculated for this whole 3D region. In point SAR, the software allocates a SAR value to a given point without doing any averaging. Table 1 shows the maxima of the mass averaged SAR values that are acceptable world-wide [12]. The results of this work are based on US and Canada SAR standards suggesting that the acceptable average SAR values are to be about 1.6 W Kg^{-1} or lower than that, as summarized in Table 1.

The research regarding the most optimal antenna solutions for hyperthermia treatment is very extensive

Table 1: SAR guide

Typical Standards	**SAR Limit** (W/Kg)
US & Canada	1.6 (W/Kg) averaged over 1 g of tissue
EU, Japan, Brazil	2 (W/Kg) averaged over 10 g of tissue

simply because the thermal characteristics of a given tissue differs from patient to patient and from tissue to tissue. The Pennes bioheat equation interestingly connects the temperature (T) and the applied energy distribution using biomedical properties of a tissue [13] as expressed by equation (5)

$$\rho * c * \frac{\partial \mathrm{T}}{\partial \mathrm{t}} = \nabla . (\mathrm{k} \nabla \mathrm{T}) + \rho * Q + \rho * SAR - \rho_b * c_b * \rho * \omega * (T - T_b), \quad (5)$$

in which, c is the specific heat capacity, T is temperature, t is the time, ρ is volume density, Q is the metabolic heat rate, SAR is the specific absorption ratio, ρ_b is the blood mass density, c_b is the specific heat capacity of blood, ω is the blood perfusion rate, and T_b is the blood temperature which is about 37 $^{\circ}C$. By applying RF electromagnetic field, we could derive equation 4 which is an approximated solution of the Pennes equation for our study. We developed an image processing tool in MATLAB that is able to extract the 2D image of tissue areas affected by maximal SAR values in each of the three antenna systems. The MATLAB code, gives us a good insight into the geometry of the heat dissipation on tissue areas and understanding how frequency variation could affect the SAR values.

IV. RESULTS AND DISCUSSION

To study the capability of each antenna system as a potential hyperthermia system, 1 g average SAR and point SAR were calculated. In point SAR study, the local SAR value is calculated but without any mass or volume averaging. In the average SAR study after the calculation of the local SAR, this value is normalized by a fixed volume. In this study, the tissue was placed in the near field of each antenna. Each antenna system was excited by gaussian excitation and the solver used was Time Domain Solver of the CST software to calculate the EM results including propagation patterns, return loss, VSWR, and the power loss densities at the given frequencies. After the EM simulation was done for each antenna, then the power loss values for targeted frequency points were calculated as a post-processing step. Based on the power loss values, the Thermal Solver of CST calculated the SAR maps on bio-tissues, where there was the option to choose between 1 g average SAR and point SAR. The main frequency of operation based on ISM regulation is around 2.45 GHz for medical instruments. However, in our study, frequency values of up to 6 GHz have been considered for simulation, in order to have a better understanding of how each antenna system operates in higher frequency bands for hyperthermia functionality. In the following section, the SAR analysis results are illustrated. There are eight figures for each antenna. Figures labeled with (a) show the average SAR results and figures labeled with (b) show the point SAR results. SAR values are summarized in the corresponding tables for each set of results. The tissue area is a constant number of $A = 2.5504 * 10^4$ mm^2 for the mushroom type, and 2D periodically slotted leaky wave antennas. The results for the mushroom-type leaky wave antenna have been shown on the Figures 7–10. We can see how the geometry of the heat distribution changes by shifting from 2 GHz to 2.45 GHz and 3 GHz up to 3.6 GHz. At 2.45 GHz, the pattern looks like a clover. Such SAR patterns could be suitable for targeting tissues which have several adjacent tumor regions. Figure 7 shows the SAR analysis for the frequency of 2 GHz. The maximal SAR value is about 1.26 W Kg^{-1}.

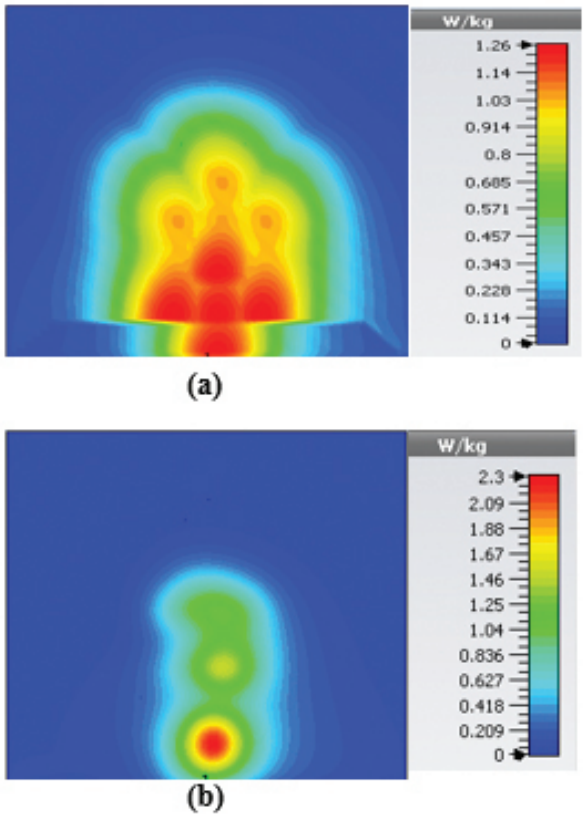

Fig. 7. SAR map [W/kg] of Mushroom LWA on kidney tissue at 2 GHz: (a) 1 g average SAR, (b) point SAR.

Figure 8 shows the SAR analysis for the frequency of 2.45 GHz. The maximal SAR value is about 1.63 W

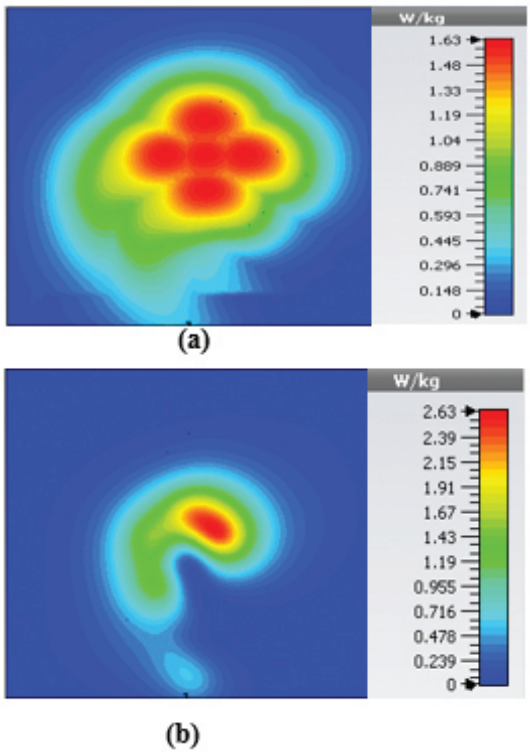

Fig. 8. SAR map [W/kg] of Mushroom LWA on kidney tissue at 2.45 GHz: (a) 1 g average SAR, (b) point SAR.

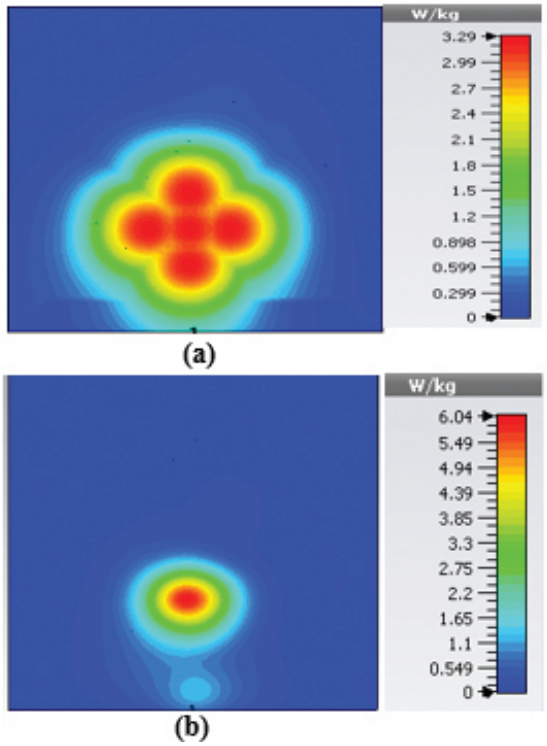

Fig. 9. SAR map [W/kg] of Mushroom LWA on kidney tissue at 3 GHz: (a) 1 g average SAR, (b) point SAR.

Table 2: SAR values for mushroom-type leaky wave antenna

Frequency (GHz)	1g Average SAR [W/kg]	Point SAR [W/kg]
2	1.26	2.3
2.45	1.63	2.63
3	3.29	6.04
3.6	2.66	4.74

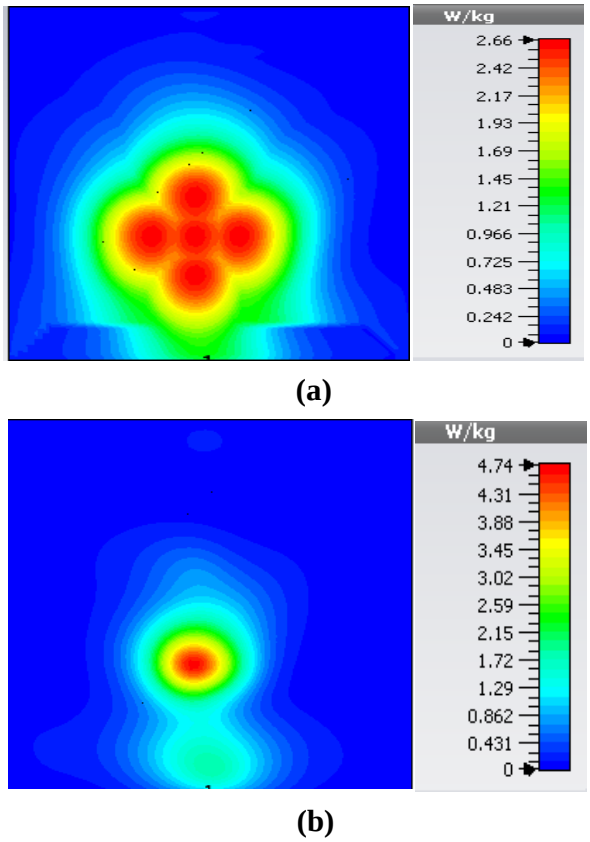

Fig. 10. SAR map [W/kg] of Mushroom LWA on kidney tissue at 3.6 GHz: (a) 1 g average SAR, (b) point SAR.

Kg^{-1}. We can observe that by frequency shift of only about 450 MHz, the main beam of the mushroom-type leaky wave antenna changes its direction.

By switching to frequencies 3 GHz and 3.6 GHz, we can observe that both the average SAR and point SAR maps illustrate more focal behavior in heat dissipation. Due to the skin effect in microwave frequencies, the penetration depth of the electromagnetic waves in the corresponding bio-tissue decreases as frequency increases and the SAR maps verify this principle.

Table 2 summarizes the results of SAR analysis for the mushroom-type leaky wave antenna. In this section, we can observe the SAR analysis results for 2D

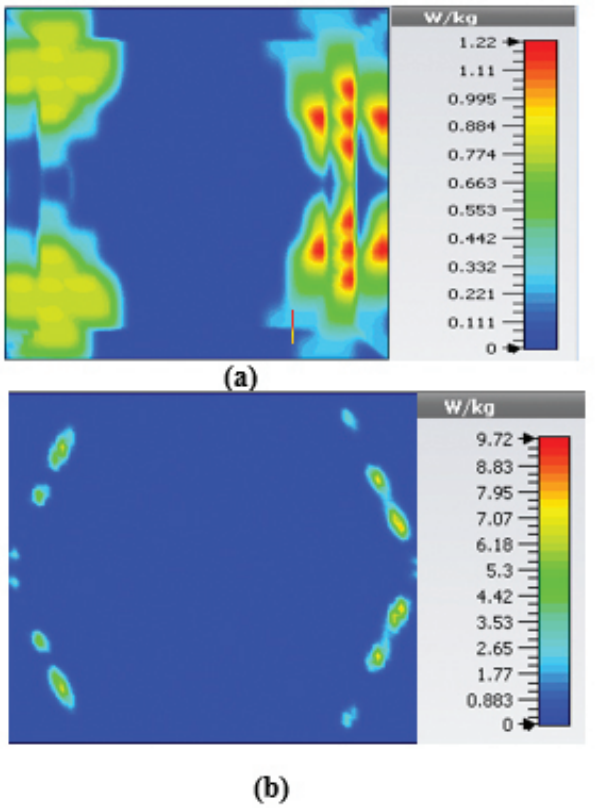

Fig. 11. SAR map [W/kg] of 2D periodically slotted LWA on kidney tissue at 2 GHz: (a) 1 g average SAR, (b) point SAR.

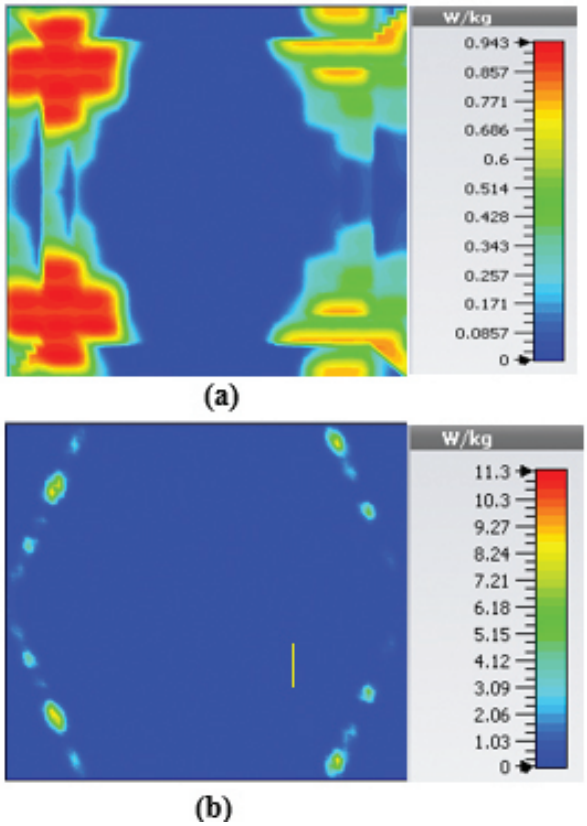

Fig. 12. SAR map [W/kg] of 2D periodically slotted LWA on kidney tissue at 2.45 GHz: (a) 1 g average SAR, (b) point SAR.

periodically slotted leaky wave antenna. Starting at the frequency of 2 GHz, the SAR results show a fuzzy heat distribution pattern.

At 2.45 GHz, we can see two cross-shaped regions with maximal SAR value of 0.943 W Kg^{-1}. By switching from 2.45 GHz to 3 GHz the affected area transforms itself from a homogeneously heated region (Figure 12) to a focused SAR pattern (Figure 13), which could be applicable to a scenario where a more focused beam is required for hyperthermia treatment.

This section illustrates the SAR results for the belt-shaped leaky wave antenna. In this case, the tissue geometry has been chosen to be a cylinder with the inner radius of 73 mm and outer radius of 76 mm, and height of 60 mm. The surface area of this geometry is $A = 1.4326 * 10^4$ mm^2. As we can see on Figures 15–18, the geometry of the heated area changes from extended heat distribution in Figure 15 to a more focused heat pattern on Figure 18.

For the belt-shaped leaky wave antenna, all the calculated average SAR values are equal to or less than 1.6 W Kg^{-1} per 1 g of the bio-tissue. For frequencies 2 GHz, 2.45 GHz, 3 GHz, and 3.6 GHz, the average SAR values are respectively 1.41 W Kg^{-1}, 1.6 W Kg^{-1}, 1.51 W Kg^{-1}, and 1.61 W Kg^{-1}.

Table 4 summarizes the SAR analysis results for the belt-shaped leaky wave antenna.

In the following section, we are going to discuss the SAR results after applying image processing code to them. The MATLAB code is able to keep the areas with maximal SAR values while filtering out the other regions and calculate the values of these areas in mm^2. The logic of this program follows the RGB coding, in which the thresholds for red, blue, and green colors need to be set carefully. Setting those thresholds could define what

Table 3: SAR values for of 2D periodically slotted

Frequency (GHz)	1g Average SAR [W/kg]	Point SAR [W/kg]
2	1.22	9.72
2.45	0.943	11.3
3	0.768	10.2
3.6	1.36	19.6

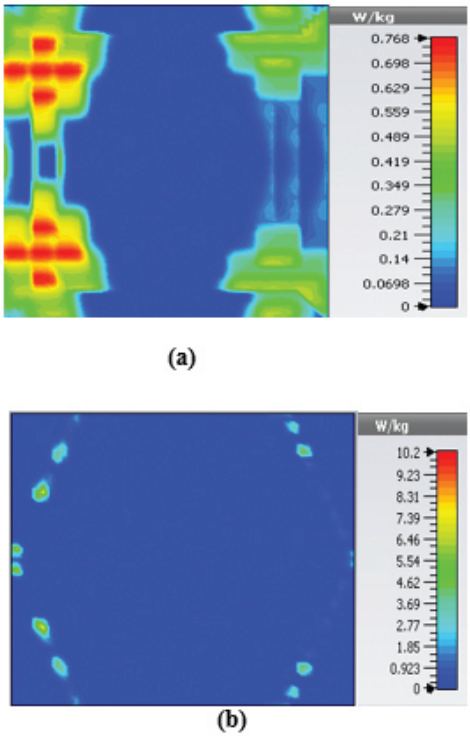

Fig. 13. SAR map [W/kg] of 2D periodically slotted LWA on kidney tissue at 3 GHz: (a) 1 g average SAR, (b) point SAR.

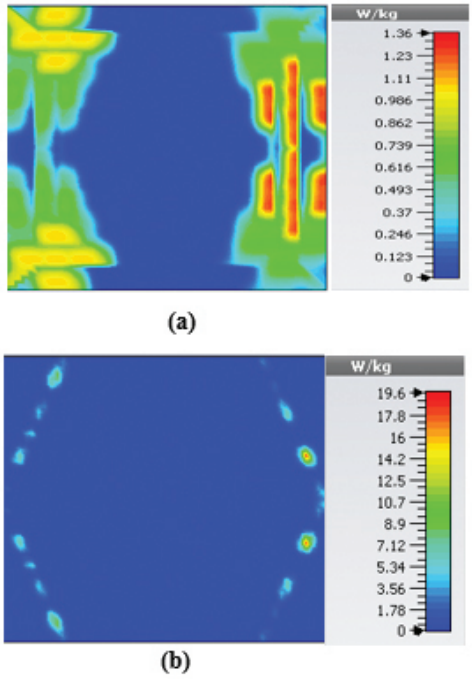

Fig. 14. SAR map [W/kg] of 2D periodically slotted LWA on kidney tissue at 3.6 GHz: (a) 1 g average SAR, (b) point SAR.

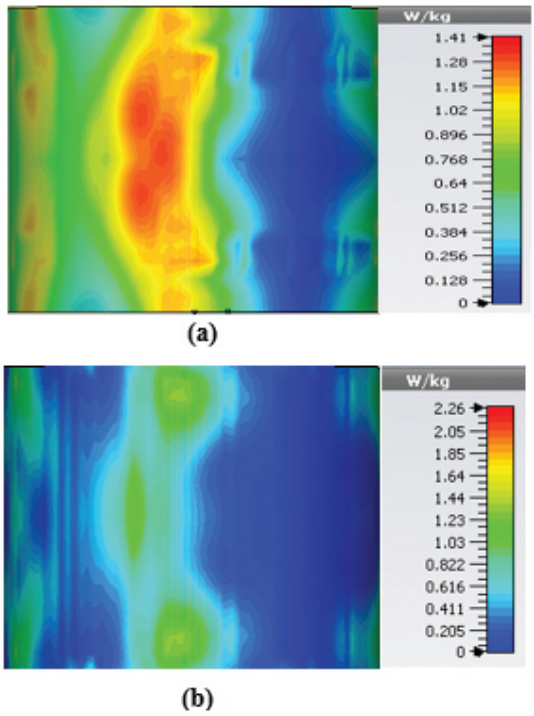

Fig. 15. SAR map [W/kg] of belt-shaped LWA on kidney tissue at 2 GHz: (a) 1 g average SAR, (b) point SAR.

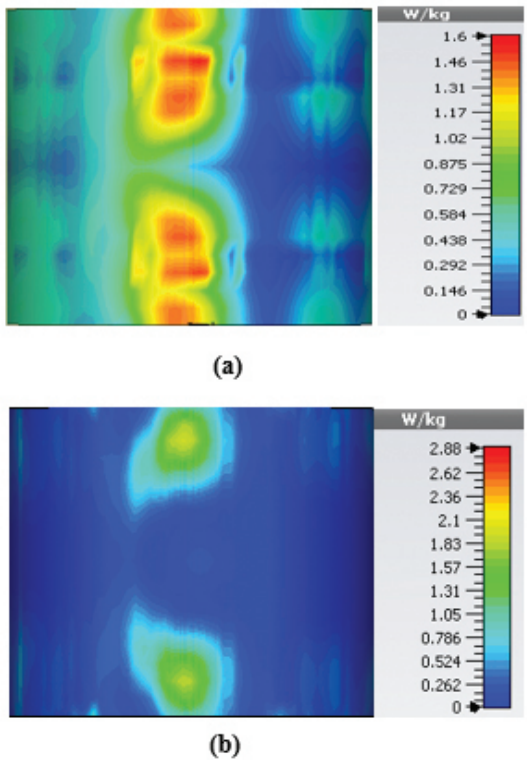

Fig. 16. SAR map [W/kg] of belt-shaped LWA on kidney tissue at 2.45 GHz: (a) 1 g average SAR, (b) point SAR.

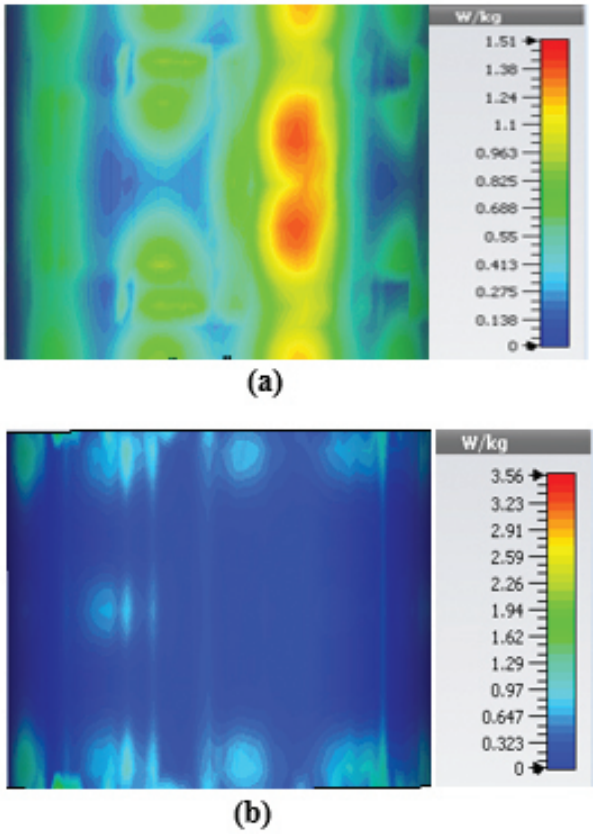

Fig. 17. SAR map [W/kg] of belt-shaped LWA on kidney tissue at 3 GHz: (a) 1 g average SAR, (b) point SAR.

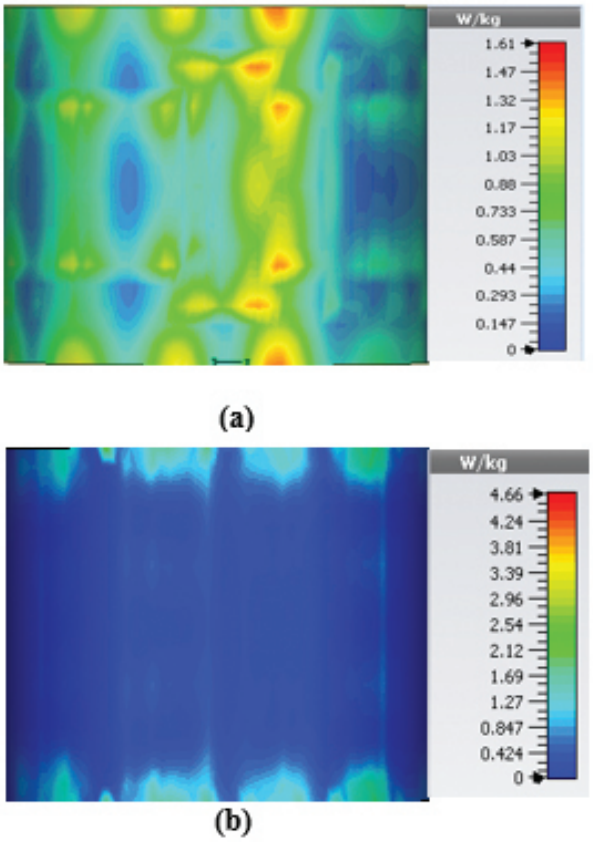

Fig. 18. SAR map [W/kg] of belt-shaped LWA on kidney tissue at 3.6 GHz: (a) 1 g average SAR, (b) point SAR.

range of "red" is acceptable for the acceptable SAR margins, e.g., around 1.6 W Kg^{-1} for hyperthermia applications. The range of numbers 0-255 are allocated to colors and each color can be defined a mixture of red, blue, and green, thus we could attribute an array of three numbers to any color. The summary of the processing steps in the CST and MATLAB code are as follows:

1. EM simulation and preliminary SAR analysis in CST Software tool.
2. SAR maps loaded in MATLAB from CST.
3. Calculation of the number of all pixels.

Table 4: SAR values for belt-shaped leaky wave antenna

Frequency (GHz)	1g Average SAR [W/kg]	Point SAR [W/kg]
2	1.41	2.26
2.45	1.6	2.88
3	1.51	3.56
3.6	1.61	4.66

Table 5: Heated tissue areas at $f = 2.45$ GHz

Antenna type	**Heated area in** mm^2
Mushroom-type LWA	1.998484e+03
2D periodically slotted LWA	2.389691e+03
Ring-shaped LWA	3.191384e+02

4. Setting RGB thresholds.
5. Filtering out the non-red areas.
6. Calculation of the areas with maximal SAR values using $\left(\frac{Number\ of\ red\ pixels}{number\ of\ all\ pixels}\right) * Tissue\ area$

The first step of the processing steps led to the EM simulations and the previously discussed SAR maps and steps 2 to 6 discuss the processing steps in MATLAB. The following MATLAB code is developed for the extraction of the tissue areas affected by maximal SAR values and the calculation of the area of such regions in mm^2.

Figures 19 and 20 illustrate the application of the MATLAB code on the SAR maps of the mushroom-type

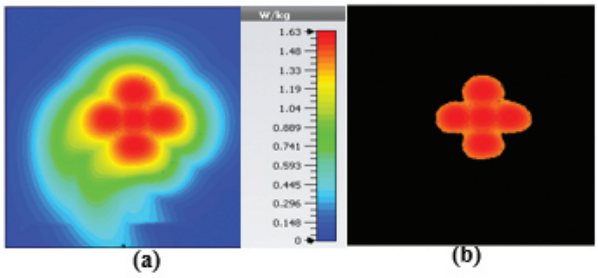

Fig. 19. SAR map [W/kg] of mushroom LWA on kidney tissue at 2.45 GHz: (a) 1 g average SAR map, (b) filtered SAR map.

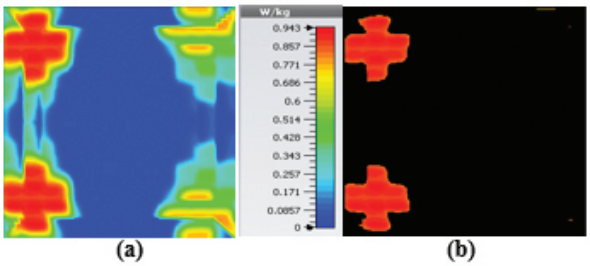

Fig. 20. SAR map [W/kg] of 2D periodically slotted LWA on kidney tissue at 2.45 GHz: (a) 1 g average SAR map, (b) filtered SAR map.

and 2D periodically slotted leaky wave antennas. We can observe that only the regions with maximal SAR values of about 1.63 W Kg^{-1} on Figure 19 and 0.943 W Kg^{-1} on Figure 20 have been preserved.

Table 5 summarizes the overall calculated areas on tissues that are exposed to maximal SAR values in the three proposed antenna systems at the frequency of 2.45 GHz.

V. DISCUSSION AND CONCLUSIONS

Three novel leaky wave antennas for application in microwave hyperthermia were investigated. Each of these microwave systems offer some distinguished frequency scanning and beam focusing properties with proven efficiency for hyperthermia applications, which make them appealing for treatment of different cancerous tumors. For the mushroom-type leaky wave antenna, the top PEC plates cause an effective suppression of the surface waves that lead to the increase of the antenna efficiency. Looking at the corresponding SAR maps for the frequency points of 2 GHz and 2.45 GHz, we can observe that the antenna shows decent focused heat distribution on the tissue while reaching the accepted standard SAR values of less than 1.6 W Kg^{-1}. For the 2D periodically slotted leaky wave antenna, we could reach high beam directivities of up to 12.3 dBi which make this antenna a very good candidate for hyperthermia treatment. In addition to the structure of the two-dimensionally placed slots causes the beam angle to have more scanning flexibility which leads to wide ranges of angles from broadside to end-fire. This antenna is capable of changing the geometry of SAR from focused shape to an extended shape with a narrow frequency shift of 450 MHz. For the belt-shaped leaky wave antenna the conformal shape of the structure makes it convenient for installation of the antenna in body regions such the neck where tumors could develop. For this antenna, it is best to use a very thin substrate to achieve two goals: (1) reducing surface waves and (2) increasing the antenna bendability. Potentially belt-shaped leaky wave antennas with two-dimensionally placed slots could provide more beam angle flexibility and control over beam displacement, which could be of interest for future works.

REFERENCES

[1] H. Trefna and M. Persson, "Heating of deep seated tumours using microwaves radiation," *ACES Conference 2007*, Verona, Italy, Mar. 19-23, 2007.

[2] W. Xi, B. Liu, and Binkai Xu, "Theoretical evaluation of high frequency microwave ablation applied in cancer therapy," *Applied Thermal Engineering*, vol. 107, pp. 501-507, 2016.

[3] J. Mallorqui, A. Broquetas, L. Jofre, and A. Cardama, "Non-invasive active thermometry with a microwave tomographic scanner in hyperthermia treatments," *Applied Computational Electromagnetics Society (ACES) Journal*, vol. 7, pp. 121-127, 1992.

[4] H. Xiaoping, W. Geyi, and S. Wang, "A hexagonal focused array for microwave hyperthermia: optimal design and experiment," *IEEE Antennas and Wireless Propagation Letters*, vol. 15, pp. 56-59, 2015.

[5] G. C. Van Rhoon and J. van der Zee, "Hyperthermia a treatment for cancer: maturation of its clinical application," *Polish Journal of Environmental Studies* vol. 15.4A, pp. 11-15, 2006.

[6] P. F. Tumer, T. Schaefermeyer, M. Latta, R. Lauritzen, and D. T. Sells, "3-D heating pattern steering using the sigma eye phased array applicator controlled by a modified BSD-2000 hyperthermic oncology," edited by C. Franconi et al. (Tor Vergata Post Graduate School of Medical Physics, Rome), pp. 571-573, 1996.

[7] O. B. Debnath, K. Ito, K. Saito, and M. Uesaka, "Design of invasive and non-invasive antennas for the combination of microwave-hyperthermia with radiation therapy," *2015 IEEE MTT-S 2015 International Microwave Workshop Series on RF and*

Wireless Technologies for Biomedical and Healthcare Applications (IMWS-BIO). IEEE, 2015.

[8] R. V. Sabariego, L. Landesa, and F. Obelleiro, "Synthesis of an array antenna for hyperthermia applications," *IEEE Transactions on Magnetics*, vol. 36, no. 4, pp. 1696-1699, 2000.

[9] M. M. Paulides, F. Jurriaan, N. Chavannes, and G. C. Van Rhoon, "A patch antenna design for application in a phased-array head and neck hyperthermia applicator," *IEEE Transactions on Biomedical Engineering*, vol. 54, no. 11, pp. 2057-2063, 2007.

[10] M. M. Paulides, S. H. J. A. Vossen, A. P. M. Zwamborn, and G. C. Van Rhoon, "Theoretical investigation into the feasibility to deposit RF energy centrally in the head and neck region," *Int. J. Rad. Onc. Biol. Phys.*, vol. 63, pp. 634-642, 2005.

[11] M. M. Paulides, J. F. Bakker, A. P. M. Zwamborn, and G. C. Van Rhoon, "A head and neck hyperthermia applicator: Theoretical antenna array design," *Int. J. Hyperthermia*, vol. 23, no. 1, pp. 59-67, 2007.

[12] H. Luyen, S. C. Hagness, and N. Behdad, "A balun-free helical antenna for minimally invasive microwave ablation," *IEEE Transactions on Antennas and Propagation*, vol. 63.3, pp. 959-965, 2015.

[13] M. Sarabi and W. Perger, "A Novel Leaky Wave Antenna for Hyperthermia," In 2019 IEEE Texas Symposium on Wireless and Microwave Circuits and Systems (WMCS). IEEE, pp. 1-4, 28 Mar. 2019.

[14] T. Hamed and M. Maqsood, "SAR calculation & temperature response of human body exposure to electromagnetic radiations at 28, 40 and 60 GHz mmWave frequencies," *Progress in Electromagnetics Research*, vol. 73, pp. 47-59, 2018.

[15] T. Wittig, "SAR overview," www.cst.com, accessed Nov. 25, 2016.

[16] https://www.sciencedirect.com/topics/medicine-and-dentistry/specific-absorption-rate.

[17] D. Colton and P. Monk, "A new approach to detecting leukemia: Using computational electromagnetics," *IEEE Trans. Comput. Sci. Eng.*, vol. 2, pp. 46-52, winter 1995.

[18] P. M. Meaney, M. W. Fanning, D. Li, S. P. Poplack, and K. D. Paulsen, "A clinical prototype for active microwave imaging of the breast," *IEEE Trans. Microwave Theory Tech.*, vol. 48, pp. 1841-1853, Nov. 2000.

[19] W. C. Chew and J. H. Lin, "A frequency-hopping approach for microwave imaging of large inhomogeneous bodies," *IEEE Microwave Guided Wave Lett.*, vol. 5, pp. 439-441, Dec. 1995.

[20] O. S. Haddadin and E. S. Ebbini, "Imaging strongly scattering media using a multiple frequency distorted Born iterative method," *IEEE Trans. Ultrason., Ferroelect., Freq. Contr.*, vol. 45, pp. 1485-1496, Nov. 1998.

[21] Q. Fang, P. M. Meaney, and K. D. Paulsen, "Microwave image reconstruction of tissue property dispersion characteristics utilizing multiple-frequency information," *IEEE Trans. Microwave Theory Tech.*, vol. 52, pp. 1866-1875, Aug. 2004.

[22] P. M. Meaney, K. D. Paulsen, A. Hartov, and R. C. Crane, "An active microwave imaging system for reconstruction of 2-D electrical property distributions," *IEEE Trans. Biomed. Imag.*, vol. 42, pp. 1017-1026, Oct. 1995.

[23] K. D. Paulsen and P. M. Meaney, "Compensation for nonactive array element effects in a microwave imaging system: Part I—Forward solution vs. measured data comparison," *IEEE Trans. Med. Imag.*, vol. 18, pp. 496-507, June 1999.

[24] P. M. Meaney, K. D. Paulsen, M. W. Fanning, and A. Hartov, "Nonactive antenna compensation for fixed-array microwave imaging: Part II—Imaging results," *IEEE Trans. Med. Imag.*, vol. 18, pp. 508-518, Jun. 1999.

[25] P. M. Meaney, K. D. Paulsen, A. Hartov, and R. K. Crane, "Microwave imaging for tissue assessment: Initial evaluation in multitarget tissue-equivalent phantoms," *IEEE Trans. Biomed. Eng.*, vol. 43, pp. 878-890, Sep. 1996.

[26] E. C. Fear, S. C. Hagness, P. M. Meaney, M. Okieniewski, and M. Stuchly, "Enhancing breast cancer detection using near field imaging," *IEEE Microwave Magazine*, pp. 48-56, Mar. 2002.

[27] S. C. Hagness, A. Taflove, and J. E. Bridges, "Two-dimensional FDTD analysis of a pulsed microwave confocal system for breast cancer detection: fixed-focus and antenna-array sensors," *IEEE Trans. Biomed. Eng.*, vol. 45, pp. 1470-1479, Dec. 1998.

[28] S. C. Hagness, A. Taflove, and J. E. Bridges, "Three-dimensional FDTD analysis of a pulsed microwave confocal system for breast cancer detection: design of an antenna-array element," *IEEE Trans. Antennas Propagat.*, vol. 47, pp. 783-791, May 1999.

[29] X. Li and S. C. Hagness, "A confocal microwave imaging algorithm for breast cancer detection," *IEEE Microwave Wireless Comp. Lett.*, vol. 11, pp. 130-132, Mar. 2001.

[30] E. Fear and M. Stuchly, "Microwave system for breast tumor detection," *IEEE Microwave Guided Wave Lett.*, vol. 9, pp. 470-472, Nov. 1999.

[31] E. C. Fear and M. A. Stuchly, "Microwave detection of breast cancer," *IEEE Trans. Microwave*

Theory Tech., vol. 48, pp. 1854-1863, Nov. 2000.

[32] X. Yun, E. C. Fear, and R. H. Johnston, "Compact antenna for radar-based breast cancer detection," *IEEE Trans. Antennas and Propagation*, vol. 53, no. 8, pp. 2374-2380, Aug. 2005.

[33] S. C. Hagness, A. Taflove, and J. E. Bridges, "Wideband ultralow reverberation antenna for biological sensing," *Electronic Lett.*, vol. 33, no. 19, pp. 1594-1595, Sep. 1997.

[34] M. A. Hernandez-Lopez, M. Pantoja, M. Fernandez, S. Garcia, A. Bretones, R. Martin, and R. Gomez, "Design of an ultra-broadband V antenna for microwave detection of breast tumors," *Microw. Opt. Tech. Lett.*, vol. 34, no. 3, pp. 164-166, Aug. 2002

[35] E. C. Fear and M. A. Stuchly, "Microwave breast tumor detection: Antenna design and characterization," *IEEE Antennas Propag. Symp. Dig.*, vol. 2, pp. 1076-1079, 2000.

[36] X. Li, S. C. Hagness, M. K. Choi, and D. W. W. Choi, "Numerical and experimental investigation of an ultrawideband ridged pyramidal horn antenna with curved launching plane for pulse radiation," *IEEE Antennas Wireless Propag. Lett.*, vol. 2, pp. 259-262, 2003.

[37] X. Yun, E. C. Fear, and R. H. Johnston, "Radar-based microwave imaging for breast cancer detection: Tumor sensing with cross-polarized reflections," *IEEE Antennas Propag. Society Symp. Dig.*, vol. 3, pp. 2432-2435, 2004.

[38] C. J. Shannon, E. C. Fear, and M. Okoniewski, "Dielectric-filled slotline bowtie antenna for breast cancer detection," *Electronics Letters*, vol. 41, no. 7, Mar. 2005.

[39] J. M. Sill and E. C. Fear, "Tissue sensing adaptive radar for breast cancer detection: a study of immersion liquid," *Electronics Letters*, vol. 41, no. 3, pp. 113-115, Feb. 2005.

[40] J. M. Sill and E. C. Fear, "Tissue sensing adaptive radar for breast cancer detection: preliminary experimental results," *IEEE MTT-S Int. Microwave Symp. Dig.*, Long Beach, CA, Jun. 2005.

[41] J. M. Sill and E. C. Fear, "Tissue sensing adaptive radar for breast cancer detection—experimental investigation of simple tumor models," *IEEE Trans. Microwave Theory Tech.*, vol. 53, no. 11, pp. 3312-3319, Nov. 2005.

[42] C. Furse, "A survey of phased arrays for medical applications," *Applied Computational Electromagnetics Society (ACES) Journal*, vol. 21, no. 3, p. 365, 2006.

[43] S. Y. Semenov, A. E. Bulyshev, A. E. Souvorov, R. H. Svenson, Y. E. Sizov, V. Y. Borisov, V. G. Posukh, I. M. Kozlov, A. G. Nazarov, and G. P. Tatsis, "Microwave tomography: theoretical and experimental investigation of the iteration reconstruction algorithm," *IEEE Trans. Micr. Theory Tech.*, vol. 46, pp. 133-141, Feb. 1998.

[44] S. Y. Semenov, R. H. Svenson, A. E. Bulyshev, A. E. Souvorov, A. G. Nazarov, Y. E. Sizov, V. G. Posukh, and A. Pavlovsky, "Threedimensional microwave tomography: initial experimental imaging of animals," *IEEE Trans. Biomed. Eng.*, vol. 49, pp. 55-63, Jan. 2002.

Masoud Sarabi has received his PhD in Electrical Engineering from the Michigan Tech university in 2021. His research interests are antenna design for biomedical hyperthermia, beamformers, and FMCW radar systems for road safety applications

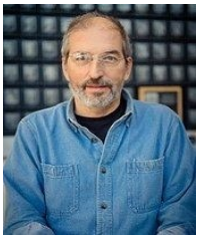

Warren F. Perger is a professor of Electrical and Computer Engineering department at Michigan Tech university and has been a faculty member since 1987.

T-Junction Power Divider Based on Rectangular Microcoaxial Structure in W-band

Zhao-Yu Huang, Bo-Yuan Liu, Yun Jiang, Wen-Tao Yuan, Qing-Ping Wang, Wei-Dong Hu, and Nai-Chang Yuan

College of Electronic Science and Technology
National University of Defense Technology, Changsha, 410073, China
huangzhaoyu10@163.com

***Abstract* –** In this paper, a W-band T-junction power divider based on rectangular microcoaxial structure is proposed. Rectangular microcoaxial line is a three-dimensional (3D) structure with the merits of wide operation bandwidth, low loss, and high integration, which is suitable for the design of radio frequency (RF) devices. A two-way power divider is designed based on the rectangular microcoaxial structure. And the two-way power divider is expanded into a four-way power divider to further illustrate the design method. Moreover, a back-to-back configuration including two identical two-way power dividers is fabricated and measured. The insertion loss of the back-to-back configuration is about 0.11–1.18 dB in W band, which agrees with the simulation one reasonably and shows good performance.

***Index Terms* –** power divider, rectangular microcoaxial structure, W band.

I. INTRODUCTION

W-band communication system has the advantages of broadband and high resolution, which makes it a research hotspot. As the frequency increases, the amplification capability of a single solid state power device decreases significantly. However, high-output power can improve the transmission distance and anti-interference ability of the system. Power divider/combiner is the component that can combine multiple power chips to increase the output power [1–5].

In W band, some rectangular waveguide power dividers based on computer numerical control (CNC) milling have been proposed [6–10]. The forms include rat-race hybrid, magic-T junction, E-plane or H-plane T-junction, and radial type. The rectangular waveguide components have the merits of low loss and high-power capacity over the planar circuits. However, the drawback is large volume, which is not conductive to the integration of the system. In [11], a substrate integrated waveguide (SIW) power divider based on the printed circuit board process is demonstrated. It has small lateral size, while the insertion loss is high because of the fabrication tolerance. With the development of micro-electromechanical systems (MEMS) technology, many RF circuits are designed based on this technology [12–14]. These circuits have the advantages of fine structure and good electromagnetic characteristics.

In this paper, we introduce a W-band T-junction power divider based on rectangular microcoaxial structure. It can be fabricated by the surface micro-machining process which is one of the MEMS technologies. First, the characteristic of the rectangular microcoaxial line is analyzed. Then, based on the above analysis, a two-way T-junction power divider is designed. And it can be expanded into a four-way power divider. Finally, a back-to-back configuration including two identical two-way power dividers is achieved and measured, which can operate in the frequency band of 75–110 GHz. The total insertion loss is less than 1.18 dB, and the simulated and measured results are in close agreement. All simulations are based on the CST simulation software with frequency domain solver.

II. CHARACTERISTIC OF THE RECTANGULAR MICROCOAXIAL LINE

The rectangular microcoaxial transmission line consists of a center conductor and metal walls surrounding it, as shown in Figure 1 (a). Since air is the medium between the center conductor and the metal wall, the dielectric loss of the transmission line is almost negligible. The transmission line is one of the coaxial lines and transmits the TEM waves so that it has a wide application frequency band (dc to over 200 GHz) [15].

Figure 1 (b) presents the electric field distribution. The crucial problem that needs to be solved to realize the rectangular microcoaxial transmission line is how to suspend the center conductor in the metal wall. The development of surface micromachining technology enables the transmission line to be well realized and the form is depicted in Figure 1 (c). The center conductor is supported by periodically distributed dielectric strips, and release holes are added to the metal wall.

Submitted On: July 20, 2021
Accepted On: September 15, 2021

https://doi.org/10.47037/2021.ACES.J.361011

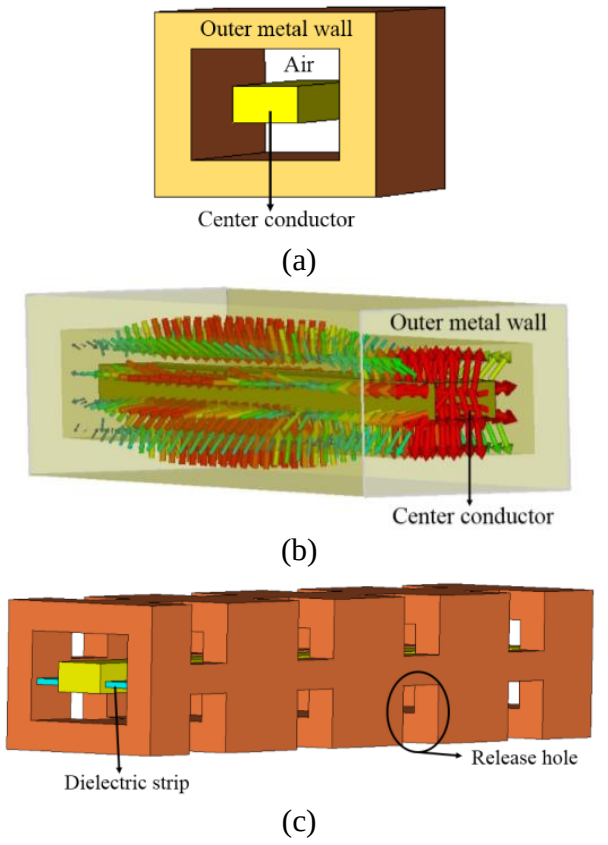

Fig. 1. Rectangular transmission line. (a) Basic model. (b) Electric filed distribution. (c) Fabricated model.

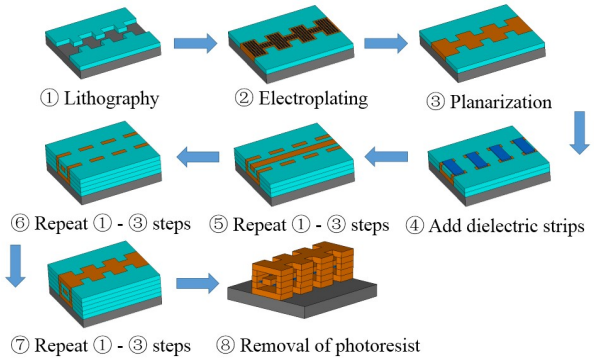

Fig. 2. Surface micromachining process.

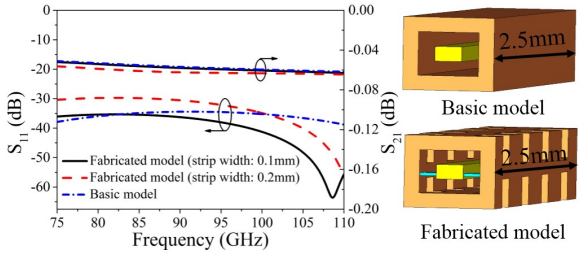

Fig. 3. Simulated S-parameters of two transmission line model.

The fabricated process of a section of rectangular microcoaxial transmission line based on surface micromachining technology is shown in Figure 2, as the following steps. The whole structure is built up layer by layer. Generally, the thickness of each layer is 50–100 um. First, the photoresist is coated on the silicon substrate as a sacrificial layer and lithographically formed into the desired shape of the structure. Then, the copper is electroplated to the gaps of the sacrificial layer to form the structural part, and the structural part is flattened by polishing. Next, dielectric strips are added to a certain layer and repeat ①-③ steps. Finally, an etching solution is used to remove the sacrificial layer to form the final rectangular microcoaxial structure. In particular, the position of the dielectric strip can be at the bottom, lower middle, or middle of the center conductor. When the dielectric strip is located in the lower middle or middle of the center conductor, the fabrication of the center conductor needs to be divided into more layers. Moreover, in order to remove the sacrificial layer cleanly, the outer wall of the transmission line is added to release holes. In the design of the T-junction power divider, the rectangular microcoaxial structure can be roughly divided into five layers, and the thickness of each layer is 100 um.

Figure 3 shows the simulated S-parameters of two transmission line models (basic model and fabricated model). With the addition of release holes and dielectric strips, S_{11} deteriorates slightly at low frequency, while it becomes better at high frequency. The S_{21} is basically unchanged. The surface current of a rectangular coaxial transmission line is presented in the Figure 4. Since the electric field intensity at the position of the release hole is relatively small, the size of the release hole does not have a significant influence on the transmission loss. However, as the width of the dielectric strip increases, the deterioration of S_{11} is obvious, which is depicted in the Figure 3. Therefore, in the design, the total volume occupied by the dielectric strips should be as small as possible.

The characteristic impedance of the rectangular coaxial line is related to the size of the air cavity and the center conductor. In order to simplify the design, we generally fix the dimension of the air cavity, and realize different characteristic impedances by changing the size of the inner conductor. The value of the height a_1 is 100 um, which is determined by the processing technology. Therefore, the characteristic impedance of rectangular microcoaxial line is only related to the width b_1 of

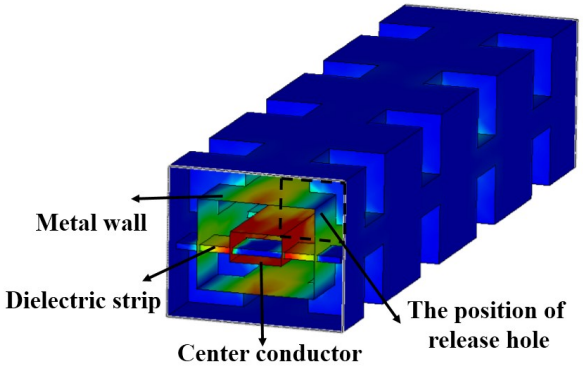

Fig. 4. The surface current of a rectangular coaxial transmission line.

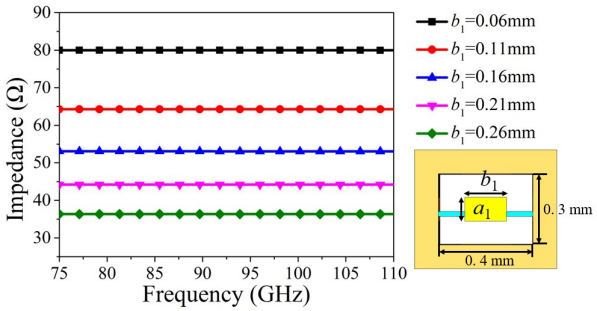

Fig. 5. Characteristic impedance versus b1.

the center conductor. And, the characteristic impedance decreases as b_1 increases, which is presented in the Figure 5. Impedance transformation is the basis of RF circuit design.

In order to facilitate the test of the rectangular microcoaxial structure and the interconnection with the microwave monolithic integrated circuits, a rectangular coaxial line to coplanar waveguide (CPW) transition structure is designed. Figure 6 demonstrates a back-to-back transition. The design of the transition structure is as follows, the width of the center conductor gradually decreases, and the upper half of the outer metal wall is shaved off. The final width of the center conductor is 60 um, and its distance from the metal wall is 45 um. This design is based on the distance between the test probes.

The structure shown in the Figure 6 is fabricated to verify the performance of the transition structure. We use a W-band vector network analyzer with ground-signal-ground (GSG) probe to test the fabricated back-to-back transition structure, which is depicted in Figure 7 (a). The vector network analyzer is first connected to the frequency expansion module through cables, and then the expansion module is connected to the GSG probes. In the process of testing, the signal probe is connected to

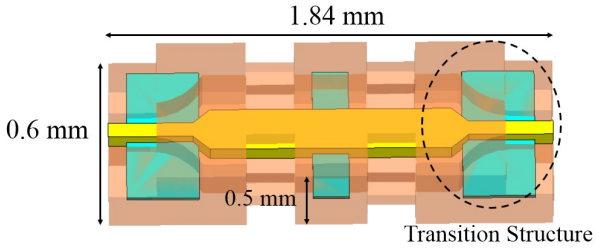

Fig. 6. The back-to-back transition of rectangular coaxial line to CPW.

the center conductor, and the two ground probes are connected to the outer metal wall. The measurement is carried out using a standard SOLT calibration process. As shown in Figure 7 (b), compared with the simulation, the measured S_{11} is slightly worse, however, it still remains below –23 dB. In addition, the measured insertion loss is about 0.38 dB at high frequencies, which is 0.2 dB lager than the simulated result. Moreover, we analyze the influence on the insertion loss induced by the surface roughness. And, these analyses are based on the CST simulator, where the parameter r represents the root mean square roughness. When r is 0.6 um, the fitting result is the best, which implies that the roughness of the processing technology can be within 0.6 um.

III. DESIGN OF T-JUNCTION POWER DIVI DER

T-junction power divider is a traditional structure, and it can be realized by many forms, such as microstrips, waveguides, and SIWs.

The ideal power divider has the following characteristics. First, the amplitudes and phases of the two output ports are equal. Second, the output power ratio of port 2 and port 3 can meet any given value. Figure 8 presents the basic circuit, and we can get the equation about the value of relevant impedance based on $\lambda/4$ transmission line impedance transformation theory [16], as the following equations (1), (2).

$$Z_{02} = Z_0\sqrt{K(1+K^2)}, \tag{1}$$

$$Z_{03} = Z_0\sqrt{(1+K^2)/K^3}, \tag{2}$$

where K^2 is the ratio of the output power of port 2 and port 3, expressed as $P_3 = K^2P_2$. When the amplitudes of the output signals of port 2 and port 3 are the same, K^2 is 1. We take Z_0 as 50 Ω, then Z_{02} and Z_{03} are both 70.7 Ω. Combined with the analysis of the characteristic impedance of the rectangular coaxial transmission line, we can get the initial widths of the corresponding branch lines. The medium between the center conductor and the outer metal wall of the rectangular microcoaxial line is

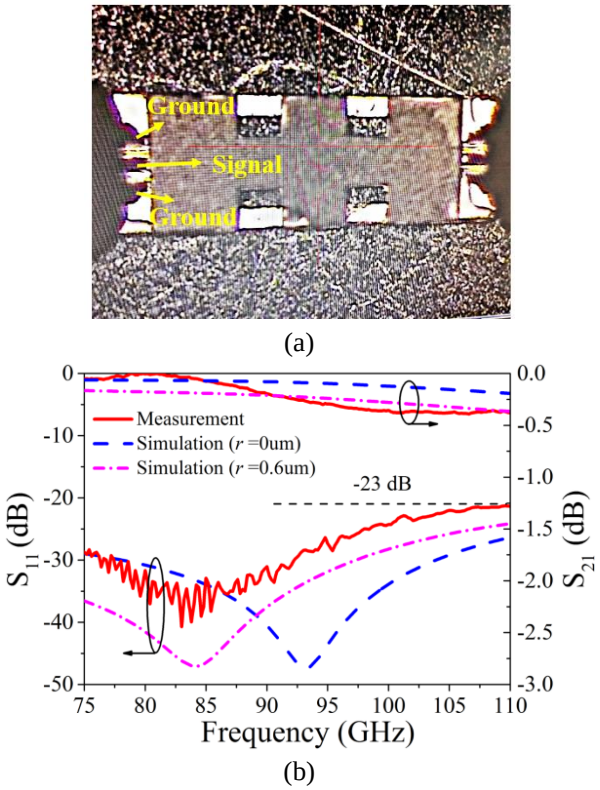

Fig. 7. Measurement of a back-to-back transition. (a) Test process. (b) Measured and simulated results.

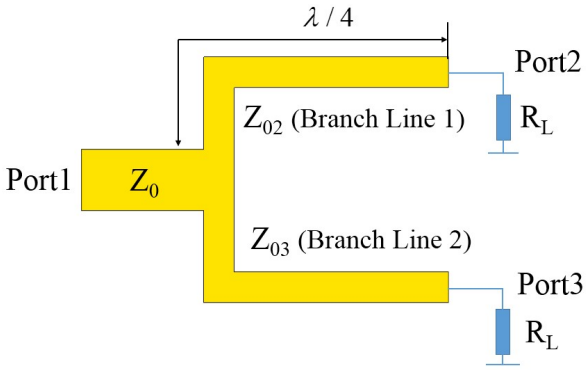

Fig. 8. Basic circuit of T-junction power divider.

air, and the guided wavelength of the rectangular coaxial line is the same as the wavelength in the medium. According to the center frequency of the component, the initial lengths of the branch lines are obtained. After optimization by CST simulator, the structure of the two-way power divider is shown in Figure 9. The branch line 1 and the branch line 2 are connected by a square matching structure. The dimensions are labeled in Figure 9 (b), as follows (units: mm): $l_1 = 0.67$, $w_1 = 0.176$, $l_2 = 0.14$,

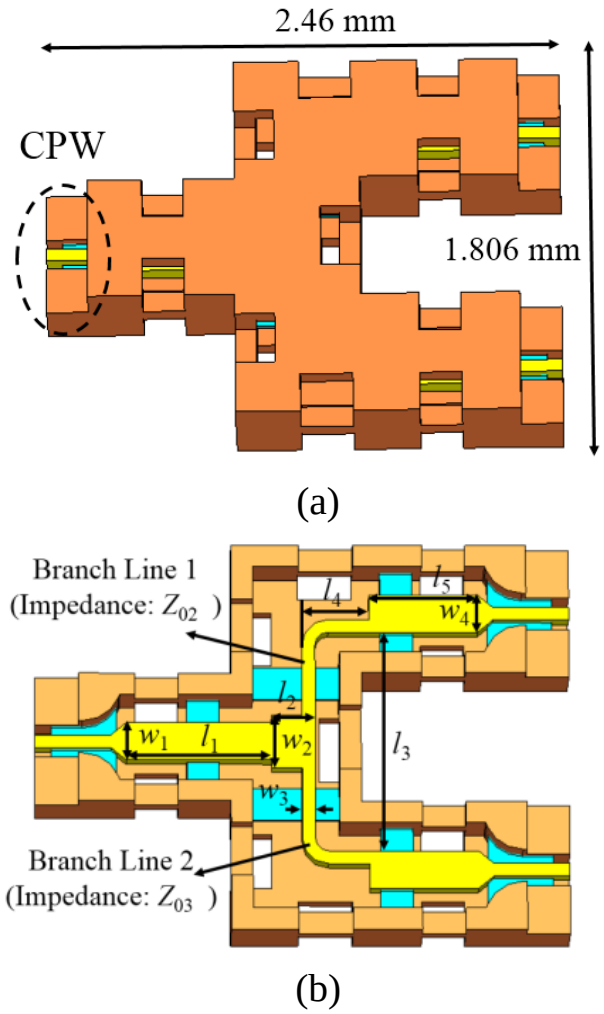

Fig. 9. The structure of the two-way power divider. (a) External structure. (b) Internal structure.

$w_2 = 0.25$, $l_3 = 1.03$, $w_3 = 0.06$, $l_4 = 0.31$, $w_4 = 0.176$, and $l_5 = 0.5$. Figure 10 illustrates the simulated results of the two-way power divider. The return loss of input port is above 17 dB and the insertion losses of two output ports are close to 3 dB from 75 to 110 GHz. The amplitude imbalance is kept within 0.03 dB. In addition, the isolation between the two output ports is about –6 dB. Since there is no isolation structure between the output ports, the isolation of this kind of power divider is generally not high. Moreover, due to the symmetric structure, the signals of the two output ports maintain nearly identical phase with a phase fluctuating between –0.015° and 0.1°.

Based on the analysis of two-way rectangular microcoaxial power divider, a four-way power divider is designed and presented in Figure 11. After optimization, the simulated results are shown in Figure 12. The return loss of port 1 is higher than 17 dB, and the insertion

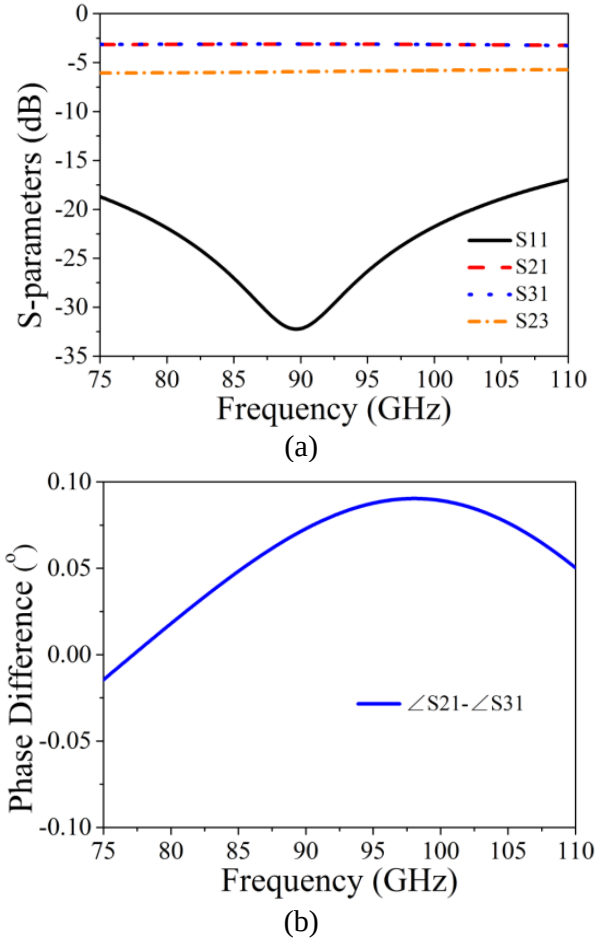

Fig. 10. Simulated results of two-way power divider. (a) S-parameter response. (b) Phase difference.

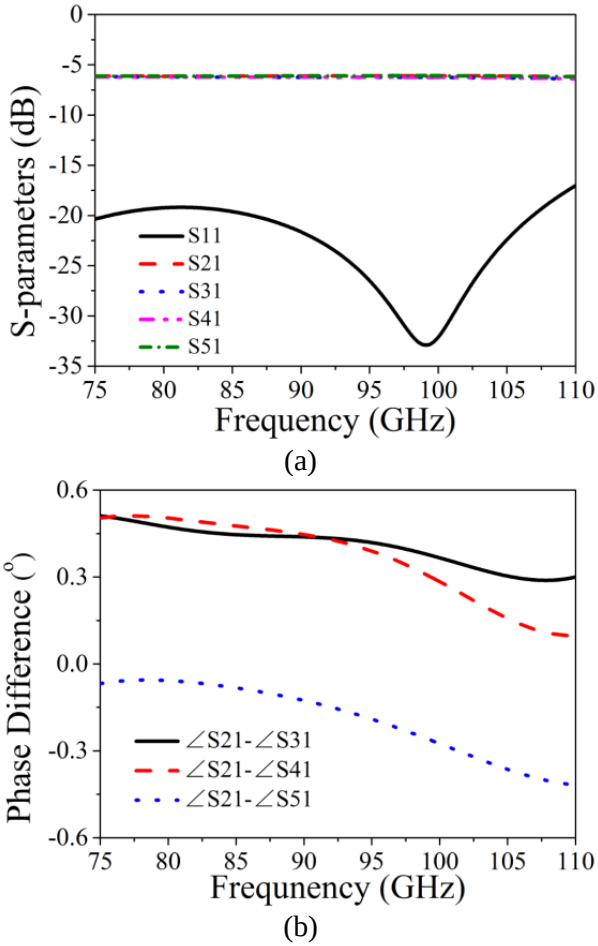

Fig. 12. Simulated results of four-way power divider. (a) S-parameter response. (b) Phase difference.

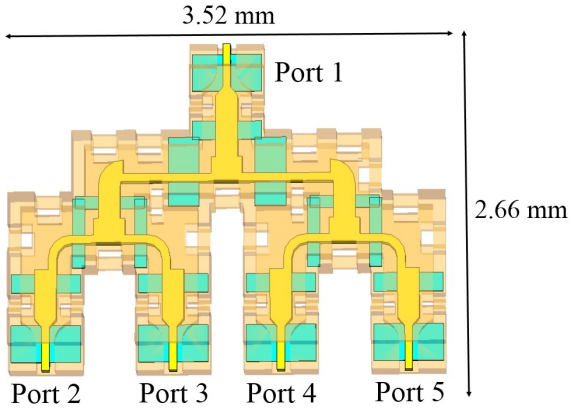

Fig. 11. The structure of four-way power divider.

losses of output ports fluctuate between 6.05 dB and 6.4 dB. It can be seen from Figure 12 (b) that the phases of port 2, 3, 4, and 5 are in phase, and the phase imbalance is between –0.42° and 0.52°.

IV. EXPERIMENT AND DISCUSSION

In order to verify the effectiveness of the design, a prototype including two identical two-way rectangular microcoaxial power dividers arranged in a back-to-back configuration is fabricated based on the surface micromachining technology, as shown in Figure 13. And its overall size is 4.18 mm × 1.89 mm × 0.5 mm. The test method is the same as that of the back-to-back transition.

The simulated and measured results of the fabricated prototype are presented in Figure 14. The measured insertion loss fluctuates between 0.11 dB and 1.18 dB, which implies to a certain extent that the insertion loss of the proposed two-way power divider is from 0.055 dB to 0.59 dB over the W band. The tested S_{21} curve is basically consistent with the simulation, which illustrates the effectiveness of the design. Moreover, the measured S_{11} is less than -10 dB at 75-110 GHz and less than -20 dB at 75-93.3 GHz.

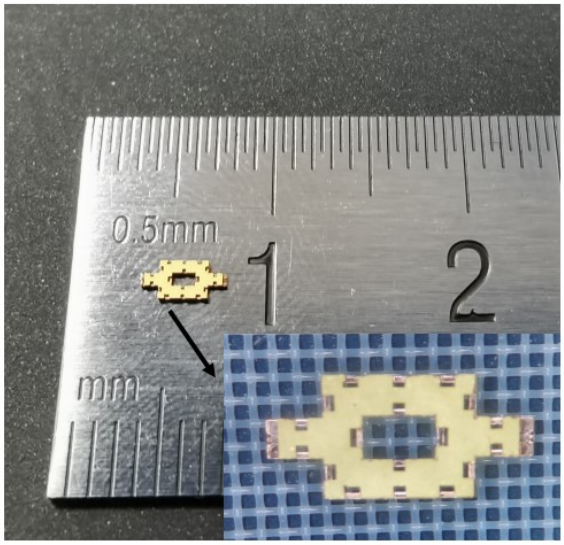

Fig. 13. Photograph of the fabricated prototype.

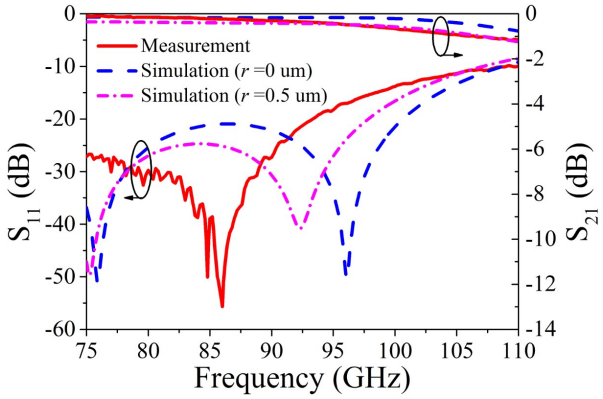

Fig. 14. Simulated and measured results of the fabricated prototype.

It can be found that the measured S_{11} response is quite different from the simulated one. The main reasons for the differences between the simulated results and the measured results include the fabrication errors and the measurement errors. Fabrication errors mainly include the surface roughness, unclean removal of photoresist and the inconsistency of the dimensions between the fabricated structure and the design model. The influence of surface roughness on insertion loss is analyzed. When r is 0.5 um, the fitting result of transmission loss is the best. The measurement errors mainly include the calibration of the measurement equipment and the contact position of the probe and the component. The contact position of the GSG probe and CPW affects the matching characteristic of the port. During testing, it is difficult to find the most suitable position.

Table 1: Comparison of some previous power dividers (back-to-back configuration)

Reference	BW (GHz)	IL (dB)	RL (dB)	Channel	Size (mm^3)
11	90.5–94.5	3.8–6	>10	4	not given
7	90–96	2	>20	14	$80 \times 80 \times 54$
17	75–110	0.8–2.6	>14	4	$75 \times 50 \times 19.1$
This work	**75–110**	**0.11–1.18**	**>10**	**2**	$\mathbf{4.18 \times 1.89 \times 0.5}$

BW: bandwidth, IL: insertion loss, RL: return loss.

Table 1 presents a comparison between the proposed power divider and some previous works. It can be found that the presented study has a small insertion loss while maintaining a compact structure.

V. CONCLUSION

In this paper, a two-way T-junction rectangular microcoaxial power divider is designed for W-band application, and the fabrication is based on surface micromachining technology. Meanwhile, the power divider can be expanded to more channels as requirement. The measured maximum insertion loss of the two-way power divider is about 0.59 dB over the entire W band, corresponding to a power-combining/splitting efficiency of 87.3%. The power divider is conductive to the W-band communication system with the compact structure and good performance.

REFERENCES

[1] Y. Jiang, Y. Ye, D. T. Li, Z. Y. Huang, C. Wang, J. J. Huang, and N. C. Yuan, "Design of W-band PIN diode SPDT switch with low loss," *Applied Computational Electromagnetics Society (ACES) Journal,* vol. 36, no. 7, pp. 901-907, Jul. 2021.

[2] T. Huang, D. Jiang, and H. Z. Hu, "Wideband power divider using novel split-ring resonator," *Applied Computational Electromagnetics Society (ACES) Journal,* vol. 30, no. 2, pp. 204-207, Feb. 2015.

[3] Y. L. Wu, J. C. Li, and Y. N. Liu, "A simple coupled-line wilkinson power divider for arbitrary complex input and output terminated impedances," *Applied Computational Electro-magnetics Society (ACES) Journal*, vol. 29, no. 7, pp. 565-570, Jul. 2014.

[4] L. Li, J. X. Li, X. Y. Wei, and A. X. Zhang, "A W-band broadband power divider/combiner using two parallel antisymmetric tapered probes," *Int J RF Microw Comput Aided Eng.,* vol. 28, no. 1, pp. 1-9, Jan. 2017.

[5] Z. Y. Huang, Y. Jiang, J. J. Huang, W. D. Hu, and N. C. Yuan, "Flexible design of W-band bandpass filter with multiple transmission zeros," *Microw Opt*

Technol Lett., vol. 63, no. 9, pp. 2355-2358, Sep. 2021.

[6] Y. G. Li, Y. H. Zhang, G. D. Zhu, Z. Sun, and Y. Fan, "A W-band miniature power divider based on E-faced-folded magic-T junction," *2016 IEEE MTT-S International Microwave Workshop Series on Advanced Materials and Processes for RF and THz Applications (IMWS-AMP),* Chengdu, China, pp. 1-3, 2016.

[7] J. Zhan, M. Z. Zhan, and W. D. He, "W-band radial power combiner based on circularly polarized TE11 mode," *2019 IEEE MTT-S International Wireless Symposium (IWS),* Guangzhou, China, pp. 1-3, 2019.

[8] S. Y. Hu, K. J. Song, F. Zhang, Y. Zhu, and Y. Fan, "A novel compact wideband four-way W-band waveguide power divider with low insertion loss," *2016 IEEE MTT-S International Microwave Workshop Series on Advanced Materials and Processes for RF and THz Applications (IMWS-AMP),* Chengdu, China, pp. 1-3, 2016.

[9] T. X. Su, C. J. Yu, and M. H. Zhao, "W-band four-way E-plane waveguide power divider," *2016 IEEE MTT-S International Microwave Workshop Series on Advanced Materials and Processes for RF and THz Applications (IMWS-AMP),* Chengdu, China, pp. 1-3, 2016.

[10] L. J. Zhang and T. Liu, "A new H-plane T-junction waveguide power divider covering the full W-band," *2020 IEEE 3rd International Conference on Electronic Information and Communication Technology (ICEICT),* Shenzhen, China, pp. 803-805, 2020.

[11] J. Li, Y. J. Huang, and G. J. Wen, "W-band longitudinal-slot coupling four-way SIW power combiner /divider," 2017 *International Applied Computational Electromagnetics Society Symposium (ACES),* Suzhou, China, pp. 1-2, 2017.

[12] Y. Li, P. L. Kirby, O. Offranc, and J. Papapolymerou, "Silicon micromachined W-band hybrid coupler and power divider using DRIE technique," *IEEE Microw. Wireless Compon. Lett.,* vol. 18, no. 1, pp. 22-24, Jan. 2008.

[13] E. R. Brown, A. L. Cohen, C. A. Bang, M. S. Lockard, B. W. Byrne, N. M. Vandelli, D. S. McPherson, and G. Zhang, "Characteristics of microfabricated rectangular coax in the Ka band," *Microw Opt Technol Lett.,* vol. 40, no. 5, pp. 365-368, Mar. 2004.

[14] N. A. Sutton and D. S. Filipovic, "Wideband micromachined broadside coupled Schiffman phase shifter," *Electron let.,* vol. 50, no. 6, pp. 454-U115, Mar. 2014.

[15] J. R. Reid, E. D. Marsh, and R. T. Webster, "Micromachined rectangular-coaxial transmission lines," *IEEE Trans Microw Theory Tech.,* vol. 54, no. 8, pp. 3433-3442, Aug. 2006.

[16] K. Chen, B. Yan, and R. M. Xu, "A novel W-band ultra-wideband substrate integrated waveguide (SIW) T-junction power divider," 2010 *International Symposium on Signals, Systems and Electronics,* Nanjing, China, pp. 1-3, 2010.

[17] J. X. Li, L. Li, L. Lu, H. Y. Shi, H. H. Huo, and A. X. Zhang, "Four-way waveguide power divider design for W-band applications," *Int J RF Microw Comput Aided Eng.,* vol. 28, no. 5, pp. 1-5, Jun. 2018.

Zhao-Yu Huang was born in 1992. He received the M.S. degree in Electronics and Communication Engineering from the University of Electronic Science and Technology of China, Chengdu, China in 2018. He is currently working toward Ph.D. degree with the College of Electronic Science and Technology, National University of Defense Technology, Changsha, China. His current research interests include passive RF/microwave circuits, microstrip antennas, and wireless communication.

Bo-Yuan Liu was born in 1991. He has received Master's Degree from University of Electronic Science and Technology, China and currently working toward the Doctor's Degree in National University of Defense Technology. His research interests are microwave and millimeter wave circuits and systems, Radar guidance, electronic countermeasures, and electromagnetic technology.

Yun Jiang was born in Hunan Province, China. He received the M.S. degree in electronics engineering from the University of Electronic Science and Technology of China (UESTC), Chengdu, China, in 2017, and currently he is working toward the Ph.D. degree in National University of Defense technology. His research interests include RF/millimeter-wave components and circuits.

Wen-Tao Yuan was born in 1990. He received his M.S. degree in Computer Science and Technology from the Anhui Normal University in 2016. Currently he is working towards the Ph.D. degree in the College of Electronic Science and Technology, National University of Defense Technology, Changsha, Hunan, China. His research interests include passive microwave circuits design and wireless communication.

Qing-Ping Wang was born in 1988. He received the Ph.D. degree from National University of Defense Technology. He is currently an associate researcher with the National University of Defense Technology. His research interests include automatic target recognition, microwave circuits and systems.

Wei-Dong Hu was born in 1967. He received the Ph.D. degree from National University of Defense Technology in 1997. He is currently a Professor with the National University of Defense Technology. His research interests include microwave and millimeter-wave circuits and systems and radar information processing.

Nai-Chang Yuan was born in Anhui, China, in 1965. He received the M.S. and Ph.D. degrees in electronic science and technology from the University of Electronic Science and Technology of China in 1991 and 1994, respectively. He is currently a Professor with the National University of Defense Technology. His research interests include microwave passive components, active components, antennas, microwave monolithic integrated circuits (MMICs), and RF integrated circuits (RFICs).

Investigation of Electromagnetic Exposure of WPT Coil to Human Body Based on Biological Electromagnetic Safety Assessment

Hongyan Sun[1], Shiliang Hou[2], Yang Zhao[3], Wei Yan[3], and Yongji Wu[3]

[1]Nanjing Normal University Taizhou College
Taizhou, Jiangsu, 225300, China

[2]State Grid Shandong Maintenance Company
Jinan, Shandong, 250118, China
nnuhsl@163.com

[3]School of Electrical and Automation Engineering
Nanjing Normal University, Nanjing, Jiangsu, 210097, China

Abstract – When the wireless power transmission (WPT) system of electric vehicle (EV) is working, the leakage of high frequency electromagnetic field (EMF) to the non-working area will be a threat to human safety. According to SAE J2954 standard, the coupling coils modeling of WPT and car shell modeling are established. WPT's bit-directional guidance technology and deviation correction control strategy are given. According to the harm degree of SAR, power density *P*, current density *J*, and magnetic induction intensity *B* to human body when the human model is in different positions of standing, lying, and sitting, the comprehensive harm index of electromagnetic radiation Σ_{hurt} is creatively proposed to assess the electromagnetic radiation hazard of EV. Field circuit co-simulation helps us to study the bio-electromagnetic safety of WPT in vehicle environment. A human exposure EMF joint test system is designed and made to measure vehicle's surrounding EMF. Through simulation and experimental verification, WPT coil's electromagnetic exposure level to the human body inside the EV meets the requirements of ICNIRP, the EMF at the ankle outside the EV exceeds the standard and needs to be protected.

Index Terms – electric vehicle wireless power transmission (EV WPT), bio-electromagnetic safety assessment, comprehensive hazard index, human body model, field circuit co-simulation, electromagnetic exposure.

I. INTRODUCTION

With the improvement of people's environmental awareness and the deepening of energy conservation and emission reduction ideas, electric vehicles (EVs) represent the development direction of the world automobile industry [1]. Wireless power transmission (WPT) technology does not need wires or other physical contacts. By converting electric energy into high-frequency magnetic energy, the energy is transmitted from the transmitting end to the receiving end, achieving complete electrical isolation [2]. The transmitting end is installed on the ground side. After rectification, power factor correction, inverter and resonance compensation network, the AC of the power grid turns into higher-frequency AC. By controlling the value of compensation capacitor, the frequency of AC is made the same as the resonance frequency of the system [3, 4]. The receiving end is located in the chassis of the vehicle, which is connected with the battery of the EV through the resonance compensation network and the rectifier and filter. It is proposed in paper [5] that there is a large air gap between the coupled transmitting coil and the receiving coil. Compared with paper [5], we find that the air gap will inevitably produce complex electromagnetic fields (EMFs) around the coil and form a strong and harmful electromagnetic radiation to human body. The human body can be regarded as a system with good electromagnetic compatibility (EMC), which can be independent from the electromagnetic environment of the surrounding space [6]. When the human body is exposed to the electromagnetic environment with great changes, the distribution characteristics of the EMF in the human body will change accordingly, which has a potential threat to human health [7, 8].

It is proposed in paper [9] that the influence of electromagnetic radiation on human body is mainly divided into thermal effect and non-thermal effect. After comparing and summarizing papers [9, 11], we found that the essence of thermal effect is that the electromagnetic wave radiated into the biological tissue makes the protein, fat, carbohydrate, and water molecules rotate and

Submitted On: May 13, 2021
Accepted On: August 28, 2021

https://doi.org/10.47037/2021.ACES.J.361012

swing, makes various inorganic ions and charged colloidal particles in the body vibrate rapidly, and makes the organism generate heat locally or integrally. Non-thermal effect refers to the destruction of weak, stable, and orderly EMFs in the human tissues and organs by external EMF. It refers to the biological changes that does not belong to temperature changes after the organism absorbs electromagnetic energy [12, 13].

According to the theory of bio-electromagnetics, human organs show different electromagnetic characteristics under different frequency and power of electromagnetic radiation, that is, different dielectric constant, conductivity, and relative permeability [14]. The basic unit of all human organs is the cell. The composition and structure of a cell determine the different electromagnetic characteristics of organs [15]. The outer layer of the cell is the cell membrane, on which some polar lipid molecules form electric dipoles. The effect of EMF on human body is realized by electric dipole, and the cell membrane has the characteristics of low leakage, so it will have a certain degree of polarization in the EMF [16, 17]. Secondly, there will be intercellular fluid between cells, which contains a certain concentration of charged particles. Because of the selective permeability of the cell membrane and high-frequency EMF, some charged ions in the intercellular fluid can pass through the cell membrane.

The organization of this article is as follows. The model of the WPT coils and vehicle shell are established in Section II. Then, simulation about electromagnetic exposure level of WPT coil to human body model in vehicle environment is studied. In Section III, by setting the comprehensive hazard index Σ_{hurt} of electromagnetic radiation, the safety of electromagnetic exposure of EV wireless charging is evaluated. In Section IV, human exposure EMF joint test system for EV wireless charging is designed, and the EMF around the wireless charging coils of EV is measured. Section V gives the conclusions of this paper.

II. ALIGNMENT GUIDANCE AND DEVIATION CORRECTION CONTROL STRATEGY FOR ALIGNMENT GUIDANCE VISUALIZATION SYSTEM

Because there are multiple solutions to the guidance path in the alignment guidance, it is necessary to study the alignment guidance path planning criteria and perform a global optimization of the path. When the car is parked for charging, it is necessary to study real-time dynamic correction due to the random operation of the driver and passengers to ensure that the vehicle runs according to the established road. In the case of improper

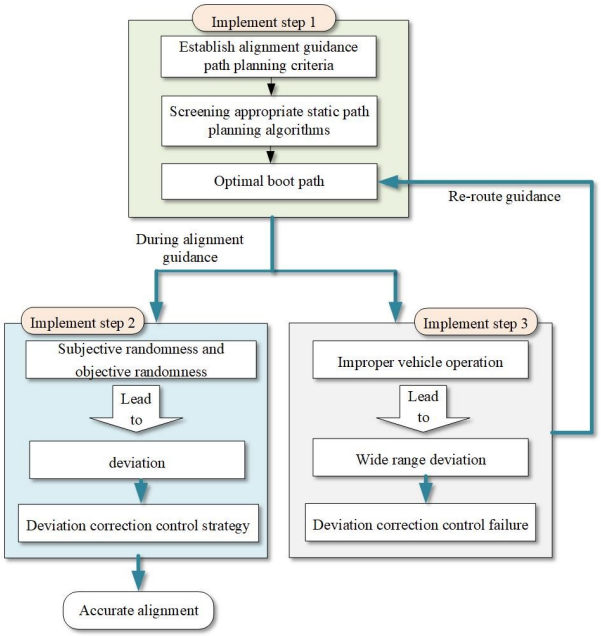

Fig. 1. Overall block diagram of alignment guidance and deviation correction control.

operation, the vehicle will deviate from the route. Therefore, it is necessary to formulate the evaluation criteria of the path deviation and study the path re-planning. As shown in Figure 1, it is the guidance and correction controller. The controller can improve the tolerance for accurate alignment of vehicles in storage.

The specific implementation steps are as follows: first of all, determine the alignment guide path planning criteria, and conduct a global optimization of the guide path. Study the characteristic parameters associated with the vehicle's warehousing path, and establish the constraint relationship between the relevant parameters and the path planning. Comprehensively, consider the size and orientation of the charging area, the surrounding environment of the garage, the distance of the guide path, the guide time, and the difficulty of the driver's operation. Based on the static path planning method of the two-dimensional binary map scene, the appropriate static path planning algorithm is screened, and the guidance path evaluation system is determined. And quantitative indicators of key parameters. The shortest distance is used as the evaluation index, and the traditional Dijkstra algorithm and the improved Dijkstra algorithm are used as the path optimization method to obtain the optimal guidance path. Construct relevant constraints, study methods to avoid falling into local optima, and study evaluation methods of guiding paths.

Then, based on the optimal alignment guidance path, study the correction control strategy of EV when

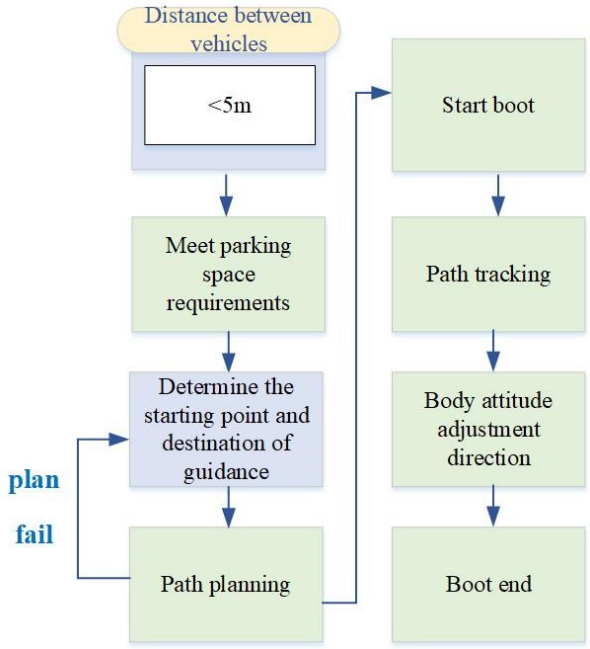

Fig. 2. Flow chart of alignment guidance and deviation correction control.

deviation occurs during parking as shown in Figure 2. In the process of real-time dynamic positioning and guidance of EVs, due to the subjective arbitrariness of human operation, certain deviations will inevitably occur, so it is necessary to propose corresponding control strategies to correct and control them. For this reason, based on real-time monitoring of deviations, in order to realize the dynamic correction control of EVs, an adaptive correction control strategy is proposed to complete the accurate alignment between the on-board end of the EV and the ground end. The specific pairing process is shown in the figure below for guidance and correction.

In the end, formulate the criteria for judging the deviation of the vehicle path, and study the method of re-planning the alignment guidance path. During the parking process, the vehicle may not enter the warehouse according to the alignment guide path, or due to improper operation, the vehicle deviates from the prescribed path in a large area, and the correction control fails. At this time, it is necessary to re-establish a new alignment guide path. Therefore, we must first study the criteria for judging that the path deviation is too large and the vehicle cannot return normally. Comprehensive consideration of the vehicle size, garage size, vehicle turning radius, and vehicle speed and other parameters, as well as the dynamic performance of the correction controller, establish the boundary conditions of whether the vehicle can follow the established path. Research on the

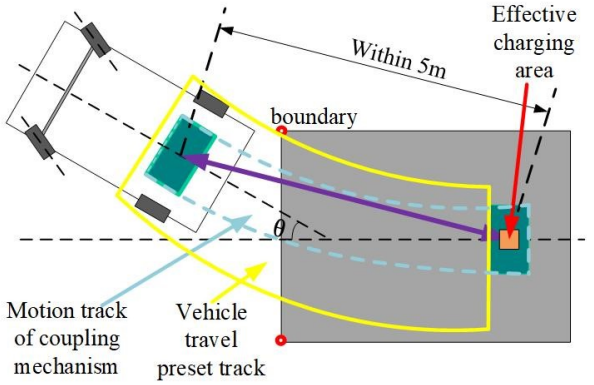

Fig. 3. Schematic diagram of parking guidance path.

comprehensive evaluation method of vehicle excursion under this boundary condition, and establish an accurate and fast judgment mechanism. Study the method of re-planning the alignment guide path when the vehicle deviates from a large-scale path. Based on the path and criteria, combined with the real-time posture of the vehicle, the guidance path is re-optimized and calculated, which improves the fault tolerance rate of vehicle alignment guidance and reduces the difficulty of warehousing.

III. FIELD CIRCUIT CO-SIMULATION OF HUMAN MODELS EXPOSED TO THE EMF OF EV WPT

A. Planar spiral WPT coil model and voxel human model and car shell model

In view of the actual situation of the impact of electromagnetic radiation on human safety when the EV WPT system is applied to the whole vehicle, the WPT coil, the ferrite core, and the whole vehicle are modeled and simulated in detail. The wireless charging coupling mechanism model in the ideal alignment state is shown in Figure 4.

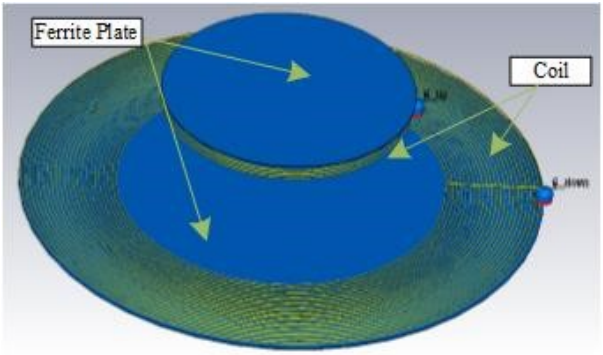

Fig. 4. The physical modeling of wireless charging coil.

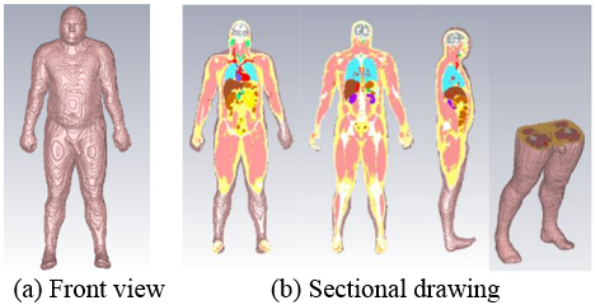

Fig. 5. Front view and sectional view of human voxel model for simulation.

CST Microwave Studio for planar spiral WPT coil modeling. The number of turns at the transmitting coil of the WPT is 23, the minimum radius of the transmitting coil is 230 mm, and the spacing between two adjacent wires is 6 mm; the number of turns at the receiving coil is 8, the minimum radius at the receiving end is 130 mm, and the spacing between two adjacent wires is 6 mm. The minimum air gap is 140 mm, the maximum air gap is 170 mm, the standard air gap is 150 mm, and the maximum tolerance offset distance is 100 mm. A simple two-coil magnetic coupling will lead to the divergence and leakage of the magnetic line of force to the non-working area, and reduce the transmission efficiency of the system. Therefore, round cake ferrite cores are respectively arranged at 2 mm above the coil on the receiving side and 2 mm below the transmitting side. The relative permeability of the core is set to 1200, and the conductivity is set to 0.01 S m^{-1}. In consideration of the cost and the weight of the WPT, the thickness of the ferrite core is 2 mm, and its radius is equal to the maximum radius of the coils on both sides.

Use the Hugo voxel model in the CST voxel family library as a human voxel anatomical model. In order to reduce simulation time and save computer resources, the accuracy of voxel dissection is set to $5 \times 5 \times 5$ mm^3. The front view and dissection diagram of human voxel model are shown in Figure 5 (a) and Figure 5 (b), respectively.

EV can be regarded as a metal shell with good conductivity, which is mainly composed of floor, body and door, similar to a metal shielding shell with cavity. When modeling the car shell, it is divided into body, door, chassis, glass, tire, and seat. Considering the complexity of mesh generation and GPU resources, only the conductive material components such as body, door, and chassis are retained. The material property is set to iron, its conductivity is 1.04×10^7 S m^{-1}, and the relative permeability is 4000. Figure 6 shows the interface after the 3D model of car shell is imported into CST. The size of car shell is 4.5 m $\times$ 1.7 m $\times$ 1.45 m. According to the requirements of GB/T38775.3-2020 *electric vehicle wireless charging system Part 3 special requirements* on the installation position of primary device, when using single module WPT charging device, the primary device of WPT coil is located between the middle and rear end of parking space.

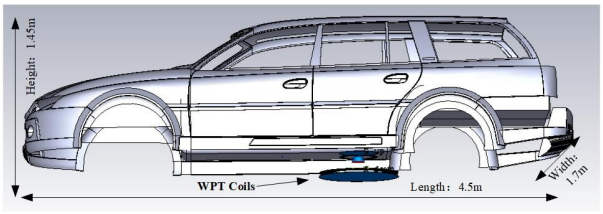

Fig. 6. Simulation model of car shell.

B. Simulation study on electromagnetic exposure level of WPT coil to human body model in vehicle environment

Here, add the transient simulation task in CST design studio, and set the sine voltage with amplitude of 380 V and frequency of 85 kHz as the excitation of EMF simulation. The space EMF around the WPT coil is simulated by field circuit co-simulation method. According to the extracted parameters and the relationship between RLC resonant frequency and capacitance (1), the circuit topology simulation structure is established, as shown in Figure 7.

$$f = \frac{1}{2\pi\sqrt{LC}}. \tag{1}$$

Take the basic full-wave formula of the electromagnetic safety numerical calculation of the human body model as the eqn (2).

$$\begin{cases} \nabla \times H = J \\ J = \sigma E + j\omega D + J_e \\ E = -\nabla V - j\omega A \\ B = \nabla \times A \end{cases}, \tag{2}$$

where, H is the magnetic field intensity, B is the magnetic induction intensity, J is the current density, A is the vector magnetic potential, E is the electric field intensity, V is the potential, and D is the potential shift vector.

Import the human body voxel model Hugo into the car shell model, the vertical magnetic coupling

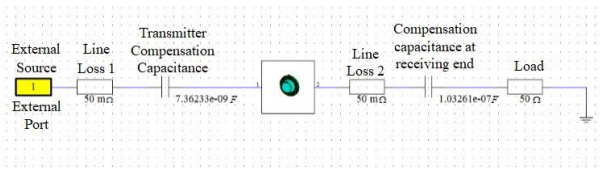

Fig. 7. Circuit topology diagram of wireless charging system.

resonance WPT system, lying and sitting positions, respectively. The body, resonator, and vehicle shell constitute a complete electromagnetic safety simulation system. The human body is set close to the resonator to simulate and calculate the electromagnetic radiation of the human body in different positions relative to the EV in different postures. They are standing close to the door (outside the car) near the resonator, lying on the front seat inside the car, and sitting on the front seat inside the car. The bio-electromagnetic safety of WPT system is evaluated in CST high-frequency simulation environment. The evaluation indexes are SAR, current density *J*, power density *P* of different organs, and magnetic induction intensity *B* of organs.

In the CST simulation, set the magnetic induction *B* probe, SAR probe, and current density *J* probe in the brain, heart, lung, liver, kidney, and foot of human voxel model, and the quantitative values of each organ under the electromagnetic radiation of WPT system in vehicle environment under three postures are calculated. According to ICNIRP, for electromagnetic waves from 3–400 kHz, the magnetic induction intensity *B* of public exposure should not exceed 27 μT, the SAR limit is 0.02 W kg^{-1}, the power density limit *P* is 10 W m^{-2}, and the current density limit *J* is 2000 mA m^{-2}.

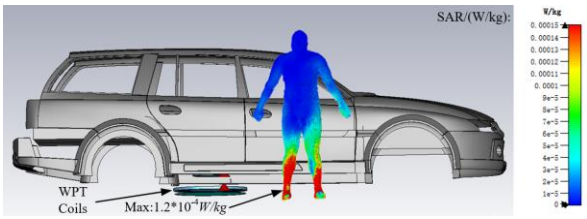

(a) SAR value map of human body in standing posture

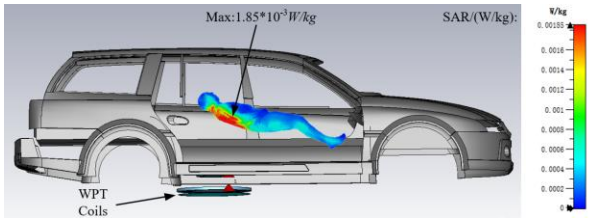

(b) SAR value map of human body in lying position

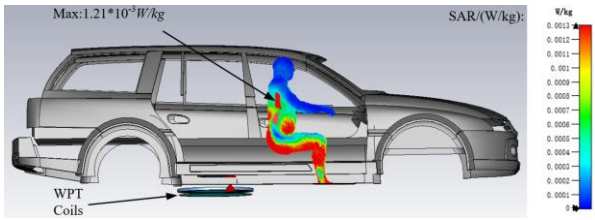

(c) SAR value map of human body in sitting posture

Fig. 8. SAR value distribution of EMF in WPT vehicle environment exposed to human body in three positions and different postures.

From Figure 8, it can be concluded that the SAR index of electromagnetic exposure meets the limit requirements of 0.02 W kg^{-1}, whether it is standing, lying and sitting, whether it is outside or in the vehicle. The results show that when lying in the car, the SAR value of lung is the largest, and the SAR value reaches 1.75×10^{-3} W kg^{-1}, which is 8.75% of the standard. As can be seen from Figure 6, for current density *J*, the *J* of the heart position in the vehicle when lying in the car is the largest, which is 629 mA m^{-2}, accounting for 31.45% of the standard limit; for magnetic induction intensity *B*, when standing at the door side, the maximum *B* at the foot reaches 45 μT, which is 1.67 times of the standard limit.

The automobile chassis is a metal material. The magnetic field formed by eddy current generated by electromagnetic induction is just opposite to the working magnetic field of WPT system. Therefore, the chassis has a better shielding effect on the interior of the EV. However, the magnetic line of the counter magnetic field excited by eddy current effect will circle under the chassis and radiate to the side of the door, and then the EMF will be strengthened. This is the reason why the electromagnetic radiation in the area sandwiched between the chassis and the transmitting coil is bad.

From Figure 9, it can be drawn that the electromagnetic radiation of EV WPT system in the vehicle environment has a more serious impact on heart and lung organs than other organs, so they need to be focused on protection. Due to the electromagnetic shielding effect of car shell and the law that the electromagnetic dose decreases sharply with the increase of distance, the electromagnetic radiation index in the area above the safe height is basically better than that in the car. But the human foot is basically in the same horizontal plane with the WPT transmitting coil, and it is not protected by the electromagnetic shielding of the metal car shell, so when the human body is on the side of the car door, the electromagnetic radiation within the foot is very strong, the magnetic induction intensity of the foot is even as high as 45 μT, which is beyond the safety limit, and the foot current density *J* is also large, about 500 mA m^{-2}. It shows that the electromagnetic environment in the area between the plane of the chassis and the ground outside the coupling mechanism is relatively bad. Therefore, it is necessary to take corresponding electromagnetic shielding measures.

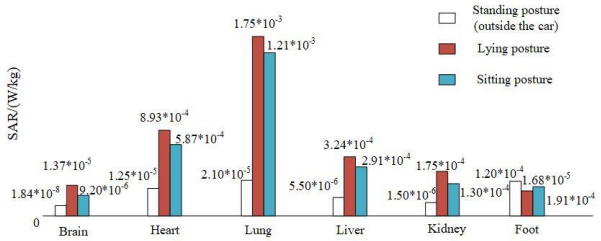

(a) SAR values of several key organs in EV wireless charging system

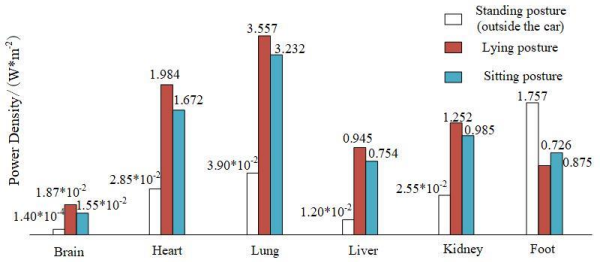

(b) Power density *P* of several key organs in EV wireless charging system

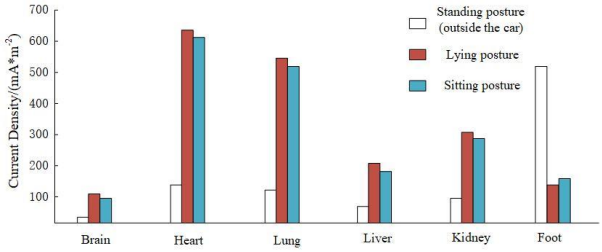

(c) Current density of several key organs in EV wireless charging system

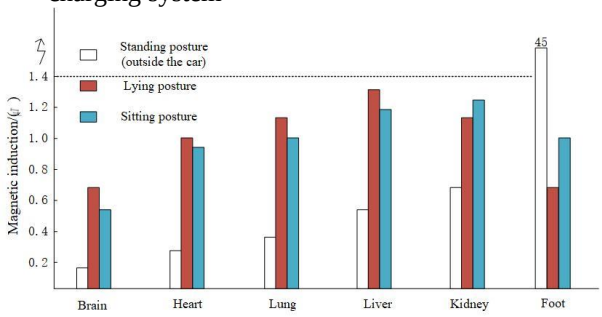

(d) Magnetic induction *B* of several organs in EV wireless charging system

Fig. 9. SAR, P, J, B of six organs in EV wireless charging system.

IV. BIO-ELECTROMAGNETIC SAFETY ASSESSMENT OF EV WPT

Through the theory of bio-electromagnetics, combined with the different weights of SAR, P, J, B damage to human organs, the comprehensive hazard index of electromagnetic radiation on human safety Σ_{hurt} is proposed. As the main factor causing bio thermal effect, SAR index can represent the amount of electromagnetic energy absorbed by local organs of human body, which can best represent the impact of electromagnetic radiation on human body. The harm weight of SAR to human body is defined as 60%; power density *P* is the power value of the local tissue in the organ per unit cross-sectional area, and it also reflects the absorption of electromagnetic radiation by organisms. According to the requirements of GB/T 38775.4 (limits and test methods for electromagnetic environment of EV WPT) for exposure limits of active implantable medical devices, the magnetic induction intensity *B* ultrasonic standard will seriously interfere with the normal operation of human implantable medical devices, and the consequences are very serious. Therefore, *B* must be included in the comprehensive hazard index, and its weight is defined as 20%. According to the knowledge of bio-electromagnetics, it is pointed out in some progress of the research on specific absorptivity rate that the effect of selecting internal electric field strength *E*, induced current *I* (induced current density *J*) or SAR is the same, so the influence of current density *J* is not considered in the comprehensive hazard index Σ_{hurt}, that is, the hazard weight of *J* to human body is defined as 0. In conclusion, the formula of comprehensive hazard index Σ_{hurt} is as follows

$$\Sigma_{hurt} = 60\% \cdot \frac{SAR}{SAR_{\lim}} + 20\% \cdot \frac{P}{P_{\lim}} + 20\% \cdot \frac{B}{B_{\lim}}, \quad (3)$$

where, SAR_{lim}, P_{lim}, and B_{lim} are the limits of SAR, power density *P*, and magnetic induction *B*, obtained from ICNIRP and GB/T 38775.4-2020 respectively, and the limits are 0.02 W kg^{-1}, 10 W m^{-2}, and 27 μT, respectively.

According to the Σ_{hurt} formula, the comprehensive hazard index of each organ with three different postures in the vehicle's different positions is summarized and calculated, as shown in Table 1. Case 1 represents human body in standing posture outside the EV. Case 2 represents human body lying in the EV. Case 3 represents human body sitting in the EV.

Generally speaking, the feet are most severely affected by electromagnetic radiation in the standing position, because the feet are close to the WPT coil or there is no metal shield in the standing position; the lung is the most seriously affected by electromagnetic radiation in lying posture, followed by the heart, which is significantly higher than other organs; in sitting posture, it is also the main cause of lung and heart. The comprehensive harm of electromagnetic radiation is greater, and the indexes of the two are slightly lower in the sitting position than in the lying position, because the organs are closer to the transmitting coil in the lying position.

Table 1: Comprehensive hazard index of organs under three conditions

	Brain(%)	Heart(%)	Lung(%)	Liver(%)	Kidney(%)	Foot(%)
Case 1	0.148483	0.316722	0.437296	0.484944	0.574019	37.207333
Case 2	0.597019	7.387741	13.252889	3.824963	3.917889	2.057956
Case 3	0.466007	5.845741	10.834741	3.269889	3.285926	3.063741

Therefore, the impact of the system on the heart and lung in the car is more serious than other organs, and it needs to be taken as the key protection object. The Σ_{hurt} of other organs outside the car is significantly lower than that inside the car, except for the foot, which is the result of the shielding effect of metal car shell and the sharp attenuation of electromagnetic parameters with distance.

V. HUMAN EXPOSURE EMF TEST SYSTEM FOR EV WIRELESS CHARGING AND EMF MEASUREMENT

A. Non-emission non-metal carrier platform

Considering that the human body is directly exposed to the EMF of EV wireless charging system, the hand-held probe for EMF measurement has great risk, this chapter proposes the design of a joint test system for human body exposure to EMF of EV wireless charging, which is composed of a non-emission non-metallic carrying platform and a three-dimensional EMF test system for EV wireless charging. The EMF three-dimensional test system for EV wireless charging consists of EMF detection module, carbon fiber rod carrying module, servo lifting module, automatic positioning module, and EMF exposure limit evaluation module. The EV wireless charging pile used in the experiment was customized by a company in Xiamen. The experiment was carried out in the 10 m anechoic chamber of EMC laboratory in the experimental verification center of State Grid Electric Power Research Institute.

This non-emission bearing platform can carry the primary and secondary coils of the electric vehicle wireless charging pile, and can freely adjust the position parameters of the air gap distance, radial offset, and tilt angle in the six-axis direction, which can meet the requirements of the electric vehicle wireless charging pile Demand. Space electromotive force measurement under various working conditions of EV WPT. It is composed of non-metallic nylon 66, and the thermoplastic resin material avoids the interference of metal to electromagnetic radiation. Figure 10 is the design model and size drawing of the bearing platform.

The device needs to manually adjust the hand wheel and rotating components to adjust the relative position and angle between the transmitting plate and the receiving plate for EMF test. Control parameters include: X, Y, Z axis travel, translation distance, pitch (tilt) angle, and yaw (rotation) angle. The adjustable effective stroke of X, Y, and Z axes are $\pm$150 mm, $\pm$150 mm, and$\pm$100 mm, respectively; the pitch angle (inclination angle) of receiving coil pad relative to transmitting coil pad is within $\pm 8°$; the rotation around Z-axis is $360°$. Figure 11 is the main view of the non-emission platform and the functional description diagram of the components. In the receiving plate element, the upper part of the receiving coil-carrying plate is covered with steel plate, which is used to simulate the automobile chassis.

As shown in Figure 12, this is the physical drawing of the nylon-66 EV WPT non-emission carrying platform customized by the manufacturer according to the design model and dimension drawing.

B. EMF 3D test system for WPT of EV

As the above has completed the description of the components of the system. It has the function of automatically locating and measuring the EMF according to the protection area and test point specified in the standard. The EMF detection module is the probe for the actual measurement of EMF, and its main component is the German Narda ELT-400 electromagnetic radiation analyzer, as shown in Figure 13, with the frequency

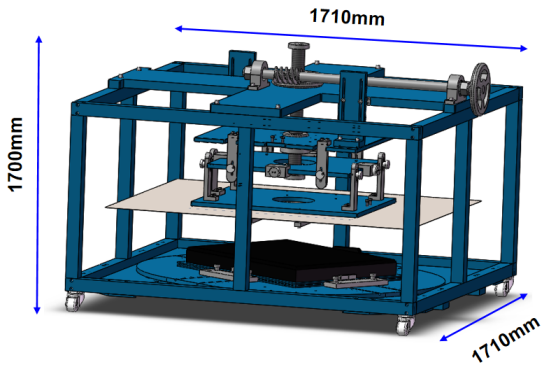

Fig. 10. Design model and dimension drawing of non-launch non-metal carrier.

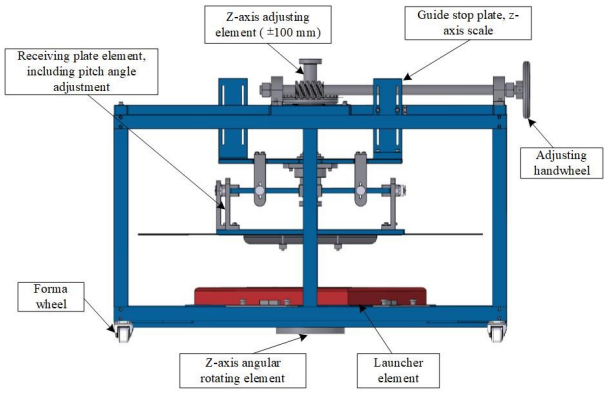

Fig. 11. Main view and component function description diagram of no launching carrier.

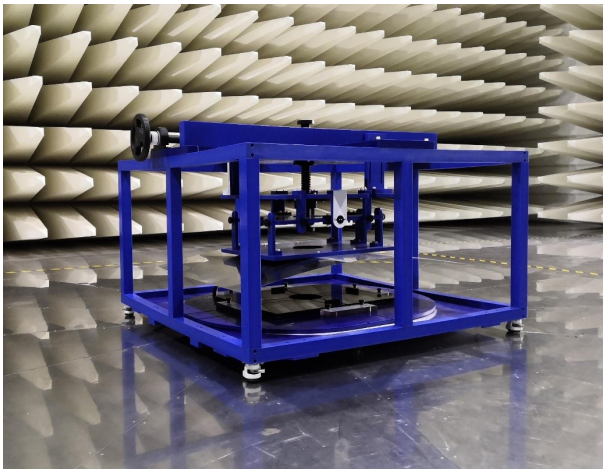

Fig. 12. Physical picture of non-emission non-metal carrying platform.

Fig. 13. Narda ELT-400 electromagnetic radiation analyzer.

range of 1 Hz–400 kHz. Narda ELT-400 instrument is compact in design and equipped with three-dimensional omnidirectional electric and magnetic field sensors. The magnetic field strength can be measured up to 80 mT. Two sets of test standards, IEC 62233 and ICNIRP 1998, are stored in the instrument. In this paper, ICNIRP 1998 standard is selected for the experiment. The instrument displays the percentage of ICNIRP 1998 standard limit value, which can be converted into standard unit Tesla after processing.

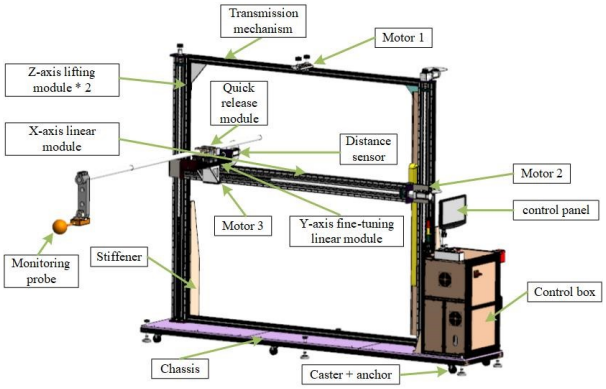

Fig. 14. Design of EMF test system for EV WPT.

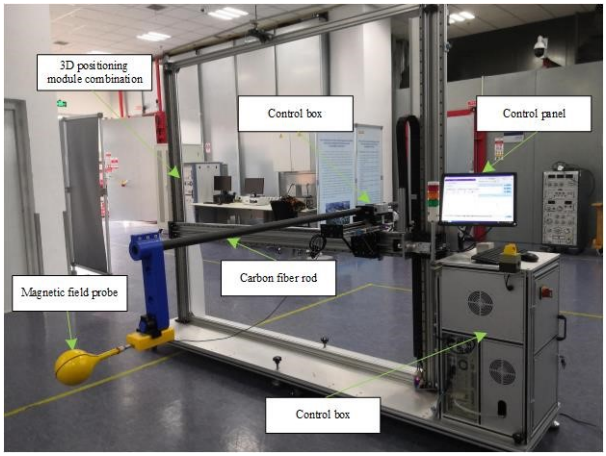

Fig. 15. Physical diagram of EMF test system for EV WPT.

The servo lift module and the carbon fiber rod carrying module form the probe positioning module. The servo lifting module can control the height of the probe and the forward distance of the probe relative to the original position. The carbon fiber rod carrying module can adjust the extended length of the carbon fiber rod, so as to control the X and Y coordinates of the probe. The automatic positioning module is controlled by the path-finding algorithm built in the host computer of the system. After the testers manually input the coordinates of the points to be tested according to the standard position, the test drive transmission system moves the probe to the points to be tested. The human exposure EMF limit evaluation module is a comprehensive processing module of three-dimensional human body model EMF simulation analysis and EV WPT electromagnetic environment evaluation method. The design diagram and physical diagram of EMF test system for EV WPT are shown in Figures 14 and 15, respectively.

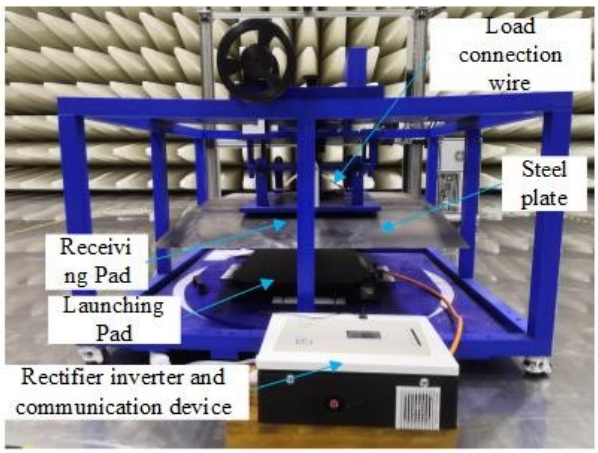

Fig. 16. Charging coil and loading platform.

WPT platform construction and surrounding EMF distribution test

According to the analysis of the circuit and hardware topology model of the magnetic coupling resonant WPT system, the primary rectifier inverter, power factor correction circuit, and WPT transmitter circuit are connected, and the secondary receiving circuit is well connected with rectifier and programmable load. The hardware diagram is shown in Figure 13. Since the electromagnetic radiation of programmable load will interfere with the test of WPT space EMF, the load is placed outside the darkroom, and the indoor WPT system is connected with the outdoor load through the connecting line. Therefore, the load is not reflected in Figure 16.

As shown in Figure 17, the division direction of the eight corners of the WPT charging platform is based on the vertical direction of its four sides and four corners. On each angle, four lines are divided according to the vertical distance of 0 cm, 6 cm, 12 cm, and 18 cm from the WPT primary side coil (above). The WPT standard air gap is 15 cm. The specific test path is shown in Figure 17. Angles 1, 2, and 3 have been marked in the figure, and the angle increases clockwise. The magnetic induction intensity of 0–80 cm is measured from the four edge lines and four corners of the outer side of WPT transmitting coil along the straight line of eight angles. The EMF distribution curve measured in the space around the WPT coil with a standard air gap of 15 cm is given below. EMF distribution joint test system is given in Figure 18.

It can be concluded from Figure 19 that when the 15 cm standard air gap is aligned, the magnetic field distribution of WPT at angles 1, 2, 3, 4, 5, and 8 is roughly the same, and the magnetic field distribution at different heights shows exponential attenuation with distance. Except for angle 2, when the distance between the primary coils is 0 cm or 6 cm, the magnetic field is the strongest, indicating that the magnetic field on the

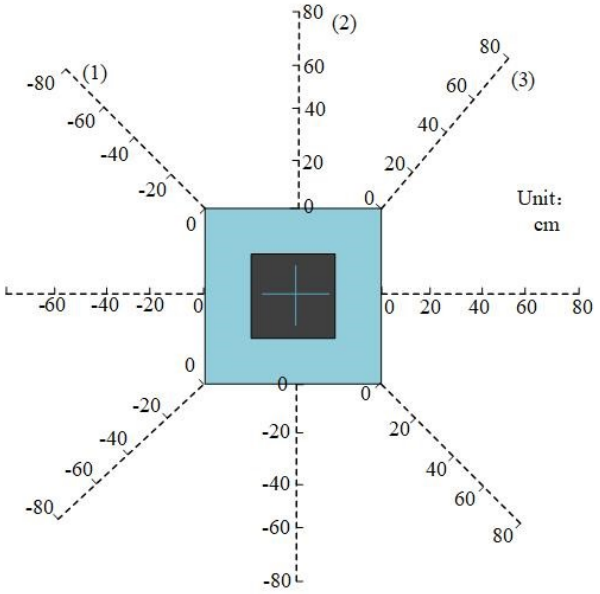

Fig. 17. EMF measurement angles and paths.

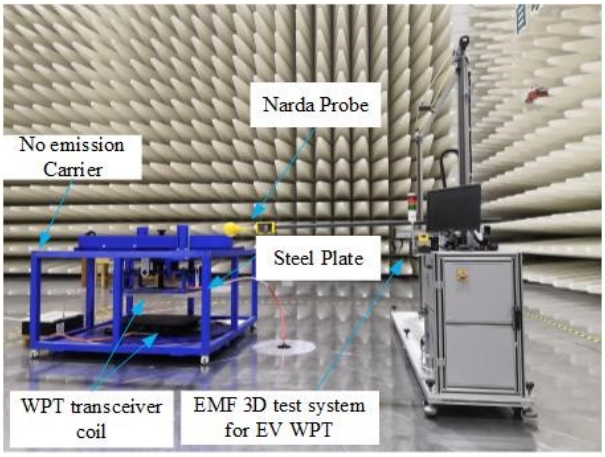

Fig. 18. EMF distribution joint test system.

transmitting coil side is strong. When the radial safety distance from the outside of the transmitting coil is set to 20 cm, all angle can meet the limit value of 27 μT. For angles 6 and 7, the EMF distribution is not quasi-exponential decay, and the magnetic induction of angle 6 is even as high as 120 μT away from the transmitting coil 0 cm. The EMF value reaches limit requirements 27 μT, when the radial distance is 40 cm from the outside of the transmitting coil. The radial safety distance which meets the magnetic field limit of angle 7, is also larger, which is 50 cm. The reason may be that the leading out direction of WPT primary and secondary side′s power lead is close to angle 6, which makes the magnetic field distribution and amplitude of

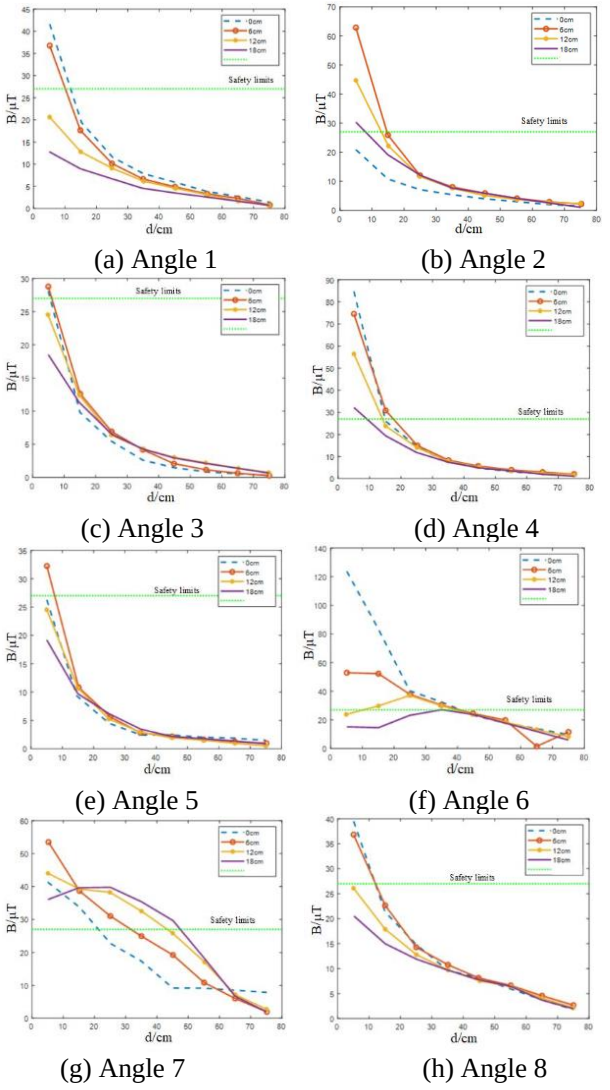

Fig. 19. EMF distribution around WPT with 15 cm air gap aligned.

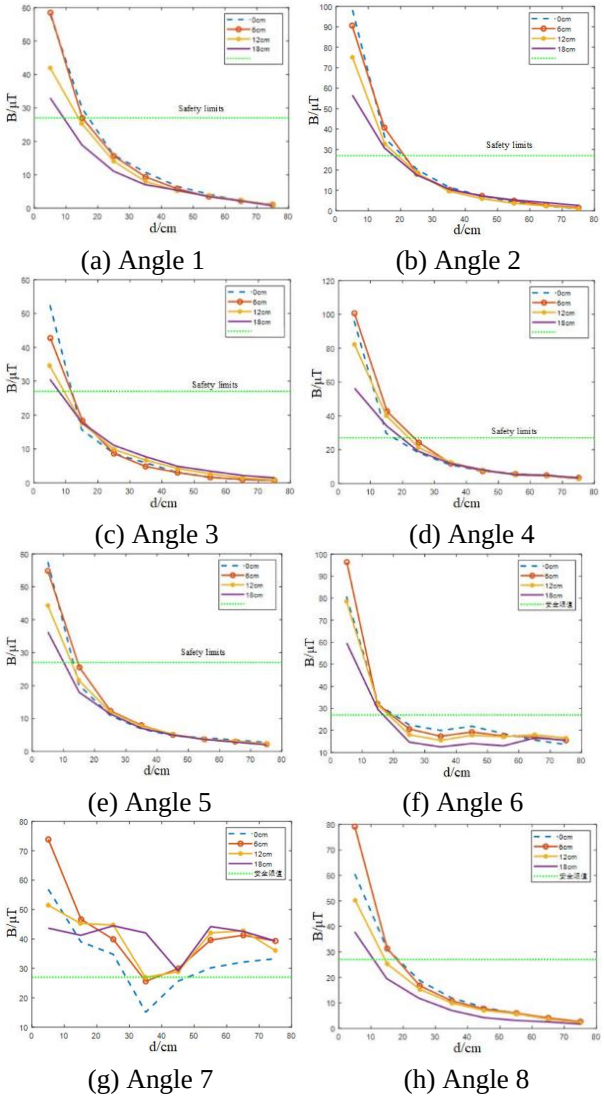

Fig. 20. EMF distribution around WPT with 10 cm radial offset.

angle 6 and 7 change obviously compared with other angles.

Next, test the distribution of EMF around WPT when the radial offset is 10 cm (maximum offset).

It can be drawn from Figure 20 that the EMF distribution around the WPT coil with the maximum radial offset of 10 cm shows that the magnetic induction intensity is increased compared with the standard air gap of 15 cm aligned, which indicates that the offset will enhance the electromagnetic leakage of WPT. From the amplitude of EMF, the strongest magnetic field appears in the direction of angle 4, and the maximum value reaches 102.5 μT when the vertical distance from the primary coil is 6 cm. The second largest magnetic field is 98.5 μT when the vertical distance from the primary coil is 6 cm in the direction of angle 6. Except for angle 6 and 7, the other angles show exponential attenuation, and the maximum value still appears at 0 cm or 6 cm above the primary side coil of WPT, which verifies that the magnetic field near the primary side in the clamping area of WPT transceiver coil is strong, and the maximum EMF of angle 2 reaches 98 μT when it is 0 cm away from the primary side coil. The maximum EMF of angle 8 is about 80 μT when it is 6 cm away from the primary coil. The larger and irregular EMF values of angle 6 and 7 are related to the current leads between angle 6 and 7. The results show that the radial safety distance from the outside of the transmitting coil is set to 30 cm, which can basically meet the requirements of the EMF safety limit under the condition of full load maximum offset. Compared with the

coil aligned, the safety distance under the condition of maximum offset is increased to 10 cm. In addition, the high magnetic field near the current leads on the primary and secondary sides should be treated separately, such as installing shielding sleeves on the leads to minimize the magnetic field.

VI. CONCLUSION

According to ICNIRP and SAE J2954 standards, based on the comprehensive hazard index Σ_{hurt} of WPT electromagnetic radiation on human safety was proposed, the electromagnetic exposure level of WPT circular spiral coil to human body model in vehicle environment was studied. The simulation results show that the indexes of other organs exposed to WPT electromagnetic radiation except feet meet the standard limit requirements. In view of the problem that the EMF of the foot on the side of the door exceeds the standard, the electromagnetic shielding scheme should be adopted. This paper also designs a joint test system for spatial EMF distribution of WPT consisting of non-metallic non-emission platform and EV wireless charging EMF three-dimensional test system. The EMF distribution at different heights of 0–80 cm from the outside of the transmitting coil at eight angles around WPT is measured under the condition of 15 cm standard air gap aligned and the maximum radial deviation of 10 cm, so as to determine the safe working distance of WPT. It provides an effective interactive channel for the guidance of simulation prediction model to experiment and the verification of experiment to simulation prediction model.

ACKNOWLEDGMENT

The support of work from GYW51202001558 of Wuhan Branch of China Electric Power Research Institute, BE2019716 of Jiangsu social development project, 5500-202055070A-0-0-00 of Electric Power Research Institute of State Grid Jiangsu Electric Power Co., Ltd and 201911021 of Nanjing international cooperation project.

REFERENCES

[1] J. Pries, V. P. Galigekere, O. C. Onar, and G. J. Su, "A 50-kW three-phase wireless power transfer system using bipolar windings and series resonant networks for rotating magnetic fields," *IEEE Trans. on Power Electro.,* vol. 35, no. 5, pp. 4500-4517, May 2020.

[2] L. Wang, U. Madawala, and M. C. Wong, "A wireless vehicle-to-grid-to-home Power Interface with an adaptive DC link," *IEEE Jour. of Emerging and Selec. Topics in Power Electro.,* vol. 9, no. 2, pp. 2373-2383, Apr. 2021.

[3] A. S. Kaddour and S. Georgakopoulos, "Wireless power transfer using magneto-electric dipoles," *in 2019 International Appl. Comp. Electro. Society (ACES),* Miami, FL, USA, pp. 1-2, Apr. 2019.

[4] Y. Liu, U. K. Madawala, R. Mai, and Z. He, "Zero-Phase-Angle controlled bidirectional wireless EV charging systems for large coil misalignments," *IEEE Trans. on Power Elrctro.,* vol. 35, no. 5, pp. 5343-5353, May 2020.

[5] L. Zhao, D. J. Thrimawithana, and U. K. Madawala, "Hubrid bidirectional wireless EV charging system tolerant to pad misalignment," *IEEE Trans. on Indus. Electro.,* vol. 64, no. 9, pp. 7079-7086, Mar. 2017.

[6] G. M. Noetscher, A. T. Htet, N. D. Maino, and P. A. Lacroix, "The visible human project male CAD based computational phantom and its use in bio-electromagnetic simulations," *2017 Annual International Conference of the IEEE Engineering in Medicine and Biology Society (EMBC)*, Jeju, Korea, pp. 4227-4230, Sep. 2017.

[7] T. Campi, S. Cruciani, G. P. Santilli, and M. Feliziani, "Numerical analysis of EMF safety and thermal aspects in a pacemaker with a wireless power transfer system," *2015 IEEE Wireless Power Transfer Conference,* Boulder, USA, pp. 1-4, May 2015.

[8] A. Christ, M. Douglas, J. Nadakuduti, and N. Kuster, "Assessing human exposure to electromagnetic fields from wireless power transmission systems," *Proceedings of the IEEE,* vol. 101, no. 6, pp. 1482-1493, Mar. 2013.

[9] J. H. Shim, K. J. Jung, and J. K. Byun, "Analysis of coupling factors for assessment of human exposure to magnetic field from wireless power transfer systems," *Journal of the Korean Institute of Illumina. and Electr. Installa. Engineers,* vol. 32, no. 3, pp. 59-65, Mar. 2018.

[10] H. Schwan and C. Kay, "The conductivity of living tissues," *Annals of the New York Academy of Sciences,* vol. 65, no. 06, pp. 1007-1013, Aug. 2010.

[11] A. Nazeri, A. Abdolali, and M. Mwhdi, "An extremely safe LOW-SAR antenna with study of its electromagnetic biological effects on human head," *Wireless Personal Communica.,* vol. 109, no. 3, pp. 1-14, Nov. 2019.

[12] L. Gun and X. F. Pang, "Biological effects of environmental electromagnetic fields," *Advanced Materials Research*, vol. 183, no. 185, pp. 532-536, Jan. 2011.

[13] L. Hardell and C. Sage, "Biological effects from electromagnetic field exposure and public exposure standards," *Biomedi. & Pharmaco.,* vol. 62, no. 2, pp. 104-109, Feb. 2008.

[14] S. T. Khang, S. C. Chae, T. D. Yeo, and J. W. Yu, "Open-loop maximum efficiency tracking

wireless power transfer for biomedical implants," *2016 European Microwave Conference*, London, UK, pp. 1147-1150, Oct. 2016.

[15] Q. Rui, D. Wu, C. Ji, S. Wang, D. Wilton, and W. Kainz, "An efficient two-dimensional FDTD method for bio-electromagnetic applications," *IEEE Trans. on Magnetics,* vol. 42, no. 4, pp. 1391-1394, May 2006.

[16] I. Meny, N. Burais, F. Buret, and L. Nicolas, "Finite-element modeling of cell exposed to harmonic and transient electric fields," *IEEE Trans. on Magnetics,* vol. 43, no. 4, pp. 1773-1776, Apr. 2007.

[17] N. Shinohara, "Trends in wireless power transfer: WPT technology for energy harvesting, mllimeter-wave/THz rectennas, MIMO-WPT, and advances in near-field WPT applications," *IEEE Microwave Magazine,* vol. 22, no. 1, pp. 46-59, Jan. 2021.

Hongyan Sun is an Assoc. Professor with Nanjing Normal University, Taizhou College. She is a graduate student from Nanyang, Henan Province, graduated in Control Theory and Control Engineering from Zhongyuan University of Technology. Her main research interests are Intelligent Control and Electromagnetic Compatibility.

Shiliang Hou was born in Shandong Province, China. He received his master's degree from School of Electrical and Automation Engineering from Nanjing Normal University, Nanjing, China, in 2021. He is currently working in State Grid Shandong Maintenance Company, Jinan, China. His major research interest is new technology of electrical engineering.

Yang Zhao received his B.E., M.E., and Ph.D. degrees in Power Electronic Technology from Nanjing University of Aeronautics and Astronautics, Nanjing, China, in 1989 and 1992, and 1995, respectively. He is currently the professor with Nanjing Normal University. His research interests are in the areas of Electromagnetic Compatibility, Power Electronics, and Automotive Electronics.

Wei Yan is a Doctor and Assoc. Professor with Nanjing Normal University. He received his M.S. degree in Electrical Engineering and obtained Ph.D. in Physics and Electronics from Nanjing Normal University in 2011 and 2014, respectively. He is the Senior Member of China Electrical Technology Association and the evaluation expert of the Electromagnetic Compatibility Calibration Specification of China.

Yongji Wu was born in Shanxi Province, China. He received his bachelor's degree from Shanxi Institute of Engineering and Technology in 2018. He is currently studying for a master's degree in Electrical Engineering at Nanjing Normal University. The main research direction is new technology of power system.

A Novel Dual-band Ambient RF Energy Harvesting System for Autonomous Wireless Sensor Node Application

Minh Thuy Le, Duc Anh Pham, Hong Tien Vu, Van Duc Ngo, and Quoc Cuong Nguyen

Department of Instrument and Industrial Informatics, School of Electrical Engineering
Hanoi University of Science & Technology, Hanoi 10000, Vietnam.
{thuy.leminh; cuong.nguyenquoc}@hust.edu.vn; {anhducbk.3i; vuhongtien98}@gmail.com; duc.ngo@hhd.vn;
Corresponding author: Quoc Cuong Nguyen (cuong.nguyenquoc@hust.edu.vn)

Abstract – This paper presents a novel dual-band ambient Wi-Fi energy harvesting system for an autonomous wireless sensor node (AWSN) which operates independently without other external power source. While conventional wireless sensor nodes are employing batteries with limited lifespans, an AWSN is supplied by harvested energy and does not require frequent battery replacement. Due to that reason, research on the energy harvesting aspect of AWSNs has been carried out intensively in recent years. By optimizing the matching network, the proposed ambient Wi-Fi energy harvesting system achieves a relatively good efficiency in dual-band at 2.45 GHz and 5.8 GHz. The efficiency reaches a peak at 47.45% and 42% at 2.45 GHz and 5.8 GHz, respectively. The proposed idea is numerically and experimentally demonstrated with the Wi-Fi source in building.

Index Terms – Ambient RF Energy Harvesting, Autonomous Wireless Sensor Node, Dual-band Rectenna.

I. INTRODUCTION

In recent years, rapid development of wireless sensor network promises a better change for life, it gives rise to many useful applications: water monitoring, animal monitoring, forest surveillance, pollution monitoring, and military system [1, 2]. In order to deploy the wireless sensor network (WSN) in real-life, there are many issues that need to be resolved like communication and information security, limited processing speed, reliability, latency, and especially the power source [3, 4]. To operating continuously, power supply for the sensor must be considered. Traditional power supply cords are not suitable due to immobility. Using batteries also has many disadvantages. The limited capacity of power source causes many problems such as short operating time, discontinuous data collection and transmission, maintenance costs, or even environment pollution caused by the batteries [5, 6]. Even though the lifetime of a sensor node can last to several years, thanks to the revolutionary development in low-power integrated circuit, there is always an expiration date and the battery will need to be recharged or replaced. For example, considering thousands of sensor nodes, covering a wide area up to several square miles. Collecting and replacing battery of one by one sin that case is nearly impossible and will dramatically increase the financial strain on operating the wireless sensor system. Furthermore, various applications of WSN are deployed in remote areas, such as forests, oceans, or on animal bodies, making any change and replacement difficult. To solve these issues, several energy harvesting techniques have been proposed as a battery replacement or an additional second power supply. Known as a potential solution for the problem, energy harvesting has the potential to make wireless sensor nodes completely autonomous [7].

Conventionally, there are various sources to harvest from. Heat from geothermal or from daily operation [8, 9], mechanical vibration [10, 11], solar energy [12, 13] and electromagnetics energy [14, 15, 16] are typical examples. Among these candidates, electromagnetic wave energy harvesting has been an especially promising direction. With the dramatic development of wireless communication system, the electromagnetic energy always exists in the ambient environment. Meanwhile, other sources such as heating, mechanical vibration, or solar energy are not always stable. RF energy harvesting utilizes the RF waves which readily exists in the ambient environment in the form of modulated signal such as Wi-Fi, GSM, 3G, 4G, and 5G with very low-input power (from -20 dBm to 0 dBm). In such RF energy harvesting systems, the most important component is rectenna. A rectenna consists of an antenna and a rectifying circuit. It was first invented by William C. Brown [17], inspired by various experiments of Nikolas Tesla about wireless power transfer [18]. Various research in RF power harvesting [19] have proved that harvesting and communicating can share the same set of antennas. However, low-power density of RF waves in the ambience leads to

Submitted On: April 6, 2021
Accepted On: July 18, 2021

https://doi.org/10.47037/2021.ACES.J.361013

poor conversion efficiency from RF power to DC power. Consequently, pursuing high efficiencies is the highest priority for any research in rectenna design.

In recent years, efforts have been done to enhance the conversion efficiency [20], such as using spin diode and backward tunnel diode [21], optimizing based on signal waveform studies [22], harmonics processed [23], and eliminating the matching circuit [24]. In [25] and [26], the authors focused on the antenna designs to achieve complex impedances which matched with the input impedances of the rectifiers, eliminating the losses from matching circuit. This method enhances the conversion efficiency of rectenna and rectifier. However, the flexibility of this rectifier is limited and not suitable with the majority kinds of antenna which are mostly designed with 50 Ohm standard characteristic impedance.

In this study, for sensor nodes in building, the most suitable ambient RF source to harvest is the Wi-Fi at 2.45 GHz and 5.8 GHz which are ubiquitous and yield high-power density. This work proposes another method for adroitly eliminating matching circuit for loss reduction, by optimizing the geometry of each microstrip line in rectifier circuit, and to achieve 50 Ohm standard impedance. Section II presents the proposed dual-band rectifier and rectenna design as well as analysis. Section III provides the results and discussion for the fabricated and simulated structure compared with the related works. Finally, Section IV summarizes and concludes the paper.

II. DUAL-BAND RECTIFIER AND RECTENNA DESIGN

A common rectenna consists of three main parts: Antenna, Rectifier and Load, as shown in Figure 1. Rectenna firstly uses the antenna for receiving RF incident power from the environment. This power is then delivered to the Rectifier and converted to the DC power and consumed in the Load.

To evaluate a rectenna or rectifier, we need to consider how efficient the device can convert from RF power to useful DC power. The conversion efficiency η of the rectenna and rectifier is used for this purpose. For the rectifier, it is defined as the ratio of the output DC power and the input power of the rectifier, as shown in Equation (1):

$$\eta_{rectifier}=\frac{P_{out\_DC}}{P_{in\_Rec}}\ \text{x}\ 100\% =\frac{V_{out\_DC}^2}{R_{load}}\ \text{x}\frac{1}{P_{in\_Rec}}\text{x}\ 100\%\ , \quad (1)$$

where P_{out_DC} and V_{out_DC} are the output power and output voltage of the rectifier, R_{load} is the load impedance, P_{in_rec} is the input power level of the rectifier.

For the rectenna, the conversion efficiency of a rectenna ($\eta_{rectenna}$) is defined as the ratio of the output DC power and the incident power to the rectenna which is corresponding with the spectrum of RF power in the environment (P_{in}), as shown in Equation (2):

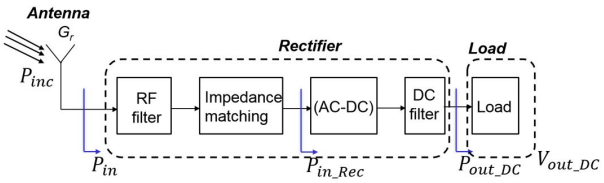

Fig. 1. Block diagram of a rectenna circuit.

$$\eta_{rectenna}=\frac{P_{out\_DC}}{P_{inc}}\ \text{x}\ 100\% =\frac{V_{out\_DC}^2}{R_{load}}\ \text{x}\frac{1}{P_{inc}}\text{x}\ 100\%, \quad (2)$$

where P_{inc} is the input power level of the rectenna that is corresponding with the radiated power from the Wi-Fi modem in the real test.

A. Rectifier design

Rectifier is the most crucial part in a rectenna design. A common rectifier for RF energy harvesting consists of four main parts: RF Filter, impedance matching, AC to DC conversion block, and DC filter as in Figure 1. The most common rectifier structure is the half-wave rectifier (1 stage). This topology includes a single diode and one capacitor for charging and discharging. It is simple. Unfortunately, due to the power requirement on some applications, half-wave rectifier is not adequate. For this reason, the voltage doubler (2 stage), full-wave (3 stage) and multistage (4 stage) rectifiers are preferable due to higher output voltage. However, using more diodes increases the loss on each diode, reducing the total conversion efficiency of the circuit. Figure 2 presents the conversion efficiency of a rectifier at 2.45 GHz and 5.8 GHz corresponding to Wi-Fi based on IEEE 802.11.ac standard with different configurations. It should be noted that in this simulation, impact of power loss is investigated with configurations of the half-wave, voltage doubler, full-wave and multistage rectifier circuits using the same load with the same incident power level to choose the suitable rectifier configuration. The resistor of 1 kΩ is used for the investigation. As observed, each topology will be only suitable for a specific range of input power. In the range of the input power from –10 dBm to 0 dBm, half-wave configuration can provide the highest conversion efficiency. However, as previously mentioned, voltage doubler can provide better output voltage, which is extremely important for supplying electronic devices operation. Therefore, to satisfy the requirements of conversion efficiency and adequate output voltage, voltage doubler configuration is chosen for the proposed design.

The key part of AC-DC block is the rectifying elements, which are usually Schottky diodes, transistors, and CMOS schemes [27]. All rectifier elements are nonlinear and can produce harmonic signals. As

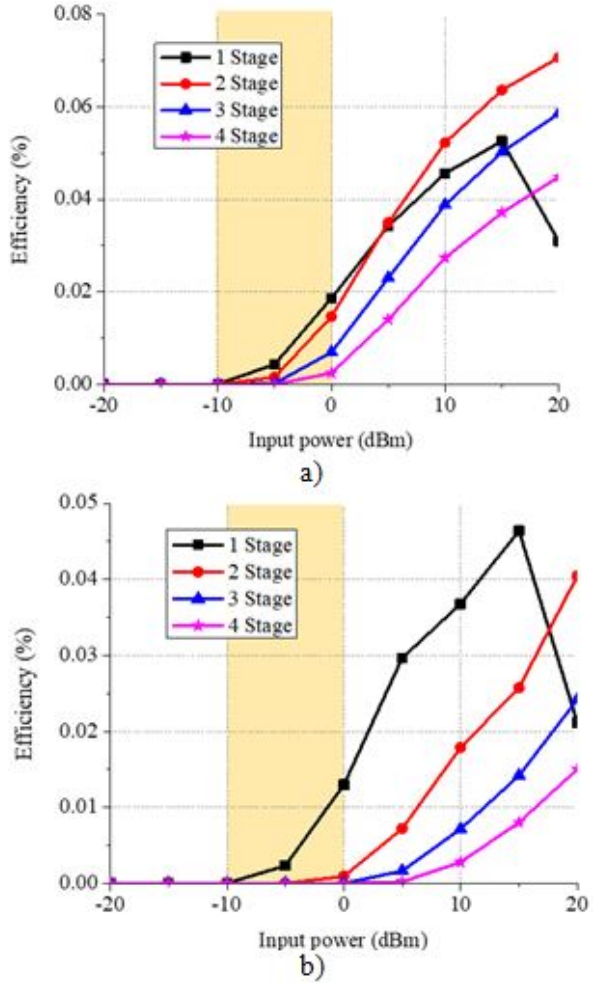

Fig. 2. Simulated conversion efficiency of rectifying circuit at 2.45 GHz (a) and at 5.8 GHz (b) with different configurations (Load R = 1 kΩ).

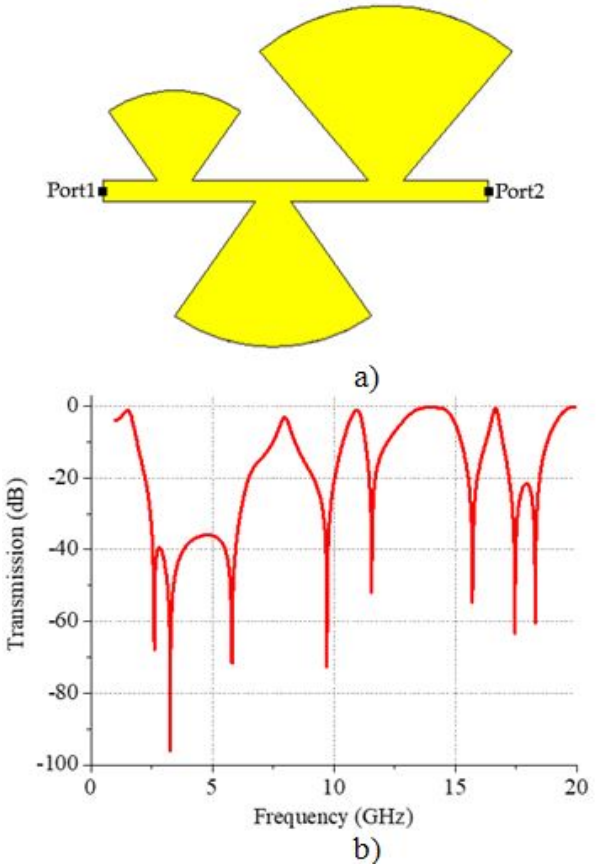

Fig. 3. The designed DC filter (a) and simulated transmission loss (b).

shown in [28], the amplitudes of harmonic signals significantly decrease the efficiency and the quality of output DC power. Thus, eliminating harmonic products is necessary for enhancing the efficiency of the whole rectenna.

In the above fundamental rectifier structure, the capacitor positioned at the output also plays the role of a DC filter. However, this DC filter can only eliminate a small amount of harmonic products. Normally, DC filter based on microstrip technologies are preferred and is employed in this design. To achieve the good filter characteristic not only at 2.45 GHz and 5.8 GHz but also at their second and third harmonics, the proposed design uses three radial stub structures with different radii and open angles, as shown in Figure 3 (a). At the fundamental frequencies, the simulated insertion loss of the designed DC filter are 30.18 dB and 71.51 dB at 2.45 GHz and 5.8 GHz, respectively (Fig. 3 (b)). At the second and the third harmonics of 2.45 GHz, the insertion losses are 35.94 dB and 11.68 dB. For the 5.8 GHz, the designed filter achieves 31.05 dB and 33.52 dB insertion loss at the second and third harmonics, respectively. Due to the fact that the third harmonics have the least effect on the quality of the output [29], the insertion losses of the designed DC filter are suitable. The efficiency of DC filter will be proved by the total conversion efficiency of rectifier in the following contents of this section.

To achieve as high conversion efficiency as possible, impedance matching network should be carefully studied. This work proposes a simple method to eliminating the matching circuit and enhancing the conversion efficiency. The input impedance of the rectifier is optimized with stub length variation which is connected to the shunted diode. Design progress can be summarized as follows:

Step 1. Design the DC filter covering fundamental and harmonic frequencies of 2.45 GHz and 5.8 GHz. The CST and Advanced System Design simulator are co-used for characterization of the DC filter's performances.

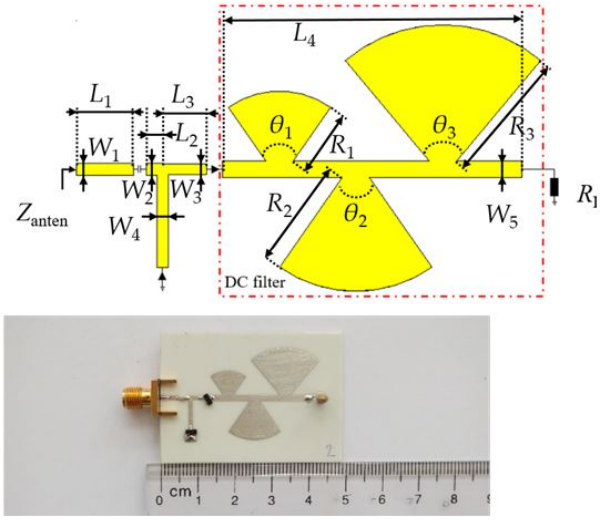

Fig. 4. The proposed rectifier.

Table 1: Geometrical dimensions of entire proposed rectenna

Parameter	L_1	L_2	L_3	L_4	W_1
Value(mm)	5.2	1	3.5	8.4	1.1
Parameter	W_2	W_3	W_4	W_5	R_1
Value (mm)	1.1	0.63	1	1.5	6
Parameter	R_2	R_3	θ_1	θ_2	θ_3
Value (mm)	10	12	70°	70°	80°
Parameter	R_4	R_5	L_5	L_6	W_6
Value (mm)	17	23.2	15.9	15	2.4

Step 2. Design original rectifier following traditional method and observe the characteristic of design. In our design, we optimized original rectifier with the optimal load resistor of 3.9 kΩ.

Step 3. Optimize the rectifier to achieve the best performance in conversion efficiency, by optimizing the geometry of each microstrip line in the AC to DC section. The major changes can be observed at the stub which connects the shunted diode to the main line. Geometrical dimensions of rectifier section (including the DC filter parameters) are listed in the Table 1.

The HSMS-2860 diode of Avago Technologies is used with low forward voltage (V_f), low series resistance (R_s). In general, the proposed design can achieve good efficiency and higher voltage than other earlier works. The detailed comparison of this work with previous works is given in the Table 2.

B. Antenna design

Figure 5 presents the simple dual-band ring antenna which was designed for integration with the proposed rectifier. The total dimension of the antenna is 50 mm × 35 mm, using RO4003C dielectric substrate with 3.5 relative permittivity and 0.0027 loss tangent.

Table 2: Comparison with the related works at the same input power level

Ref.	**Diode**	**Freq.**	**Eff.**	**Volt.**	**Size**
		(MHz)	(%)	(V)	(λ x λ)
[26]	SMS7630	2450	35	N/A	N/A
[30]	SMS7630	1800	40	0.25	0.5 × 0.42
		2450	33	0.22	
[31]	SMS7630	1800	25	0.3	0.3 × 0.3
		2450	19	0.2	0.3 × 0.3
[32]	SMS7630	950	31	0.3	N/A
		1860	32	0.91	
[33]	HSMS2852	2450	45	-	0.6 × 0.73
		5500	8*		
[34]	HSMS2860	24505000	12	0.352	0.97 x 0.68
			4	0.174	
This work	**HSMS2860**	**2450**	**47.4***	**1.36***	0.28 × 0.4*
		5800	**42**	**1.28**	

*The results of only rectifier in proposed structure.

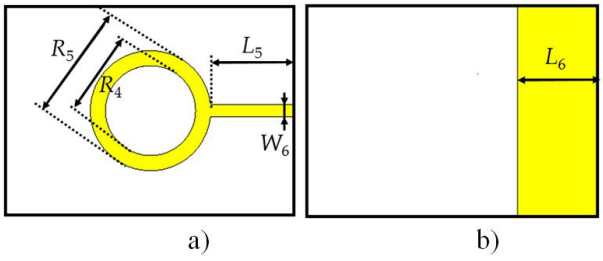

Fig. 5. The dual-band ring antenna in top (a) and bottom side (b).

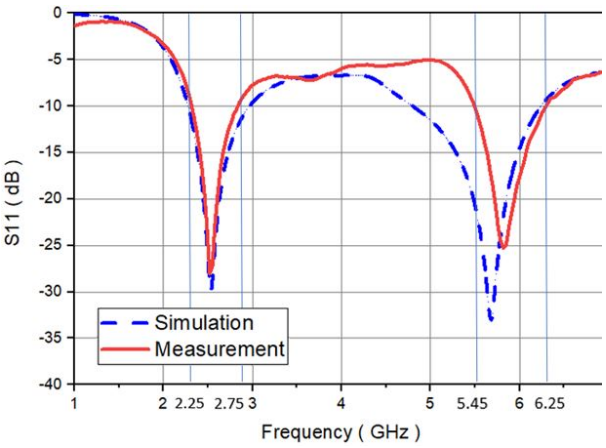

Fig. 6. Simulated and measured reflection coefficient.

Designed antenna is experimentally investigated with a Keysight E5063A vector network analyzer. As can be observed in Figures 6 and 7, full-wave simulation and experimental results show a high agreement.

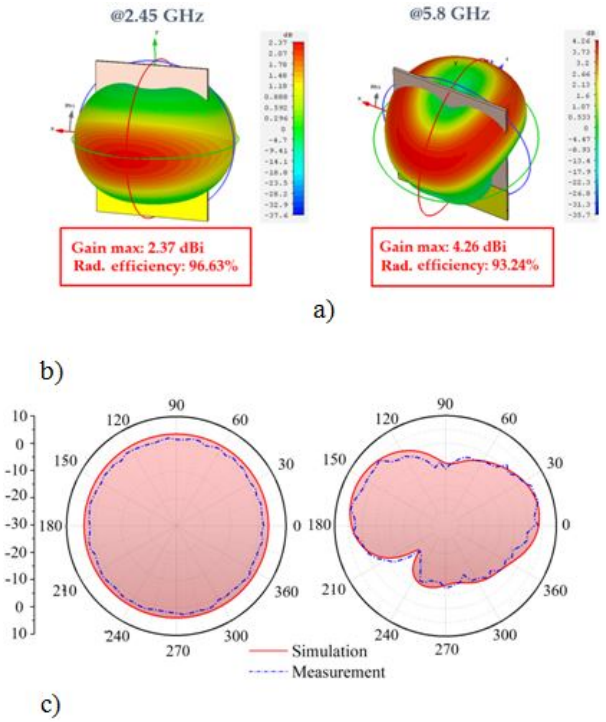

Fig. 7. 3D radiation pattern of the ring antenna (a), simulated and measured radiation pattern of the ring antenna at 2.45 GHz (b) and 5.8 GHz (c).

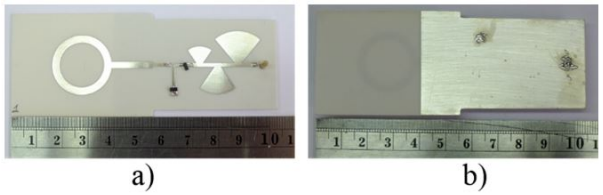

Fig. 8. The dual-band rectenna prototype: front (a) and bottom (b) view.

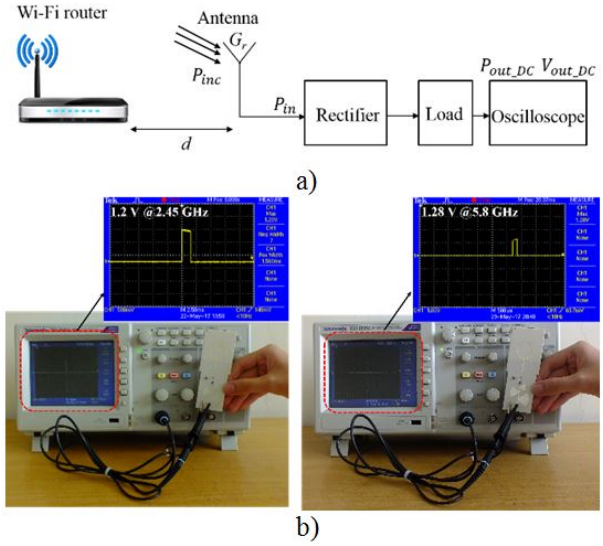

Fig. 9. Output voltage and conversion efficiency measurement setup using Wi-Fi TP-link modem in the building (a) and (b) actual rectenna DC output voltage measured by oscilloscope.

Specifically, –10 dB measured impedance bandwidth is covered from 2.25 GHz to 2.75 GHz and from 5.45 GHz to 6.25 GHz. The omnidirectional radiation patterns of the dual-band antenna are presented in Figure 7, the antenna achieves the peak gain of 2.37 dBi and 4.26 dBi at 2.45 GHz and 5.8 GHz, respectively. Simulated and measured 2D radiation pattern of designed antenna at 2.45 and 5.8 GHz are shown in Figures 7 (b) and (c), respectively.

The proposed rectifier and rectenna was fabricated by the low-cost chemical etching system in RF3I laboratory, Hanoi University of Science and Technology (HUST).

III. EXPERIMENTS AND DISCUSSION

A. Measurement results

Figure 8 shows the image of the dual band rectenna prototype with the total dimension of 40 mm × 103 mm. The measurement for harvested output voltage and conversion efficiency was performed in the building environment. Figure 9 (a) shows the measurement setup, which consists of three main parts: (1) RF source transmitter-Wi-Fi router, (2) rectenna, and (3) oscilloscope to measure the DC voltage at the load of the rectenna. To achieve different input power P_{in}, distance (d) between rectenna and Wi-Fi router are changed. The Wi-Fi signal radiated sources from a TP-link modem router in the building operates at two frequency bands 2.45 GHz and 5.8 GHz.

The resulted output voltage and conversion efficiency of rectifier and rectenna in simulation and measurement is compared in Figures 10 and 11. As observed, the simulated and measured results are agreeable.

For the rectifier case in Figure 10, the measurement of the proposed rectifier has been carried out with several antenna samples from RF3I laboratory. The proposed design achieves the best performances at 2.452 GHz and 5.745 GHz. In particular, at 2.452 GHz, the proposed rectifier achieves a 1.2 V output and 36.14% conversion efficiency in simulation, while in measurement, they are 1.28 V and 42%. Meanwhile, at 5.745 GHz, the output voltage and conversion efficiencies are 1.47 V and 54.26% in simulation and 1.36 V and 47.4% in measurement.

The similarity remains with the results of simulation and measurement of the proposed rectenna in Figure 11.

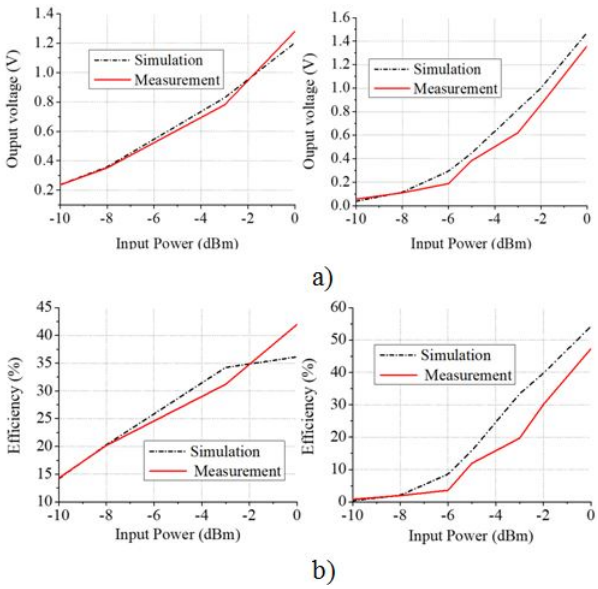

Fig. 10. Simulated and measured output voltage (a) and conversion efficiency (b) of the proposed rectifier.

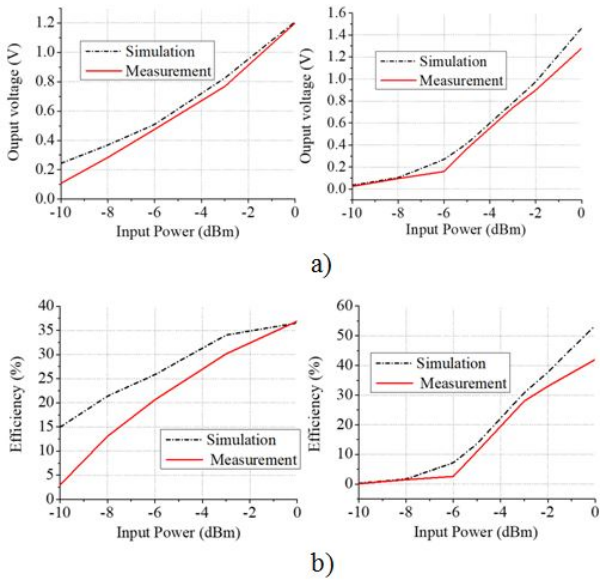

Fig. 11. Simulated and measured output voltage (a) and conversion efficiency (b) of the proposed rectenna.

At 2.452 GHz, the proposed rectenna achieves 1.21 V output and 34.03% conversion efficiency in simulation, while in measurement, these results are 0.77 V and 30.13%. At 5.745 GHz, the output voltage and rectenna conversion efficiencies are 1.46 V and 53.55% in simulation and 1.28 V and 42% in measurement. Obviously, both the output voltage and conversion efficiency of the proposed rectenna are smaller than these characteristics of the proposed rectifier. The main reason is on the difference of antenna used in the measurement. While the rectifier measurement was performed with several antennas which were specially designed for each desired frequency, the proposed rectenna uses a dual-band ring antenna, whose performances in gain, efficiency, and impedance bandwidth was carefully designed with various compromised. The harvested energy using the proposed rectenna is enough to go to the storage circuit which uses super-capacitors to power a wireless sensor node.

B. Discussion

A comparison between the proposed structure and several previous works on rectenna and rectifier is presented in Table 2. As observed, compared to the previous works in [26] [30–33], the proposed structure has better efficiency, much higher output voltage, and more compact size. A plausible explanation is that the impedance matching circuit has been reduced in our work. Meanwhile, the earlier works employ multiple open stubs, shorted stubs, and radial stubs for this purpose [30] [32–34]. Even a simple matching circuit, such as a single inductor [31], can cause losses.

The proposed rectenna is suitable for practical applications. In real life situations, it can be equipped with a power management circuit. However, the integration of this circuit causes additional losses and lowers the overall efficiency [35]. This matter is reserved for future works.

IV. CONCLUSION

This paper proposed a dual-band rectenna for Wi-Fi energy harvesting system. The rectenna exhibited a 1.28 V output voltage and 42% conversion efficiency at 5.8 GHz and 0.77 V and 30.13% at 2.4 GHz from the in-building experiment. This amount harvested energy is enough for storage circuit which uses supercapacitors to power a wireless sensor node. Due to this advantage, the proposed rectenna can be used in practical application, such as supplying low-power wireless sensors. For that purpose, it has to be equipped with a proper power-management circuit, which not only stores the power but also boosts the output voltage to a suitable level, i.e., 3.3 VDC. This matter will be addressed in future works.

ACKNOWLEDGMENT

This research is funded by the Ministry of Education and Training (MOET) under grant number B2020-BKA-11.

REFERENCES

[1] R. J. M. Vullers, R. van Schaijk, H. J. Visser, and J. Penders, “Energy harvesting for autonomous wireless sensor networks,” *IEEE Solid-State Circuits Magazine*, vol. 2, no. 2, pp. 29-38, 2010.

[2] S. Zhang and H. Zhang, "A review of wireless sensor networks and its applications," in *2012 IEEE International Conference on Automation and Logistics*, Zhengzhou, China, pp. 386-389, Aug. 2012.

[3] C. Buratti, A. Conti, D. Dardari, and R. Verdone, "An overview on wireless sensor networks technology and evolution," *Sensors*, vol. 9, no. 9, pp. 6869-6896, Aug. 2009.

[4] M. A. Matin and M. M. Islam, "Overview of wireless sensor network," in Wireless Sensor Networks - Technology and Protocols, M. Matin, Ed. InTech, London, UK, 2012.

[5] N. H. Nguyen, T. D. Bui, A. D. Le, A. D. Pham, T. T. Nguyen, Q. C. Nguyen, and M. T. Le, "A novel wideband circularly polarized antenna for RF energy harvesting in wireless sensor nodes," *International Journal of Antennas and Propagation*, vol. 2018, pp. 1-9, 2018.

[6] K. S. Adu-Manu, N. Adam, C. Tapparello, H. Ayatollahi, and W. Heinzelman, "Energy-harvesting wireless sensor networks (EH-WSNs): a review," *ACM Trans. Sen. Netw.*, vol. 14, no. 2, pp. 1-50, Jul. 2018.

[7] M. Magno, S. Sigrist, A. Gomez, L. Cavigelli, A. Libri, E. Popovici, and L. Benini, "SmarTEG: an autonomous wireless sensor node for high accuracy accelerometer-based monitoring," *Sensors*, vol. 19, no. 12, p. 2747, Jun. 2019.

[8] M. Chen, H. Yu, G. Wang, and Y. Lian, "A batteryless single-inductor boost converter with 190 mV self-startup voltage for thermal energy harvesting over a wide temperature range," *IEEE Trans. Circuits Syst. II*, vol. 66, no. 6, pp. 889-893, Jun. 2019.

[9] L. Hou, S. Tan, Z. Zhang, and N. W. Bergmann, "Thermal energy harvesting WSNs node for temperature monitoring in IIoT," *IEEE Access*, vol. 6, pp. 35243-35249, 2018.

[10] L. A. J. Friedrich, J. J. H. Paulides, and E. A. Lomonova, "Modeling and Optimization of a Tubular Generator for Vibration Energy Harvesting Application," *IEEE Trans. Magn.*, vol. 53, no. 11, pp. 1-4, Nov. 2017.

[11] Z. Yang and J. Zu, "Toward harvesting vibration energy from multiple directions by a nonlinear compressive-mode piezoelectric transducer," *IEEE/ASME Trans. Mechatron.*, vol. 21, no. 3, pp. 1787-1791, Jun. 2016.

[12] Z. Chen, M.-K. Law, P.-I. Mak, and R. P. Martins, "A single-chip solar energy harvesting IC using integrated photodiodes for biomedical implant applications," *IEEE Trans. Biomed. Circuits Syst.*, vol. 11, no. 1, pp. 44-53, Feb. 2017.

[13] S. Mondal and R. Paily, "On-Chip Photovoltaic Power Harvesting System With Low-Overhead Adaptive MPPT for IoT Nodes," *IEEE Internet Things J.*, vol. 4, no. 5, pp. 1624-1633, Oct. 2017.

[14] Y. Zhang, S. Shen, C. Y. Chiu, and R. Murch, "Hybrid RF-solar energy harvesting systems utilizing transparent multiport micromeshed antennas," *IEEE Trans. Microwave Theory Techn.*, vol. 67, no. 11, pp. 4534-4546, Nov. 2019.

[15] J. Liu, K. Xiong, P. Fan, and Z. Zhong, "RF Energy Harvesting Wireless Powered Sensor Networks for Smart Cities," *IEEE Access*, vol. 5, pp. 9348-9358, 2017.

[16] U. Muncuk, K. Alemdar, J. D. Sarode, and K. R. Chowdhury, "Multiband Ambient RF Energy Harvesting Circuit Design for Enabling Batteryless Sensors and IoT," *IEEE Internet Things J.*, vol. 5, no. 4, pp. 2700-2714, Aug. 2018.

[17] W. C. Brown, "The History of Power Transmission by Radio Waves," *IEEE Trans. Microwave Theory Techn.*, vol. 32, no. 9, pp. 1230-1242, Sep. 1984.

[18] K. Adachi, *Radiant Energy: Unraveling Tesla's Greatest Secret*, Educate-Yourself.org, 2001.

[19] T. D. Ponnimbaduge Perera, D. N. K. Jayakody, S. K. Sharma, S. Chatzinotas, and J. Li, "Simultaneous wireless information and power transfer (SWIPT): recent advances and future challenges," *IEEE Commun. Surv. Tutorials*, vol. 20, no. 1, pp. 264-302, 2018.

[20] Hucheng Sun, Yong-xin Guo, Miao He, and Zheng Zhong, "Design of a high-efficiency 2.45-GHz rectenna for low-input-power energy harvesting," *Antennas Wirel. Propag. Lett.*, vol. 11, pp. 929-932, 2012.

[21] C. H. P. Lorenz, S. Hemour, W. Li, Y. Xie, J. Gauthiers, P. Fay, and K. Wu , "Breaking the efficiency barrier for ambient microwave power harvesting with heterojunction backward tunnel diodes," *IEEE Trans. Microwave Theory Techn.*, vol. 63, no. 12, pp. 4544-4555, Dec. 2015.

[22] C. R. Valenta, M. M. Morys, and G. D. Durgin, "Theoretical Energy-Conversion Efficiency for Energy-Harvesting Circuits Under Power-Optimized Waveform Excitation," *IEEE Trans. Microwave Theory Techn.*, vol. 63, no. 5, pp. 1758-1767, May 2015.

[23] M. Roberg, T. Reveyrand, I. Ramos, E. A. Falkenstein, and Z. Popovic, "High-Efficiency Harmonically Terminated Diode and Transistor Rectifiers," *IEEE Trans. Microwave Theory Techn.*, vol. 60, no. 12, pp. 4043-4052, Dec. 2012.

[24] A. Lopez-Yela and D. Segovia-Vargas, "A triple-band bow-tie rectenna for RF energy harvesting without matching network," in *2017 IEEE Wireless*

Power Transfer Conference (WPTC), Taipei, Taiwan, May 2017, pp. 1-4.

[25] T. S. Almoneef, "Design of a rectenna array without a matching network," *IEEE Access*, vol. 8, pp. 109071-109079, 2020.

[26] C. Song, Y. Huang, J. Zhou, P. Carter, S. Yuan, Q. Xu, and Z. Fei, "Matching network elimination in broadband rectennas for high-efficiency wireless power transfer and energy harvesting," *IEEE Trans. Ind. Electron.*, vol. 64, no. 5, pp. 3950-3961, May 2017.

[27] L.-G. Tran, H.-K. Cha, and W.-T. Park, "RF power harvesting: a review on designing methodologies and applications," *Micro and Nano Syst Lett*, vol. 5, no. 1, p. 14, Dec. 2017.

[28] J. Guo, H. Zhang, and X. Zhu, "Theoretical analysis of RF-DC conversion efficiency for class-F rectifiers," *IEEE Trans. Microwave Theory Techn.*, vol. 62, no. 4, pp. 977-985, Apr. 2014.

[29] S. Ladan and K. Wu, "Nonlinear modeling and harmonic recycling of millimeter-wave rectifier circuit," *IEEE Trans. Microwave Theory Techn.*, vol. 63, no. 3, pp. 937-944, Mar. 2015.

[30] S. Chandravanshi, K. K. Katare, and M. J. Akhtar, "A Flexible Dual-Band Rectenna With Full Azimuth Coverage," *IEEE Access*, vol. 9, pp. 27476-27484, 2021.

[31] E. Vandelle, G. Ardila, S. Hemour, K. Wu, and T. P. Vuong, "Compact dual-band rectenna on a new paper substrate based on air-filled technology," in *2019 IEEE Wireless Power Transfer Conference (WPTC)*, London, United Kingdom, pp. 307-311, Jun. 2019.

[32] S.-B. Liu, T. Ngo, and F.-S. Zhang, "Dual-band polarization-independent rectenna for RF energy harvesting," in *2020 IEEE MTT-S International Microwave Workshop Series on Advanced Materials and Processes for RF and THz Applications (IMWS-AMP)*, Suzhou, China, pp. 1-3, Jul. 2020.

[33] M. Mattsson, C. I. Kolitsidas, and B. L. G. Jonsson, "Dual-band dual-polarized full-wave rectenna based on differential field sampling," *Antennas Wirel. Propag. Lett.*, vol. 17, no. 6, pp. 956-959, Jun. 2018.

[34] O. M. Dardeer, H. A. Elsadek, E. A. Abdallah, and H. M. Elhennawy, "A dual band circularly polarized rectenna for RF energy harvesting applications," *Applied Computational Electromagnetics Society (ACES) Journal*, vol. 34, no. 10, pp. 1594-1600, Oct. 2019.

[35] X. Bai, J.-w. Zhang, L.-j. Xu, and B.-h. Zhao, "A broadband CPW fractal antenna for RF energy harvesting," *Applied Computational Electromagnetics Society (ACES) Journal*, vol. 33. no. 5, pp. 482-487, May 2018.

Minh Thuy Le received her engineering (2006), M.S. (2008) degree in Electrical Engineering from Hanoi University of Science and Technology and Ph.D. (2013) in Optique and Radio Frequency from Grenoble Institute of Technology, France. She is an assistant professor at the Department of Instrument and Industrial Informatics and also a Group leader of Radio Frequency group at Department of Instrumentation and Industrial Informatic (3I), School of Electrical Engineering (SEE), Hanoi University of Science and Technology (HUST). Her current interests include Antenna, Beamforming, Meta-materials, RF energy harvesting, indoor localization, and wireless sensors.

Duc Anh Pham was born in Stollberg, Germany, in 1994. He received his B.Eng. degree in Electrical Engineering from Hanoi University of Science and Technology (HUST), Hanoi, Vietnam, in 2017, and the M.S. degree in Microwave and Optics from the School of Electrical and Electronics Engineering, Chung-Ang University (CAU), Seoul, South Korea, in 2020.

From 2017 to 2018, he was an RF engineer with the Viettel Aerospace Institute, involved in researching and developing microwave circuits and systems for aerospace and defense industry. He is currently pursuing his Ph.D. with the School of Electrical and Electronics Engineering, Chung-Ang University (CAU), Seoul, South Korea. His research interests include millimeter-wave antennas, reconfigurable antennas, metasurfaced antennas, and RF energy harvesting.

Hong Tien Vu is currently a 5th-year student, major in Electrical Engineering, School of Electrical Engineering (SEE), Hanoi University of Science and Technology (HUST), Vietnam. His current interests include Antenna, Microwave circuits, and substrate integrated waveguide technology.

Van Duc Ngo was born in Ha Nam, Vietnam, in 1991. He received the B.Eng. degree and M.S. degree in Electrical Engineering from Hanoi University of Science and Technology (HUST), Hanoi, Vietnam, in 2014 and 2018, respectively. His research interests include design and analysis of antenna, RF energy harvesting, RF circuits/systems, and metamaterial.

Quoc Cuong Nguyen received his engineering (1996) and M.S. (1998) degrees in Electrical Engineering from Hanoi University of Science and Technology (HUST), Vietnam, and Ph.D. in Signal-Image-Speech-Telecoms from INP Grenoble, France, in 2002. He is a professor at the Department of Instrumentation and Industrial Informatics and also the head of Department of Instrumentation and Industrial Informatics, School of Electrical Engineering (SEE), Hanoi University of Science and Technology (HUST). His research interests include Signal Processing, Speech Recognition, Beamforming, Smart sensor, and RF communication.

Crosstalk Prediction of Handmade Cable Bundles for New Energy Vehicles

Jinghua Guo[1,*] and Yuanyuan Liu[1,2]

[1]School of Intelligent Manufacturing
Wuxi Vocational College of Science and Technology, Wuxi, Jiangsu, 214028, China
*2697244379@qq.com

[2]School of IoT Engineering
Jiangnan University, Wuxi, Jiangsu, 214122, China

Abstract – This paper presents an effective solution for the crosstalk prediction of handmade cable bundles. The outer- and inner-layer topology of the cross section are analyzed respectively, combined with the actual physical model of the cable bundles. The cascading method is used to deal with the relationship between the structure of cable bundles and the distributed per unit length (p.u.l.) parameter matrices. The random exchange of the wires in the cable bundles is equivalent to the row–column transformation of the p.u.l. parameter matrix, and the values of the p.u.l. parameter matrix after the transformation are modified by equal interval rotation degree. Then, the unconditionally stable finite difference time domain (FDTD) method is used to solve the crosstalk. The verification analysis shows that the change of the element value of the p.u.l. parameter matrix caused by the rotation of the cross-section relative to the ground cannot be ignored. The accuracy of the proposed method is evaluated through comparison to the probability method for a seven-core handmade cable bundles, especially in the high frequency.

Index Terms – Handmade cable bundles, crosstalk, multiconductor transmission line, electromagnetic interference, finite-difference time-domain (FDTD).

I. INTRODUCTION

Electromagnetic compatibility (EMC) plays an important role in the field of automotive electronics [1]. New energy vehicles have been rapidly developed and applied. Compared with traditional vehicles, new energy vehicles need more electronic devices with high voltage, high current, and high frequency. Multiconductor transmission line (MTL) is a bridge to realize energy and signal transmission among electronic devices. Therefore, the electromagnetic environment of new energy vehicles is more complex.

Generally, some transmission lines with similar characteristics will be tightly tied together by hand for the sake of simplicity and beauty. In addition, the assembly of the automobile wiring harness is completed manually from offline, crimping, subassembly, assembly, inspection, and packaging. Therefore, the relative position among the wires in the handmade cable bundles is random. The handmade cable bundles are a kind of random wiring harnesses. A large number of wires are closely arranged, and unintentional electromagnetic radiation may cause crosstalk [2].

Changes in the position between the wires will cause changes in system parameters [3]. It is very important to accurately predict this effect in the early stage of design. The discretization method is introduced by P. Besnier to establish the nonuniform MTL model [4]. The nonuniform MTL is approximated as a large number of small uniform MTLs connected end to end. Monte Carlo (MC) method has been used to analyze the crosstalk of random exchange of wires [5]. The random wiring harness is modeled by random midpoint displacement (RMD) algorithm [6], but the reduced model is too rough. The random displacement spline interpolation (RDSI) method is proposed in [7] considering the smooth change between cascaded segments on the basis of RMD. However, RDSI has a high requirement for the numerical solution of wiring harness and the amount of calculation is large. Assuming that the topological shape of the harness cross section relative to the ground is constant, only the exchange of the position of the wires exits in wiring harness, and the "reasonable worst-case" crosstalk of the wiring harness is predicted by using the probability distribution of the per unit length (p.u.l.) parameter matrix of a single cross section [8][9]. Considering that there is only the exchange of adjacent wires in the harness, the random bundles of twisted wire pairs are modeled and the response value is solved by using the commercial software FEKO based on the method of moments [10]. A simple mathematical model of handmade cable bundles is proposed in [11], which is based on the cascade method and MC method. In all aforementioned papers,

Submitted On: July 5, 2021
Accepted On: July 28, 2021

https://doi.org/10.47037/2021.ACES.J.361014

the influence of the rotation of the topological shape of the harness cross section relative to the ground on the crosstalk has not been considered, and the influence is discussed in detail in this paper.

The finite-difference time-domain (FDTD) method is a common method in the field of crosstalk solution. The FDTD method can segment time and space, and can effectively describe the nonuniformity along with the cable bundles. The conventional FDTD method needs to meet the stability conditions to iterative convergence, which seriously affects the efficiency of the solution [15–17]. Therefore, combined with the unconditionally stable difference scheme [18], the crosstalk solution method of handmade cable bundles is derived in this paper.

The rest of this paper is arranged as follows. The model of handmade cable bundles is established in Second II. In Section III, the distribution p.u.l. parameter matrix of the model is solved. Section IV gives the experimental verification and analysis. Finally, Section V draws the conclusion.

II. MODELING OF HANDMADE CABLE BUNDLES

The application of handmade cable bundles under a certain type of car window is shown in Figure 1. The wire harness has the characteristics that the wires are close to each other, and the relative positions between the wires change randomly. Several wire types are shown in Figure 1. However, the physical parameters of the wires, including the material and radius of the conductor, the material and thickness of the insulation, are assumed to be consistent due to the simplification of the model. All the wires are close together to keep the topological shape of the outer circle of the cross section unchanged.

The cross section equivalent model is shown in Figure 2. The blue- and red-dashed lines represent the outer layer topology and the inner layer topology respectively. The cross section of different points along the cable bundles can be realized in two steps. The wires position from cross section 1 to cross section 2 are first exchanged. The second is the rotation of the inner topology from cross section 2 to cross section 3.

Handmade cable bundles are segmented by using cascade method and differential method. Cable bundles in each segment are regarded as parallel MTLs, and the position of wires in each cross section is independent of each other. Cable bundles with different twisting degrees can be equivalent to N-segment cascaded transmission line, which can be obtained from the empirical formula:

$$N = \begin{cases} [\beta l_{cable}], & \beta > 1/l_{cable} \\ 1, & \beta \le 1/l_{cable} \end{cases}, \quad (1)$$

where, β indicates the twisting degree (segment/m), obtained from experience. The physical meaning of twisting degree is the degree of random exchange between wires in the same length of the cable bundles, corresponding to the number of cascaded segments. l_{cable} stands for the length of the cable bundles (m), and [] is the round down symbol.

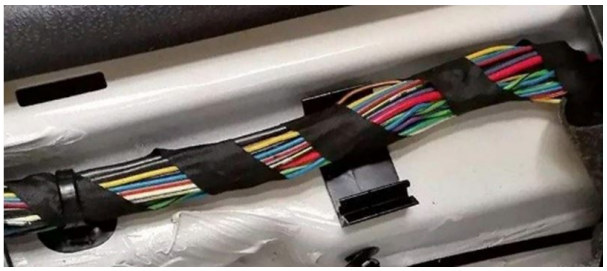

Fig. 1. Handmade cable bundles under car window.

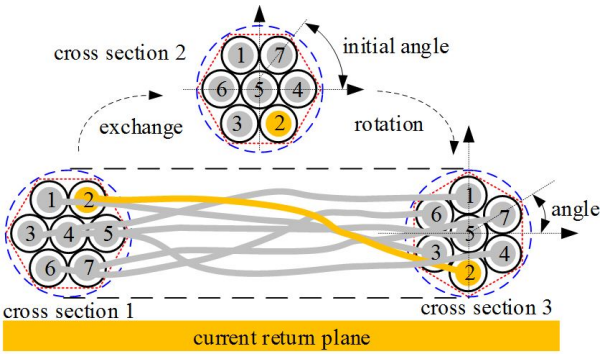

Fig. 2. Cross section equivalent model of handmade cable bundles.

III. PARAMETER MATRIX AND CROSSTALK SOLUTION OF HANDMADE CABLE BUNDLES

A. MTL model

The p.u.l. equivalent circuit of n-core MTLs on the current return plane is shown in Figure 3. The current return plane is selected as the reference conductor. dz stands for the infinitely short transmission line. l, c, g, and r are the p.u.l. parameters. r_i and r_j are the resistance. l_{ii} and l_{ij} are the self-inductance and mutual inductance, respectively. c_{ii} and c_{ij} are the self-capacitance and mutual capacitance, respectively. g_{ii} and g_{ij} are the self-conductivity and mutual conductivity, respectively. The matrix form is

$$\boldsymbol{X} = \begin{bmatrix} x_{11} & x_{12} & \cdots & x_{1i} & \cdots & x_{1j} & \cdots & x_{1n} \\ x_{21} & x_{22} & \cdots & x_{2i} & \cdots & x_{2j} & \cdots & x_{2n} \\ \vdots & \vdots & \ddots & \vdots & \vdots & \vdots & \vdots & \vdots \\ x_{i1} & x_{i2} & \cdots & x_{ii} & \cdots & x_{ij} & \cdots & x_{in} \\ \vdots & \vdots & \vdots & \vdots & \ddots & \vdots & \vdots & \vdots \\ x_{j1} & x_{j2} & \cdots & x_{ji} & \cdots & x_{jj} & \cdots & x_{jn} \\ \vdots & \vdots & \vdots & \vdots & \vdots & \vdots & \ddots & \vdots \\ x_{n1} & x_{n2} & \cdots & x_{ni} & \cdots & x_{nj} & \cdots & x_{nn} \end{bmatrix}, \quad (2)$$

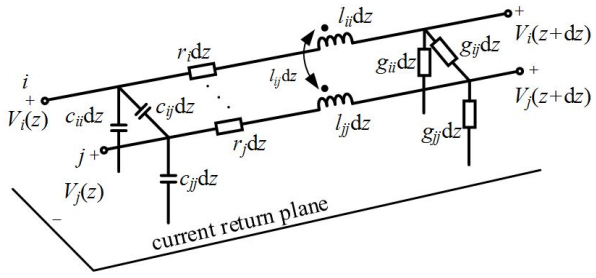

Fig. 3. The p.u.l. equivalent circuit of *n*-core MTL.

where $\boldsymbol{X}$ is p.u.l. the parameter matrix $\boldsymbol{L}$, $\boldsymbol{C}$, $\boldsymbol{G}$, or $\boldsymbol{R}$, x is the corresponding element of l, c, g, and r, $x_{ij} = x_{ji}$. $\boldsymbol{X}$ is a symmetric parameter matrix of order n, the upper and lower triangular elements of the matrix are equal, and the elements in the matrix can be divided into main diagonal and non-main diagonal elements. The main diagonal element value of the parameter matrix is mainly determined by the height of the wire from the reference plane since the physical parameters of the wire are consistent. Similar to the main diagonal elements, the non-main diagonal elements are determined by the relative position between wires and their height from the reference plane.

B. Parameter matrix analysis

The wire position exchange in the cross section can be equivalent to the arrangement and combination of wire numbers in the inner layer topology when changing from cross section 1 to cross section 2 in Figure 2.

The distance between the conductors and the distance between the conductor and the reference plane are constant if the topology of the inner layer is consistent. Therefore, the p.u.l. mutual inductance, self-inductance, mutual capacitance, and self-capacitance will remain unchanged. When only wire i and wire j are exchanged, the parameter matrix of the cable bundles is:

$$\boldsymbol{X}' = \begin{bmatrix} x_{11} & x_{12} & \cdots & x_{1j} & \cdots & x_{1i} & \cdots & x_{1n} \\ x_{21} & x_{22} & \cdots & x_{2j} & \cdots & x_{2i} & \cdots & x_{2n} \\ \vdots & \vdots & \ddots & \vdots & \vdots & \vdots & \vdots & \vdots \\ x_{j1} & x_{j2} & \cdots & x_{jj} & \cdots & x_{ji} & \cdots & x_{jn} \\ \vdots & \vdots & \vdots & \vdots & \ddots & \vdots & \vdots & \vdots \\ x_{i1} & x_{i2} & \cdots & x_{ij} & \cdots & x_{ii} & \cdots & x_{in} \\ \vdots & \vdots & \vdots & \vdots & \vdots & \vdots & \ddots & \vdots \\ x_{n1} & x_{n2} & \cdots & x_{nj} & \cdots & x_{ni} & \cdots & x_{nn} \end{bmatrix}. \quad (3)$$

The transformation of the parameter matrix in (3) and (2) can be expressed as:

$$\boldsymbol{X}' = \boldsymbol{P}\boldsymbol{X}\boldsymbol{P}, \quad (4)$$

where $\boldsymbol{P}$ is the elementary matrix after exchanging rows i and j. When the inner layer topology is the same, the two kinds of cross sections can always be obtained by exchanging each other for up to n-1 times.

The inner layer topology has a certain degree of rotation difference with respect to the reference plane when changing from cross section 2 to cross section 3 in Figure 2, and the clockwise direction is taken as the rotation direction. The inner layer topology is consistent with the initial inner layer topology after rotating 60° clockwise in the seven-core cable bundles. Therefore, only rotation from 0° to 60° needs to be considered. The rotation of the inner layer topology affects the position of each wire to the ground.

The effect of $\boldsymbol{R}$ and $\boldsymbol{G}$ on crosstalk actually is small, which can be ignored. $\boldsymbol{L}$ and $\boldsymbol{C}$ play a decisive role in crosstalk. The cross section of handmade cable bundles under the mirror method is shown in Figure 4. The right side is the reference cross section of rotation degree. i' and j' are the mirror images of wire i and wire j respectively. According to Ampere's law, the self-inductance of wire i is:

$$l_i = \frac{\psi_i}{I_i} = \frac{\mu_0}{2\pi}\ln\left(\frac{h_i}{r_{wi}}\right) + \frac{\mu_0}{2\pi}\ln\left(\frac{2h_i}{h_i}\right) = \frac{\mu_0}{2\pi}\ln\left(\frac{2h_i}{r_{wi}}\right), \quad (5)$$

where μ_0 is the permeability in vacuum. Ψ_i is the magnetic flux of wire i and reference plane when only wire i is excited. I_i is the current in wire i. r_{wi} is the conductor radius of the wire i. The self-inductance is only related to the height above the ground and its radius. The change of height before and after rotation is

$$\Delta h_i = \Delta h_j = 2(r_{wi} + r_{ti})\left[\cos\theta_0 - \cos(\theta+\theta_0)\right], \quad (6)$$

where r_{ti} is the thickness of the insulating layer, and θ_0 is the angle shown in Figure 4.

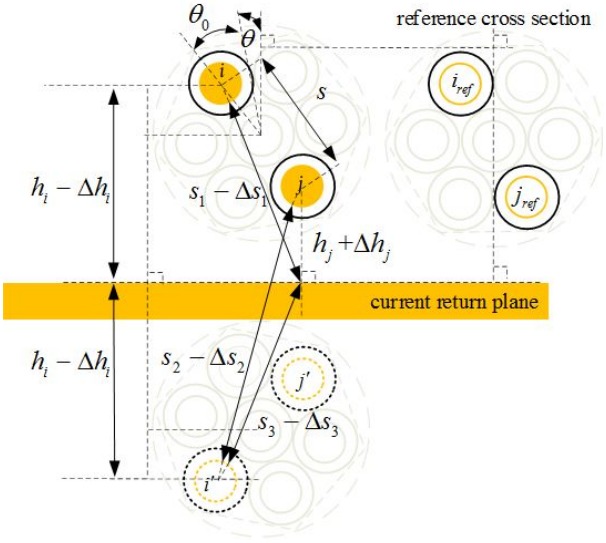

Fig. 4. Cross section of handmade cable bundles under the mirror image method.

The mutual inductance of wire *i* and wire *j* is:

$$l_{ij} = \frac{\psi_{ij}}{I_i} = \frac{\mu_0}{2\pi}\ln\left(\frac{s_1}{s}\right) + \frac{\mu_0}{2\pi}\ln\left(\frac{s_2}{s_3}\right) = \frac{\mu_0}{2\pi}\ln\left(\frac{s_2}{s}\right), \tag{7}$$

where s is the center distance between wire *i* and wire *j*. s_1 is the distance between the wire *i* and the projection point of the wire *j* on the reference ground. s_2 is the distance between the wire *j* and the wire *i'*. s_3 is the distance between the wire *i'* and the projection point of wire *j* on the reference ground. The mutual inductance is only related to s_2 and s. The change of s_2 before and after rotation is:

$$\Delta s_2 = \sqrt{(h_i + h_j)^2 + s\cdot\sin\theta_0} - \sqrt{(h_i + h_j)^2 + s\cdot\sin(\theta+\theta_0)}. \tag{8}$$

It can be seen from (5)–(8) that the element values of the inductance parameter matrix change with the change of rotation angle θ. The inductance parameters of the wire in the cable bundles with or without insulation layer can be calculated according to (5) and (7). The capacitance matrix without insulation is

$$\boldsymbol{C} = \mu_0\varepsilon_0\boldsymbol{L}^{-1}, \tag{9}$$

where ε_0 is the permittivity in vacuum.

The rotation of the cross section to the ground changes the parameter matrix of $\boldsymbol{C}$ and $\boldsymbol{L}$ when the conductor is uninsulated. The finite element method (FEM) is not limited by the insulation layer, but its solving process is complex. The parameter matrix of parallel MTL can be quickly extracted by commercial software ANSYS Q3D based on FEM.

The changes of Δh_i and Δs_2 caused by small rotation angle are also small. In the interval [0, 60°), a series of parameter matrices with equal interval are selected as the parameter matrix library of cable bundles to describe the rotation of cross section. The smaller the rotation degree interval is, the larger the parameter matrix library is, the more accurate the model is and the longer the consumption time is.

C. Crosstalk solution

The handmade cable bundles model described in this paper has the characteristics of cascade, and the FDTD method has the characteristics of spatial segmentation. Therefore, the FDTD method can be used to solve the handmade cable bundles. The conventional FDTD method needs to meet the stability condition to converge, while the difference scheme proposed by Kambiz Afrooz is unconditionally stable when applied to solve the transmission line equation [18]. In this section, the crosstalk solution of handmade cable bundles is mainly realized by combining with the difference scheme proposed by Kambiz Afrooz.

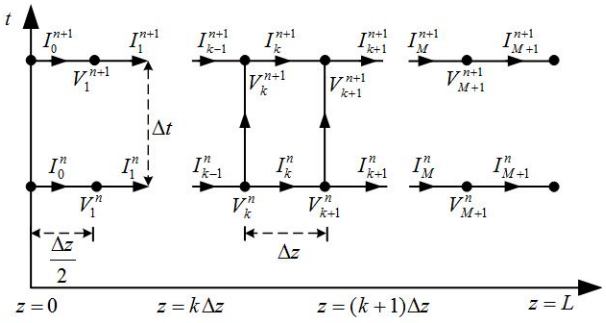

Fig. 5. Schematic diagram of voltage and current on MTL after discretization.

The telegraph equations of MTL are [19]:

$$\frac{\partial}{\partial z}\boldsymbol{V}(z,t) = -\boldsymbol{R}(z)\boldsymbol{I}(z,t) - \boldsymbol{L}(z)\frac{\partial}{\partial t}\boldsymbol{I}(z,t), \tag{10a}$$

$$\frac{\partial}{\partial z}\boldsymbol{I}(z,t) = -\boldsymbol{G}(z)\boldsymbol{V}(z,t) - \boldsymbol{C}(z)\frac{\partial}{\partial t}\boldsymbol{V}(z,t), \tag{10b}$$

where $\boldsymbol{V}(z, t)$ and $\boldsymbol{I}(z, t)$ are the voltage and current at time t at point z on the MTL respectively. The MTL is divided into M segments. The values of $\boldsymbol{R}(z)$, $\boldsymbol{L}(z)$, $\boldsymbol{G}(z)$, and $\boldsymbol{C}(z)$ at different positions on the handmade cable bundles are different. The parameter matrix of segment k is expressed as $\boldsymbol{R}_k$, $\boldsymbol{L}_k$, $\boldsymbol{G}_k$, and $\boldsymbol{C}_k$ respectively.

The forward and backward difference approximations are made for the derivatives of z in (10a) and (10b) respectively:

$$\frac{\boldsymbol{V}_{k+1} - \boldsymbol{V}_k}{\Delta z} = -\boldsymbol{R}_k\boldsymbol{I}_k - \boldsymbol{L}_k\frac{\partial \boldsymbol{I}_k}{\partial t}, \tag{11}$$

$$\frac{\boldsymbol{I}_k - \boldsymbol{I}_{k-1}}{\Delta z} = -\boldsymbol{G}_k\boldsymbol{V}_k - \boldsymbol{C}_k\frac{\partial \boldsymbol{V}_k}{\partial t}, \tag{12}$$

where Δz is the spatial step, $\boldsymbol{V}_k$=$\boldsymbol{V}$($k\Delta z$, t), $\boldsymbol{I}_k$=$\boldsymbol{I}$($k\Delta z$, t). The form can be expressed as:

$$\boldsymbol{V}_{k+1} - \boldsymbol{V}_k + \Delta z\boldsymbol{R}_k\boldsymbol{I}_k + \Delta z\boldsymbol{L}_k\frac{\partial \boldsymbol{I}_k}{\partial t} = 0, \quad k = 1, ..., M, \tag{13}$$

$$\boldsymbol{I}_k - \boldsymbol{I}_{k-1} + \Delta z\boldsymbol{G}_k\boldsymbol{V}_k + \Delta z\boldsymbol{C}_k\frac{\partial \boldsymbol{V}_k}{\partial t} = 0, \quad k = 2, ..., M. \tag{14}$$

The MTL after discretization is shown in Figure 5, the subscript indicates the position of the MTL and the superscript represents the time, Δt is the time step. The terminal diagram of MTL is shown in Figure 6. $\boldsymbol{R}_S$ and $\boldsymbol{R}_L$ are the $n\times n$ dimensional impedance matrix of the source end and the load end of the MTL respectively, and $\boldsymbol{V}_S$ is the n dimensional vector of excitation. Terminal conditions can be expressed as:

$$\boldsymbol{I}_0 = \frac{\boldsymbol{V}_S - \boldsymbol{V}_1}{\boldsymbol{R}_S} = \boldsymbol{I}_S - \frac{\boldsymbol{V}_1}{\boldsymbol{R}_S}, \tag{15}$$

$$\boldsymbol{I}_{M+1} = \frac{\boldsymbol{V}_{M+1}}{R_L}, \tag{16}$$

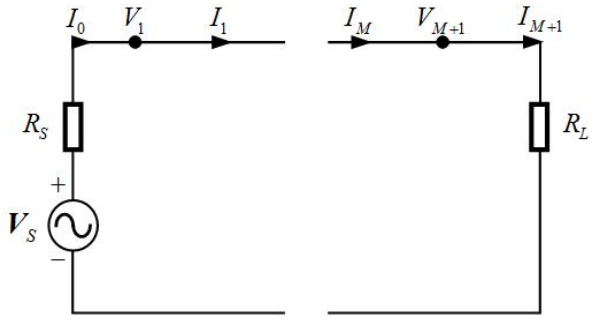

Fig. 6. Schematic diagram of terminal conditions of MTL after discretization.

where

$$\boldsymbol{I}_S = \frac{\boldsymbol{V}_S}{\boldsymbol{R}_S}. \tag{17}$$

The Δz is replaced by $\Delta z/2$ for k = 1, and (15) is

$$\boldsymbol{I}_1 - \boldsymbol{I}_S + \left(\frac{\Delta z \boldsymbol{G}_1}{2} + \frac{1}{\boldsymbol{R}_S}\right)\boldsymbol{V}_1 + \frac{\Delta z \boldsymbol{C}_1}{2}\frac{\partial \boldsymbol{V}_1}{\partial t} = 0. \tag{18}$$

The Δz is replaced by $\Delta z/2$ for $k = M+1$, and (16) is

$$\boldsymbol{I}_M - \left(\frac{\Delta z \boldsymbol{G}_{M+1}}{2} + \frac{1}{R_L}\right)\boldsymbol{V}_{M+1} - \frac{\Delta z \boldsymbol{C}_{M+1}}{2}\frac{\partial \boldsymbol{V}_{M+1}}{\partial t} = 0. \tag{19}$$

The iterative equations are composed of (13), (14), (18), and (19), which are expressed in the form of matrix:

$$\boldsymbol{V}^{n+1} = \left(\left(\frac{\tilde{\boldsymbol{G}}}{2} + \frac{\tilde{\boldsymbol{C}}}{\Delta t}\right) - \frac{\boldsymbol{A}}{4}\left(\frac{\tilde{\boldsymbol{R}}}{2} + \frac{\tilde{\boldsymbol{L}}}{\Delta t}\right)^{-1}\boldsymbol{B}\right)^{-1} \cdot \left\{\frac{\boldsymbol{I}_S^n + \boldsymbol{I}_S^{n+1}}{2} - \left(\left(\frac{\tilde{\boldsymbol{G}}}{2} - \frac{\tilde{\boldsymbol{C}}}{\Delta t}\right) - \frac{\boldsymbol{A}}{4}\left(\frac{\tilde{\boldsymbol{R}}}{2} + \frac{\tilde{\boldsymbol{L}}}{\Delta t}\right)^{-1}\boldsymbol{B}\right)\boldsymbol{V}^n - \left(\frac{\boldsymbol{A}}{2} - \frac{\boldsymbol{A}}{2}\left(\frac{\tilde{\boldsymbol{R}}}{2} + \frac{\tilde{\boldsymbol{L}}}{\Delta t}\right)^{-1}\left(\frac{\tilde{\boldsymbol{R}}}{2} - \frac{\tilde{\boldsymbol{L}}}{\Delta t}\right)\right)\boldsymbol{I}^n\right\}, \tag{20}$$

$$\boldsymbol{I}^{n+1} = \left(\frac{\boldsymbol{R}}{2} + \frac{\boldsymbol{L}}{\Delta t}\right)^{-1} \times \left\{\left(\frac{\boldsymbol{L}}{\Delta t} - \frac{\boldsymbol{R}}{2}\right)\boldsymbol{I}^n - \frac{\boldsymbol{B}}{2}(\boldsymbol{V}^n + \boldsymbol{V}^{n+1})\right\}, \tag{21}$$

where the superscript T denotes transpose,

$$\boldsymbol{A} = \begin{bmatrix} \boldsymbol{I} & 0 & 0 & \cdots & 0 & 0 \\ -\boldsymbol{I} & \boldsymbol{I} & 0 & \cdots & 0 & 0 \\ 0 & -\boldsymbol{I} & \boldsymbol{I} & \cdots & 0 & 0 \\ \vdots & \vdots & \vdots & \vdots & \vdots & \vdots \\ 0 & 0 & 0 & \cdots & -\boldsymbol{I} & \boldsymbol{I} \\ 0 & 0 & 0 & \cdots & 0 & -\boldsymbol{I} \end{bmatrix}, \tag{22}$$

$$\boldsymbol{B} = \begin{bmatrix} -\boldsymbol{I} & \boldsymbol{I} & 0 & \cdots & 0 & 0 \\ 0 & -\boldsymbol{I} & \boldsymbol{I} & \cdots & 0 & 0 \\ \vdots & \vdots & \vdots & \vdots & \vdots & \vdots \\ 0 & 0 & 0 & \cdots & -\boldsymbol{I} & \boldsymbol{I} \end{bmatrix}, \tag{23}$$

$$\tilde{\boldsymbol{G}} = \begin{bmatrix} \frac{\Delta z}{2}\boldsymbol{G}_1 & 0 & \cdots & 0 & 0 \\ 0 & \frac{\Delta z}{2}\boldsymbol{G}_2 & \cdots & 0 & 0 \\ \vdots & \vdots & \ddots & \vdots & \vdots \\ 0 & 0 & \cdots & \frac{\Delta z}{2}\boldsymbol{G}_M & 0 \\ 0 & 0 & \cdots & 0 & \frac{\Delta z}{2}\boldsymbol{G}_{M+1} + \frac{1}{\boldsymbol{R}_L} \end{bmatrix}, \tag{24}$$

$$\tilde{\boldsymbol{C}} = \begin{bmatrix} \frac{\Delta z}{2}\boldsymbol{C}_1 & 0 & \cdots & 0 & 0 \\ 0 & \frac{\Delta z}{2}\boldsymbol{C}_2 & \cdots & 0 & 0 \\ \vdots & \vdots & \ddots & \vdots & \vdots \\ 0 & 0 & \cdots & \frac{\Delta z}{2}\boldsymbol{C}_M & 0 \\ 0 & 0 & \cdots & 0 & \frac{\Delta z}{2}\boldsymbol{C}_{M+1} \end{bmatrix}, \tag{25}$$

$$\tilde{\boldsymbol{L}} = \begin{bmatrix} \Delta z\boldsymbol{L}_1 & 0 & \cdots & 0 & 0 \\ 0 & \Delta z\boldsymbol{L}_2 & \cdots & 0 & 0 \\ \vdots & \vdots & \ddots & \vdots & \vdots \\ 0 & 0 & \cdots & \Delta z\boldsymbol{L}_M & 0 \\ 0 & 0 & \cdots & 0 & \Delta z\boldsymbol{L}_{M+1} \end{bmatrix}, \tag{26}$$

$$\tilde{\boldsymbol{R}} = \begin{bmatrix} \Delta z\boldsymbol{R}_1 & 0 & \cdots & 0 & 0 \\ 0 & \Delta z\boldsymbol{R}_2 & \cdots & 0 & 0 \\ \vdots & \vdots & \ddots & \vdots & \vdots \\ 0 & 0 & \cdots & \Delta z\boldsymbol{R}_M & 0 \\ 0 & 0 & \cdots & 0 & \Delta z\boldsymbol{R}_{M+1} \end{bmatrix}, \tag{27}$$

$$\boldsymbol{V} = \begin{bmatrix} \boldsymbol{V}_1 & \boldsymbol{V}_2 & \cdots & \boldsymbol{V}_{M+1} \end{bmatrix}^T, \tag{28}$$

$$\boldsymbol{I} = \begin{bmatrix} \boldsymbol{I}_1 & \boldsymbol{I}_2 & \cdots & \boldsymbol{I}_{M+1} \end{bmatrix}^T. \tag{29}$$

Notably, the number of difference segments must be a positive integer multiple of the number of cascade segments when (20) and (21) are used to solve the crosstalk of handmade cable bundles.

IV. VERIFICATION AND ANALYSIS

Taking the seven-core handmade cable bundles as an example, the radius of each wire is 0.4 mm, the insulation thickness is 0.6 mm, and the insulation material is polyvinyl chloride (PVC) with relative permittivity of 2.7, the length is 3 m, and the termination impedance of both ends is 50 Ω. Cable bundle is close to the copper current return plane.

A. Deviation rate of inductance and capacitance parameter matrix

The relative deviation rate curves of the $\boldsymbol{L}$ and $\boldsymbol{C}$ parameter matrix with different rotation degrees are shown in Figures 6 and 7, respectively. The reference cross section is selected as the initial cross section, that is, the degree of rotation is 0°. The relative deviation rate is obtained by the p.u.l. parameter ratio of the cross section, which is after rotating 5°, 10°, 20°, and 40° clockwise relatives to the reference plane, and the reference

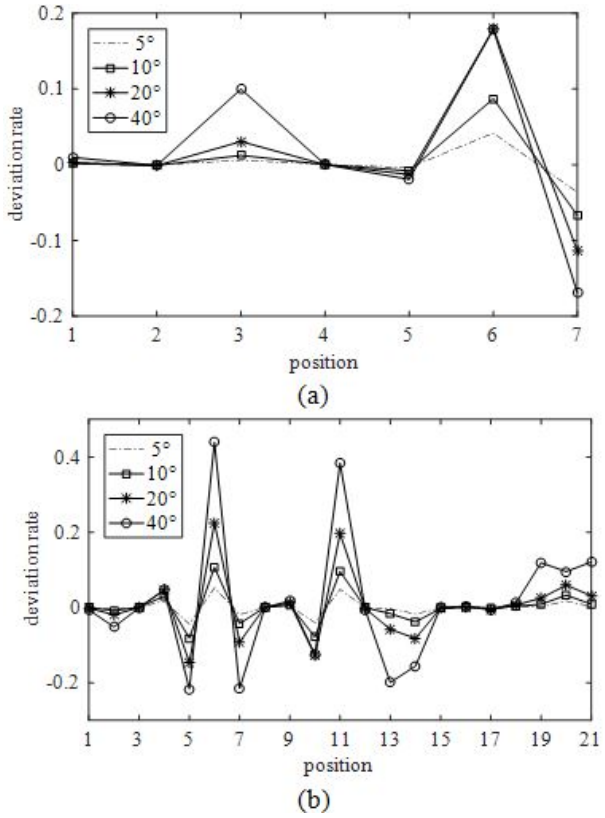

Fig. 7. Capacitance parameter deviation rate: (a) self-capacitance, (b) mutual capacitance.

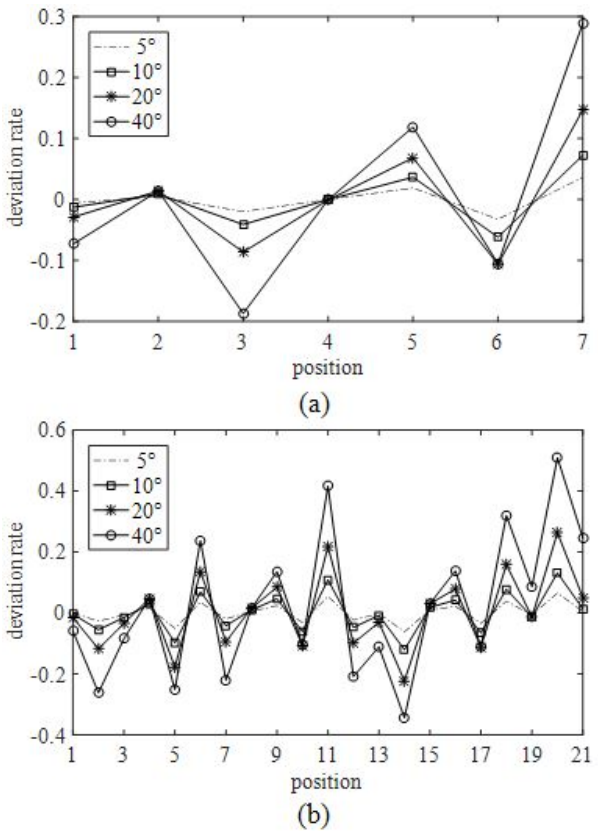

Fig. 8. Inductance parameter deviation rate: (a) self-inductance, (b) mutual inductance.

cross section. Specifically,

$$\text{deviation rate} = \frac{x_{rot} - x_{ref}}{x_{ref}} \times 100\%, \qquad (30)$$

where x_{ref} and x_{rot} represent the element values of the p.u.l. parameter matrix of the reference cross section and the cross section after rotation change, respectively.

The deviation rates of self-capacitance, mutual capacitance, self-inductance, and mutual inductance increase with the increase of rotation degree in Figures 7 and 8. The maximum deviation rates in different cases are given in Table 1. The maximum deviation rates of the four parameters for the 5° are small, which are 3.8%, 3.1%, 2.6%, and 5.6% respectively. Therefore, the rotation degree interval of the parameter matrix library for solving crosstalk is selected as 5°.

Table 1: Maximum deviation rate of parameter matrix under different degrees of rotation

Angle	Capacitance		Inductance	
	Self	Mutual	Self	Mutual
5°	3.8%	3.1%	2.6%	5.6%
10°	8.4%	10.1%	7.5%	12.8%
20°	17.9%	22.9%	14.9%	26.2%
40°	17.9%	43.6%	29.8%	50.9%

B. Crosstalk

The solution result of the near-end crosstalk of the handmade cable bundles is shown in Figure 9 when the twisting degree β = 2. The thick black dashed line and

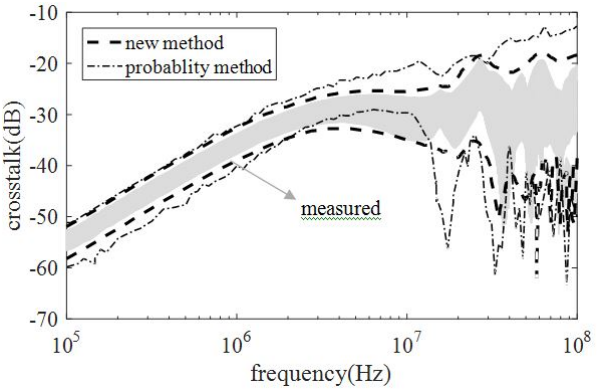

Fig. 9. Near-end crosstalk of the seven-core handmade cable bundles.

Table 2: Absolute values of upper and lower envelope error compared with the measured values

Frequency	New Method		Probability Method	
(Hz)	Upper	Lower	Upper	Lower
10^5	0.73dB	1.10dB	0.73dB	3.13dB
10^6	1.01dB	1.10dB	1.62dB	2.76dB
10^7	1.09dB	0.36dB	5.84dB	5.17dB
10^8	1.73dB	4.93dB	7.49dB	15.02dB

thin black ant line are the upper and lower envelope of the solution result of the proposed method and probability method [20], respectively. The upper envelope is the worst-case crosstalk. The gray area is the range of experimental values [20].

The absolute values of the upper and lower envelope error are shown in Table 2. Compared with the probability method, the proposed method has better agreement with the experimental results, especially at high frequency. Taking 10 MHz as an example, the absolute values of the upper and lower envelope error of the new method and the probability method are 1.09 dB, 0.36 dB, 5.84 dB, and 5.17 dB respectively. The proposed method has good accuracy in the frequency band of 100 kMz–20 MHz. However, the accuracy of the proposed method is reduced in the frequency band of 20 MHz–100 MHz, which is mainly due to the high frequency characteristics of experimental equipment. The worst-case crosstalk predicted by the proposed method can accurately reflect the actual crosstalk of the handmade cable bundles.

V. CONCLUSION

This paper proposes a novel prediction method of crosstalk for handmade cable bundles. The proposed method studies the cable bundles model from the outer- and inner-layer topology of the cross section. By considering the rotation angle of the cross section to the reference plane, the cascade harness model can be closer to the actual handmade cable bundles. The crosstalk of handmade cable bundles can be predicted by combining the unconditionally stable FDTD method. The rotation of the cross section relative to the reference plane cannot be ignored, which is verified by the deviation rate of the p.u.l. parameter matrix under different rotation angles. The technique is verified by an example of seven-core handmade cable bundles. Compared with the experimental results, the proposed method has higher precision than the probability method.

REFERENCES

[1] S. Chabane, P. Besnier, and M. Klingler, "An embedded double reference transmission line theory applied to cable harnesses," *IEEE Trans. Electromagn. Compat.*, vol. 60, no. 4, pp. 981-990, Aug. 2018.

[2] S. Chabane, P. Besnier, and M. Klingler, "A modified enhanced transmission line theory applied to multiconductor transmission lines," *IEEE Trans. Electromagn.c Compat.*, vol. 59, no. 2, pp. 518-528, Apr. 2017.

[3] C. R. Paul, "Sensitivity of crosstalk to variations in cable bundles," *Proc. 1987 IEEE Int. Symp. EMC*, pp. 617-622, 1987.

[4] P. Besnier and P. Degauque, "Electromagnetic topology: investigations of non-uniform transmission line networks," *IEEE Trans. Electromagn. Compat.*, vol. 37, no. 2, pp. 227-233, May 1995.

[5] A. Ciccolella and F. G. Canavero, "Stochastic prediction of wire coupling interference," *Proc. 1995 IEEE Int. Symp. EMC*, pp. 51-56, 1995.

[6] S. Salio, F. Canavero, D. Lecointe, and W. Tabbara, "Crosstalk prediction on wire bundles by Kriging approach," *IEEE Int. Symp. Electromagn. Compat*., pp. 197-202, 2000.

[7] S. Sun, G. Liu, J. Drewniak, and D. Pommerenke, "Hand-assembled cable bundle modeling for crosstalk and common-mode radiation prediction," *IEEE Trans. Electromagn. Compat*., vol. 49, no. 3, pp. 708-718, Aug. 2007.

[8] M. Wu, D. Beetner, T. Hubing, H. Ke, and S. Sun, "Estimation of the statistical variation of crosstalk in wiring harnesses," *2008 IEEE Int. Symp. Electromagn. Compat.*, 2008, pp. 1-7.

[9] M. Wu, D. G. Beetner, T. H. Hubing, H. Ke, and S. Sun, "Statistical Prediction of "Reasonable Worst-Case" Crosstalk in Cable Bundles," *IEEE Trans. Electromagn. Compat.*, vol. 51, no. 3, pp. 842-851, Aug. 2009.

[10] G. Spadacini, F. Grassi, and S. A. Pignari, "Field-to-wire coupling model for the common mode in random bundles of twisted-wire pairs," *IEEE Trans. Electromagn. Compat.*, vol. 57, no. 5, pp. 1246-1254, Oct. 2015.

[11] S. A. Pignari, G. Spadacini, and F. Grassi, "Modeling field-to-wire coupling in random bundles of wires," *IEEE Electromagn. Compat. Mag.*, vol. 6, no. 3, pp. 85-90, Third Quarter 2017.

[12] V. Ramesh Kumar, A. Alam, B. K. Kaushik, and A. Patnaik, "An unconditionally stable FDTD model for crosstalk analysis of VLSI interconnects," *IEEE Trans. Compon., Packag. Manuf. Technol*., vol. 5, no. 12, pp. 1810-1817, Dec. 2015.

[13] C. Huang, Y. Zhao, W. Yan, Q. Liu, and J. Zhou, "A new method for predicting crosstalk of random cable bundle based on BAS-BP neural network algorithm," *IEEE Access*, vol. 8, pp. 20224-20232, Jan. 2020.

[14] Z. Pei, X. Li, Y. Li, and J. Mao, "Transient coanalysis of multicoupled passive transmission lines and

josephson junctions based on FDTD," *IEEE Trans. Appl. Supercond*., vol. 30, no. 1, pp. 1-7, Jan. 2020.

[15] F. Zheng and Z. Chen, "Numerical dispersion analysis of the unconditionally stable 3-D ADI-FDTD method," *IEEE Trans. Microw. Theory Tech*., vol. 49, no. 5, pp. 1006-1009, May 2001.

[16] F. Zheng, Z. Chen, and J. Zhang, "A finite-difference time-domain method without the Courant stability conditions," *IEEE Microw. Guided Wave Lett*., vol. 9, no. 11, pp. 411-443, Nov. 1999.

[17] M. Tang and J. Mao, "A precise time-step integration method for transient analysis of lossy nonuniform transmission lines," *IEEE Trans. Electromagn. Compat*., vol. 50, no. 1, pp. 166-174, Feb. 2008.

[18] K. Afrooz and A. Abdipour, "Efficient method for time-domain analysis of lossy nonuniform multiconductor transmission line driven by a modulated signal using FDTD technique," *IEEE Trans. Electromagn. Compat*., vol. 54, no. 2, pp. 482-494, Apr. 2012.

[19] C. R. Paul, *Analysis of Multiconductor Transmission Lines*, New York, USA: Wiley, 1994.

[20] Z. Zhang, S. Wang, and L. Zhao, "Prediction of crosstalk probability distribution in cable bundles," *Transactions of China Electrotechnical Society*, vol. 32, no. 7, pp. 203-214, Apr. 2017.

Jinghua Guo graduated from Northeast Agricultural University in July 1989, majoring in mechanization. He is currently an associate professor in Wuxi Vocational College of Science and Technology. Mr. Guo's current research directions are automotive electricians & electronics, automotive electromagnetic compatibility, automotive electronic control technology, automotive network technology, and new energy vehicles.

Yuanyuan Liu was born in Shandong, China, in 1983. She received her B.S. degree in mechanical manufacturing and automation from Shandong University of Technology, Zibo, China, in 2004, M.S. degree in mechanical manufacturing and automation from Nanjing University of Aeronautics and Astronautics, Nanjing, China, in 2007. Ms. Liu is currently pursuing Ph.D. in control theory and control engineering in Jiangnan University, Wuxi, China. She is also an associate professor in Wuxi Vocational College of Science and Technology. Her current research interests include electric control technology and wireless power transfer technology of electric vehicles.

Design and Analysis of a Novel Linear Oscillating Actuator with Dual Stator Rectangular Geometry

Muhammad Jawad, Yu Haitao, Zahoor Ahmad, and Yulei Liu

School of Electrical Engineering, Southeast University Nanjing 210096, China
engrjawad@seu.edu.cn, htyu@seu.edu.cn, engrzahoor@seu.edu.cn, liuyulei@seu.ed.cn

Abstract – This paper proposes a new design of a linear oscillating actuator (LOA) with rectangular topology of stator and mover. The shape of a permanent magnet (PM) has a major impact on cost, mechanical strength, and generation of magnetic flux density. This design uses rectangular PMs that are relatively cheaper than tubular PMs. Proposed LOA operates on single phase AC loading source. All the design parameters are optimized by using parametric sweep and the response of the LOA in terms of thrust force is compared. The electromagnetic (EM) force received by the mover is investigated at various mover positions as well as at different values of the current. Motor constant is examined toward both directions of the force. Resonance phenomena is analyzed using input and output power of the LOA, which is the unique advantage of the LOA. Compared to the conventional LOA designs, the output parameters of the LOA, such as EM force, stroke, operating frequency and power, show great improvement with regards of volume of the proposed LOA. This topology shows significant development in terms of thrust force, motor constant, easy manufacturing and cost. Moreover, range of the stroke of proposed LOA is feasible for linear refrigeration system.

Index Terms – FEM, linear oscillating actuator, moving magnet, rectangular topology, resonance.

I. INTRODUCTION

Linear oscillating actuators (LOAs) provide linear oscillatory thrust force directly without using special mechanism (crank shaft) for converting rotary motion to linear oscillations [1]. Compared to conventional mechanism where rotary motion is converted to linear oscillation, mover of the LOA is directly attached to the piston and resonant springs. On the basis of simple structure, high power density and high efficiency, LOA received extensively more attention in industrial applications, such as compressor, vehicle suspension system, and bio-medical equipment [2, 3].

There are three types of LOA configurations of conventional topologies of LOA: moving magnet, moving coil, and moving iron. Moving magnet configuration is generally composed of coil housed in the stator and mover has permanent magnets (PMs) [4]. Moving coil LOA is comprised of coils placed on both stator and mover [5]. Moving iron LOA has winding coils on the stator and mover is only composed of iron of different shapes. The performance of moving magnet type LOA is lot better in contrast to the other type of LOAs on the count of high thrust density, high efficiency, smaller mover mass, and easy manufacturability [6, 7].

Tubular topology has squeezed structure and produces high flux density but the lamination of the core materials is very challenging. The core part of classical rotational equipment is laminated radially for the reduction of core loses. However, due to limitation of low flux density and small stacking factor, a new technique of axial lamination is analyzed in [8]. This investigation improves stacking factor that further improves amount of flux density in the air gap of LOA. Furthermore, back emf and thrust force of the LOA are also enhanced by using this new methodology. In contrast to this approaches, rectangular topology of LOA is more feasible for laminations. Conventionally, a rectangular topology is analyzed in [9, 10] where an E core stator is used and four PMs with opposite polarities are placed on the mover. This topology is simple and easy to fabricate. Moreover, PM used in rectangular LOA is also of rectangular shape and shape of the PM has significant effect on cost and housing on the mover. Reduction of iron loses is studied in [11], where a special formation of grove in the inner yoke is analyzed. Furthermore, the effect of number of groves is also examined.

There are two additional significances of LOA over conventional actuation mechanism: oscillations with adjustable stroke and operation at resonance frequency. Stroke of the LOA can be adjusted by input loading to the LOA. By increasing input power to the LOA, stroke of LOA increases, enhancing the cooling capacity of the refrigeration system [12]. Main limitation of high-input power is more copper loses due to which efficiency of system reduces [13]. Resonance at LOA is achieved by exciting it with frequency equal to mechanical

Submitted On: April 9, 2021
Accepted On: September 26, 2021
https://doi.org/10.47037/2021.ACES.J.361015

resonance frequency of the system. Mechanical resonance frequency is calculated by using the value of mover mass and spring stiffness [14]. At resonance condition, least amount of current is required for feasible operation of the LOA that improves the efficiency of the LOA [15, 16].

Moving magnet LOA with capability of self-holding is studied in [17]. This paper analyzed the effect of slot opening and magnetic circuit on thrust force and self-holding force. An E-core and C-core LOAs with different configurations of PMs placed on mover is analyzed and compared in [18]. A new topology of ferrite PM LOA is compared with conventional rare earth PM LOA in [19]. In this study, all the output parameters of LOA are investigated using ferrite PM, that indicates promising improvement. Another moving magnet machine is studied that provides both rotary and linear motion. This design uses rotary and linear arrangement of coils connected axially and circumferentially [20, 21].

This paper describes a detailed analysis of moving magnet, rectangular-shaped LOA for compressor in refrigeration system. Design topology and operating principle of the investigated LOA is explained. To show proposed topology in real view, CAD model is used. All the design parameters are optimized using parametric sweep tool. Output parameters like thrust force and stroke are analyzed and compared. Resonance phenomena are discussed by using design parameters, spring stiffness, and mover mass. Furthermore, all the output parameters are compared with conventional design of LOA.

II. DESIGN AND OPERATING PRINCIPLES

Mechanical structure of proposed LOA is composed of two main parts, two C-shaped rectangular stator cores and mover, as shown in Figure 1. Stators, stationary parts of the LOA, are further composed of core material and windings. Concentrated type winding is convoluted through back side of C-shaped stator core. Pole shoes, the end of two sides of the C-shaped core, are expanded to provide ease to the magnetic flux as magnetic flux lines rebound back through sharp edges of the core. Direction of the current through upper and lower stator coils is opposite for that it is wound in opposite directions. When the coils are excited by single phase AC, magnetic flux lines are started at one stator leg and end at the corresponding other stator leg.

Mover, moving part of LOA, is comprised of mover core and PMs. Two axially magnetized, rectangular-shaped PMs are housed at both ends of the mover. PMs' magnetization direction is opposite and toward the centered mover core. Mover core is placed between two PMs and poses a least reluctance rout for magnetic flux

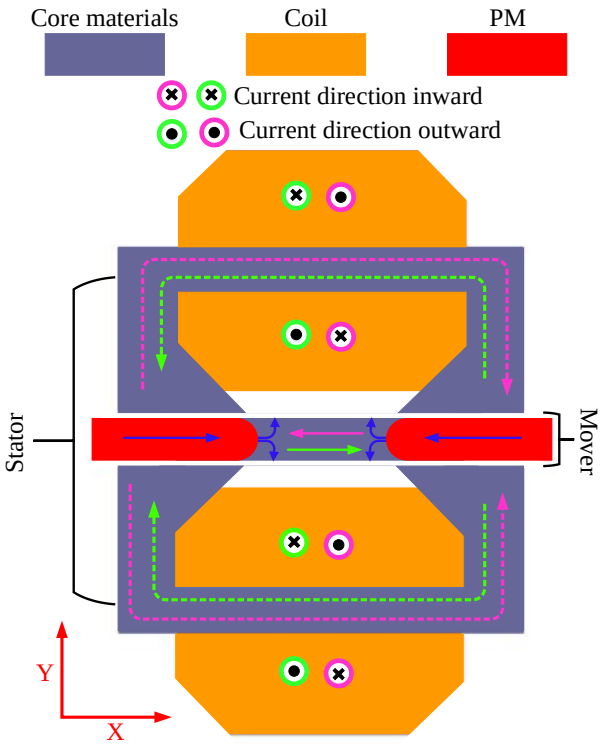

Fig. 1. 2-D topology of proposed LOA.

originated from one stator pole and ending at the other stator pole. The faces of the PMs toward the mover core are made fillet to generate flux lines in diverging mode. Additionally, fillet PMs help the mover to interact easily with stator poles.

Operating principles: when the coils of both the stators are energized in opposite directions, magnetic flux density is produced in opposite directions. Magnetic flux density produced by one stator leg links with mover core and then enters to the corresponding opposite pole of the same stator. Magnetic flux density of both coils and PM tends to enters into the corresponding other stator legs. According to the basic principles of magnetic field alignment phenomena, magnetic field lines strive to pass through least reluctance path. To provide least reluctance path, mover adjusts its position. Moreover, mover experiences an electromagnetic (EM) force in one direction. Since proposed LOA is operating on single phase AC so for a positive cycle of an AC, mover experiences EM force in one direction. Figure 2 (a) shows extreme $-x$ position of the mover. Direction of the current and rout followed by magnetic flux density is depicted by symbols and arrows, respectively. During remaining negative cycle of an AC, direction of electric current becomes opposite. Hence, the direction of magnetic flux density through stator poles becomes altered. At this time, mover receives EM force in the opposite direction, as shown in

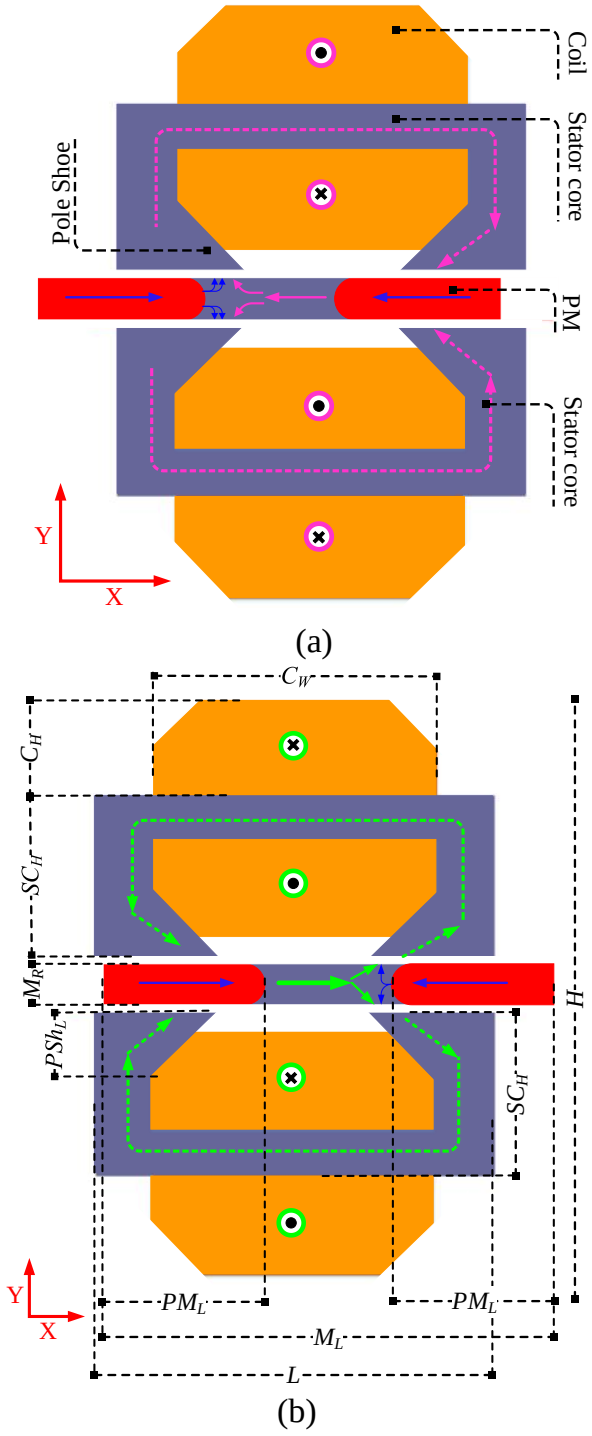

Fig. 2. Proposed LOAs: (a) $-x$ extreme position of the mover, (b) $+x$ extreme position of the mover.

Figure 2 (b). In Figure 2 (b), mover is displaced to $+x$ extreme position of the oscillations, as shown. Mover will receive a reciprocating EM when the coil is loaded by single phase alternating electric power. CAD model of proposed LOA is shown in Figure 3. Table 1 shows

Table 1: Dimensions of design parameters of the LOA

Description	Symbol	Value (mm)
Length of LOA	L	80
Height of LOA	H	116
Depth of LOA	D	100
Mover radius	M_R	5
Mover Length	M_L	90
Stator core height	SC_H	33
Pole shoe length	PSH_L	13
Coil height	C_H	20
Coil width	C_W	56
PM length	PM_L	32
Air gap	A_G	1

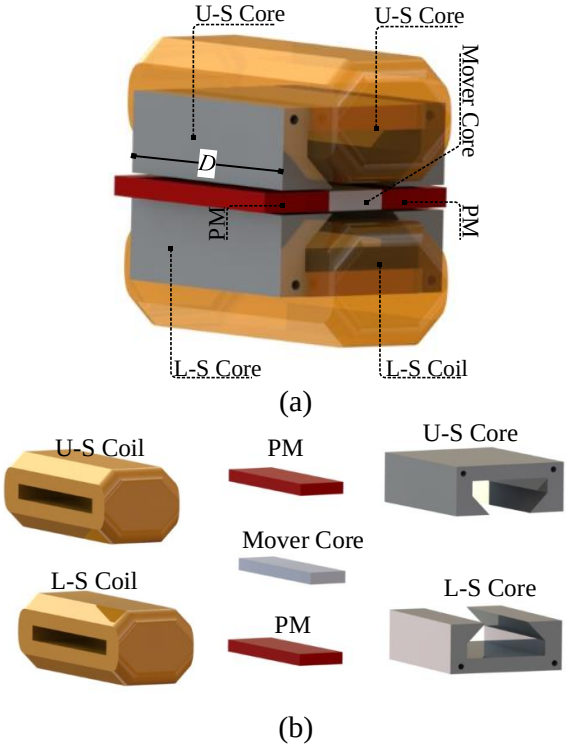

Fig. 3. 3-D topology of investigated LOA: (a) Complete view, (b) Open parts view.

the dimensions of different parameters of investigated LOA.

III. PARAMETRIC ANALYSIS

Parametric analysis of different parameters of the LOA is made by adopting parametric analysis technique and selecting the best magnitude of the investigated design parameter. Effect of different parameters like pole area and air gap is studied [23]. Effect of mover core length on thrust force, mover mass and operating resonance frequency is depicted in Figure 4.

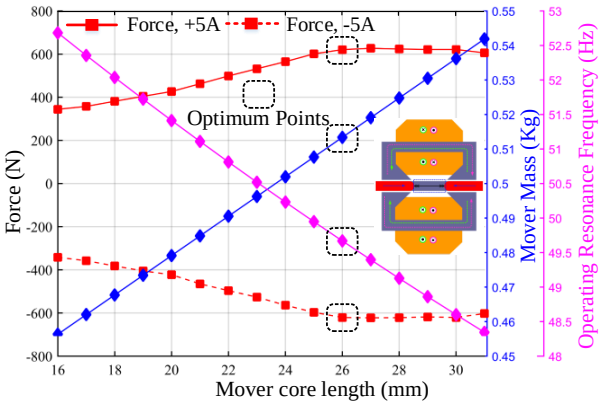

Fig. 4. Mover length optimization.

In this procedure, length of the PM is kept constant while mover core length is varied, due to which the overall length of the mover is also changed. EM force is verified for both directions of the current of value 5 A, as shown by red lines. Since, by increasing mover length, mover mass is also increased which further effects the value of operating resonance frequency. Blue and pink lines show effect of mover core length on mover mass and operating resonance frequency for spring stiffness of 50 KN/m, respectively. Optimum points are shown by dotted black squares. Figure 4 concludes that optimum value of mover core length is 26 mm. Additionally, at optimum value of mover core length, value of operating resonance frequency and mover mass are 50 Hz and 0.51 kg, respectively.

Furthermore, another parameter of LOA known as stator leg width is optimized and response is recorded in terms of EM force, as shown in Figure 5. During this procedure, position of the mover is fixed at mean position: from where the mover can move 6 mm back

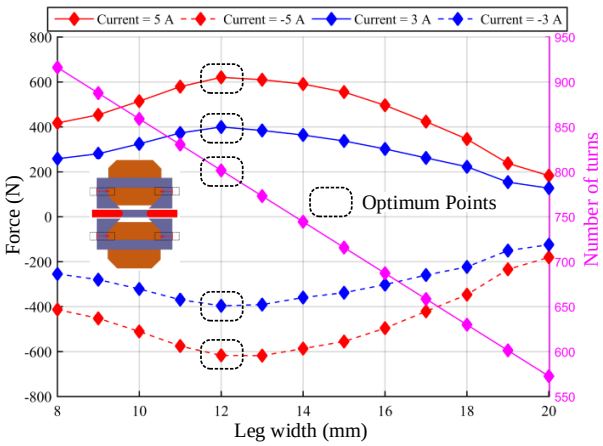

Fig. 5. Stator pole width optimization.

and forward. Other parameters of LOA like LOA height and length are kept constant. Stator leg width is varied toward the coil slot. Number of turns of coil is also kept changing. This process is repeated for 5 A, 3 A, –5 A, and –3 A shown by solid and dotted red and blue lines in Figure 5. This process concludes that optimum value of stator leg width is 12 mm at which the number turns of coil is 800.

IV. RESULTS AND DISCUSSIONS

Investigated LOA is simulated and its view is shown in Figure 6 where mover is displaced to extreme positions of oscillations. Current applied to the coil is 5 A DC with suitable arrangement of the current direction. Figure 6 (a) represents $+x$ extreme position of the mover and rout followed by magnetic field line is shown by an arrow. At this arrangement of the coil current direction, mover experiences EM force toward $+x$ direction. By altering the direction of the coils current, magnetic flux density direction becomes reverse, as shown in Figure 6 (b). At this route of current, direction of EM force becomes reverse and mover experiences EM force toward $-x$ direction. Hence by applying single phase AC, mover will experience an oscillatory EM force. Legend to the right of simulated view of the LOA shows magnitude of magnetic flux density at different portions of the LOA.

Magnetic flux density received by stator poles using 5 A DC is depicted in Figure 7. In this procedure, magnetic flux density is measured in the mid of air gap through a line in front of stator poles. Doted red and solid black lines show magnitude of magnetic flux density received by right, upper, and lower stator poles, respectively. Similarly, doted blue and solid pink lines show magnetic flux density received by left, upper, and lower stator poles, respectively.

Electromagnetic force response of proposed LOA for distinct magnitudes of the direct current is shown in Figure 8. This figure shows bi-directional EM force of the LOA for both direction of the DC. From the figure it is clear that there is linear relation between current and EM force. Current exceeding from 5 A value of the DC, there is some decrease in EM force per change in current due to saturation of the core materials. Motor constant (MC): EM force per Ampere current of the proposed LOA is 120 N/A. Proposed LOA shows identical MC toward both directions of the EM force.

EM force response of proposed LOA at different positions of the mover is presented in Figure 9. For proper explanation, every quarter of the figure is described separately. EM force shown in second quadrant displaces the mover from negative extreme position to the mean position of the oscillations. Mover will be

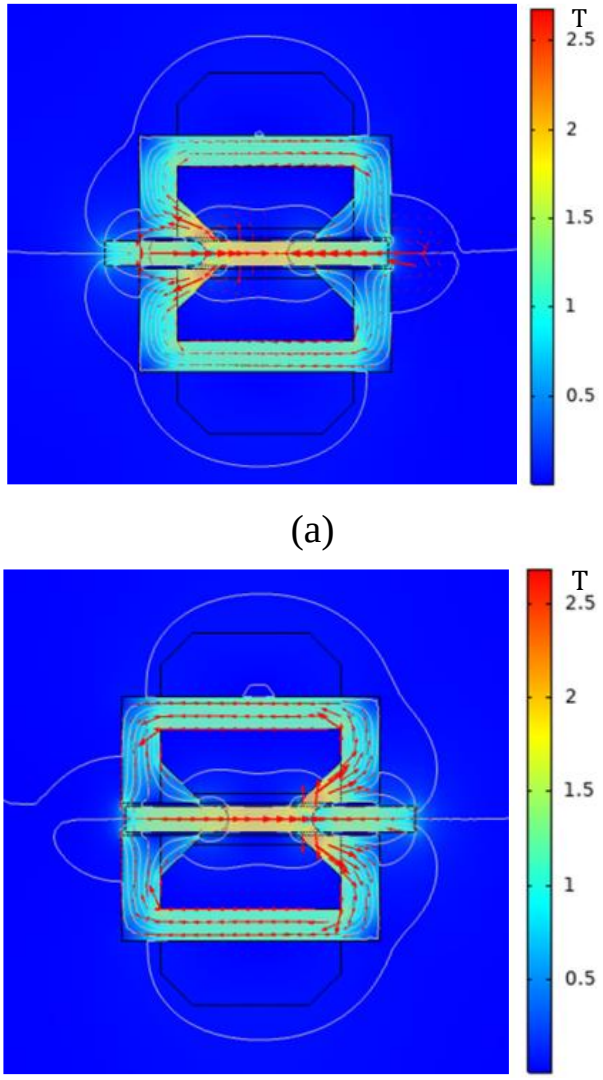

Fig. 6. Magnetic flux distribution view after simulating the proposed LOA. (a) EM force toward $+x$ direction, (b)EM force toward $-x$ direction.

further displaced to the positive extreme position by EM force shown by first quadrant of the Figure 9. By changing the direction of the current, direction of EM force becomes opposite as shown in third and fourth quadrants. EM force shown in third and fourth quadrants assists the mover to move from positive extreme position to the mean position and furthermore to the negative extreme position.

Figure 10 shows EM force produced by proposed LOA for different peak to peak values of an AC at mean position of the mover. Positive value of the force indicates that force is toward $+x$ axis and negative value of the force shows that the force is toward $-x$ axis. From

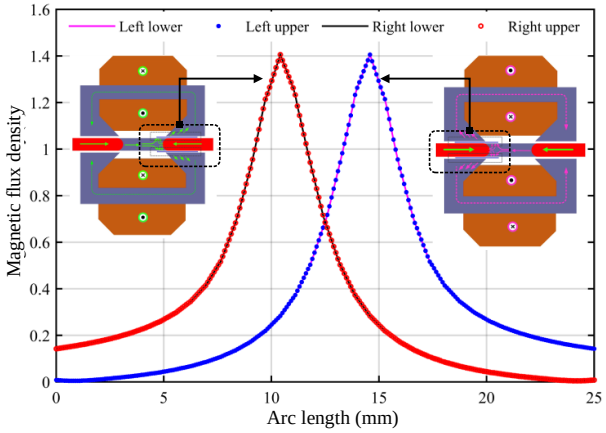

Fig. 7. Magnetic flux density linking with stator.

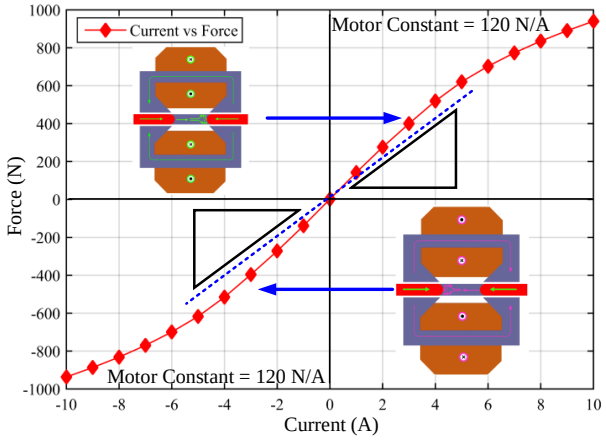

Fig. 8. EM force for different values of the DC.

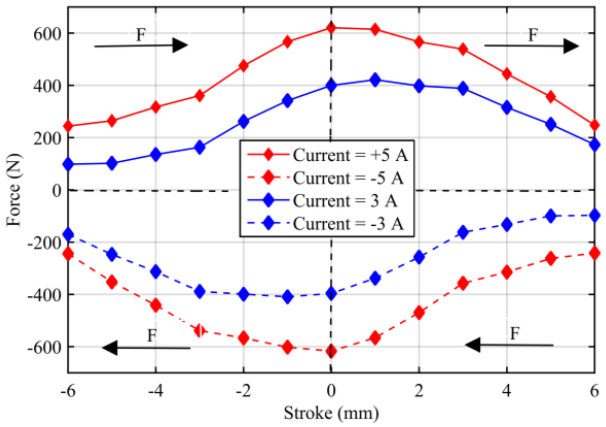

Fig. 9. EM force on different positions of the stroke.

Figure 10, it is also clear that by increasing peak to peak value of single-phase supply, EM force is increased equally to both sides. This analysis concludes that on sinusoidal input loading, force experienced by mover is sinusoidal.

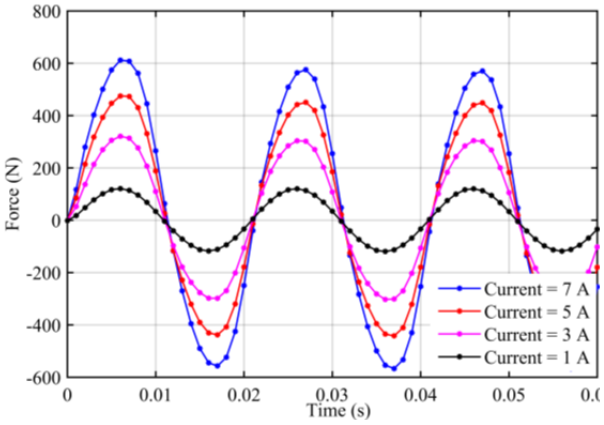

Fig. 10. Time-dependent EM force response.

V. RESONANCE

A. Mechanical resonance

By comparison with conventional reciprocating compressor, LOA is normally operating under resonance condition that enhances the operational results of the LOA to a great extent. For proper operation of the LOA, minimum input current is needed at resonance condition that further leads to high efficiency of the system. Output results of the LOA in response to the input current, like stroke to electromagnetic force fraction and stroke to current relation of the LOA are high at resonance conditions [12]. Resonance frequency is calculated on the basis of mover mass and stiffness of the springs installed. Mover mass is a design parameter of the LOA and cannot be reduced to a great extent. However, mover mass can be optimized to some range keeping other parameters, like EM force and stroke of the LOA at optimum value. Resonance condition of LOA is achieved by exciting the coils at resonance frequency. Relationship for determining the mechanical resonance frequency is

$$f_{mr} = \frac{1}{2\pi}\sqrt{k/m}, \tag{1}$$

where f_{mr} is the mechanical resonance frequency in Hz, k is the spring stiffness, and m is the mass of the mover. Value of spring stiffness selected in this analysis is 50 KN/m. The general demonstration of mass spring system of the LOA is depicted in Figure 11. Mechanical springs release and absorb energy to and from the system when it is required.

B. Electrical resonance

General representation of electrical system of the LOA is shown in Figure 12. In this figure, R is the resistance of actuator windings, X_L is the coil inductance, X_c is the required capacitance to get electrical resonance and αv is the back emf constant. At electrical resonance, inductive reactance of the coil is canceled out by capacitive reactance of capacitor. For producing capacitive reactance, an external capacitor is used. At electrical resonance condition, electrical system of the LOA act as a resistive load. Due to electrical resonance, LOA offers minimum impedance that improves the efficiency of the system. Relationship for finding necessary capacitance to produce electrical resonance in LOA is

$$C = 1/4\pi^2 f^2 L, \tag{2}$$

where C is the value of necessary capacitance to produce electrical resonance, f is the operative frequency of alternating loading, and L is the coil inductance.

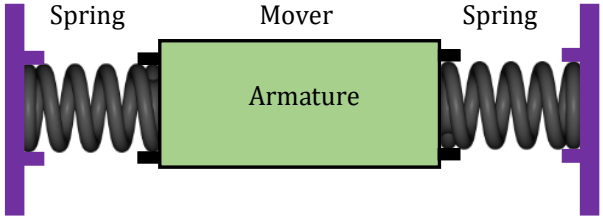

Fig. 11. Mechanical model of proposed LOA.

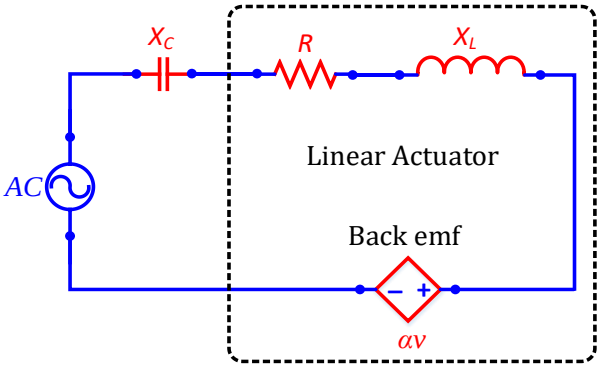

Fig. 12. Electrical circuit model of proposed LOA.

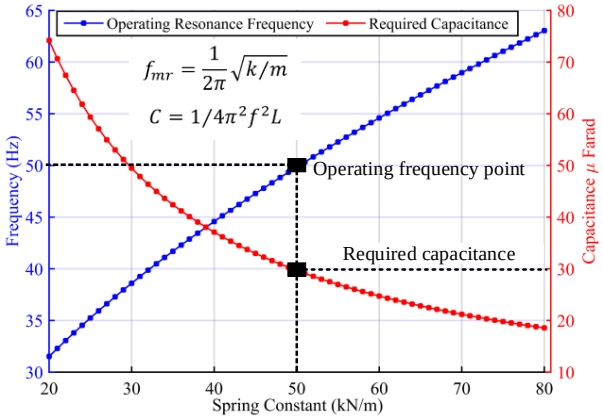

Fig. 13. Relation between spring constant, operating resonance frequency, and required capacitance.

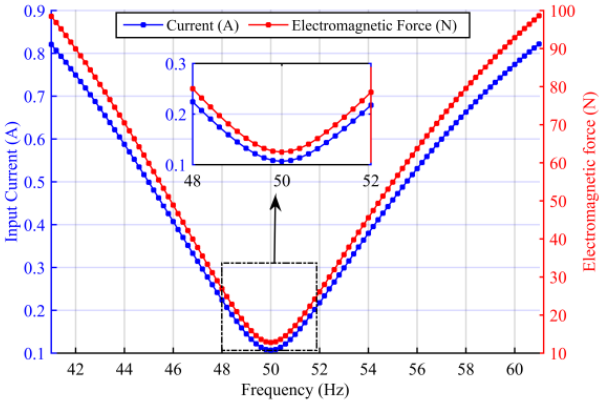

Fig. 14. Influence of operating frequency on input current and electromagnetic force.

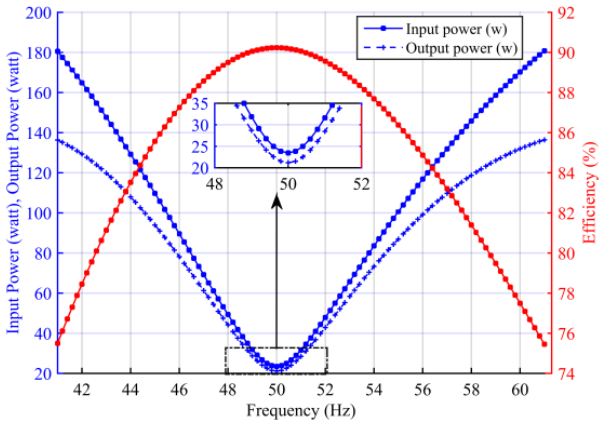

Fig. 15. Efficiency at various frequencies of the proposed LOA.

C. Simulation results of resonance analysis

As deliberated in earlier section, mechanical resonance frequency of LOA is calculated by using Equation (1). Additionally, on the basis of operating frequency, external capacitance required for creating electrical is determined by using Equation (2). Figure 13 shows the relation of spring constant with resonance frequency which further influences value of external capacitance attached in series. During this analysis, value of mover mass is 0.51 kg. Figure 13 reveals that for spring constant of value 50 KN/m, operating resonance frequency of proposed LOA is 50 Hz. Furthermore, necessary capacitance to create electrical resonance is 30 μF.

At resonance, due to minimum variance between applied voltage and back emf, minimum amount of current is passed through LOA that further provides minimum electromagnetic force [22]. Current and electromagnetic force relation derived in [12] are used to calculate influence of operating frequency on input current and electromagnetic force. Figure 14 shows the values of input current and electromagnetic force for different values of operational frequency. Since mechanical resonance frequency of proposed LOA is 50 Hz, there is only a minimum current that passes through LOA which further yields minimum electromagnetic force.

LOA input power is calculated by multiplying voltage across the coils and current flowing through the coils. Similarly, output power is determined by using the product of electromagnetic force and velocity of the mover. Mathematical formulas for current, electromagnetic force, and velocity are used which is derived in [12]. Figure 15 shows effect of operating frequency on output power, input power which further effects on efficiency of the LOA. Figure 15 reveals that on resonance frequency, proposed LOA operates at maximum efficiency. Shifting from the value of resonance frequency in either direction, difference between input power and output power increases and due to that efficiency reduces. At resonance frequency, proposed LOA gives maximum efficiency.

VI. COMPARISON WITH CONVENTIONAL DESIGNS OF LOAS

Performance parameters like volume, stroke, moving mass, MC, and efficiency comparison are shown in Table 2. This section overviews the design and performance comparison of investigated LOA with currently designed topologies of LOA for compressor application. Topology explored in [19] is moving magnet LOA where rare earth PM is replaced by ferrite PMs. PMs used in this topology of LOA is radially magnetized. Fabrication of such topology is complex and degrades the mechanical strength of mover structure. Moving magnet actuator investigated in [4] comprised of axially magnetized disk-shaped PMs. This topology is low cost and easy to fabricate. The main limitation of topology used in [4] is high mover mass (MM) due to which the value of operating resonance frequency is low. Another design analyzed in [6] is moving iron with coil housed on the stator. This topology has no PMs due to which the design cost is very low; however, MC of this design is very small. LOA topology investigated in [12] is E-core stator and mover composed of radially magnetized PM. Main complication of this topology is complex mover structure due to radially magnetized PMs housed. Performance behavior of this design is fair and feasible for refrigeration application.

Design topology of proposed LOA is simple and easy to manufacture compared to the conventional topologies of LOA. Structure of the PMs used in this topology is low cost and easy to arrange multiple PMs and to get desired dimensions. Winding of coil is open to the air, on account of that, cooling arrangement and replacing are feasible. Moreover, lamination of the core

Table 2: Parameters comparison of the investigated LOA with currently designed actuators

Spec....	**Ref. [19]**	**Ref. [4]**	**Ref. [6]**	**Ref. [12]**	**Prop. LOA**
Moving Type	PM	PM	Iron	PM	PM
Volume mm^3	6.5×10^5	7.8×10^5	1.5×10^6	1.7×10^6	9.3×10^5
Stroke (mm)	15	14	23	8.8	12
Moving Mass (Kg)	0.27	1	0.62	0.68	0.51
MC (N/A)	115	34.6	14	38	120
Efficiency (%)	——	89	87	94	90

part of the proposed LOA is very simple and easy to assemble.

VII. CONCLUSION

This article investigates and analyzes a novel design of rectangular structured moving magnet LOA for compressor in refrigeration system. Rectangular-shaped axially magnetized PMs are housed on the mover. Structure and operating principle are explained in detail. For better understanding, CAD model is designed. All the parameters are optimized on the basis of EM force and mover mass. Output results, like EM force and stroke amplitude are analyzed. Time-dependent EM force is examined for different peak to peak time-dependent input loading. Resonance phenomena are described and the influence of resonance frequency on input current, EM force, and efficiency are investigated. Finally, performance and design parameters of proposed and already designed LOAs are compared. Performance results of proposed LOA show significant outcomes while having simple structure and low cost. Moreover, fabrication complication in proposed LOA is minimum compared to conventional LOAs. Lamination of core materials is the most problematic part in tubular topology which is resolved. Proposed LOA is easy to laminate their core part. Hence it can be concluded that, proposed rectangular LOA is the best alternative of conventional tubular topologies of LOA.

REFERENCES

[1] K. H. Kim, S. M. Jang, J. H. Ahn, J. Y. Choi, and S. S. Jeong, "Design and characteristics analysis of linear oscillatory actuator with ferrite permanent magnet for refrigerator compressor," [J]. *Journal of Applied Physics,* vol. 117, no. 17, pp. 17C120, May. 2015.

[2] S. J. Wang, Z. D. Weng, and B. Jin, "Multi-objective Optimization of Linear Proportional Solenoid Actuator," In 2020 *International Applied Computational Electromagnetics Society Symposium (ACES) IEEE,* pp. 1-2, Jul. 2020.

[3] I. I. Abdalla, T. B. Ibrahim, and N. M. Nor, "A study on different topologies of the tubular linear permanent magnet motor designed for linear reciprocating compressor applications," *Applied Computational Electromagnetics Society (ACES) Journal,* vol. 31, no. 1, pp. 85-91, Jan. 2016.

[4] Z. Ahmad, A. Hassan, F. Khan, I. Lazoglu, "Design of a high thrust density moving magnet linear actuator with magnetic flux bridge," *IET Electric Power Applications,* vol. 14, no. 7, pp. 1256-1262, Mar. 2020.

[5] H. Kim, M. Yoon and J. Hong, "Design and performance analysis of moving-coil type linear actuator," 2011 *International Conference on Electrical Machines and Systems,* Beijing, China, pp. 1-4, Aug. 2011.

[6] A. Bijanzad, A. Hassan, and I. Lazoglu, "Analysis of solenoid based linear compressor for household refrigerator," *International Journal of Refrigeration,* vol. 74, pp. 116-128, Feb. 2017.

[7] N. Ahmad, F. Khan, N. Ullah, and M. Z. Ahmad, "Performance analysis of outer rotor wound field flux switching machine for direct drive application," *Applied Computational Electromagnetics Society (ACES) Journal,* vol. 33, no. 8, pp. 913-922, Aug. 2018.

[8] K. H. Kim, H. I. Park, S. S. Jeong, S. M. Jang, and J. Y. Choi, "Comparison of characteristics of permanent-magnet linear oscillating actuator according to laminated method of stator core," *IEEE Transactions on Applied Superconductivity,* vol. 26, no. 4, pp. 1-4, June 2016.

[9] Y. Asai, K. Hirata, and T. Ota, "Amplitude control method of linear resonant actuator by load estimation from the back-EMF," *IEEE Transactions on Magnetics,* vol. 49, no. 5, pp. 2253-2256, May 2013.

[10] Y. Asai, T. Ota, T. Yamamoto, and K. Hirata, "Proposed of novel linear oscillating actuator's structure using topology optimization," *IEEE Transactions on Magnetics,* vol. 53, no. 6, pp. 1-4, June 2017.

[11] J. Dai, Z. Zhao, S. Xu, C. Wang, J. Zhu, and X. Fan, "Inhibition of iron loss of the inner yoke in electromagnetic linear actuator," *IET Electric Power Applications*, vol. 13, no. 4, pp. 419-425, Jan. 2019.

[12] A. Hassan, A. Bijanzad, and I. Lazoglu, "Dynamic analysis of a novel moving magnet linear actuator," *IEEE Transactions on Industrial Electronics,* vol. 64, no. 5, pp. 3758-3766, May 2017.

[13] Z. Zhu, K. Liang, Z. Li, H. Jiang, and Z. Meng, "Thermal-economic-environmental analysis on household refrigerator using a variable dis-

placement compressor and low-GWP refrigerants," *International Journal of Refrigeration,* vol. 123, pp. 189-197, Mar. 2021.

[14] S. Khalid, F. Khan, Z. Ahmad, and B. Ullah, "Design and finite element analysis of modular C-Core stator tubular linear oscillating actuator for miniature compressor," *World Journal of Engineering,* 2021. https://doi.org/10.1108/WJE-03-2021-0142.

[15] A. Bijanzad, A. Hassan, I. Lazoglu, and H. Kerpicci, "Development of a new moving magnet linear compressor Part B: Design and modeling," *International Journal of Refrigeration,* vol. 113, pp. 70-79, May 2020.

[16] A. Hassan, A. Bijanzad, and I. Lazoglu, "Electromechanical modeling of a novel moving magnet linear oscillating actuator," *Journal of Mechanical Science and Technology,* vol. 32, no. 9, pp. 4423-4431, Sep. 2018.

[17] P. Immonen, V. Ruuskanen, and J. Pyrhönen, "Moving magnet linear actuator with self-holding functionality," *IET Electrical Systems in Transportation,* vol. 8, no. 3, pp. 182-187, Feb. 2018.

[18] X. Chen, Z. Q. Zhu, D. Howe and J. S. Dai, "Comparative study of alternative permanent magnet linear oscillating actuators," 2008 *International Conference on Electrical Machines and Systems,* Wuhan, China, IEEE, pp. 2826-2831, Oct. 2008.

[19] C. W. Kim, G. H. Jang, S. W. Seo, I. J. Yoon, S. H. Lee, S. S. Jeong, and J. Y. Choi, "Comparison of electromagnetic and dynamic characteristics of linear oscillating actuators with rare-earth and ferrite magnets," *IEEE Transactions on Magnetics*, vol. 55, no. 7, pp. 1-4, Jan. 2019.

[20] S. Mirić, M. Schuck, A. Tüysüz and J. W. Kolar, "Double stator linear-rotary actuator with a single set of mover magnets," 2018 *IEEE Energy Conversion Congress and Exposition (ECCE),* pp. 750-757, Sep. 2018

[21] H. Feng, J. Si, Z. Cheng, C. Gao, and W. Cao, "Rotary coupling magnetic field characteristics of a two-degree-of-freedom direct drive induction motor," *Applied Computational Electromagnetics Society (ACES) Journal,* vol. 34, no. 11, 2019.

[22] Z. Ahmad, A. Hassan, F. Khan, N. Ahmad, B. Khan and J. -S. Ro, "Analysis and design of a novel outer mover moving magnet linear oscillating actuator for a refrigeration system," *IEEE Access,* vol. 9, pp. 121240-121252, Aug. 2021.

[23] R. Trentini, D. dos Santos, O. H. Reichow, and R. Piontkewicz, "Dynamic modeling and parametric analysis of the magnetic stiffness on a radial heteropolar rotor magnetic bearing (RMB)," *International Journal of Electrical and Computer Engineering Research,* vol. 1, no. 1, pp. 9-14, 2021.

Muhammad Jawad was born in Pakistan in 1993. He received his B.S. degree in electrical engineering from University of Science and Technology, Bannu, KP, Pakistan in 2016. He got his M.S. degree from Southeast Univeristy in 2021. Currently, he is doing PhD degree in Southeast University, Nanjing, Jiangsu, China. His research interest is linear motor.

Haitao Yu PhD, professor, doctoral Supervisor. He received his PhD from Huazhong University of Science and Technology (HUST) in 1995. In 1997, he served as an associate professor in the School of Electric Engineering, HUST. During 1998–2003, academic exchange visits to Duke University and Canada. He served as editor of "Ocean Power Generation" special issue of Advances in Mechanical Engineering (SCI), and reviewer of various IEEE journals.

Zahoor Ahmad was born in KPK, Pakistan in 1993. He received BS degree in Electrical Engineering from University of Science and Technology, Bannu, KP, Pakistan in 2016 and MS degree in Electrical Engineering from COMSATS University Islamabad, Abbottabad Campus, Pakistan. He worked on research exchange program in GIK Institute for one plus year in Electrical Machine and Drive Lab. He is currently studying PhD in Electrical Engineering at Southeast University, Nanjing, Jiangsu, China. His research area is design of permanent magnet motors, linear oscillating actuator, and flux switching helical motors.

Yulei Liu was born in Jurong, Jiangsu, China in 1992. He received the B.S. degree in electric engineering from China University of mining and technology, in 2014 and M.S. degree in electric engineering from South China University of Technology, in 2018. He is currently pursuing the Ph.D. degree in electric engineering at Southeast University, Nanjing, Jiangsu, China. His research interests include permanent magnet motor, linear motor, magnetic gear motor, and magnetic lead screw.